THÈSE POUR OBTENIR LE GRADE DE DOCTEUR DE L'UNIVERSITÉ DE MONTPELLIER

En chimie physique

École doctorale Sciences Chimiques Balard (ED 459)

Préparé à l'I Institute de Chimie Séparative de Marcoule (UMP 5257)

Superchaotropic effect of anionic boron clusters on weakly soluble compounds and proteins in aqueous solutions

Présentée par Ioanna CHAZAPI

Le 26 Juin 2023

Sous la direction de Dr. Pierre BAUDUIN et Dr. Olivier DIAT

Devant le jury composé de

M Werner NAU, Pr., Jakobs Universität Bremen, Allemagne	Rapporteur
Mme Valérie RAVAINE, Pr., Université de Bordeaux, France	Rapporteur
Mme Evamarie HEY-HAWKINS, Pr., Universität Leipzig, Allemagne	Examinateur
Mme Christine EBEL, Directeur de recherche, IBS, France	Examinateur
M Martin IN, Pr., Université de Montpellier, France	Examinateur
Mme Christine ALMUNIA, Dr., JOLIOT/LI2D CEA Marcoule, France	Invitée
M Epameinondas LEONTIDIS, Pr., University of Cyprus, Cyprus	Invitée
M Olivier DIAT, Dr. Directeur de Recherche, ICSM CEA Marcoule, France	Co-directeur de thèse
M Pierre BAUDUIN, Dr., ICSM CEA Marcoule, France	Directeur de thèse

UNIVERSITÉ DE MONTPELLIER

Table of Contents

Acknowledgements 7
Abstract 9
Abstract en français 11
List of Figures 13
List of Tables 23
List of abbreviations 25
Introduction 29
References 32
Chapter I: State of the art 35
I.1 Specific ion effects 35
I.2 Specific nano-ion effect of nanometric-sized ions / the extension to superchaotropic ions 38
I.3 Boron clusters and their superchaotropic behavior 38
I.4 Cobalt bis-dicarbollide anion 42
I.4.1 Surfactant behavior of cobalt bis-dicarbollide anion 43
I.5 Summary history of boron clusters 46
References 48
Chapter II: Solubilization of hydrophobic compounds by boron clusters 55
II.1 Solubilization of hydrophobic compounds 55
II.1.1 Micellar solubilization 55
II.1.2 Microemulsions 58
II.1.3 Hydrotropes 58
II.1.4 Co-solvency 59
II.1.5 Solubilization by complexation (host-guest) 59
II.2 Results 60
II.2.1 Solubilization of hydrophobic compounds by NaCOSAN 60
II.2.2 Solubility of butanol in the presence of NaCOSAN 64
II.2.3 Molecular level: 2-BuOH solubility in the presence of COSAN (UV-Visible) 67
II.2.4 Supramolecular level: 2-BuOH and 1-BuOH solubility in the presence of NaCOSAN and its derivatives 69
II.2.4.1 Supramolecular level: 2-BuOH solubility in the presence of NaCOSAN 69
II.2.4.2 Supramolecular level: 2-BuOH solubility in the presence of NaI_2COSAN 74

II.2.4.3 Supramolecular level: 1-BuOH solubility in the presence of NaCOSAN 76
II.2.5 Size, shape and molecular distribution of 1-BuOH and 2-BuOH in the presence of NaCOSAN (SANS, ellipsoidal model) 76
II.2.6 Solubilization of more hydrophobic compounds by NaCOSAN/2-BuOH co-assemblies 83
II.2.6.1 Supramolecular level: Hydrophobic compounds solubility in the presence of COSAN/2-BuOH co-assemblies (SWAXS-SANS) 86
II.2.7 Solubility of butanol in the presence of halogenated dodecaborate clusters 88
II.2.8 SAXS- and SANS-fit parameters used in this chapter 92
II.3 Conclusions of chapter II 100
References 101
Supporting Information of Chapter IV 105
Chapter III: Specific interactions of boron clusters with proteins 116
III.1 Proteins under investigation 121
III.2 NaCOSAN in interaction with myoglobin (Mb) 129
III.2.1 Interaction between NaCOSAN and Mb followed by UV-Vis 129
III.2.2 Interaction of NaCOSAN/Hemin followed by UV-Vis 131
III.2.3 Interaction of NaCOSAN/Mb followed by fluorescence technique. 132
III.2.4 Interaction of NaCOSAN/ApoMb followed by fluorescence 134
III.2.5 Interaction of NaCOSAN/Mb followed by circular dichroism (CD) 135
III.2.6 Interaction of NaCOSAN/Mb followed by dynamic light scattering (DLS) 140
III.2.7 Supramolecular level: Interaction of NaCOSAN/Mb followed by small angle X-ray scattering 141
III.2.8 Interaction of NaCOSAN/Mb followed by small angle X-ray scattering at different temperatures 143
III.3 NaCOSAN in interaction with two other proteins: carbonic anhydrase or trypsin inhibitor 144
III.3.1 Interaction of NaCOSAN/BCA and NaCOSAN/SKTI followed by fluorescence . 145
III.3.2 Interaction of NaCOSAN/BCA and NaCOSAN/SKTI followed by circular dichroism (CD) 145
III.3.3 Formation of NaCOSAN/BCA fibrils followed by fluorescence 148
III.3.4 Interaction of NaCOSAN/BCA and NaCOSAN/SKTI followed by dynamic light scattering (DLS) 149

III.3.5 Supramolecular level: Interaction of NaCOSAN/BCA and NaCOSAN/SKTI followed by small angle X-ray scattering 150
III.4 Chaotropic salt in interaction with myoglobin-comparison at pH=10 153
III.4.1 Classical chaotropic (NaSCN) in the presence of Mb-comparison with NaCOSAN 153
III.4.2 NaCOSAN in comparison with dodecaborates ($Na_2B_{12}X_{12}$) in the presence of Mb 154
III.4.2.1 NaCOSAN in comparison with dodecaborates ($Na_2B_{12}X_{12}$) in the presence of BCA or SKTI 157
III.4.3 Effect of the classical surfactant (SDS) on Mb and comparison to NaCOSAN 159
III.4.3.1 NaCOSAN in comparison with a classical surfactant (SDS) in the presence of BCA or SKTI 160
III.5 pH effect 161
III.5.1 Mb in the presence of NaCOSAN at two different pH. 161
III.5.2 BCA or SKTI in the presence of NaCOSAN at two different pH. 164
III.5.3 Mb in the presence of NaSCN at two different pH. 165
III.5.4 Mb in the presence of SDS at two different pH. 166
III.6 SAXS-fit parameters used in this chapter 168
III.7 Conclusions of Chapter III 170
References 173
Supporting information of Chapter III 179
Chapter IV: Photophysical investigation of cobalta-bis dicarbollides 193
IV.1 Steady state absorption of NaCOSAN 193
IV.2 Fluorescence of NaCOSAN in H_2O 194
IV.3 Photoluminescence of NaCOSAN in H_2O 199
IV.4 Pump probe photoluminescence of NaCOSAN in H_2O 202
IV.4.1 Pump probe results of NaCOSAN in H_2O 202
IV.5 Photophysical study of NaI_2COSAN 205
IV.5.2 Fluorescence of NaI_2COSAN in H_2O 205
IV.5.3 Pump probe results of NaI_2COSAN in H_2O 206
IV.6 Photophysical study of NaCOSAN in the presence of 2-BuOH 207
IV.6.1 Fluorescence of NaCOSAN in the presence of 2-BuOH 208
IV.6.2 Pump probe results of NaCOSAN in the presence of 2-BuOH 210

IV.7 Conclusions of Chapter IV 213
References 215
Supporting information of Chapter IV 217
General Conclusions 231
Perspectives 233
Résumé en français 235
References 241

Acknowledgements

As this thesis comes to an end, I would like to express my sincere gratitude to each person who has supported me in any manner.

First and foremost, I would like to thank my thesis supervisors Olivier Diat and Pierre Bauduin. I appreciate your guidance and support throughout my Ph.D. research. You both contributed immensely to my growth and learning to become a researcher with greater independence. I would additionally like to thank you for all the chances you gave me to participate in international conferences, summer schools, and experiments at various synchrotrons, thereby enhancing my scientific qualifications.

In addition, I would like to extend my gratitude to Dr. Christine Almunia for her guidance, and cordial and perpetual advice throughout our collaboration. Thank you for all of your support, patience, and hilarious coffee breaks.

In addition, I would like to thank Dr. Epameinondas Leontidis, professor at the chemistry department of the University of Cyprus, for his unwavering support throughout my years of research. I would also like to thank him for his invaluable help in organizing and conducting photophysical studies. Special thanks to Dr. Andrea Othonos and Dr. Grigorio Itsko, professors at the physics department of the University of Cyprus. Dr. Othonos gave me valuable help with the pump-probe experiments conducted at his Laboratory of Ultrafast Science, and Dr. Grigorio Itsko and his group made it possible for me to have time-resolved photoluminescence experiments performed at their Experimental Condensed Matter Physics Lab.

I would like to extend a big thank you to all the members of the L2IA group, from 2019 to 2023, for the positive atmosphere in the lab and our outstanding collaboration throughout the years. A special thank you to Amelie Cartier, whose internship I had the privilege of supervising, who contributed to parts of my thesis through her diligent lab work, and for her patience in understanding my French. I would also like to thank Dr. Tony Chave and Dr. Matthieu Virot.

I would like to express my gratitude for the collaborations and discussions with the many scientists I have met throughout this thesis. Thank you to Dr. Kuno Schwärzer for synthesizing and providing a deuterated compound that was used in this thesis. Thank you to the beam line contacts, Theyencheri Narayanan (ESRF) and Joachim Kohlbrecher (PSI), for their support

during the experiments. I would like to thank Clara Vinãs and Francesc Teixidor for our fruitful discussion at the Autonomous University of Barcelona (UAB). Thank you to Jordi Faraudo for his interest in conducting DFT calculations and MD simulations on our systems, as well as for our fruitful discussions. At the beginning of my thesis, I had the opportunity to participate in experiments at the DESY synchrotron in Hamburg for a different research project. I would like to thank Dr. Emanuel Schneck for our collaboration and Dr. Gerald Brezesinski for his patience and explanations throughout these DESY synchrotron experiments. A special thank you to my supervisors once again, for giving me this opportunity at the very beginning of my PhD.

There are many more people at the ICSM who have made this thesis period very pleasant. I am truly thankful to all of my colleagues and close friends, particularly Mohan, Elizabeth, and Ali, for their unwavering support throughout the entirety of my thesis and our international dinners.

I want to express my gratitude to my family and friends for their unending support. My parents deserve special recognition for their inexhaustible advice and moral support. My aunt Evdokia is also deserving of special recognition for all of her helpful advice. Furthermore, I want to thank my Cypriot friends, Anna, Despina, and Kostas, for their unending support from my earliest steps in chemistry to today.

In addition, I would like to thank my best friend Anastasia and my brother Nickos, who were always there to remind me of my goal. I thank them for their patience, support, and countless phone calls.

Abstract

Ion Specific Effects (ISE) are implicated across several physicochemical and biological phenomena. Ions were classified as salting-in or salting-out depending on the capacity of their salts to affect the solubility of macromolecules and colloids in aqueous solutions. Recently, ISE were investigated with inorganic nanometric-sized ions (nano-ions), such as anionic polyoxometalates and boron clusters. Since the salting-in effects of low-charge density nano-ions are substantially more pronounced than those of classical chaotropic ions, they have been named "superchaotropes". This thesis examines the impact of anionic boron nano-ions on sparingly soluble hydrophobic molecules and proteins in aqueous solutions in order to draw conclusions on their superchaotropic nature.

Solubilization of hydrophobic compounds in water is commonly accomplished by the addition of organic solubilizers, e.g., amphiphiles, solvents, macrocycles. In the first part of this research, non-amphiphilic boron nano-ions were used as a novel method for the solubilization of sparingly water-soluble (hydrophobic) substances. Combining spectroscopic and scattering methods, the solubilization mechanism of hydrophobic substances by nano-ions was understood at the molecular and supramolecular levels. It was established that nano-ions solubilize hydrophobic compounds through the formation of thermodynamically stable co-assemblies. It was also shown that these co-assemblies effectively solubilize a wider variety of hydrophobic compounds.

In the second part, the effect of nano-ions on more complex molecules, e.g., proteins, was investigated. By combining spectroscopic and scattering techniques, a similar strategy was followed to probe the structure at molecular and supramolecular scales. It was found that boron clusters induce protein assembly without strong protein denaturation. The efficiency of the boron clusters to promote protein assembly increases with their (super)chaotropicity. Moreover, it appears that the nano-ion induced protein assembly increases the stability of proteins against denaturation by temperature.

The formation of supramolecular assemblies has a significant impact on electron transfer processes and, consequently, on photocatalytic efficiency. In the third part, the focus was on the effect of self-assembly and co-assembly with organic solutes on the photophysical properties of the cobalta-bis dicarbollide boron clusters. To achieve this aim, a combination of fluorescence and photoluminescence techniques in steady state and time-resolved mode were used. Despite earlier claims in the literature, it was discovered that cobalta-bis dicarbollide boron clusters do indeed exhibit fluorescence. It was found that changes in fluorescence signals

correlate with the transitions in the self-assembly sequence of cobalta-bis dicarbollide in water, from monomers to vesicles to micelles. It is noteworthy that so far the transition from monomers to vesicles has never been determined experimentally due to the lack of sensitivity of other techniques in the dilute regime. Pump-probe photoluminescence identifies potential new transitions resulting from the formation of supramolecular assemblies. Moreover, an increase in lifetime in the picosecond range was observed at cluster concentration, where the transition from the vesicle/monomer to the micellar state takes place. This work shows that fluorescence and photoluminescence techniques can elucidate molecular assembly properties and intermolecular forces of nano-ions.

To conclude, the superchaotropic behavior of nano-ions is a versatile tool to be used in novel formulations of soft matter materials and applications.

Abstract en français

Les effets spécifiques des ions (ISE) sont impliqués dans plusieurs phénomènes physicochimiques et biologiques. Les ions ont été classés en tant que salting-in ou salting-out en fonction de la capacité de leurs sels à affecter la solubilité des macromolécules et des colloïdes dans les solutions aqueuses. Récemment, ISE a été étudié avec des anions inorganiques de taille nanométrique (nano-ions), tels que les polyoxometalates et les clusters de bore. Comme les effets de salting-in des nano-ions à faible densité de charge sont nettement plus prononcés que ceux des ions chaotropes classiques, ils ont été qualifiés "superchaotropes". Cette thèse examine l'impact des nano-ions de bore sur des molécules peu solubles et des protéines dans des solutions aqueuses afin de comprendre les mécanismes physico-chimiques sous-jacents à leur nature superchaotrope.

La solubilisation de composés hydrophobes dans l'eau est généralement réalisée par l'ajout de solubilisant organiques, par exemple des amphiphiles, des solvants, des macrocycles. Dans la première partie de cette recherche, des nano-ions de bore non amphiphiles ont été utilisés comme nouvelle approche de solubilisation de substances peu solubles dans l'eau. En combinant des méthodes spectroscopiques et de diffusion du rayonnement, le mécanisme de solubilisation de substances hydrophobes par les nano-ions a été compris aux niveaux moléculaire et supramoléculaire. Il a été établi que les nano-ions solubilisent les composés peu solubles par la formation de co-assemblages thermodynamiquement stables. Il a également été démontré que ces co-assemblages solubilisent efficacement une plus grande variété de composés hydrophobes.

Dans la deuxième partie, l'effet des nano-ions sur des molécules plus complexes, comme les protéines, a été étudié. En combinant des techniques spectroscopiques et de diffusion, une stratégie similaire a été suivie pour sonder leurs structures à l'échelle moléculaire et supramoléculaire. Il a été constaté que les clusters ioniques de bore induisent l'assemblage des protéines sans dénaturation importante de celles-ci. L'efficacité des clusters de bore à promouvoir l'assemblage des protéines augmente avec leur (super)chaotropicité. De plus, il se l'assemblage de protéines induit par les nano-ions semble prévenir de leur dénaturation par la température.

La formation d'assemblages supramoléculaires à un impact significatif sur les processus de transfert d'électrons et, par conséquent, sur l'efficacité photocatalytique. C’est pourquoi dans

la troisième partie, l'accent a été mis sur l'effet de l'auto-assemblage et du co-assemblage avec des solutés organiques sur les propriétés photophysiques des clusters de bore cobalta-bis dicarbollide. Pour atteindre cet objectif, une combinaison de techniques de fluorescence et de photoluminescence en mode statique et en mode résolu dans le temps a été utilisée. En dépit d'affirmations antérieures dans la littérature, il a été découvert que les clusters de bore cobalta-bis dicarbollide présentent effectivement une fluorescence. Il a été constaté que les changements dans les signaux de fluorescence sont corrélés avec les transitions dans la séquence d'auto-assemblage du cobalta-bis dicarbollide dans l'eau, du monomère à la vésicule puis à la micelle. Il convient de noter qu'en particulier, la transition monomère-vésicule n'a jamais été déterminée précisément en raison du manque de sensibilité de nombreuses techniques dans le régime dilué. Les travaux de cette thèse ont mis en évidence une augmentation d'un temps caractéristique de la durée de vie de l'ordre de la picoseconde et lié au transition électronique à la transition de l'état monomère/vésicule à l'état d'agrégation micellaire. Ce travail montre que les techniques de fluorescence et de photoluminescence peuvent permettre d'approfondir nos connaissances des propriétés d'assemblage moléculaire des nano-ions et des forces intermoléculaires associées.

En conclusion, par ces travaux il est montré que l'usage de l'effet superchaotropique des nano-ions peut être un outil polyvalent à utiliser pour de nouvelles formulations en matière molle et des applications matériaux.

List of Figures

Figure 1.1. Typical ordering of anions of Hofmeister series…….35
Figure 1.2. Separation of alkali metal cations and halides between strong hydrated (kosmotropes) and weakly hydrated (chaotropes) species (left). Formation of inner sphere ion pairs occurs between ions with similar hydration free energy and similar water affinity (right), considering an ion as a sphere with a point charge at its center……..37
Figure 1.3. The classic hofmeister series (left) and the extended one (right)……38
Figure 1.4. Nanometer-sized anionic boron clusters were investigated in this thesis……...39
Figure 1.5. The cobalt bis-dicarbollide (COSAN) anion is composed of two bulky dicarbollide semi cages that sandwich a cobalt(III) whose shape is compared to the Greek letter q (far right).....42
Figure 1.6. Atomic structure of the cobalt bis-dicarbollide anion in its three rotameric forms (cis-, gauche- and trans-)……...43
Figure 1.7. Surface tension of air-water interface as a function of COSAN concentration…...44
Figure 1.8. Timeline of selected events from the history of boron cluster chemistry and supramolecular chemistry…….47
Figure 2.1. Schematic view of direct micelles formation in aqueous phase……..55
Figure 2.2. Critical packing parameter and the expected aggregates shape in solution……56
Figure 2.3. Schematic view of the three basic domain of a direct surfactant's micelle…….56
Figure 2.4. Three schematic representations of the incorporation of the solutes (black squares) into micelles depending on the hydrophobic characteristics of the solute…….57
Figure 2.5. Schematic representation of solubilisation increase of hydrophobic solutes "S" just above the CMC of the surfactant / solute mixture……..57
Figure 2.6. Comparison of solubilization curve of solute between surfactant and hydrotropes……...58
Figure 2.7. Schematic representation of host-guest solubilization……..……59
Figure 2.8. Illustration of examples of solubilization curve of cyclodextrins. Blue curves correspond to A-type solubility profiles, and red curve corresponds to B-type solubility profiles……..……60
Figure 2.9. The compounds that can be solubilized by COSAN are shown on the log P scale, where **1** corresponds to 2-BuOH (LogP = 0.66), **2** 1-BuOH (0.88), **3** n-pentanol (1.51), **4** n-

hexanol (2.03), **5** n-octanol (3.0), **6** quinizarine (3.7) and **7** Sudan I (5.6). The given logP values were taken from PubChem……61
Figure 2.10. 1- and 2-phase limits in the ternary COSAN/water/2-BuOH system with mass fraction of butanol in water on the x-axis and molar concentration of COSAN on the y-axis. Phase diagram obtained at ambient temperature. The dashed green area of the graph corresponds to the dashed green area of the tie line graph……62
Figure 2.11. Absorptivity of NaCOSAN as a function of different 2-BuOH percentages……63
Figure 2.12. Solubility of 2-BuOH in water (S in mol/L) at 22°C as a function of NaCOSAN concentration. The horizontal dark dashed line corresponds to the solubility value of 2-BuOH in pure water, S_0. The arrow indicates the break observed in the evolution of the 2-BuOH solubility curves……64
Figure 2.13. Solubility of 2-BuOH in water (S in mol/L) at 22°C as a function of NaDS concentration. The horizontal dark dashed line corresponds to the solubility value of 2-BuOH in water, S_0. The arrows indicate the breaks observed in the evolution of the 2-BuOH solubility curves……...65
Figure 2.14. Solubility of 2-BuOH in aqueous γ-cyclodextrin (green circles) and β-cyclodextrin (red circles) solution of varying concentrations at 22°C. The inset corresponds to a zoom of β-cyclodextrin's solubility curve……65
Figure 2.15. Solubility of 2-BuOH in water (S in mol/L) at 22°C as a function of NaI_2COSAN concentration. The horizontal dark dashed line corresponds to the solubility value of 2-BuOH in water, S_0……68
Figure 2.16. Solubility of 1-BuOH in water (S in mol/L) at 22°C as a function of NaCOSAN concentration. The horizontal dark dashed line corresponds to the solubility value of 1-BuOH in water, S_0……...…67
Figure 2.17. Solubility of 2-BuOH (blue triangles) as a comparison with the solubility of 1-BuOH (orange squares) in water at 22°C as a function of NaCOSAN concentration……67
Figure 2.18. UV-Visible spectra of a) 0.0008 mol L^{-1}, b) 0.004 mol L^{-1}, c) 0.007 mol L^{-1}, d) 0.01 mol L^{-1}, e) 0.013 mol L^{-1} and f) 0.020 mol L^{-1} NaCOSAN in the presence of different 2-BuOH concentrations……...68

Figure 2.19. λ_{max} evolution of NaCOSAN at different concentration: 0.0008 mol L^{-1} (dark circles), 0.004 mol L^{-1} (red square), 0.007 mol L^{-1} (dark blue triangles), 0.01 mol L^{-1} (light blue triangles), 0.013 mol L^{-1} (orange rhombus) and 0.02 mol L^{-1} (green circles), as a function of 2-BuOH concentration expressed here as S/S_0. The red dashed line corresponds to λ_{max} of

NaCOSAN in pure H_2O $\left(\lambda_{max}^{NaCOSAN^w}\right)$ and the dark dashed line is the λmax in 2-BuOH$\left(\lambda_{max}^{NaCOSAN^o}\right)$……...68
Figure 2.20. SWAXS spectra of water (blue), 2-BuOH (orange), 2 mol L^{-1} 2-BuOH (red), 0.09 mol L^{-1} NaCOSAN (dark) and 0.09 NaCOSAN in the presence of 4 mol L^{-1} 2-BuOH (green).69
Figure 2.21. SAXS (top) and WAXS (bottom) spectra of NaCOSAN in water (0.09 mol L^{-1}) increasing 2- BuOH concentration, as shown on the solubility phase diagram in the inset. In the upper graph, the red dashed line corresponds to a Guinier fit……..71
Figure 2.22. The evolution of the scattered intensity at q = 1 nm^{-1}, increasing 2-BuOH concentration at a fixed NaCOSAN concentration……72
Figure 2.23. SAXS fit of 0.09 mol L^{-1} NaCOSAN concentration in the presence of (a) 4, (b) 3.8, (c) 3.6, (d) 3.4, (e) 3.2 and (f) 3 mol L^{-1} 2-BuOH. The red points corresponds to the experimental data and the dark dashed line to the Guinier fit……73
Figure 2.24. Radius of gyration of hybrid co-assemblies of 0.024 mol L^{-1} (orange circles), 0.04 mol L^{-1} (light blue circles) and 0.09 mol L^{-1} (dark circles) NaCOSAN in the presence of different concentrations of 2-BuOH……..74
Figure 2.25. SWAXS spectra of a) 0.075 mol L^{-1}, b) 0.050 mol L^{-1} NaI_2COSAN in aqueous solution in the presence of different 2-BuOH concentrations, as shown on the solubility phase diagram in the inset of a) and b)……75
Figure 2.26. Radius of gyration of hybrid co-assemblies of 0.04 mol L^{-1} NaI_2COSAN in the presence of different concentrations of 2-BuOH……...75
Figure 2.27. SWAXS spectra of different NaCOSAN concentrations in the presence of different 1-BuOH concentrations, as shown on the solubility phase diagram in the inset…...76
Figure 2.28. SANS spectra in absolute scattering unit of a) 0.015 mol L^{-1}, b) 0.04 mol L^{-1} NaCOSAN in D_2O in the presence of 1.3 mol L^{-1} and c) 1.6 M hydrogenated 1-butanol (BuOH, contrast I in red) and fully deuterated 1-butanol (BuOD, contrast II in blue). The sample with hydrogenated BuOH was also measured by SAXS (in green). Full lines represent simultaneous fits of the three scattering spectra (i.e. with same composition but with three different contrasts: two contrasts in SANS using deuterated and hydrogenated BuOH and the contrast in SAXS) using the same triaxial ellipsoid model, the details on the fitting procedure and parameters are listed below in the section II.2.6……77
Figure 2.29. Sketch of the co-assemblies with the two contrasts in SANS with BuOH (left, contrast I) and with BuOD (right, contrast II) color coded with the scattering length densities

of the different components. Deuterium-rich region in light blue and hydrogen-rich region in light orange……...77
Figure 2.30. SWAXS spectra of 0.04 mol L^{-1} NaCOSAN in the presence of 1.6 mol L^{-1}deteurated 1-BuOH (red line) and 1.6 mol L^{-1} protonated 1-BuOH (dark line)……78
Figure 2.31. SANS spectra of a) 0.015 mol L^{-1}, b) 0.04 mol L^{-1} NaCOSAN in D_2O in the presence of 3 mol L^{-1} hydrogenated 2-BuOH and c) 0.04 mol L^{-1} NaCOSAN in D_2O in the presence of 4 mol L^{-1} hydrogenated 2-BuOH.. The sample with hydrogenated 2-BuOH was also measured by SAXS (in green). Full lines represent simultaneous fits of the scattering spectra using the same triaxial ellipsoid model, the details on the fitting procedure and parameters are listed below in the section II.2.6……81
Figure 2.32. The compounds that can be solubilized by COSAN (yellow region) and by the COSAN/2-BuOH co-assemblies (blue region) are shown on the logP scale, where 1 corresponds to 2-BuOH (LogP = 0.61), 2 1-BuOH (0.88), 3 benzyl alcohol (1.1), 4 1-pentanol (1.51), 5 toluene (2.73), 6 eucalyptol (2.74), 7 linalool (2.97), 8 b-citronellol (3.239), 9 curcumin (3.29), 10 citral (3.45), 11 geraniol (3.56) and 12 sudan I (5.6). The given logP values were taken from PubChem……84
Figure 2.33. Solubility of a) benzyl alcohol, b) toluene, c) eucalptol, d) linalool, e)b-citronellol, f) curcumin, g) citral, h) geraniol and k) sudan I as a function 2-BuOH concentration (S/S_0) and for different NaCOSAN concentrations: 0 (dark squares), 10 (red circles) and 20 mM NaCOSAN (blue triangles)……...86
Figure 2.34. SWAXS spectra of different compositions of NaCOSAN/2-BuOH co-assemblies in the presence of different concentrations of (a), (b) eucalyptol **6** and (c), (d)citral **10**. The (a), (c) corresponds to 0.01 mol L^{-1} and the (b), (d) 0.02 mol L^{-1} NaCOSAN.……..…87
Figure 2.35. SANS spectra of NaCOSAN/2-BuOH co-assemblies (0.02 mol L^{-1}NaCOSAN and 2 mol L^{-1} 2-BuOH) in the presence of different concentrations of 25 (blue curve), 50 (grey curve) and 75 (green curve) mmol L^{-1}eucalyptol (left) and 18 (dark curve), 38 (blue curve), 56 (grey curve) and 75 (green curve) mmol L^{-1} toluene (right). The red curve corresponds to 25 mmol L^{-1}eucalyptol(left) and 18 mmol L^{-1}toluene in 2M 2-BuOD…….87
Figure 2.36. Solubility of 2-BuOH in water (S in mol/L) at 22°C as a function of halogenated dodecaborate clusters concentration. The vertical dashed line corresponds to the increase of solubility value of 2-BuOH more concentrated halogenated dodecaborate cluster solutions…88
Figure 2.37. Solubility of hydrophobic compounds: eucalyptol (dark), citral (red), linalool (blue), geraniol (green) and b-citronellol (grey) a) 0.01 mol L^{-1} $Na_2B_{12}I_{12}$, b) 0.02 mol L^{-1}

$Na_2B_{12}I_{12}$, c) 0.01 mol L^{-1} $Na_2B_{12}Br_{12}$ and d) 0.02 mol L^{-1} $Na_2B_{12}Br_{12}$ as a function of 2-BuOH concentration (S/S_0)……..90
Figure 2.38. Solubility of (A) eucalyptol by 0.01 mol L^{-1} and (B) b-citronellol of 0.02 mol L^{-1} boron clusters as a function of 2-BuOH concentration S/S_0. The curves correspond to COSAN (dark), $B_{12}I_{12}^{2-}$ (red), and $B_{12}Br_{12}^{2-}$ (blue)……90
Figure 2.39. A tri-axial ellipsoid in cartesian coordinates, a, b and c are the length of the ellipse semi-axis……...98
Figure 3.1. IEF marker 3-10, SERVA Liquid Mix……122
Figure 3.2. Mixture of nine standard proteins of isoelectric focusing marker (left) and mixture of nine standard proteins in the presence of 4 mmol L^{-1} NaCOSAN (right).The identification of the proteins on the gel bands is made by mass spectrometry……...123
Figure 3.3. The 20 types of amino acids. The figure were modified from Explorations of everyday chemical compounds Ci……..124
Figure 3.4. Ionizable Functional Groups in Common Amino Acids. The functional group's favored states are shown either above or below their respective pK_a values……125
Figure 3.5. zeta-potential of (A) 0.01 mmol L^{-1} Mb, (B) 0.0055 mmol L^{-1} and (C) 0.0084 mmol L^{-1} in the presence of different NaCOSAN concentrations in PBS at pH=10……128
Figure 3.6. Heme group of Mb…….…..129
Figure 3.7. (a) Subtracted UV-Vis spectra of 0.01 mmol L^{-1} Mb in PBS at pH=10 in the presence of different NaCOSAN concentrations (Ratio: [NaCOSAN]/[Mb]=0-16)……...130
Figure 3.8. UV-Vis spectra of 0.01 mmol L^{-1} Hemin in the presence of different NaCOSAN concentrations (Ratio: [NaCOSAN]/[Hemin]=0-20)……..131
Figure 3.9. The evolution of heme absorption in Mb at 410 nm and 'in' Hemin at 395 nm as a function of NaCOSAN concentration, expressed here as [NaCOSAN]/[protein]……..132
Figure 3.10. 3D structure of Mb, where the tryptophan residues are highlighted……..132
Figure 3.11. (A) Emission fluorescence spectra of Myoglobin (Tryptophan) in the absence (dark) and in the presence of NaCOSAN ([Mb]=0.01 mmol L^{-1}). The excitation wavelength of the spectra was 275 nm and the band pass was 5 nm. From top to the bottom, the concentration of NaCOSAN increased stepwise from 0 to 0.4 mmol L^{-1}. (B)Normalized fluorescence intensity as a function of [NaCOSAN]/[Mb] ratio.....133
Figure 3.12. The plot of the derived Stern-Volmer equation is given with (R^2=0.98). From the plot, n and Kq were calculated to be 1.6 and 5.6 x 10^6 mol L^{-1}, respectively……134
Figure 3.13. Emission fluorescence spectra of ApoMb in the absence and in the presence of NaCOSAN ([ApoMb] = 0.01 mmol L^{-1}). From top to the bottom, the concentration of

NaCOSAN increased stepwise from 0 to 0.2 mM. In the inset, the plot of the derived Stern-Volmer equation is given with (R^2=0.96). From the plot, n and Kq were calculated to be 2 and 6.3 x 10^{10} $mmol^{-1}$ L^{-1}, respectively……..135
Figure 3.14. (A) Far-UV CD spectrum of Mb in the absence and presence of NaCOSAN at pH=10 and 298 K. The dark dashed line corresponds to 1 mmol L^{-1} NaCOSAN in PBS at pH=10. (B) NaCOSAN-induced partial unfolding of Mb in PBS at 25 °C. The unfolding transition curve monitored by the CD ellipticity at 208 (triangles) and 222 (circles) nm as a function of [NaCOSAN]/[Mb]……...137
Figure 3.15. Molar ellipticity of 0.01 mmol L^{-1} Mb in the absence (left) and in the presence of 0.5 mmol L^{-1} NaCOSAN (right). The dark lines correspond to the experimental spectra and the red dashed lines to the predicted spectra, as fitted by K2D3 analysis……..137
Figure 3.16. Percentage of a-helixes of 0.01 mmol L-1 Mb in the presence of NaCOSAN as a function of NaCOSAN/Mb ratio…….137
Figure 3.17. Evolution of the ellipticity at 208 nm of 0.01 mmol L^{-1} Mb for various NaCOSAN/Mb ratios, 0 (dark circles), 5 (blue rhombus), 10 (orange triangle), 20 (red cross) and 30 (green cross) as a function of temperature……138
Figure 3.18. (A) Far-UV CD spectrum of ApoMb in the absence and presence of NaCOSAN at pH=10 and 298 K. (B) NaCOSAN-induced slight changes to the unfolding of ApoMb in PBS at 25 °C. The unfolding transition curve monitored by the CD ellipticity at 208 (triangles) and 222 (circles) nm as a function of [NaCOSAN]/[ApoMb]……139
Figure 3.19. Ellipticity at 208 nm of 0.01 mmol L^{-1} ApoMb in the absence (dark circles) and at a ratio NaCOSAN/ApoMb=20 (red triangles) as a function of temperature……139
Figure 3.20. Hydrodynamic diameter of 0.01 mmol L^{-1} Mb in PBS at pH=10 in the presence of different NaCOSAN concentrations as a function of [NaCOSAN]/[Mb]……..140
Figure 3.21. SAXS spectra of 0.1 mmol L^{-1} Mb in PBS at pH=10 increasing the NaCOSAN concentrations. Dashed lines represent simultaneous data adjustment with parameters listed in SI. The spectra were recorded at Soleil……...141
Figure 3.22. Representation of NaCOSAN/Mb assemblies, which are elongated in 2D, forming flattened assemblies……143
Figure 3.23. SAXS spectra of 0.1 mmol L^{-1} Mb in PBS at pH=10 in the presence of (A) 0.2 mmol L^{-1} and (B) 1 mmol L^{-1} NaCOSAN concentrations at different temperatures. The spectra were recorded at the beamline ID02 at ESRF……..144

Figure 3.24. The plot of the derived Stern-Volmer equation for BCA (left) and SKTI (right) as a function of NaCOSAN concentration. From the plot, n and Kq were calculated to be 3.3 and 6.3 x 10^7 for BCA and 2.2 and 3.9 x 10^9 mol^{-1} L for SKTI……145
Figure 3.25. (A) Far-UV CD spectrum of BCA in the absence and presence of NaCOSAN at pH=10 and 298 K. The dark dashed line corresponds to 1 mmol L^{-1} NaCOSAN in PBS at pH=10. (B) The transition curve monitored by the CD ellipticity at 215 nm as a function of [NaCOSAN]/[BCA]……...146
Figure 3.26. Molar ellipticity of 0.0055 mmol L^{-1} BCA in the absence (left) and in the presence of 0.01 mmol L^{-1} NaCOSAN (right). The dark lines correspond to the experimental spectra and the red dashed lines to the predicted spectra, as fitted using a K2D3-type analysis……146
Figure 3.27. Percentage of β-strand of 0.055 mmol L-1 BCA in the presence of NaCOSAN as a function of NaCOSAN/BCA concentrations……146
Figure 3.28. (A) Far-UV CD spectrum of SKTI in the absence and presence of NaCOSAN at pH=10 and 298 K. The dark dashed line corresponds to 1 mmol L^{-1} NaCOSAN in PBS at pH=10. (B) The transition curve monitored by the CD ellipticity at 225 nm as a function of [NaCOSAN]/[SKTI]……..147
Figure 3.29. (A)Evolution of the ellipticity at 215 nm of 0.0055 mmol L^{-1} BCA for various NaCOSAN/BCA ratios, 0 (dark circles), 2.4 (red rhombus) and 5.5(green squares) as a function of temperature. (B)Evolution of the ellipticity at 225 nm of 0.0084 mmol L^{-1} SKTI for various NaCOSAN/SKTI ratios, 0 (dark circles), 1 (red rhombus) and 70 (blue crosses) as a function of temperature……148
Figure 3.30. Emission fluorescence spectra of 0.3 mmol L^{-1} NaCOSAN (light blue), 0.09 mmol L^{-1} Thioflavin T (orange), 0.018 mmol L^{-1} BCA in the presence of 0.3 mmol L^{-1} NaCOSAN and 0.09 mmol L^{-1} Thioflavin T (dark blue), 0.3 mmol L^{-1} NaCOSAN in the presence of 0.09 mmol L^{-1} Thioflavin T (red). The excitation wavelength was 450 nm …….……...149
Figure 3.31. Hydrodynamic diameter of 0.055 mmol L^{-1} BCA (left) and 0.0084 mmol L^{-1} SKTI (right) in PBS at pH=10 in the presence of different NaCOSAN concentrations as a function of [NaCOSAN]/[BCA] or [NaCOSAN]/[SKTI]……149
Figure 3.32. SAXS spectra of 0.055 mmol L^{-1} BCA (red curve) in PBS at pH=10 increasing the NaCOSAN concentrations. The NaCOSAN concentrations were recorded in the presence of BCA were 0.055 mmol L^{-1}(green curve), 0.5mmol L^{-1}(dark orange) and 1.1 mmol L^{-1}(dark yellow). Dashed lines represent simultaneous data adjustment with parameters listed in SI. The spectra were recorded at ESRF……...150

Figure 3.33. SAXS spectra of 0.084 mmol L^{-1} SKTI in PBS at pH=10 increasing the NaCOSAN concentrations. Dashed lines represent simultaneous data adjustment with parameters listed in SI. The spectra were recorded at ESRF……151
Figure 3.34. Aggregation number of the protein assemblies as a function of the NaCOSAN/protein ratio for each of Mb (dark circles), BCA (red rhombus) and SKTI (green squares)……...152
Figure 3.35. (A) Soret band absorption, (B) fluorescence intensity at 340 nm, (C) ellipticity at 208 nm and (D) hydrodynamic diameter as a function of the ratio NaCOSAN(red) and NaSCN (blue) with Mb……153
Figure 3.36. Ellipticity of 0.01 mmol L^{-1} Mb in the absence (dark circles) and in the presence of 0.1 mmol L^{-1} (red squares) NaCOSAN and 0.1 mmol L^{-1}NaSCN (green rhombus) at 208 nm as a function of temperature……154
Figure 3.37. (A) Soret band absorption, (B) fluorescence intensity at 340 nm, (C) ellipticity at 208 nm and (D) hydrodynamic diameter as a function of the ratio NaCOSAN(red), $Na_2B_{12}H_{12}$ (blue) and $Na_2B_{12}I_{12}$ (green) with Mb……155
Figure 3.38. SANS spectra of 0.1 mmol L^{-1} Mb in PBS at pH=10 in the absence and in the presence of different concentrations of $Na_2B_{12}I_{12}$. The spectra were recorded at PSI…….....156
Figure 3.39. SAXS spectra of 0.1 mmol L^{-1} Mb in PBS at pH=10 in the absence and in the presence of different concentrations of (A) $Na_2B_{12}I_{12}$ and (B) $Na_2B_{12}Cl_{12}$. The grey curve corresponds to 4 mmol L^{-1} $Na_2B_{12}Cl_{12}$ in the absence of Mb. The spectra were recorded at ESRF……..156
Figure 3.40. Hydrodynamic diameter of (A) 0.055 mmol L^{-1} BCA and (B) 0.084 mmol L^{-1} SKTI in the absence and in the presence of different $Na_2B_{12}I_{12}$ concentrations……157
Figure 3.41. SANS spectra of (A) 0.055 mmol L^{-1} BCA and (B) 0.084 mmol L^{-1} SKTI in PBS at pH=10 in the absence and in the presence of different concentrations of $Na_2B_{12}I_{12}$. The dark line corresponds to 10 mmol L^{-1} $Na_2B_{12}I_{12}$ in PBS at pH=10 in the absence of BCA or SKTI. The spectra were recorded at PSI……158
Figure 3.42. SAXS spectra of (A) 0.055 mmol L^{-1} BCA and (B) 0.084 mmol L^{-1} SKTI in PBS at pH=10 in the absence and in the presence of different concentrations of $Na_2B_{12}I_{12}$. The curves colored by light shades of (A) blue and green correspond to 1 and 4 mmol L^{-1} $Na_2B_{12}I_{12}$, respectively, and (B) green correspond to 1 and 4 mmol L^{-1} $Na_2B_{12}I_{12}$ in the absence of BCA or SKTI. The spectra were recorded at ESRF……..158
Figure 3.43. SAXS spectra of (A) 0.055 mmol L^{-1} BCA and (B) 0.084 mmol L^{-1} SKTI in PBS at pH=10 in the absence and in the presence of different concentrations of $Na_2B_{12}Cl_{12}$. The

green line corresponds to 4 mmol L^{-1} $Na_2B_{12}Cl_{12}$ in PBS at pH=10 in the absence of BCA or SKTI……...159
Figure 3.44. (A) Soret band absorption, (B) fluorescence intensity at 340 nm, (C) ellipticity at 208 nm (D) hydrodynamic diameter as a function of the ratio NaCOSAN (red), SDS (blue) with Mb…….……..160
Figure 3.45. (A) Ellipticity at 215 nm and (B) hydrodynamic diameter of BCA in the absence and in the presence of different SDS concentrations as a function of the ratio SDS/BCA. (C) Ellipticity at 225 nm and (D) hydrodynamic diameter of SKTI in the absence and in the presence of different SDS concentrations as a function of the ratio SDS/SKTI……161
Figure 3.46. (A) Soret band absorption, (B) fluorescence intensity at 340 nm derived by Stern-Volmer equation, (C) ellipticity at 208 nm (D) hydrodynamic diameter as a function of the ratio NaCOSAN/Mb at pH=10 (red) and at pH=7 (blue)…….162
Figure 3.47. Ellipticity of 0.01 mmol L^{-1} Mb in PBS at pH=7 (blue squares) and pH=10 (red circles) at 208 nm as a function of temperature……...163
Figure 3.48. SAXS spectra of 0.1 mmol L^{-1} Mb in PBS at pH=7 increasing the NaCOSAN concentrations. The spectra were recorded at Soleil……163
Figure 3.49. The plot of the derived Stern-Volmer equation for 0.0084 mmol L^{-1} SKTI in PBS at pH=7 (blue) and pH=10 (red) as a function of NaCOSAN concentration. From the plot, n and Kq were calculated to be 2.2 and 3.9 x 10^9 for pH=10 and 1.6 and 3.1 x 10^7 mol^{-1} L for pH=7……...164
Figure 3.50. (A) The transition curve of 0.0055 mmol L^{-1} BCA in PBS at pH=7 in the absence of NaCOSAN monitored by the CD ellipticity at 215 nm as a function of [NaCOSAN]/[BCA]. (B) Ellipticity of 0.0055 mmol L^{-1} BCA in PBS at pH=7 (blue squares) and pH=10 (red circles) at 215 nm as a function of temperature……165
Figure 3.51. Hydrodynamic diameter of 0.055 mol L^{-1} BCA (left) and 0.0084 mol L^{-1} SKTI (right) in PBS at pH=7 in the presence of different NaCOSAN concentrations as a function of [NaCOSAN]/[BCA] or [NaCOSAN]/[SKTI]…….165
Figure 3.52. (A) The transition curve of 0.01 mol L^{-1} Mb in PBS at pH=7 (blue squares) and pH=10 (red squares) in the absence and in the presence of NaSCN monitored by the CD ellipticity at 208 nm as a function of [NaSCN]/[Mb]. (B) Ellipticity of 0.01 mmol L^{-1} Mb in the presence of 0.1 mmol L^{-1} NaSCN in PBS at pH=7 (blue squares) and pH=10 (red circles) at 208 nm as a function of temperature……166
Figure 3.53. (A) Soret band absorption and (B) fluorescence intensity at 340 nm as a function of the ratio SDS/Mb at pH=10 (red circles) and at pH=7 (blue squares)……166

Figure 4.1. (A) UV-Vis spectra of different NaCOSAN concentrations in H_2O. The inset shows a zoom-in of the visible range. (B) Calibration curve of NaCOSAN obtained by UV-VIS data of (A)……..194
Figure 4.2. 2D fluorescence spectrum of (A) water and (B) of 0.017 mmol L^{-1} NaCOSAN in H_2O…….195
Figure 4.3. Fluorescence spectra of different NaCOSAN concentrations at λ^{exc}= 210 nm (red line Figure 4.3)……196
Figure 4.4. Fluorescence intensity at about 550 nm for λexc=210 nm (red line on Figure 4.3), as a function of NaCOSAN concentration……..196
Figure 4.5. Fluorescence intensity at about 390 and 550 nm for λ^{exc}=300 nm (dark line on Figure 4.3), as a function of NaCOSAN concentration in H_2O……..197
Figure 4.6. Fluorescence intensity and peak shift at about 390 for λexc=330 nm (blue line on Figure 4.3), as a function of NaCOSAN concentration……...198
Figure 4.7. Normalized intensity decay at excitation wavelength 400 nm as a function of time in ns……199
Figure 4.8. Normalized intensity decay of 0.1 mmol L^{-1} NaCOSAN concentration (dark circles) and fitted normalized intensity decay (red line) as a function of time in ns…….200
Figure 4.9. Two characteristic lifetimes in the nanosecond range of the fluorescent signal at 530 nm and under an excitation at 400nm, as a function of NaCOSAN concentration in H_2O (from fitting data figure 4.8 and S4.11)……...201
Figure 4.10. Amplitudes as a function of NaCOSAN concentration in H_2O, where blue circles represent the A_1 and red circles the A_2 of the double exponential function, which were used for the fitting…….201
Figure 4.11. Schematic diagram illustrating the evolution of carriers to explain space-filling effects…….203
Figure 4.12. Pump probe 3D-spectra of 0.05 mmol L^{-1} NaCOSAN in H_2O. The excitation wavelength was 400 nm…….203
Figure 4.13. Normalized differential transmission of different NaCOSAN concentrations at the maxima around 520 nm as a function of the time in ps derived from the pump probe spectra. The excitation wavelength was 400 nm……..204
Figure 4.14. Relaxation times (A) t_1, (B) t_2, and (C) t_3 at the maximum probe wavelength in ps as a function of NaCOSAN concentrations…….204
Figure 4.15. (A) UV-Vis spectra of different NaI_2COSAN concentrations in H_2O. (B) Calibration curve of NaCOSAN obtained by UV-VIS data of (A)……..205

Figure 4.16. (A) Fluorescence spectra and (B) fluorescence intensity of different NaI_2COSAN concentrations in H_2O at λ^{exc}= 210 nm……206
Figure 4.17. Normalized differential transmission of different NaI_2COSAN concentrations at the maxima as a function of the time in ps derived from the pump probe spectra. The excitation wavelength was 400 nm……..206
Figure 4.18. Relaxation times of (A) t_1, (B) t_2 and (C) t_3 as a function of NaI2COSAN concentration……..207
Figure 4.19. Fluorescence spectra of (A) 5, (C) 10, (E) 15 and (G) 20 mmol L^{-1} NaCOSAN in the presence of different 2-BuOH concentrations at λ^{exc}= 210 nm. Fluorescence intensity of (B) 5, (D) 10, (F) 20 and (H) 25 mmol L^{-1} NaCOSAN in the presence of different 2-BuOH concentrations as a function of 2-BuOH concentrations. The red points correspond to the fluorescence intensity at 390 nm and the blue points at 550 nm……..…209
Figure 4.20. Fluorescence intensity at around λmax≈390 nm (left) and at around λmax≈390 nm (right) of 0 (green squares, S/S_0=0), 0.1 (blue rhombus, S/S_0=0.04), 0.5 (orange triangles, S/S_0=0.2), 1 (grey squares, S/S_0=0.4), 2 (yellow rhombus, S/S_0=0.85) and 2.5 (blue triangle, S/S_0=1.1) mol L^{-1} 2-BuOH as a function of NaCOSAN concentration……...209
Figure 4.21. Normalized intensity decay at maxima of (A) 5, (B) 15 and (C) 20 mmol L^{-1} NaCOSAN in the presence of different 2-BuOH concentrations as a function of time in ps...210
Figure 4.22. Relaxation times of (A), (B) 5 mmol L^{-1}, (C), (D) 15 mmol L^{-1} and (E), (F) 20 mmol L^{-1} NaCOSAN as a function of S/S_0. The blue circles correspond to t_1, the red circles to t_2 and the dark circles to t_3……...211

List of Tables

Table 1.1: Kosmotropes and chaotropes characteristics……...36
Table 1.2: The structural parameters of cyclodextrins and dodecaborate anions (size match)..40
Table 1.3: Features of NaCOSAN and SDS……47
Table 2.1: Radius of gyration of hybrid co-assemblies of NaCOSAN in the presence of different 2-BuOH concentrations……..75
Table 2.2: Radius of gyration of hybrid co-assemblies of NaI_2COSAN in the presence of different 2-BuOH concentrations……75
Table 2.3: Best fit parameters of the SANS-fits. Fixed parameters are shown with a grey background……...……80

Table 2.4: Fitting parameters obtained for the best fits of the SANS spectra in Fig.S16. Fixed parameters are shown with a grey background……82
Table 2.5: Solubility values of the hydrophobic compounds……...84
Table 2.6: Estimation of 2-BuOH molecules for the first and the second solvation shell in comparison with the slope values obtained from the solubility curves of the boron cluster…...89
Table 2.7: Scattering Length Densities for X-rays……93
Table 2.8: Scattering lengths of the relevant elements……93
Table 2.9: Scattering Length Densities for Neutrons……94
Table 2.10: Prefactor parameters……..97
Table 2.11: Example of results obtained for the prefactor calculation for 0.04 M COSAN and 1.6 M 1-BuOH in D_2O……...…97
Table 3.1. Proteins of the isoelectric focusing (IEF) marker 3-10, SERVA Liquid Mix…….121
Table 3.2: Features of proteins under investigation……124
Table 3.3: Number of amino acid residues of myoglobin……...126
Table 3.4: Charges of residue in myoglobin expected in buffer at pH=7 and pH=10. $N_{residue}$ is the number of residues in myoglobin……126
Table 3.5: The results of mass spectrometry on selected proteins from the mixture……..127
Table 3.6: Percentages of a-helixes……137
Table 3.7: Aggregation number of flattened assemblies and dimensions (fittings were made on data were collected at Soleil / SWING and at ESRF / ID02)……...142
Table 3.8: Percentages of b-strand……..146
Table 3.9: Aggregation number of flattened [NaCOSAN]/[BCA] aggregates and dimensions (fittings were made on data were collected at Soleil/SWING and ESRF/ID02)……..151
Table 3.10: Aggregation number of flattened [NaCOSAN]/[SKTI] aggregates and dimensions……..152
Table 3.11: Volumes, charges and charge densities of the used dodecaborates $B_{12}X_{12}^{2-}$ in comparison to NaCOSAN……..154
Table 3.12: Results of the SAXS fits (Figure 3.39)……157
Table 3.13: Aggregation number of flattened [NaCOSAN]/[Mb] aggregates and dimensions.....164
Table 3.14: Scattering length Densities for X-rays……....168
Table 3.15: Some examples of the best-fitting parameters for the SAXS data of NaCOSAN/Mb assemblies. Fixed parameters are shown with a grey background……169

List of abbreviations

ApoMb	-	Apomyoglobin
α-CD	-	Alpha-cyclodextrin
β-CD	-	Beta-cyclodextrin
γ-CD	-	Gamma-cyclodextrin
δ-CD	-	Delta-cyclodextrin
ε-CD	-	Epsilon-cyclodextrin
ε	-	Exctiction coefficient
ζ-CD	-	Zeta-cyclodextrin
BCA	-	Bovine Carbonic Anhydrase
BNCT	-	Boron Neutron Capture Therapy
BSA	-	Bovine Serum Albumin
CAC	-	Critical aggregation concentration
CAIX	-	Carbonic Anhydrase IX
CD	-	Circular dichroism
CEA	-	Commissariat à l'énergie Atomique et aux énergies alternatives
CMC	-	Critical micellar concentration
COSAN	-	Cobalta-bis-dicarbollides
CPP	-	Critical packing parameter
DLS	-	Dynamic Light Scattering
ECMPL	-	Experimental Condensed Matter Physics Lab
ESRF	-	European Synchrotron Radiation Facility
FRET	-	Förster resonance energy transfer
His	-	Histidine

HSA	-	Human Serum Albumin
ICSM	-	Institute de Chimie Séparative de Marcoule
I_2COSAN	-	di-iodo-COSAN
IEF	-	Isoelectric focusing
ILL	-	Institut Laue–Langevin
ISE	-	Ion specific effects
ITC	-	Isothermal titration calorimetry
JCNS	-	Jülich Centre for Neutron Science
L2IA	-	Laboratoire des Ions aux Interfaces Actives
mM	-	mmol/L
M	-	mol/L
Mb	-	Myoglobin
mdeg	-	millidegrees
MLZ	-	Heinz Maier-Lebniz Zentrum
MMAF	-	Monomethyl auristatin F
Mw	-	Molecular weight
N_A	-	Avogadro number
PBS	-	Phosphate-buffered saline
Phe	-	Phenylalanine
PI	-	Protease inhibitors
pI	-	Isoelectric point
PL	-	Photoluminescence
PMT	-	Photomultiplier tube
PSI	-	Institut Paul Scherrer
RMSA	-	Rescaled mean squared approximation
S	-	Solubility

SA	-	Serum Albumin
SS	-	Surrounding solvent
SANS	-	Small Angle Neutron Scattering
SKTI	-	Soybean Kunitz Trypsin Inhibitor
SDS	-	Sodium dodecyl sulfate
SLD	-	Scattering Length Density
SWAXS	-	Small and Wide Angle X-ray Scattering
Tβ4	-	Thymosin β4
TEM	-	Transmission electron microscopy
ThT	-	Thioflavin T
TOC	-	Total Organic Compound
Trp	-	Tryptophan
TCSPC	-	Time-Correlated-Single-Photon Counting
Tyr	-	Tyrosine
Vm	-	Molecular volume

Introduction

The term "specific ion effects" refers to a phenomenon in which ions of the same charge have considerably diverse effects on the investigated systems, resulting in alterations to their properties. Around 150 years ago, Franz Hofmeister was one of the first scientists to investigate this effect in biological systems and classify the ions based on their strength of effect in the so-called Hofmeister series.[1] Prior to Hofmeister's work, Poiseuille, a French physicist, observed that the addition of salts to water affected its viscosity.[2] This discovery was made several decades before Hofmeister's work, and it laid the foundation for future research into the specific ion effect.

The ions in the Hofmeister series are classified as being kosmotropic and chaotropic, based on their ability to interact with water molecules and affect the hydrogen network in aqueous solutions. Chaotropes are weakly hydrated ions able to increase the solubility of macromolecules and colloids in aqueous solutions (salting-in). In contrast, kosmotropes are highly hydrated ions that decrease the solubility of hydrophilic macromolecules and colloids (salting-out). [3]

Recently, specific ion effects with nanometric-sized ions have been studied. These nanometric-sized ions are included in the extended Hofmeister series and are called "superchaotropic" anions.[4,5] It was found that the salting-in effect of nanometric-sized ions is much prominent than that of classical chaotropic ions.[6] More specifically, it has been demonstrated that some polyoxometalates anions, and boron clusters adsorb on hydrophilic surfaces, i.e., to the micellar surfaces of sugar based[4,7] and polyethoxylated surfactants,[4,8] or bind to the hydrophobic pockets of macrocycle molecules such as cyclodextrin at millimolar concentrations.[9,10]

The thesis was carried out at the Laboratory of Ions at Active Interfaces (L2IA) at the Institute of Separation Chemistry in Marcoule (ICSM). The research of L2IA focuses on the physicochemical behavior of ions at interfaces, in the context of metal extraction, formulation, or biologically relevant systems. In the last few years, the laboratory's attention has been increasingly focused on nanometer-sized ionic species (polyoxometalates, metal clusters, ionic boron clusters, and hydrophobic ions).

In the scope of this thesis, our research focused on the solution and surfactant properties of anionic boron clusters, specifically cobalta-bis dicarbolide (Co $(C_2B_9H_{11})_2^-$, COSAN) and their derivatives, as well as closo-dodecaborates ($B_{12}X_{12}^{2-}$ with X=H, F, Cl, Br, and I). Boron

clusters are appealing for many applications due to their unique chemical and physical properties, such as high stability, thermal stability, low reactivity, and tunable electronic structures.[11–16]

In Chapter I, the current state of the art on specific ion effects and nano-ions was reviewed. Among all the classical surfactant features, the ability to solubilize hydrophobic compounds has not been evaluated so far for inorganic nano-ions. In Chapter II, we investigate the ability of COSAN (and its di-iodinated derivative, I_2COSAN) to solubilize organic compounds with different hydrophobic characters, such as alcohols and hydrophobic dyes. Phase diagrams water/COSAN/alcohol ternary systems were established to evaluate the solubilization efficiency of COSAN. SDS and cyclodextrins were also evaluated as standard solubilizers in order to compare the solubilization efficiency of COSAN to classical micellar and host-guest solubilization. In order to decipher the solubilization mechanism of 2-butanol by COSAN at the molecular and supramolecular scales, different techniques were combined. UV-vis measurements were carried out to probe the solvation shell of COSAN, i.e., its local molecular environment, in water upon increasing the alcohol concentration, and small-angle X-ray and neutron scattering techniques (SAXS and SANS) were used to characterize COSAN/2-butanol hybrid assemblies. Using the same experimental strategy, we studied the solubilization efficiency of the COSAN/2-butanol assemblies on more hydrophobic compounds with diverse chemical natures. Moreover, a focus was made on the comparison between the effect of COSAN and closo-dodecaborates on the solubility of hydrophobic compounds and the closo-dodecaborates/2-butanol assemblies on the solubility of more hydrophobic compounds.

Subsequently, we studied the effect of interactions of nano-ions with proteins as systems with increasing complexity. Proteins have a large diversity in terms of their physicochemical local environment, in terms of electrical charge, and in terms of polarity. Therefore, the investigation of nano-ions with proteins enables the study of a large set of intermolecular forces, including hydrophobic, electrostatic, and H-bonds. In Chapter III, we investigate the protein/nano-ion interactions for three different proteins and different nano-ions. In order to decipher the key interactions of nano-ions with proteins at the molecular and supramolecular levels, different techniques were combined. UV-vis and circular dichroism measurements were carried out to obtain information on the local environment of the nano-ions and on the secondary structure of proteins, respectively. Scattering techniques, such as small angle dynamic light (DLS), X-ray (SAXS) and neutron (SANS) scattering were used to obtain information on protein assemblies. We studied the interactions of NaCOSAN with three proteins—myoglobin,

carbonic anhydrase, and trypsin inhibitor—that have different features, such as their secondary structure. Moreover, the focus was made on the comparison between the effects of a classical chaotropic salt, the effects of other superchaotropic ions, and the effects of classical surfactants on these three proteins in comparison with NaCOSAN.

The photophysics of COSAN and its derivatives in aqueous solutions have not been thoroughly investigated so far. The nano-ion specific effect observed in Chapters II and III appears to significantly influence electron transfer processes and, thus, photocatalytic efficiency. In Chapter IV, we have examined the effect on the photophysical properties of the self-assembly of NaCOSAN and its derivatives in aqueous solutions and of NaCOSAN interaction with organic solutes, as observed and studied in Chapter II, using fluorescence and photoluminescence. The state transitions in the self-assembly sequence of COSAN from monomer to vesicles to micelle-like aggregates was also investigated.

References

[1] W. Kunz, J. Henle, B.W. Ninham, “Zur Lehre von der Wirkung der Salze” (about the science of the effect of salts): Franz Hofmeister’s historical papers, Curr. Opin. Colloid Interface Sci. 9 (2004) 19–37. https://doi.org/10.1016/j.cocis.2004.05.005.

[2] J.L. Poiseuille, Sur le mouvement des liquides de nature très différente dans les tubes de très petits diamètres, Ann Chim Phys. 21 (1847) 76–110.

[3] Y. Marcus, Effect of ions on the structure of water, Pure Appl. Chem. 82 (2010) 1889–1899. https://doi.org/10.1351/PAC-CON-09-07-02.

[4] B. Naskar, O. Diat, V. Nardello-Rataj, P. Bauduin, Nanometer-Size Polyoxometalate Anions Adsorb Strongly on Neutral Soft Surfaces, J. Phys. Chem. C. 119 (2015) 20985–20992. https://doi.org/10.1021/acs.jpcc.5b06273.

[5] K.I. Assaf, M.S. Ural, F. Pan, T. Georgiev, S. Simova, K. Rissanen, D. Gabel, W.M. Nau, Water structure recovery in chaotropic anion recognition: High-affinity binding of dodecaborate clusters to γ-cyclodextrin, Angew. Chemie - Int. Ed. 54 (2015) 6852–6856. https://doi.org/10.1002/anie.201412485.

[6] K.I. Assaf, W.M. Nau, The Chaotropic Effect as an Assembly Motif in Chemistry, Angew. Chemie - Int. Ed. 57 (2018) 13968–13981. https://doi.org/10.1002/anie.201804597.

[7] T. Merhi, A. Jonchère, L. Girard, O. Diat, M. Nuez, C. Viñas, P. Bauduin, Highlights on the Binding of Cobalta-Bis-(Dicarbollide) with Glucose Units, Chem. - A Eur. J. 26 (2020) 13935–13947. https://doi.org/10.1002/chem.202002123.

[8] M. Hohenschutz, I. Grillo, O. Diat, P. Bauduin, How Nano-Ions Act Like Ionic Surfactants, Angew. Chemie Int. Ed. 59 (2020) 8084–8088. https://doi.org/10.1002/anie.201916193.

[9] K.I. Assaf, B. Begaj, A. Frank, M. Nilam, A.S. Mougharbel, U. Kortz, J. Nekvinda, B. Grüner, D. Gabel, W.M. Nau, High-Affinity Binding of Metallacarborane Cobalt Bis(dicarbollide) Anions to Cyclodextrins and Application to Membrane Translocation, J. Org. Chem. 84 (2019) 11790–11798. https://doi.org/10.1021/acs.joc.9b01688.

[10] J. Warneke, C. Jenne, J. Bernarding, V.A. Azov, M. Plaumann, Evidence for an intrinsic binding force between dodecaborate dianions and receptors with hydrophobic binding pockets, Chem. Commun. 52 (2016) 6300–6303. https://doi.org/10.1039/c6cc01233g.

[11] J. Cebula, K. Fink, J. Boratyński, T.M. Goszczyński, Supramolecular chemistry of anionic boron clusters and its applications in biology, Coord. Chem. Rev. 477 (2023). https://doi.org/10.1016/j.ccr.2022.214940.

[12] J.C. Axtell, L.M.A. Saleh, E.A. Qian, A.I. Wixtrom, A.M. Spokoyny, Synthesis and Applications of Perfunctionalized Boron Clusters, Inorg. Chem. 57 (2018) 2333–2350. https://doi.org/10.1021/acs.inorgchem.7b02912.

[13] A.B. Buades, Z. Kelemen, V.S. Arderiu, A. Zaulet, C. Viñas, F. Teixidor, A fast and simple B-C bond formation in metallacarboranes avoiding halometallacarboranes and transition metal catalysts, Dalt. Trans. 49 (2020) 3525–3531. https://doi.org/10.1039/c9dt04695j.

[14] S. Mukherjee, P. Thilagar, Boron clusters in luminescent materials, Chem. Commun. 52 (2016) 1070–1093. https://doi.org/10.1039/c5cc08213g.

[15] B.P. Dash, R. Satapathy, J.A. Maguire, N.S. Hosmane, Polyhedral boron clusters in materials science, New J. Chem. 35 (2011) 1955–1972. https://doi.org/10.1039/c1nj20228f.

[16] A. Barba-Bon, G. Salluce, I. Lostalé-Seijo, K.I. Assaf, A. Hennig, J. Montenegro, W.M. Nau, Boron clusters as broadband membrane carriers, Nat. |. 603 (2022) 637. https://doi.org/10.1038/s41586-022-04413-w.

Chapter I: State of the art

I.1 Specific ion effects

In September 1847, the “Annales de chimie et de physique” published an article from Jean Léonard Marie Poiseuille on water flow in capillaries, taking into account the impact of solutes and their salts.[1] His work had begun in the 1840s to better understand blood flow in the body's microcirculation. Poiseuille had noticed that some salts made water more viscous, while others had the opposite effect.[2] Then, in the 1880s, Franz Hofmeister was the first to consider specific ion effects working on proteins solubility and to classify ions according to the strength of these effects. The term "specific ion effects" refers to phenomena in which ions of the same charge have significantly different effects on the investigated systems, affecting their physical-chemistry properties.[3] In the basic experiment conducted by Hofmeister and his group (studying the effect of a large number of salts), they observed, for instance, that phosphate salts caused immediate precipitation of proteins in contrast to other electrolytes, such as thyocyanate salts. Based on these and later results, scientists classified anions and cations into separate series based on their ability to increase protein solubility and more generally to affect the colloidal stability in an aqueous solution. These series are known today as the Hofmeister or lyotropic series (Figure 1.1). As observed experimentally, the anion series progresses from highly charged small anions to weakly charged large anions. The effect of cations, on the other hand, were less pronounced and showed the opposite ordering, that is, from weakly charged large ions to strongly charged small ions.

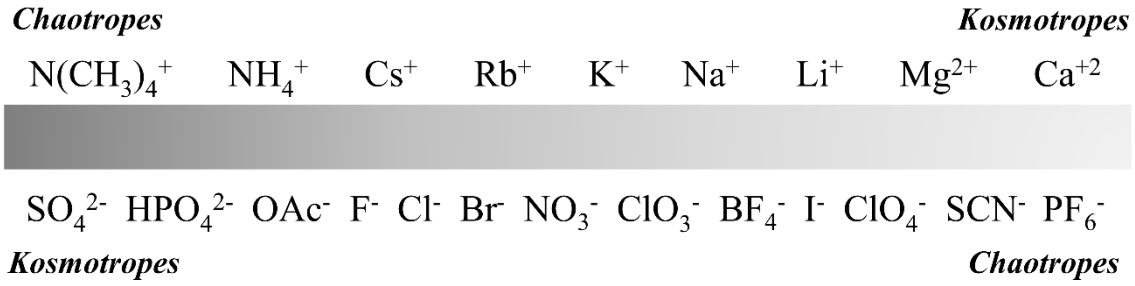

Figure 1.1*. Typical ordering of anions of Hofmeister series, modified from* [2].

According to their ability to interact with the water molecule and consequently impact the hydrogen network, the ions in the Hofmeister series are classified into kosmotropic and chaotropic ions. Kosmotropic ions decrease the solubility of hydrophilic macromolecules and

colloids by reorganizing the water molecules around them (order, kosmos), thus creating an unfavorable environment for the macromolecules and colloids to be dispersed in solution. Kosmotropic ions decrease the water activity and induce an effect called salting-out that reduces the stability domain of dispersed colloids. On the other hand, chaotropic ions increase the solubility of macromolecules and colloids by disrupting the organization of water molecules around them (disorder, chaos), creating a more favourable environment for the macromolecules and colloids to be dispersed in solution. As a result, kosmotropic ions cause an effect called salting-in (Table 1.1).[4]

Table 1.1: Kosmotropes and chaotropes characteristics, modified from [5]

Kosmotropes		Chaotropes	
Salt out (colloidal aggregation)		Salt in (colloidal solubilization)	
⬆	Surface tension	Surface tension	⬇
⬇	Protein denaturation	Protein denaturation	⬆
⬆	Protein stability	Protein stability	⬇

This salt classification was conceptualized by different scientists such as Pr. Kim Collins et al. with the notion of matching water affinities (with a representation in Figure 1.2) or Pr. Vojko Vlachy via the extension of this concept to ionic functions at substrates or colloidal surfaces. In all cases, the order of the "ions specific effect" is due to an entropical gain or penalty of the water molecules in the system through the hydration of the various species in solutions, whether the ion is strongly (for small ions, e.g., Li^+, F^-) or weakly hydrated (for bigger ions, e.g., Cs^+, I^-) and this taking always into account the cation-anion couples.[6,7] At this point, it worth to highlight that the freedom of the water molecules to move, in the hydration shells, depends on the ion concentration and is decreased at high salt concentrations for both chaotropic and kosmotropic ions.[8]

The concept of Collins et al. was a useful principle to explain and anticipate the interaction between ions or ionic functions in aqueous solutions. It follows the principle of "like seeks like" in physical chemistry.[9] As mentioned above, this concept has been found to extend beyond just ion-ion interactions. Leontidis et al. demonstrated that the interaction between chaotropic ions and lipids (polar, uncharged surfaces) can still be described as a competition for hydration water molecules between the ion and the lipidic head groups.[10]

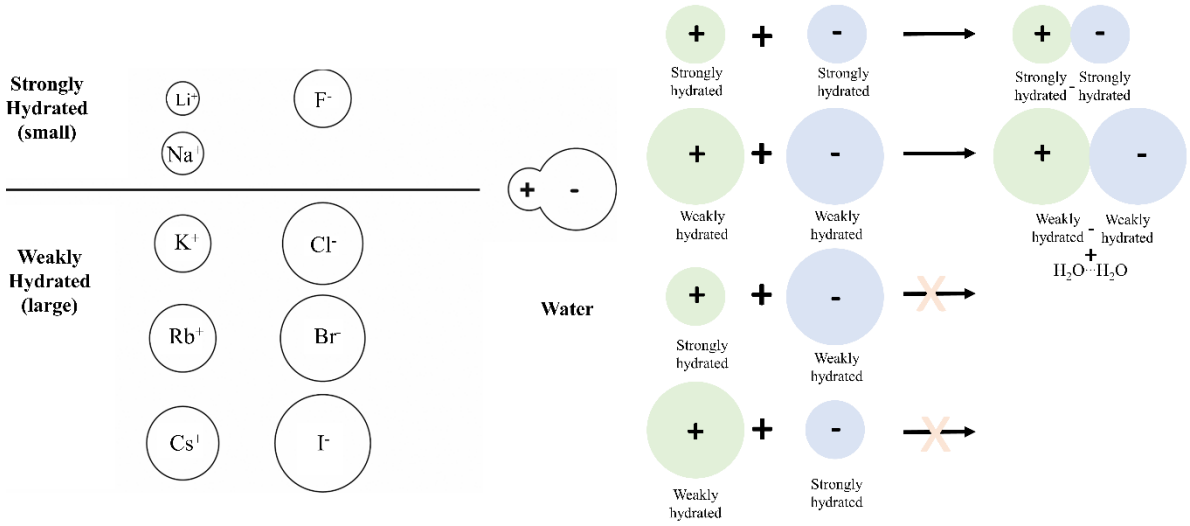

***Figure 1.2**. Separation of alkali metal cations and halides between strong hydrated (kosmotropes) and weakly hydrated (chaotropes) species (left). Formation of inner sphere ion pairs occurs between ions with similar hydration free energy and similar water affinity (right), considering an ion as a sphere with a point charge at its center, figure modified from [9].*

The Hofmeister series effects are encountered in various systems, including biological, colloidal, polymer, surfactant, and crystallization systems. In biological media rich in proteins, liposomes and cells, certain ions have been found to have an impact on the stability and activity of enzymes,[11,12] the permeability of cell membranes,[13–15] the stability and folding of proteins,[16,17] and the binding of drugs to their target receptors.[18] In colloidal systems, ions can affect the stability of suspensions of particles,[19] emulsions,[20] and foams,[21] influencing their rheological properties and overall stability.[22–25] The Hofmeister effect has also been observed in polymer systems, such as solutions and gels of polymers, where certain ions can affect the conformation, stability, solubility, and mechanical properties of these systems.[26–29] In surfactant systems, ions can affect the formation and stability of micelles and the surface tension of solutions.[30] The Hofmeister effect has been observed in crystallization systems, where certain ions can affect the rate and pathways of crystallization in solutions of macromolecules.[9] It's worth noting that the reversed order in Hofmeister series were also observed.[31] The reversed Hofmeister series is caused by changing the sign of the surface charge from negative to positive, altering the nature of functional surface groups from hydrophobic to hydrophilic, increasing the salt concentration, or modifying the pH.[31,32]

I.2 Specific nano-ion effect of nanometric-sized ions / the extension to superchaotropic ions

Classical Hofmeister ions range from kosmotropic (highly charged, small, and strongly hydrated) to chaotropic (less charged, larger, and weakly hydrated) ions. Recently, the Hofmeister series has been extended to include so-called "superchaotropic" anions, which are nanometric-sized anions that exhibit low charge density. Superchaotropic anions have distinct hydration and thermochemical properties compared to hydrophobic or amphiphilic solutes. On a scale of solvation in water, they lie between typical chaotropes and hydrophobic ions. The solvation classification spans from hydrogen bonding to the hydrophobic effect, with the chaotropic effect located in the transition region.[33] The chaotropic effect, which refers to the interaction of superchaotropes with hydrophobic phases, surfaces, and concavities, is enthalpically driven and results from a combination of desolvation and strong dispersion interactions. This differs from the thermochemical behavior of the classic hydrophobic effect, which is entropically driven.[34] The discovery of superchaotropic nano-ions led to significant research interest in their basic behavior and potential applications, resulting in substantial progress in understanding the chaotropic effect as an assembly motif.

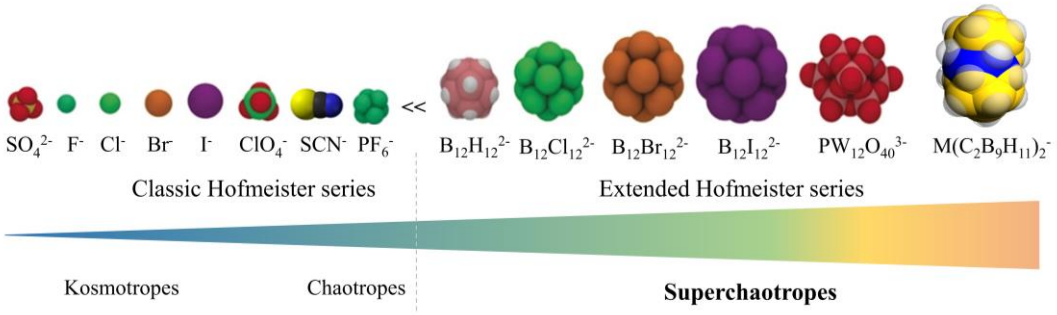

***Figure 1.3**. The classic Hofmeister series (left) and the extended one (right), modified from* [35].

I.3 Boron clusters and their superchaotropic behavior

In 1912, Alfred Stock made the initial discovery of boron hydrides.[36,37] Boron is exceptional in its ability to form molecules of unlimited size through covalent bonds with itself, a feature referred to as catenation, which sets it apart from all other elements besides carbon. Boron, unlike carbon, which tends to form chains and rings, adopts a cluster motif due to having only three electrons in its valence shell. [38] Significant advancement has been made in the boron cluster chemistry due to the discovery of numerous different architecture designs for ionic and

non-ionic boranes, as well as their derivatives, that incorporate heteroatoms such as carbon (carboranes), metals (metallaboranes), or a combination of both (metallacarboranes). Both types of boranes, ionic and non-ionic, show 3D aromaticity, making them highly stable under thermal and chemical conditions.[38,39] Boron clusters are appealing for many applications due to their unique chemical and physical properties, such as high stability, thermal stability, low reactivity, and tunable electronic structures.[40] These properties make boron clusters suitable for a wide range of applications, including: boron neutron capture therapy,[41] serving as carriers for drugs,[34,42] functioning as contrast agents in medical imaging,[42] enzyme inhibition[43] and displaying antimicrobial activity.[44,45] Boron clusters can also find applications as catalysts in chemical reactions,[46] in metal extraction,[38] as active components in photoluminescent materials, [47] and more generally in material science.[48] These are just a few examples of the potential applications of boron clusters.

The focus of this research is on anionic boron clusters because they are nanometer-sized ions with delocalized charges, which are part of the chaotropic end of the Hofmeister series. Following that, closo-dodecaborates, $B_{12}X_{12}^{2-}$ with respectively X=H, F, Cl, Br, I and metalla bis-dicarbollides, $M(C_2B_9H_{11})_2^-$ with M=Co will be investigated (Figure 1.4).

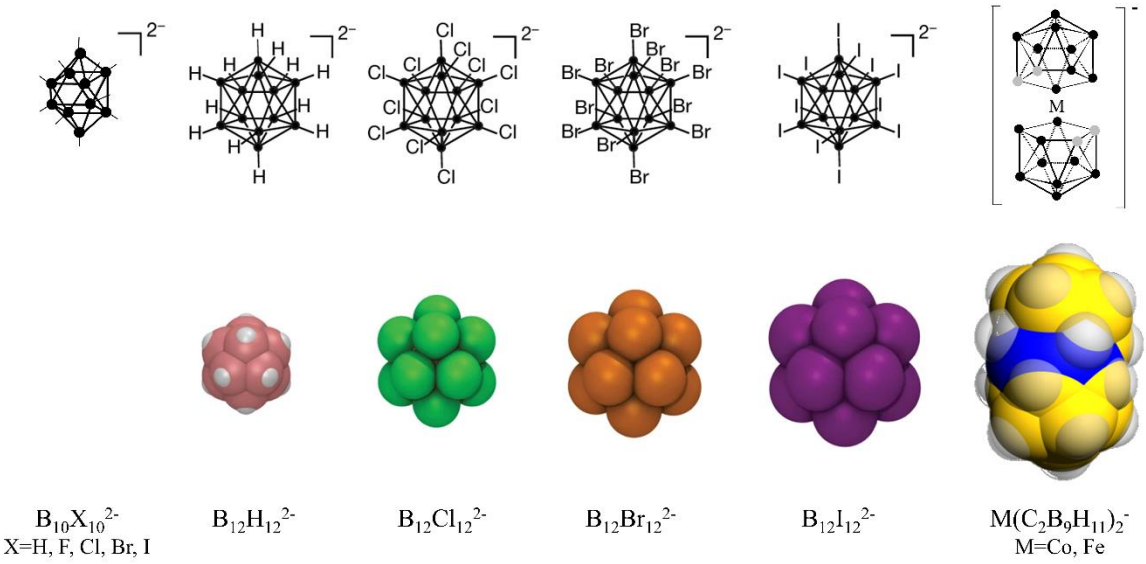

Figure 1.4*. Nanometric-sized anionic boron clusters were investigated in this thesis, modified from* [35].

The anionic boron clusters, mentioned above in aqueous solutions tend to have weak binding with the water due to their low charge density and their lack of ability to form classical hydrogen bonds with the surrounding water molecules. The boron clusters have hydridic hydrogens on their surface and form peculiar dihydrogen bonds ($O^{\delta-}$-$H^{\delta+}\cdots H^{\delta-}$-$B^{\delta+}$) with the

acidic hydrogens of water molecules in the first solvation shell.[33,49] It has been found that hydrogenated decaborates, hydrogenated dodecaborates, and metalla bis-dicarbollides have the ability to adsorb to the air-water interface,[50] reducing surface tension and causing self-assembly in aqueous solutions.[51] Decaborates and dodecaborates tend to aggregate weakly at high concentrations (>0.1 mol L^{-1}), while metalla bis-dicarbollides exhibit strong self-assembly, similar to that behavior of amphiphilic surfactants,[52] as will be discussed in detail in a few sections later.

Decaborates, dodecaborates, including their perhalogenated derivatives and metalla-bis-dicarbollides strongly bind to the hydrophobic cavities of macrocyclic host molecules like cyclodextrins (CD) in aqueous solution. Assaf et al. investigated the binding constant of dodecaborate cluster dianions ($B_{12}X_{12}^{2-}$, X: H, Cl, Br, and I) with γ-cyclodextrin. The binding constant with γ-CD are as follows: $B_{12}H_{12}^{2-}$<$B_{12}Cl_{12}^{2-}$<$B_{12}Br_{12}^{2-}$. $B_{12}Br_{12}^{2-}$ appears to have the highest binding constant and best geometrical fit with γ-CD, whereas $B_{12}I_{12}^{2-}$ binds weaker due to a mismatch in the size of the cavity of γ-CD and $B_{12}I_{12}^{2-}$, despite being more chaotropic than $B_{12}Br_{12}^{2-}$.[35,53,54] Subsequently, Assaf et al. investigated smaller and larger CD homologues than γ-cyclodextrin and their complexation with dodecaborate anions. The size match is significant for the stability of these complexes (see Table 1.2), as $B_{12}H_{12}^{2-}$ (smallest dodecarborate) is too small to efficiently fill the cavity of large CD analogues, but fits well inside the small CD analogues, such as α- and β-CD. On the other hand, $B_{12}I_{12}^{2-}$ (largest dodecarborate), is too large to fit inside the small CD analogues, but binds tightly to larger analogues such as δ-CD up to ζ-CD.[54]

Table 1.2: The structural parameters of cyclodextrins and dodecaborate anions (size match), modified from [54]

Host	**V_{cavity} / Å^3**	**Guest**	**V/ Å^3**
α-CD	174	$B_{12}H_{12}^{2-}$	152
β-CD	262	$B_{12}F_{12}^{2-}$	176
γ-CD	427	$B_{12}Cl_{12}^{2-}$	333
δ-CD	541	$B_{12}Br_{12}^{2-}$	416
ε-CD	667	$B_{12}I_{12}^{2-}$	520
ζ-CD	794	COSAN	≈448

Similarly, COSAN and its derivatives were shown to bind to the hydrophobic cavities of cyclodextrins in aqueous solution and their binding affinities reach those of perhalogenated dodecaborate clusters. The strong and selective binding of COSAN to cyclodextrins was used in conjunction with an indicator dye to test the translocation of COSAN and its derivatives through lipid bilayer membranes. This was accomplished using supramolecular tandem membrane assays, which allow fluorescence to track the real time translocation of COSAN and its derivatives.[55]

Chaotropic anions have been shown to bind to hydrophobic pockets in proteins with the same thermodynamic signature as boron clusters bind to cyclodextrins.[56] Following that, Goszczyński et al. investigated the interaction of various boron clusters and their derivatives with serum albumin by fluorescence quenching, circular dichroism, scattering techniques, and MALDI-TOF mass spectrometry. The strength of boron cluster interactions with serum albumin are as follows: metallacarboranes $[M(C_2B_9H_{11})_2]^-$ > carboranes ($C_2B_{10}H_{12}$) >> dodecaborate anion $[B_{12}H_{12}]^{2-}$. The binding of metallacarboranes to albumin occurs in two ways: it binds specifically and strongly to the hydrophobic cavity at low concentrations and non-specifically to the surface of the protein at high concentrations. On the other hand, $B_{12}H_{12}^{2-}$ binds weakly and only non-specifically to the surface of albumin at high concentrations.[57] Kuperman et al. investigated the ability of per-halogenated decaborates and dodecaborates to bind to albumins and they have shown that these two perhalogenated closo-borates interact with hydrophobic albumin moieties such as tryptophan residues. The strength of the binding increased as the size of the closo-borates increased, from hydrogenated to iodinated clusters.[58] Recently, it has been demonstrated that dodecaborate clusters, can serve as anionic inorganic carriers for various hydrophilic cargo molecules. The membrane affinity and activity of dodecaborates in the presence or absence of cargo are as follows: $B_{12}H_{12}^{2-}$<$B_{12}Cl_{12}^{2-}$<$B_{12}Br_{12}^{2-}$< $B_{12}I_{12}^{2-}$. The largest and most chaotropic cluster, $B_{12}I_{12}^{2-}$, appears to be overly active, causing membrane disruption even in the absence of cargo. On the other hand, the smallest and least chaotropic cluster in this series, $B_{12}H_{12}^{2-}$, demonstrated no ability to transport peptide cargo. The intermediate-sized and chaotropicity clusters, $B_{12}Cl_{12}^{2-}$ and $B_{12}Br_{12}^{2}$, effectively transport peptides across the lipid membrane. The highest transport activity was shown in the $B_{12}Br_{12}^{2}$ in this series of homologue clusters. [34]

To conclude, boron clusters have the ability to interact and form complexes with a diverse range of hosts, from macrocycles to biomolecules. The driving force behind the interactions of

boron clusters with all the aforementioned hosts is the superchaotropic effect, or non-classical hydrophobic effect.[40]

I.4 Cobalt bis-dicarbollide anion

Cobalt bis-dicarbollide anion $[Co(C_2B_9H_{11})_2]^-$ (Figure 1.5) was one of the first metallacarboranes discovered.[59] There are few alternative names, which are commonly used by the boron community such as cobalt bis(dicarbolide) and cobaltabisdicarbollide.[60] Although, IUPAC recently introduces new recommendations on the existing nomenclature of cobalt bis-dicarbollide which is 3,3′-commo-bis[closo-1,2-dicarba-3-cobaltadodecaborane]. [61] The cobalt bis-dicarbollide anion or COSAN (Co = cobalt; SAN = sandwich) is a nanometer-sized inorganic anion with an ellipsoidal shape. It consists of a central metal ion, commonly Co^{3+}, sandwiched between two bulky and highly hydrophobic dicarbollide semi cages $(C_2B_9H_{11})^{2-}$, where each of them bearing two negative charges. The remaining negative charge is delocalized over the whole COSAN structure. [62] The dicarbollide semi cages have a dihedral angle of 3.7°.[63] The vector distances from cobalt to the C_2B_9 planes are nearly identical (1.466 and 1.476 Å). Despite the fact that Co-C distances are slightly shorter than Co-B distances, the metal appears to be equidistant from the facial boron and carbon atoms (2.046 and 2.097, respectively).[64]

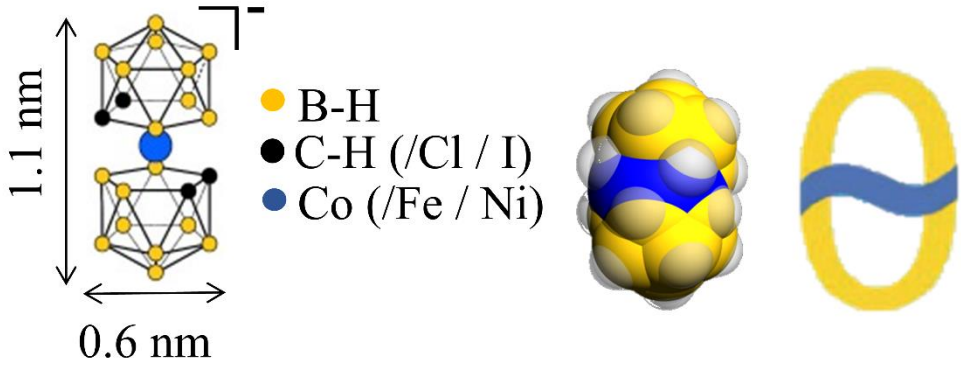

Figure 1.5. *The cobalt bis-dicarbollide (COSAN) anion is composed of two bulky dicarbollide semi cages that sandwich a cobalt(III) whose shape is compared to the Greek letter θ (far right).*

The two dicarbollide cages are mutually rotated by 37°, which results in staggered orientation of the carborane cages with the two C-C edges in close proximity and overall C_2 symmetry.[63,64] The B-H or C-H bonds of COSAN tilt away from the C_2B_3 towards the metal that prevents free rotation, thus possessing three different rotamers (cisoid, gauche and transoid) with different energies, see Figure 1.6.[63,65,66]

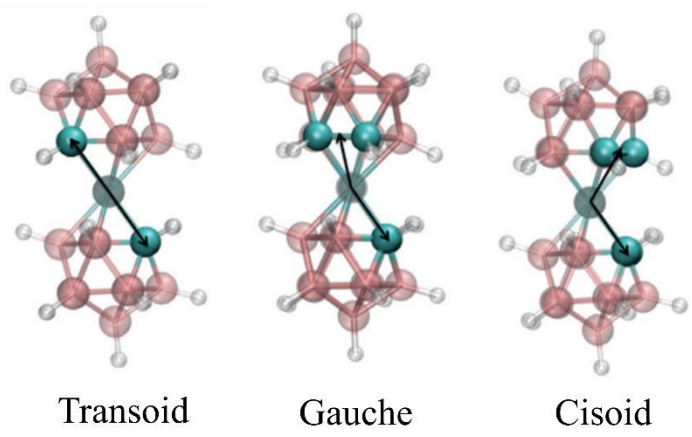

***Figure 1.6**. Atomic structure of the cobalt bis-dicarbollide anion in its three rotameric forms (cis-, gauche- and trans-), modified from [65].*

The rotameric forms cis- and gauche- are able to have clockwise and counterclockwise forms. According to quantum chemical calculations, the transoid rotamer has the lowest energy in vacuum but is the least abundant rotamer in the crystal structure.[67] The cisoid rotamer of COSAN is the most stable form in aqueous solution and solid state, according to DFT calculations and crystal data. The design of cis-COSAN is most likely the origin of its surfactant behavior, which will be discussed in detail in the following section.[65]

I.4.1 Surfactant behavior of cobalt bis-dicarbollide anion

Surfactants are molecules that absorb at the liquid interface and then modify the surface tension between two fluid phases, with the common one being water and the second being air or oil. Surfactants are amphiphilic molecules made of a long hydrocarbon tail (hydrophilic) and a polar head group (hydrophobic). Despite the fact that surfactants modify the surface tension of water, they form aggregates (micelles, vesicles, lamellae etc.) in the bulk aqueous phase.[65] The aggregation mechanism is regulated by the tendency of the hydrophobic part to avoid being in contact with water (hydrophobic effect), while the hydrophilic part tends to be strongly hydrated. The formation of aggregates is a result of the minimization of free energy (by avoiding the contact of the hydrophobic part with water) and the maximization of entropy.[62] This brief description of surfactants generates an easy structure activity connection.[65] Even though COSAN does not have the structure of a conventional surfactant (hydrophobic tail and hydrophobic head), and thus the structure connection activity referred to above is not obvious, it appears to have surfactant behavior. It was found that COSAN shows surface activity[50,68] and self-assembly.[62,69,70] The surface activity of COSAN evolves similarly to that of

conventional surfactants. Surface tension reduces with increasing concentration, suggesting that surfactant molecules begin to adsorb at the water surface, and once the surface is completely covered, surface tension remains constant with further concentration increases. The apparent break in the surface tension evolution upon increasing surfactant concentration is termed "critical micellar concentration" (CMC), and it is correlated to the formation of micelles-like aggregates in bulk solution. The concentration at which the surface tension curve for COSAN (H+ as the counterion) breaks is around 0.01 - 0.02 mol L^{-1} (see Figure 1.7), which coincides with the range of concentrations above which small aggregates are formed in water as found by Bauduin et al. using small angle neutron scattering (0.0186 mol L^{-1}).[62] Moreover, they have demonstrated that COSAN (H^+ as the counterion) forms unconventional large aggregates with a radius of more than 20 nm around the critical concentration of around 0.01 mol L^{-1}. These non-expectedly large self-aggregates were characterized as "monolayered vesicles" and have an aggregation number of about 12.500 ± 100. The monolayered vesicles are charged, arising from the charge of the COSAN, and at the CAC mentioned above, a Coulombic blow-up of the vesicles induces the formation of smaller aggregates. Small aggregates with a radius of about 1.16 nm start to form as COSAN concentration increases above the critical aggregation concentration (CAC) of about 0.01 mol L^{-1}. Above this concentration, small aggregates with an aggregation number of about 14 start forming, leading to their coexistence with vesicles.[62]

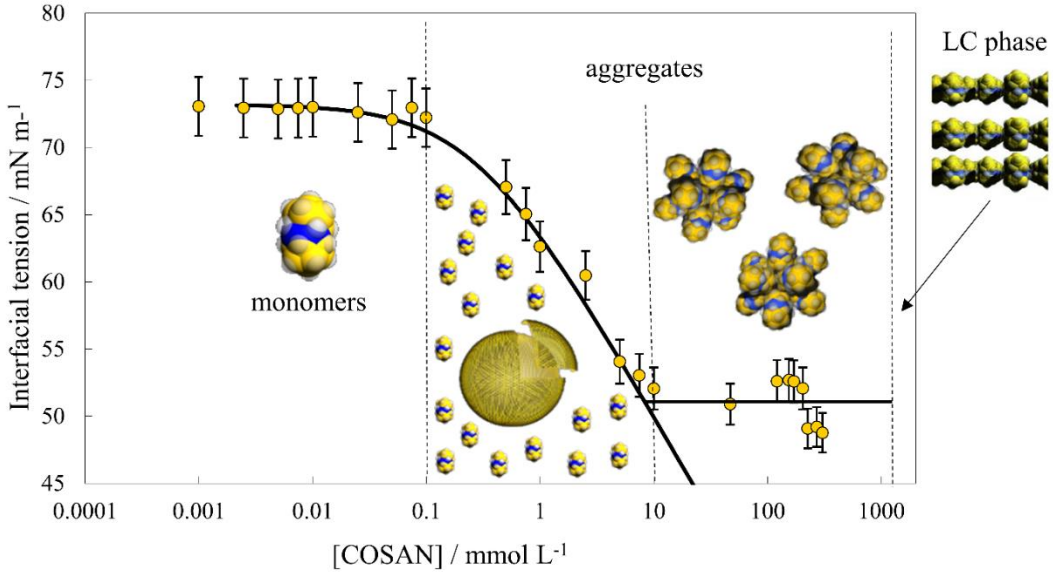

Figure 1.7. *Surface tension of air-water interface as a function of COSAN concentration, modified from [50].*

Recently, Zigas et al. proposed a model to describe isothermal titration calorimetry (ITC), and they found a value for the aggregation number of COSAN (Na^+ as the counter cation) of 5. Calculations based on quantum mechanics and simulations of molecular dynamics partially supported their findings.[71]

By increasing COSAN concentration at higher concentrations (over 0.1 mol L^{-1}), the formation of the lamellar phases was also observed, which was still surprising for an inorganic ion. Brusselle et al. have thus shown that the formation of lamellar phases is not an exclusive property of surfactants with well-defined amphiphilic structures but also a property of COSAN and its derivatives, such as I_2COSAN.[70]

The surfactant properties of COSAN result from a combination of repulsive forces, due to their ionic nature, and attractive forces. However, the origin of these attractive forces is different for classical surfactants, such as sodium dodecylsulfate (SDS), and for COSAN. On the one hand, for classical surfactants, the hydrophobic effect and the amphiphilic structure are at the origin of the surfactant properties. On the other hand, for COSAN anions, the surfactant properties result from the hydrophobic and superchaotropic effects and from the formation of intermolecular di-hydrogen bonds between C-$H^{\delta+ \cdots \delta-}$H-B with opposite polarities.[70] It was proposed by Malaspina et al., based on molecular dynamic simulations, that the cisoid rotamer of COSAN shows a hydrophobic polar "head". The molecular architecture of the cisoid rotamer of COSAN shows a more hydrophobic part and a more hydrophilic part, which are delimited by the four carbon atoms and the boron atoms, respectively.[65]

In this project, COSAN is used with sodium (Na^+) as a counter cation. Zaulet et al. studied the role of the counter cations on the aggregate formation in aqueous solutions of COSAN and its derivatives. The type of counterions, among H+, Li+, Na+, K+, has apparently not effect on the transitions between the assemblies.[72]

The choice of sodium as a counter cation in COSAN stems from the following project interests:
i) Study on the solubilization of hydrophobic compounds by COSAN and its sodium form is highly soluble in water compared to other cations such as Cs^+.

ii) Study on the interactions of COSAN with proteins, where the sodium form is a good choice since Na^+ is the most abundant cation in the physiological serum of the human body.

In many aspects, COSAN behaves as a conventional surfactant, such as SDS. In this project, SDS, the most commonly used surfactant, was selected to be compared with NaCOSAN

because they share several features. SDS and NaCOSAN have comparable numbers of atoms, molecular weights, and critical micellar (or aggregation) concentrations, and both are anionic with one negative charge and the same counter cation.

Table 1.3: Features of NaCOSAN and SDS.

Features	NaCOSAN	SDS
Formula	$[Co(C_4B_{18}H_{22})]^-$	$[C_{12}H_{25}SO_4]^-$
Counter cation	Na^+	Na^+
Number of atoms	46	43
Molecular weight / g mol^{-1}	346.74	288.37
Critical aggregation concentration / mmol L^{-1}	~10-20	~8
Aggregation number	~ 14[62]	~ 60[73]
Charge	Negative (1)	Negative (1)

I.5 Summary history of boron clusters

In Figure 1.8, the timeline of selected publications about the history of boron clusters over the years is presented.

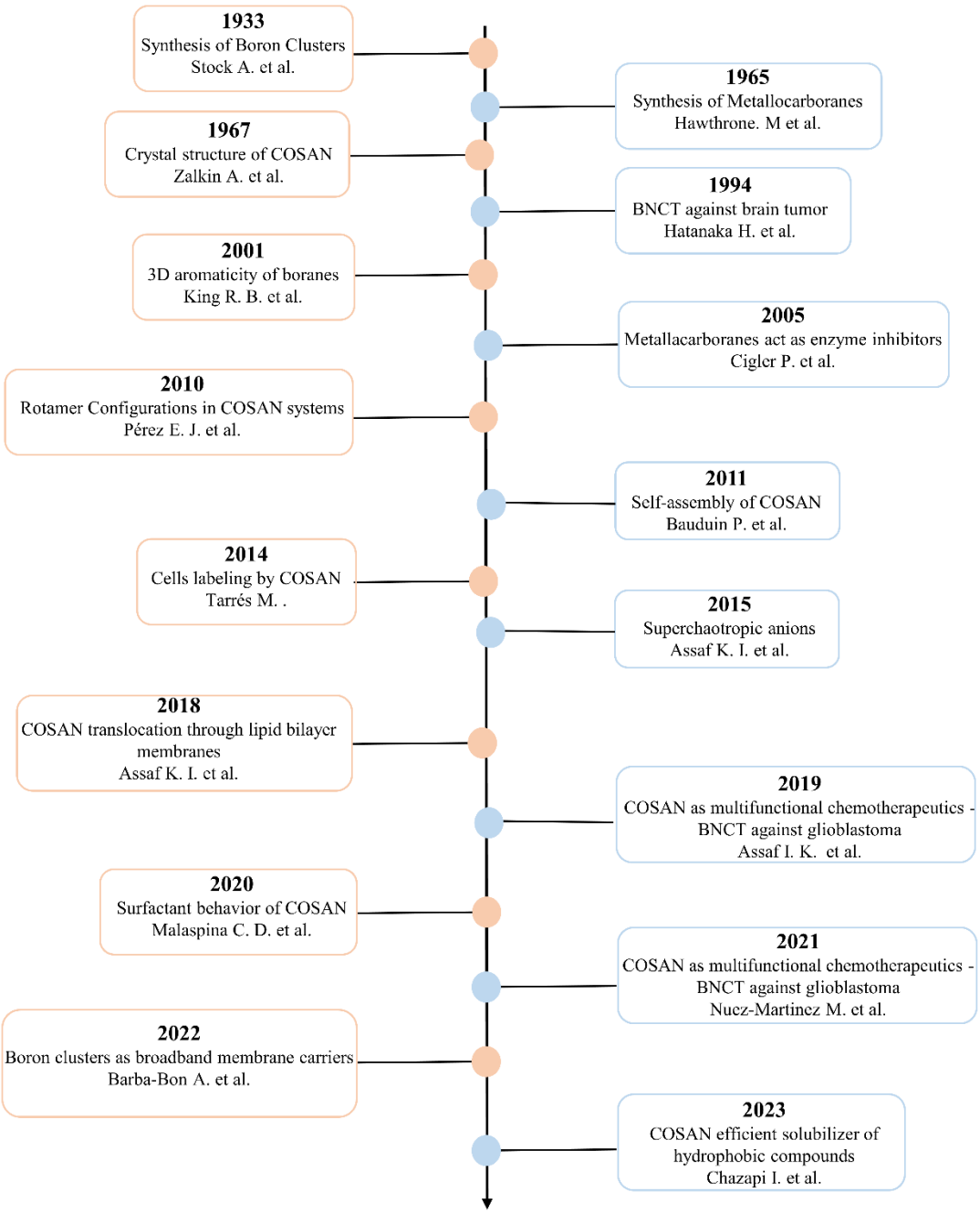

***Figure 1.8**. Timeline of selected events from the history of boron cluster chemistry and supramolecular chemistry.*

References

[1] J.L. Poiseuille, Sur le mouvement des liquides de nature très différente dans les tubes de très petits diamètres, Ann Chim Phys. 21 (1847) 76–110.

[2] W. Kunz, Specific Ion Effects, Evidences. Encyclopedia of Applied Electrochemistry., Springer, New York, 2014. https://doi.org/https://doi.org/10.1007/978-1-4419-6996-5_26.

[3] W. Kunz, J. Henle, B.W. Ninham, "Zur Lehre von der Wirkung der Salze" (about the science of the effect of salts): Franz Hofmeister's historical papers, Curr. Opin. Colloid Interface Sci. 9 (2004) 19–37. https://doi.org/10.1016/j.cocis.2004.05.005.

[4] Y. Marcus, Effect of ions on the structure of water, Pure Appl. Chem. 82 (2010) 1889–1899. https://doi.org/10.1351/PAC-CON-09-07-02.

[5] W. Kunz, Specific Ion Effects, World Scie, 2010.

[6] Y. Chen, H.I. Okur, C. Liang, S. Roke, Orientational ordering of water in extended hydration shells of cations is ion-specific and is correlated directly with viscosity and hydration free energy, Phys. Chem. Chem. Phys. 19 (2017) 24678–24688. https://doi.org/10.1039/c7cp03395h.

[7] A. Salis, B.W. Ninham, Models and mechanisms of Hofmeister effects in electrolyte solutions, and colloid and protein systems revisited, Chem. Soc. Rev. 43 (2014) 7358–7377. https://doi.org/10.1039/c4cs00144c.

[8] G. Stirnemann, E. Wernersson, P. Jungwirth, D. Laage, Mechanisms of acceleration and retardation of water dynamics by ions, J. Am. Chem. Soc. 135 (2013) 11824–11831. https://doi.org/10.1021/ja405201s.

[9] K.D. Collins, Ions from the Hofmeister series and osmolytes: Effects on proteins in solution and in the crystallization process, Methods. 34 (2004) 300–311. https://doi.org/10.1016/j.ymeth.2004.03.021.

[10] E. Leontidis, M. Christoforou, C. Georgiou, T. Delclos, The ion-lipid battle for hydration water and interfacial sites at soft-matter interfaces, Curr. Opin. Colloid Interface Sci. 19 (2014) 2–8. https://doi.org/10.1016/j.cocis.2014.02.003.

[11] J. Zeng, X. Gao, Z. Dai, B. Tang, X.F. Tang, Effects of metal ions on stability and activity of hyperthermophilic pyrolysin and further stabilization of this enzyme by modification of a Ca2+-binding site, Appl. Environ. Microbiol. 80 (2014) 2763–2772. https://doi.org/10.1128/AEM.00006-14.

[12] H. Zhao, Protein Stabilization and Enzyme Activation in Ionic Liquids: Specific Ion Effects, J. Chem. Technol. Biotechnol. 91 (2016) 25–50. https://doi.org/10.1002/jctb.4837.

[13] M.L. Berkowitz, R. Vácha, Aqueous solutions at the interface with phospholipid bilayers, Acc. Chem. Res. 45 (2012) 74–82. https://doi.org/10.1021/ar200079x.

[14] H.I. Petrache, T. Zemb, L. Belloni, V.A. Parsegian, Salt screening and specific ion adsorption determine neutral-lipid membrane interactions, Proc. Natl. Acad. Sci. U. S. A. 103 (2006) 7982–7987. https://doi.org/10.1073/pnas.0509967103.

[15] H.C. Visser, D.M. Rudkevich, W. Verboom, F. Jong, D.N. Reinhoudt, Anion carrieer mediated membrane transport of phosphate: selectivity of $H_2PO_4^-$ over Cl^-, J. Am. Chem. Soc. 116 (1994) 11554–11555.

[16] M. Boström, D.R.M. Williams, B.W. Ninham, Specific ion effects: Why the properties of lysozyme in salt solutions follow a hofmeister series, Biophys. J. 85 (2003) 686–694. https://doi.org/10.1016/S0006-3495(03)74512-3.

[17] J. Kozuch, C. Steinem, P. Hildebrandt, D. Millo, Combined electrochemistry and surface-enhanced infrared absorption spectroscopy of gramicidin A incorporated into tethered bilayer lipid membranes, Angew. Chemie - Int. Ed. 51 (2012) 8114–8117. https://doi.org/10.1002/anie.201203214.

[18] R. Holm, C. Schönbeck, P. Somprasirt, P. Westh, H. Mu, A study of salt effects on the complexation between β-cyclodextrins and bile salts based on the Hofmeister series, J. Incl. Phenom. Macrocycl. Chem. 80 (2014) 243–251. https://doi.org/10.1007/s10847-014-0383-9.

[19] P. Rouster, M. Pavlovic, I. Szilagyi, Destabilization of Titania Nanosheet Suspensions by Inorganic Salts: Hofmeister Series and Schulze-Hardy Rule, J. Phys. Chem. B. 121 (2017) 6749–6758. https://doi.org/10.1021/acs.jpcb.7b04286.

[20] H. Lai, Q. Shen, F. Zhan, S. Jiang, H. Sui, Y. Chen, B. Li, J. Li, Effect of Hofmeister series anions on freeze-thaw stability of emulsion stabilized with whey protein isolates, Food Hydrocoll. 134 (2023) 108015. https://doi.org/10.1016/j.foodhyd.2022.108015.

[21] S. Sett, S.I. Karakashev, S.K. Smoukov, A.L. Yarin, Ion-specific effects in foams, Adv. Colloid Interface Sci. 225 (2015) 98–113. https://doi.org/10.1016/j.cis.2015.08.007.

[22] T. López-León, A.B. Jódar-Reyes, J.L. Ortega-Vinuesa, D. Bastos-González, Hofmeister effects on the colloidal stability of an IgG-coated polystyrene latex, J. Colloid Interface Sci. 284 (2005) 139–148. https://doi.org/10.1016/j.jcis.2004.10.021.

[23] M. Van Der Linden, B.O. Conchúir, E. Spigone, A. Niranjan, A. Zaccone, P. Cicuta, Microscopic Origin of the Hofmeister Effect in Gelation Kinetics of Colloidal Silica, J. Phys. Chem. Lett. 6 (2015) 2881–2887. https://doi.org/10.1021/acs.jpclett.5b01300.

[24] V. Merk, C. Rehbock, F. Becker, U. Hagemann, H. Nienhaus, S. Barcikowski, In Situ Non-DLVO Stabilization of Surfactant-Free, Plasmonic Gold Nanoparticles: E ff ect of Hofmeister ' s Anions, (2014).

[25] C. Kaulen, U. Simon, Ion specific effects on the immobilisation of charged gold nanoparticles on metal surfaces, RSC Adv. 8 (2018) 1717–1724. https://doi.org/10.1039/c7ra10374c.

[26] S.Z. Moghaddam, E. Thormann, The Hofmeister series: Specific ion effects in aqueous polymer solutions, J. Colloid Interface Sci. 555 (2019) 615–635. https://doi.org/10.1016/j.jcis.2019.07.067.

[27] Y. Zhang, S. Furyk, D.E. Bergbreiter, P.S. Cremer, Specific ion effects on the water solubility of macromolecules: PNIPAM and the Hofmeister series, J. Am. Chem. Soc. 127 (2005) 14505–14510. https://doi.org/10.1021/ja0546424.

[28] Y. Zhang, P.S. Cremer, Interactions between macromolecules and ions: the Hofmeister series, Curr. Opin. Chem. Biol. 10 (2006) 658–663.

https://doi.org/10.1016/j.cbpa.2006.09.020.

[29] H.I. Okur, J. Hladílková, K.B. Rembert, Y. Cho, J. Heyda, J. Dzubiella, P.S. Cremer, P. Jungwirth, Beyond the Hofmeister Series: Ion-Specific Effects on Proteins and Their Biological Functions, J. Phys. Chem. B. 121 (2017) 1997–2014. https://doi.org/10.1021/acs.jpcb.6b10797.

[30] L. Abezgauz, K. Kuperkar, P.A. Hassan, O. Ramon, P. Bahadur, D. Danino, Effect of Hofmeister anions on micellization and micellar growth of the surfactant cetylpyridinium chloride, J. Colloid Interface Sci. 342 (2010) 83–92. https://doi.org/10.1016/j.jcis.2009.08.045.

[31] N. Schwierz, D. Horinek, U. Sivan, R.R. Netz, Reversed Hofmeister series—The rule rather than the exception, Curr. Opin. Colloid Interface Sci. 23 (2016) 10–18. https://doi.org/10.1016/j.cocis.2016.04.003.

[32] N. Schwierz, D. Horinek, R.R. Netz, Reversed anionic hofmeister series: The interplay of surface charge and surface polarity, Langmuir. 26 (2010) 7370–7379. https://doi.org/10.1021/la904397v.

[33] K.I. Assaf, W.M. Nau, The Chaotropic Effect as an Assembly Motif in Chemistry, Angew. Chemie - Int. Ed. 57 (2018) 13968–13981. https://doi.org/10.1002/anie.201804597.

[34] A. Barba-Bon, G. Salluce, I. Lostalé-Seijo, K.I. Assaf, A. Hennig, J. Montenegro, W.M. Nau, Boron clusters as broadband membrane carriers, Nat. 603 (2022) 637. https://doi.org/10.1038/s41586-022-04413-w.

[35] K.I. Assaf, W.M. Nau, The Chaotropic Effect as an Assembly Motif in Chemistry, Angew. Chemie - Int. Ed. 57 (2018) 13968–13981. https://doi.org/10.1002/anie.201804597.

[36] A. Stock, C. Massenez, Boron hydrides. Berichte, 45 (1913) 3539–3568.

[37] A. Stock, Hybrides of Boron and Silicon, J. Phys. Chem. 38 (1934) 714–715. https://doi.org/doi.org/10.1021/j150356a019.

[38] R.N. Grimes, Boron Clusters Come of Age, J. Chem. Educ. 81 (2004) 657–672.

[39] R.B. King, Three-Dimensional Aromaticity in Polyhedral Boranes and Related Molecules, Chem. Rev. 101 (2001) 1119–1152. https://doi.org/10.1002/chin.200131286.

[40] J. Cebula, K. Fink, J. Boratyński, T.M. Goszczyński, Supramolecular chemistry of anionic boron clusters and its applications in biology, Coord. Chem. Rev. 477 (2023). https://doi.org/10.1016/j.ccr.2022.214940.

[41] F.R. Barth, P. Mi, W. Yang, Boron delivery agents for boron neutron capture therapy of cancer, Cancer Commun. 38 (2018) 1–15. https://doi.org/https://doi.org/10.1186/s40880-018-0299-7.

[42] J.C. Axtell, L.M.A. Saleh, E.A. Qian, A.I. Wixtrom, A.M. Spokoyny, Synthesis and Applications of Perfunctionalized Boron Clusters, Inorg. Chem. 57 (2018) 2333–2350. https://doi.org/10.1021/acs.inorgchem.7b02912.

[43] B. Grüner, M. Kugler, S. El Anwar, J. Holub, J. Nekvinda, D. Bavol, Z. Růžičková, K.

Pospíšilová, M. Fábry, V. Král, J. Brynda, P. Řezáčová, Cobalt Bis(dicarbollide) Alkylsulfonamides: Potent and Highly Selective Inhibitors of Tumor Specific Carbonic Anhydrase IX, Chempluschem. 86 (2021) 352–363. https://doi.org/10.1002/cplu.202000574.

[44] E. Vaňková, K. Lokočová, O. Maťátková, I. Křížová, J. Masák, B. Grüner, P. Kaule, J. Čermák, V. Šícha, Cobalt bis-dicarbollide and its ammonium derivatives are effective antimicrobial and antibiofilm agents, J. Organomet. Chem. 899 (2019) 1–8. https://doi.org/10.1016/j.jorganchem.2019.120891.

[45] M. Gozzi, B. Schwarze, E. Hey-Hawkins, Preparing (Metalla)carboranes for Nanomedicine, ChemMedChem. 16 (2021) 1533–1565. https://doi.org/10.1002/cmdc.202000983.

[46] A.B. Buades, Z. Kelemen, V.S. Arderiu, A. Zaulet, C. Viñas, F. Teixidor, A fast and simple B-C bond formation in metallacarboranes avoiding halometallacarboranes and transition metal catalysts, Dalt. Trans. 49 (2020) 3525–3531. https://doi.org/10.1039/c9dt04695j.

[47] S. Mukherjee, P. Thilagar, Boron clusters in luminescent materials, Chem. Commun. 52 (2016) 1070–1093. https://doi.org/10.1039/c5cc08213g.

[48] B.P. Dash, R. Satapathy, J.A. Maguire, N.S. Hosmane, Polyhedral boron clusters in materials science, New J. Chem. 35 (2011) 1955–1972. https://doi.org/10.1039/c1nj20228f.

[49] K. Karki, D. Gabel, D. Roccatano, Structure and dynamics of dodecaborate clusters in water, Inorg. Chem. 51 (2012) 4894–4896. https://doi.org/10.1021/ic300223z.

[50] P.M. Gassin, L. Girard, G. Martin-Gassin, D. Brusselle, A. Jonchère, O. Diat, C. Viñas, F. Teixidor, P. Bauduin, Surface activity and molecular organization of metallacarboranes at the air-water interface revealed by nonlinear optics, Langmuir. 31 (2015) 2297–2303. https://doi.org/10.1021/acs.langmuir.5b00125.

[51] V. Ďorďovič, Z. Tošner, M. Uchman, A. Zhigunov, M. Reza, J. Ruokolainen, G. Pramanik, P. Cígler, K. Kalíková, M. Gradzielski, P. Matějíček, Stealth Amphiphiles: Self-Assembly of Polyhedral Boron Clusters, Langmuir. 32 (2016) 6713–6722. https://doi.org/10.1021/acs.langmuir.6b01995.

[52] C. Viñas, M. Tarrés, P. González-Cardoso, P. Farràs, P. Bauduin, F. Teixidor, Surfactant behaviour of metallacarboranes. A study based on the electrolysis of water, Dalt. Trans. 43 (2014) 5062–5068. https://doi.org/10.1039/c3dt52825a.

[53] K.I. Assaf, M.S. Ural, F. Pan, T. Georgiev, S. Simova, K. Rissanen, D. Gabel, W.M. Nau, Water structure recovery in chaotropic anion recognition: High-affinity binding of dodecaborate clusters to γ-cyclodextrin, Angew. Chemie - Int. Ed. 54 (2015) 6852–6856. https://doi.org/10.1002/anie.201412485.

[54] K.I. Assaf, D. Gabel, W. Zimmermann, W.M. Nau, High-affinity host-guest chemistry of large-ring cyclodextrins, Org. Biomol. Chem. 14 (2016) 7702–7706. https://doi.org/10.1039/c6ob01161f.

[55] K.I. Assaf, B. Begaj, A. Frank, M. Nilam, A.S. Mougharbel, U. Kortz, J. Nekvinda, B. Grüner, D. Gabel, W.M. Nau, High-Affinity Binding of Metallacarborane Cobalt Bis(dicarbollide) Anions to Cyclodextrins and Application to Membrane

Translocation, J. Org. Chem. 84 (2019) 11790–11798. https://doi.org/10.1021/acs.joc.9b01688.

[56] J.M. Fox, K. Kang, W. Sherman, A. Héroux, G.M. Sastry, M. Baghbanzadeh, M.R. Lockett, G.M. Whitesides, Interactions between Hofmeister anions and the binding pocket of a protein, J. Am. Chem. Soc. 137 (2015) 3859–3866. https://doi.org/10.1021/jacs.5b00187.

[57] T.M. Goszczyński, K. Fink, K. Kowalski, Z.J. Leśnikowski, J. Boratyński, Interactions of Boron Clusters and their Derivatives with Serum Albumin, Sci. Rep. 7 (2017) 1–12. https://doi.org/10.1038/s41598-017-10314-0.

[58] M. V. Kuperman, M.Y. Losytskyy, A.Y. Bykov, S.M. Yarmoluk, K.Y. Zhizhin, N.T. Kuznetsov, O.A. Varzatskii, E. Gumienna-Kontecka, V.B. Kovalska, Effective binding of perhalogenated closo-borates to serum albumins revealed by spectroscopic and ITC studies, J. Mol. Struct. 1141 (2017) 75–80. https://doi.org/10.1016/j.molstruc.2017.03.059.

[59] M.F.. Hawthorne, D.C.. Young, P.A.. Wegner, Carbametallic boron hydride derivatives I. apparent analogs of ferrocene and ferricinium ion, J. Am. Chem. Soc. 87 (1965) 1818–1819.

[60] F. Teixidor, C. Viñas, A. Demonceau, R. Nuñez, Boron clusters: Do they receive the deserved interest?, Pure Appl. Chem. 75 (2003) 1305–1313. https://doi.org/10.1351/pac200375091305.

[61] M.A. Beckett, B. Brellochs, I.T. Chizhevsky, T. Damhus, K.H. Hellwich, J.D. Kennedy, R. Laitinen, W.H. Powell, D. Rabinovich, C. Viñas, A. Yerin, Nomenclature for boranes and related species (IUPAC Recommendations 2019), Pure Appl. Chem. 92 (2020) 355–381. https://doi.org/10.1515/pac-2018-0205.

[62] P. Bauduin, S. Prevost, P. Farràs, F. Teixidor, O. Diat, T. Zemb, A theta-shaped amphiphilic cobaltabisdicarbollide anion: Transition from monolayer vesicles to micelles, Angew. Chemie - Int. Ed. 50 (2011) 5298–5300. https://doi.org/10.1002/anie.201100410.

[63] B.P. Dash, R. Satapathy, B.R. Swain, C.S. Mahanta, B.B. Jena, N.S. Hosmane, Cobalt bis(dicarbollide) anion and its derivatives, J. Organomet. Chem. 849–850 (2017) 170–194. https://doi.org/10.1016/j.jorganchem.2017.04.006.

[64] I.B. Sivaev, V.I. Bregadze, Chemistry of cobalt bis(dicarbollides). A review, Collect. Czechoslov. Chem. Commun. 64 (1999) 783–805. https://doi.org/10.1135/cccc19990783.

[65] D.C. Malaspina, C. Viñas, F. Teixidor, J. Faraudo, Atomistic Simulations of COSAN: Amphiphiles without a Head-and-Tail Design Display “Head and Tail” Surfactant Behavior, Angew. Chemie - Int. Ed. 59 (2020) 3088–3092. https://doi.org/10.1002/anie.201913257.

[66] F. Teixidor, C. Viñas, Boron and carbon: Antagonistic or complementary? proposal for a simple prototype of a molecular clutch or molecular switch, Pure Appl. Chem. 84 (2012) 2457–2465. https://doi.org/10.1351/PAC-CON-12-05-02.

[67] E.J. Juárez-Pérez, R. Núñez, C. Viñas, R. Sillanpää, F. Teixidor, The role of C-H···H-B interactions in establishing rotamer configurations in metallabis(dicarbollide)

systems, Eur. J. Inorg. Chem. (2010) 2385–2392. https://doi.org/10.1002/ejic.201000157.

[68] G. Chevrot, R. Schurhammer, G. Wipff, Surfactant behavior of “ellipsoidal” dicarbollide anions: A molecular dynamics study, J. Phys. Chem. B. 110 (2006) 9488–9498. https://doi.org/10.1021/jp060930q.

[69] P. Matějíček, P. Cígler, K. Procházka, V. Král, Molecular assembly of metallacarboranes in water: Light scattering and microscopy study, Langmuir. 22 (2006) 575–581. https://doi.org/10.1021/la052201s.

[70] D. Brusselle, P. Bauduin, L. Girard, A. Zaulet, C. Viñas, F. Teixidor, I. Ly, O. Diat, Lyotropic lamellar phase formed from monolayered θ-shaped carborane-cage amphiphiles, Angew. Chemie - Int. Ed. 52 (2013) 12114–12118. https://doi.org/10.1002/anie.201307357.

[71] Ž. Medoš, B. Hleli, Z. Tošner, P. Ogrin, T. Urbič, K. Kogej, M. Bešter-Rogač, P. Matějíček, Counterion-Induced Aggregation of Metallacarboranes, J. Phys. Chem. C. 126 (2022) 5735–5742. https://doi.org/10.1021/ACS.JPCC.2C00107/SUPPL_FILE/JP2C00107_SI_001.PDF.

[72] A. Zaulet, F. Teixidor, P. Bauduin, O. Diat, P. Hirva, A. Ofori, C. Viñas, Deciphering the role of the cation in anionic cobaltabisdicarbollide clusters, J. Organomet. Chem. 865 (2018) 214–225. https://doi.org/10.1016/j.jorganchem.2018.03.023.

[73] C.D. Bruce, S. Senapati, M.L. Berkowitz, L. Perera, M.D.E. Forbes, Molecular dynamics simulations of sodium dodecyl sulfate micelle in water: The behavior of water, J. Phys. Chem. B. 106 (2002) 10902–10907. https://doi.org/10.1021/jp025872x.

Chapter II: Solubilization of hydrophobic compounds by boron clusters

II.1 Solubilization of hydrophobic compounds

Solubilization of hydrophobic compounds in water is essential in many areas of application, such as the detergency domain [1], as the basic process of this concept is to remove clinging soils from multiple substrates; pharmacy,[2–5], many drugs being water-poorly soluble; fragrance,[6,7], perfume molecules being often strongly water insoluble molecules, and crop science for phosphorus fertilizers.[8] Among the different approaches for increasing the solubility of sparingly soluble (hydrophobic) molecules in water, (i) micellar or hydrotropic solubilization, using long or short chained amphiphilic molecules such as surfactants or hydrotropes,[9] (ii) co-solvency using a water soluble organic solvent and (iii) host-guest complexation using macrocycles are by far the most common ones.[10,11] The solubilization takes place with different mechanisms, which will be described in the following sections of this chapter.

II.1.1 Micellar solubilization

Surface active agents, or surfactants, are the most studied class of solubilizing agents. In fact, the term "solubilization" was originally reserved solely for surfactant solubilization.[12] Surfactants are amphiphiles, which are characterized by two distinct antagonist regions, one hydrophobic (non-polar) and one hydrophilic (polar). Direct surfactant micelles are supramolecular self-assemblies in aqueous phases. They are made of a given number of surfactant molecules arranged into a single compact structure in equilibrium with monomers.[13,14] The formation of the micelles (Figure 2.1) occurs when the concentration of the surfactant monomers in solution exceeds a critical value (its monomeric solubility). This value is called critical micellar concentration (CMC).

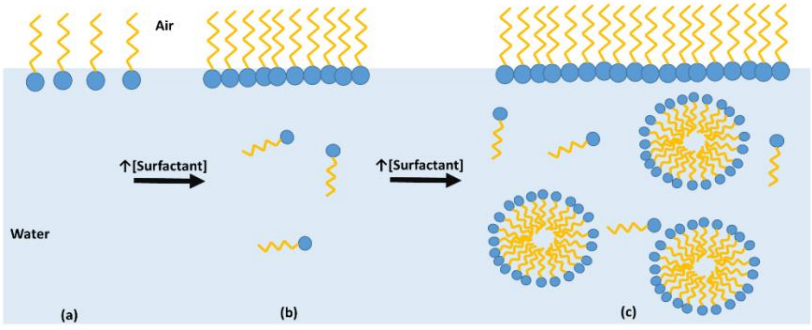

Figure 2.1. Schematic view of direct micelles formation in aqueous phase.*[15]*

The self-assembly (micellization) of surfactants is the result of the minimization of free energy of the system. The resulting structure of aggregates depends on the interaction forces between the molecules, the molecules and the water and the geometry of the amphiphiles, all compiled under the concept on the amphiphiles close packing. The critical packing parameter (CPP) was proposed by Ninham et al. to describe the aggregate shape and geometrical parameters of the surfactant. [16] It is defined as the ratio between the volume of the hydrophobic chain and the product of the area a_0 per head group by the length of the hydrophobic chain l_c, which is approximately 80% of the extended chain length,[17] due to gauche/trans isomerism of linear alkanes. Depending on the CPP value of a surfactant, different aggregate shapes, which are illustrated in the figure 2.2, can be formed.

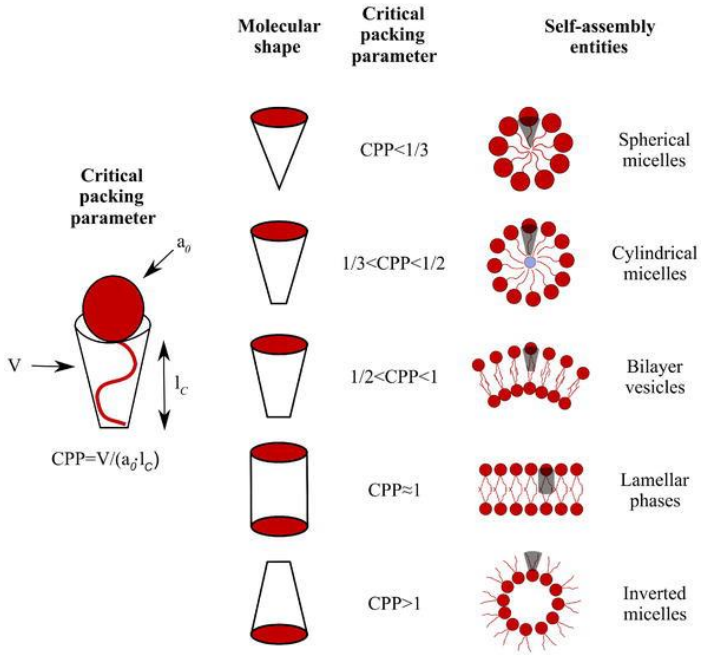

Figure 2.2. *Critical packing parameter and the expected aggregates shape in solution. [18]*

The micelles consist of three basic regions the core, the palisade layer, and the shell (Figure 2.3).

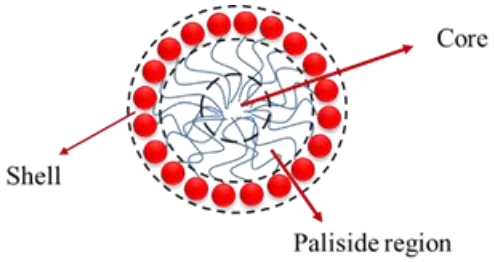

Figure 2.3. *Schematic view of the three basic domain of a direct surfactant's micelle.*

The core of the micelle is the region in the center that is composed almost entirely made of the hydrophobic part of the surfactant. The palisade layer is the region surrounding the core. It consists of the hydrophobic part and polar moieties from the hydrophilic part of the surfactant and water. The composition of the palisade layer is not homogeneous. The shell of the micelle, which consists of the hydrophilic part (surfactant head groups), and hydration water molecule.

Organic solutes can be solubilized when they are incorporated into one of the three regions. The more nonpolar the solute, the more probable it will be integrated towards the core, the center of the micelle. Similarly, the more polar the solute, the more likely it is to be found near the surface or in bulk water. Figure 2.4 illustrates the incorporation of nonpolar, semi-polar and polar solutes into the core, palisade layer and shell of the micelle, respectively.

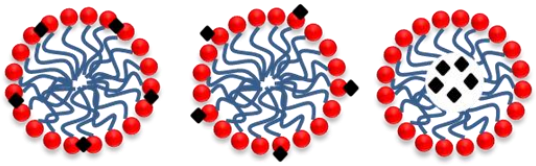

Figure 2.4. *Three schematic representations of the incorporation of the solutes (black squares) into micelles depending on the hydrophobic characteristics of the solute.*

Figure 2.5 illustrates the general curve of solubilization of organic compounds by surfactants, where S_0 is their solubility in pure water. The slope of the solubilization curve indicates the efficiency of surfactants at increasing the solubility of organic compounds. The CMC of the surfactant can be affected by the hydrophobic compounds (cooperative effect [19]) even if the monomers of the surfactants do not interact directly with the hydrophobic chemicals. However, just above the new CMC, the solubility increases linearly with the surfactant concentration.[12]

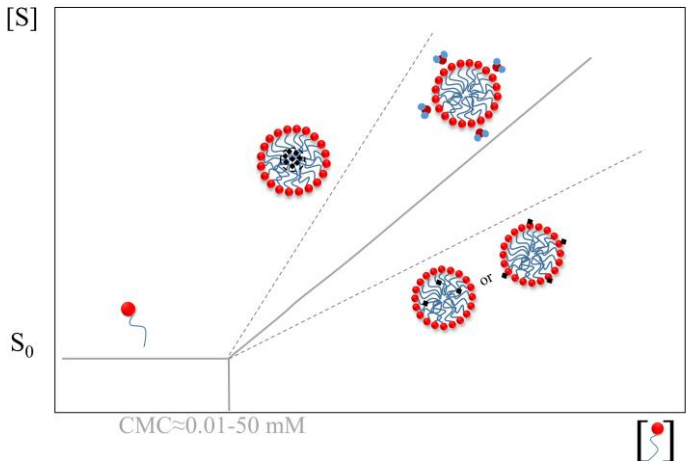

Figure 2.5. *Schematic representation of solubilisation increase of hydrophobic solutes "S" just above the CMC of the surfactant / solute mixture*

II.1.2 Microemulsions

Oil-in-water microemulsions, or swollen micelles, form when an organic liquid phase, which is immiscible with water, is added to the direct micelles. The inverse case, oil-in-water microemulsions, also exists. Microemulsions are isotropic solutions containing substantial amounts of a strongly polar component (water) and a strongly apolar component (oil) that are stabilized thermodynamically by amphiphilic molecules. There are limitations for the content of the three components in microemulsions, and their phase behavior is described by phase diagrams.[20]

Phase diagrams are a type of map that can be used to identify phase transitions as a function of thermodynamical conditions (temperature, pressure, concentration of the compounds, etc.) and provide information at the molecular and supramolecular structures.[21] McBain et al.[22] reported for the first time that the phase rule, which is derived from Gibbs laws, predicts the number of phases that can coexist in a given system and could be used to thermodynamically stable colloidal systems in equilibrium.

II.1.3 Hydrotropes

Hydrotropes are amphiphilic molecules and highly soluble in water as surfactants. The alkyl chain of a hydrotrope is too short (limited hydrophobic part) to induce micellization at relatively low concentrations, as it is observed with the surfactants having a linear alkyl chain with at least seven carbon atoms.[23] Compared to surfactants, forming well-defined micelles at low concentrations, most of the hydrotropes form ill-defined aggregates at high concentrations in water, typically above 0.5-1 M.

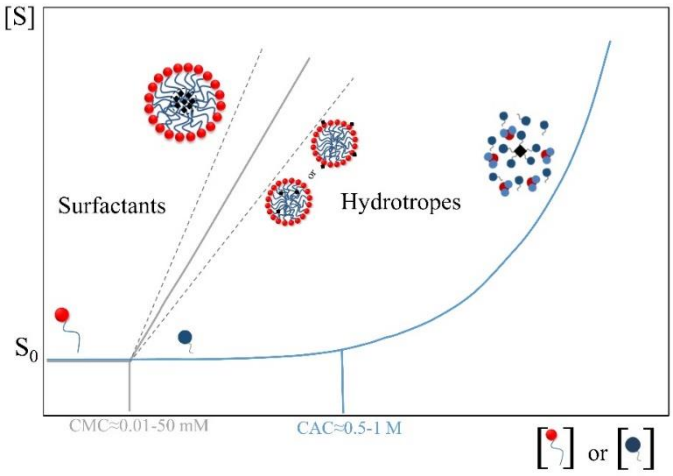

Figure 2.6. *Comparison of solubilization curve of solute between surfactant and hydrotropes.*

Often, hydrotropes only form such aggregates in the presence of a hydrophobic compound that the hydrotropes surround and, as a consequence, solubilize in aqueous medium. Therefore, in order to solubilize a significant amount of a hydrophobic component, a much higher concentration of the hydrotrope is required than in the case of the surfactant, as illustrated in Figure 2.6.[9,24–26]

II.1.4 Co-solvency

Cosolvency is the addition of water miscible solvents to an aqueous system and is one of the most powerful means of solubilizing nonpolar solutes in aqueous media. Most cosolvents are polar solvents that have hydrogen bond donor groups and/or hydrogen bond acceptor groups and as well as hydrocarbon regions. These hydrophilic hydrogen bonding groups interact strongly with water and ensure miscibility or at least high aqueous solubility. Meanwhile, the hydrophobic hydrocarbon regions interfere with water's hydrogen bonding network, resulting in a decrease in the overall intermolecular attraction of water. Co-solvents reduce the ability of water to squeeze out non-polar, hydrophobic compounds by disrupting their self-association, increasing their solubility. [27]

II.1.5 Solubilization by complexation (host-guest)

In comparison to micelles, inclusion or host-guest complexes have stricter geometric requirements and a well-defined stoichiometry. In recent years, cyclodextrins have attracted attention for solubilization of hydrophobic compounds. A cyclodextrin molecule has polar exterior and nonpolar interior that can accommodate a hydrophobic compound (Figure 2.7). In aqueous media, solubilization by cyclodextrins results from the insertion of the hydrophobic molecule (known as the guest) into the cavity of another molecule (known as the host).[28]

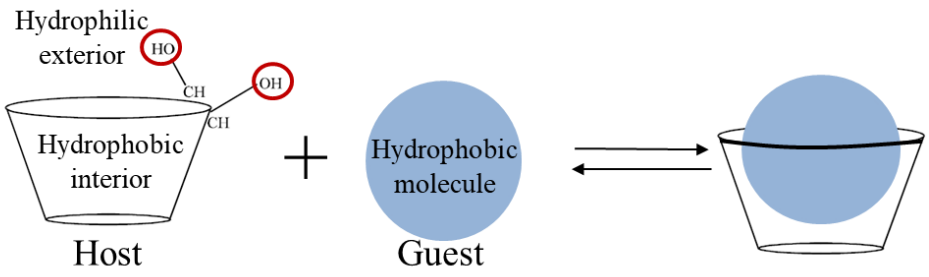

Figure 2.7. *Schematic representation of host-guest solubilization.*

Figure 2.8 illustrates the general curves of solubilization by cyclodextrins, where S_0 is the aqueous solubility (interception) of the hydrophobic compound. A-type phase-solubility profiles are obtained when the solubility of the hydrophobic compound substrate increases with increasing cyclodextrin concentration. B-type phase-solubility profiles indicate formation of complexes with limited solubility in the aqueous complexation medium. In general, the water-soluble cyclodextrin derivatives, such as α-CD, form A-type phase-solubility profiles (Figure 2.8, blue curves) while the less soluble cyclodextrins, such as β-CD and γ-CD, frequently form B-type profiles (Figure 2.8, red curve).[12]

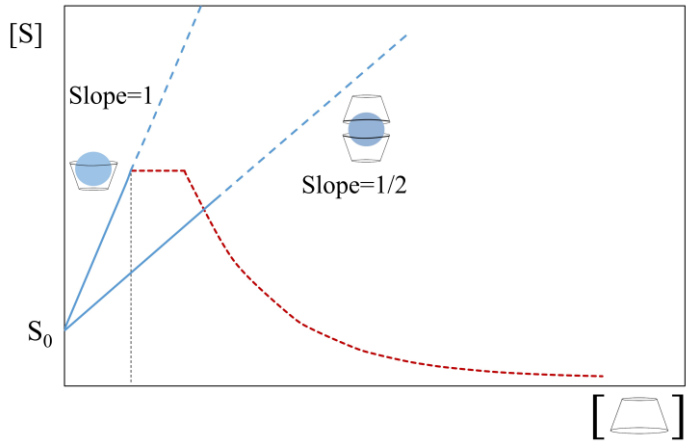

Figure 2.8*. Illustration of examples of solubilization curve of cyclodextrins. Blue curves correspond to A-type solubility profiles, and red curve corresponds to B-type solubility profiles.*

To summarize, molecular solubilization of hydrophobic compounds in water is commonly made by the addition of organic solubilizers through (i) micellar association or hydrotropic solvent pre-structuration using amphiphilic molecules, (ii) co-solvency using water-soluble solvents, and (iii) host-guest complexation using macrocycles. Thus, in this work, we will show that the cobalta-bis-dicarbollide and their derivatives (COSANs), which are fully inorganic and non-amphiphilic ionic boron clusters with nanometric size (nano-ions) and superchaotropic properties, efficiently act as solubilizers of model hydrophobic compounds in water.

II.2 Results

II.2.1 Solubilization of hydrophobic compounds by NaCOSAN

In this chapter, we investigated the ability of NaCOSAN (and di-iodinated NaCOSAN) to solubilize organic compounds with different hydrophobic characters (log *P* from 0.6 to 5.6):

alcohols and hydrophobic dyes, see Figure 2.9. The log *P* is defined as the ratio of the concentration of a compound in the organic phase (n-octanol) over the concentration in the aqueous phase. After a few tests in the laboratory, we have found that NaCOSAN increases (i) significantly the solubility of organic compounds with the lowest log *P* values, such as 2-butanol and 1-butanol, and (ii) slightly the solubility of organic compounds with higher log *P* values, such as n-pentanol. Therefore, a first focus will be made on 1-butanol (1-BuOH) and 2-butanol (2-BuOH) hereafter.

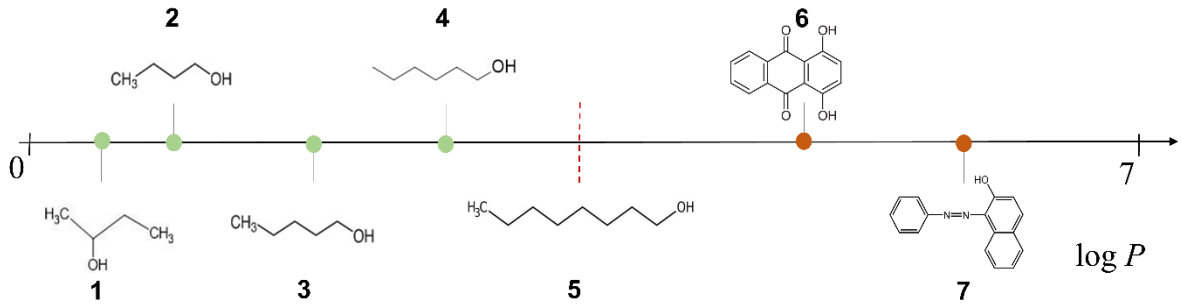

***Figure 2.9**. The compounds that can be solubilized by COSAN are shown on the log P scale, where **1** corresponds to 2-BuOH (LogP = 0.66), **2** 1-BuOH (0.88), **3** n-pentanol (1.51), **4** n-hexanol (2.03), **5** n-octanol (3.0), **6** quinizarine (3.7) and **7** Sudan I (5.6). The given logP values were taken from PubChem.*

In this section, the solubilization efficiency of NaCOSAN with 1- and 2- butanol in aqueous solution is investigated, and the corresponding ternary phase diagrams (water/alcohol/COSAN) were determined. Using NaCOSAN solutions at different concentrations, successive additions of 2-BuOH in µL range were carried out until the visual phase separation was observed, adding in a water bath at 22°C for 5–10 minutes between each addition, and then the solution was thoroughly mixed with a vortex. On the other hand, preparing NaCOSAN/2-BuOH solution at different NaCOSAN concentrations we determined the water solubility in the NaCOSAN/2-BuOH mixtures. The mixture of water/2-BuOH and 2-BuOH/water is monophasic up to 20 % of water in pure 2-BuOH and 2-BuOH in water. These observations are compiled in Figure 2.10 (and detailed in figure S2.1). The one-phase (presented as 1Φ) regions represent the water-rich and the alcohol rich phases whereas the central part and a tiny domain on the alcohol side are biphasic. The dots define the solubility of either alcohol in water or water in the alcohol. In the former case, this limit in increasing as a function of NaCOSAN concentration, whereas in the alcohol-rich part, the water solubility is rather constant at the first order. I did not observe the closing of the immiscibility gap.

We initially studied the solubility (Figure 2.10), tie lines (Figure S2.1), and then, with further analytical, and physical analysis, we tried to determine the phase diagram. The tie lines within the biphasic region were determined using different techniques: Total Organic Carbon analysis (TOC), UV-Visible spectroscopy, Karl Fisher Titration and Densimeter.

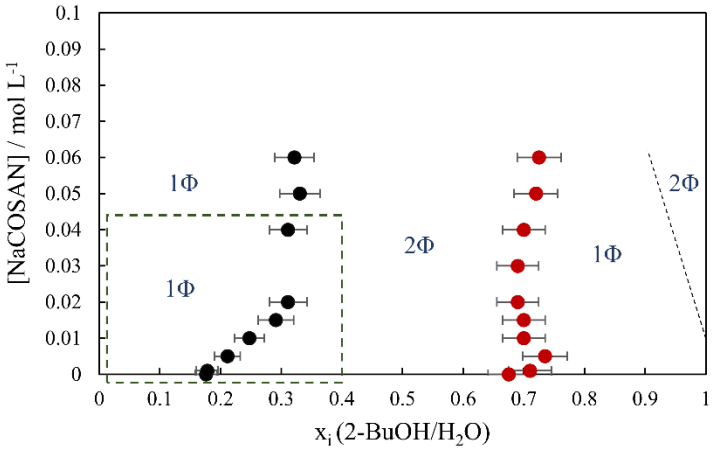

***Figure 2.10**. 1- and 2-phase limits in the ternary COSAN/water/2-BuOH system with mass fraction of butanol in water on the x-axis and molar concentration of COSAN on the y-axis. Phase diagram obtained at ambient temperature. The dashed green area of the graph corresponds to the dashed green area of the tie line graph.*

In fact, the TOC analysis enables the detection of the amount of total organic and inorganic carbon in the solutions, with a maximum detection limit of about 50 ppm carbon. We performed TOC analysis on different concentrations of NaCOSAN and 2-BuOH in order to get the calibration curve (Figure S2.2 in the supporting information) and to determine the organic and inorganic amount of carbon in the biphasic systems of NaCOSAN/2- BuOH. The initial assumption was that the NaCOSAN carbons would be negligible due to the difference between NaCOSAN and 2-BuOH concentration, which was in fact not really the case as it was observed from the calibration curve of NaCOSAN (Figure S2.2). The calibration curves were used for the determination of the amounts of inorganic and organic compounds that were in the biphasic system. However, the concentration that were calculated during the dilutions were not in agreement with the concentration of the experimental samples that we obtained through TOC analysis.

The determination of NaCOSAN concentration in each phase of the biphasic system NaCOSAN/2-BuOH/water was carried out by UV-Visible spectroscopy (Figure S2.6). The UV-vis absorption of NaCOSAN at different concentrations (Figure S2.3) was recorded and the calibration curve was made (Figure S2.4) to determine the concentration of NaCOSAN in

each phase. The upper phase has a higher NaCOSAN concentration than the lower phase, as expected given the color difference between the two phases (Figure S2.5).

As an additional experiment to the above, different percentages of 2- BuOH (0.5%, 1%, 2%, 5%, 10%, 15%, 20%, 80%, 85%, 90%, and 98%) in the presence of different NaCOSAN concentrations (Figure S2.7) were prepared. The absorptivity of NaCOSAN as a function of the percentage of 2- BuOH (Figure 2.11) was made in order to study the effect on NaCOSAN absorptivity in the presence of 2- BuOH, as it was used for the calculations of NaCOSAN in each phase of the biphasic system.

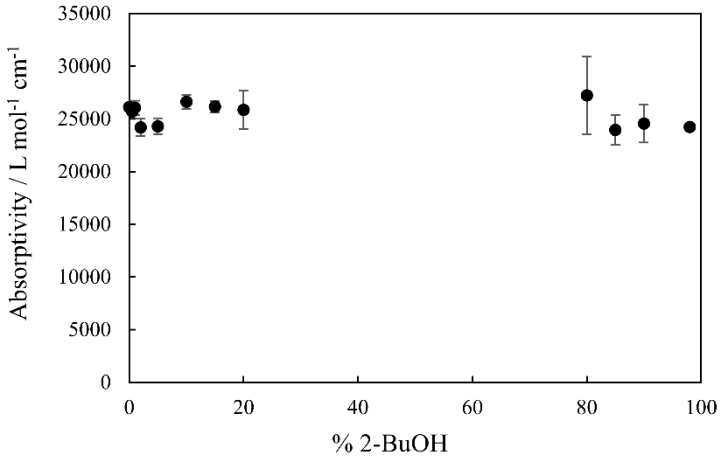

Figure 2.11. *Absorptivity of NaCOSAN as a function of different 2-BuOH percentages.*

The determination of 2- BuOH concentration was carried out through the density. Successive additions of water to 2- BuOH and 2- BuOH to water were performed in order to make the calibration curves (Figure S2.8). It was also verified that adding NaCOSAN to water did not affect its density (Figure S2.9). Therefore, the change in density is attributed to being mostly due to the 2-BuOH concentration. The H_2O content in the upper/organic phase was determined by Karl Fisher titration. The results of the titration are given in Table S2.2 in the appendix.

To conclude, the concentration of each component in the biphasic system NaCOSAN/2-BuOH/water can be determined by combining the above-mentioned techniques. However, the determination of the ternary phase diagram is not achieved by all these techniques. The study of the monophasic system NaCOSAN/2-BuOH/water was performed.

II.2.2 Solubility of butanol in the presence of NaCOSAN

The NaCOSAN/2-BuOH/H_2O phase diagram was established to evaluate the solubilization efficiency of NaCOSAN for 2-BuOH in water. Sodium dodecyl sulfate (SDS) and cyclodextrins were also used as standard solubilizers in order to compare the solubilization efficiency of NaCOSAN to the classical micellar mechanism for SDS and the host-guest mechanism for cyclodextrin. Different techniques were combined to decipher the solubilization mechanism at the molecular and supramolecular levels.

The evolution of the solubility of 2-BuOH in water upon addition of NaCOSAN is shown in Figure 2.12 and Figure S2.10. The solubility starts to increase at very low NaCOSAN concentrations, and it levels off at a concentration above around 0.016 mol L^{-1}, which is in the same range as the CAC of NaCOSAN in pure water (0.010 mol L^{-1}).[29–31]

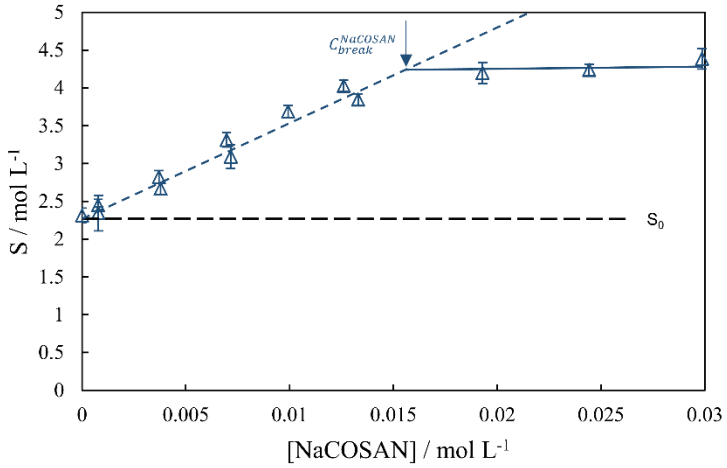

***Figure 2.12**. Solubility of 2-BuOH in water (S in mol/L) at 22°C as a function of NaCOSAN concentration. The horizontal dark dashed line corresponds to the solubility value of 2-BuOH in pure water, S_0. The arrow indicates the break observed in the evolution of the 2-BuOH solubility curves.*

In the case of SDS (Figure 2.13), the solubility starts to increase suddenly above a concentration of about 0.002 mol L^{-1}. In micellar solubilization, a sudden increase in solubility is classically attributed to the formation of micelles in the bulk solution. In pure water, SDS has a CMC of about 0.008 mol L^{-1}.[32] The CMC of SDS [33] (and of surfactants in general) is effectively decreased in the presence of medium-chained alcohols, with the alcohol molecules acting as a co-surfactant (upon the hydrophobic effect), which favors then the formation of micelles at lower concentrations of surfactants.[34] This explains why the break in the solubility curve for SDS appears at a concentration (0.002 mol L^{-1}) below its CMC in pure water (0.008 mol L^{-1}).

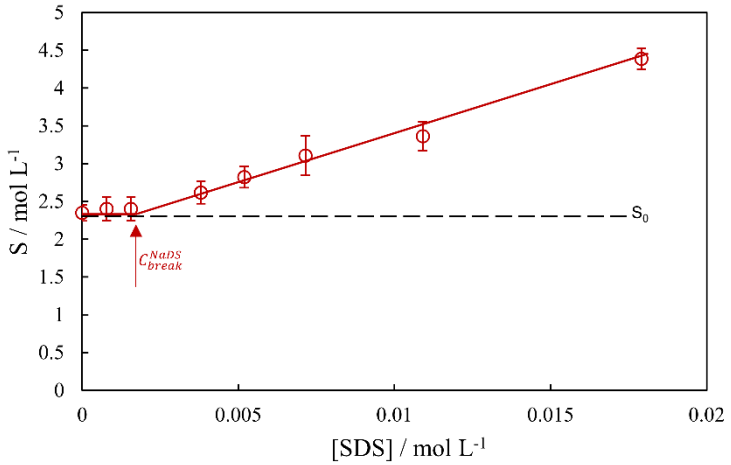

Figure 2.13. *Solubility of 2-BuOH in water (S in mol/L) at 22°C as a function of SDS concentration. The horizontal dark dashed line corresponds to the solubility value of 2-BuOH in water, S_0. The arrows indicate the breaks observed in the evolution of the 2-BuOH solubility curves.*

Interestingly, the increase in solubility at low NaCOSAN concentrations is comparable to the increase in solubility observed with a typical host-guest solubilization process, for example using cyclodextrins.[12]

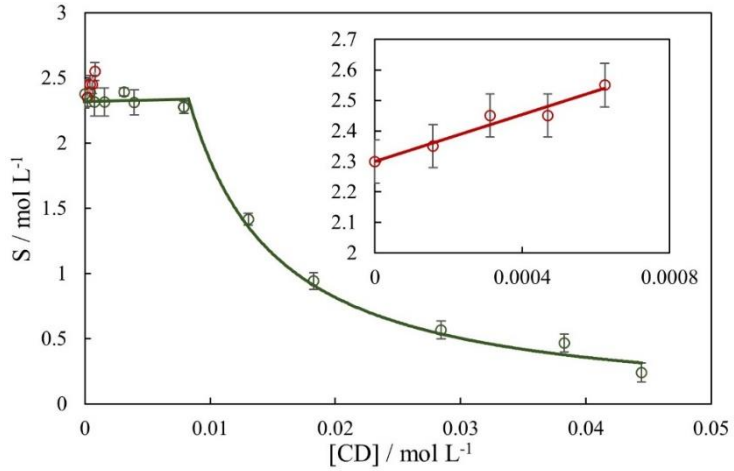

Figure 2.14*. Solubility of 2-BuOH in aqueous γ-cyclodextrin (green circles) and β-cyclodextrin (red circles) solution of varying concentrations at 22°C. The inset corresponds to a zoom of β-cyclodextrin's solubility curve.*

In the present case, the solubility of 2-BuOH upon addition of β-CD, composed of 7 glucose units, leads to an increase in the solubility but the low solubility of β-CD strongly limits its use as a solubilizer (Figure 2.14). For γ-CD, which is much more water soluble, no increase in the 2- butanol solubility was observed mostly because of the size mismatch between 2-BuOH and γ-CD cavity (Figure 2.14).

The slope of the solubility increases in Figure 2.12 and Figure S2.10 gives information on the efficiency of the solubilization processes. For NaCOSAN at low concentrations below C_{break}^{COSAN},

the slope is about 120, meaning that one NaCOSAN ion solubilizes approximately one hundred twenty 2-BuOH molecules, in excess beyond the solubility of 2- BuOH (S_0) in water. S_0 at 22°C was determined here (2.35 mol L^{-1}) by total organic carbon analysis (TOC) and is in agreement with the literature.[35,36] The slope of the solubility curve for SDS, above the CMC, is also about 120. However, it is worth mentioning that at high NaCOSAN or SDS concentrations, above around 0.015 mol L^{-1} SDS is more efficient in solubilizing 2-BuOH (forming large swollen micelles i.e., direct oil-in-water micro-emulsions). In conclusion, at low concentrations (<CAC or C_{break}^{COSAN}), NaCOSAN is a much better solubilizer than SDS and it is the opposite at high concentrations.

The 2-BuOH solubility curve obtained with NaI_2COSAN (Figure 15) is similar in shape to the NaCOSAN solubility curve. However, the solubility curve break of NaCOSAN appears at approximately 0.016 mol L^{-1}, whereas for NaI_2COSAN, it is approximately 0.014 mol L^{-1}. NaI_2COSAN is more hydrophobic than NaCOSAN, indicating that it has a lower CAC, which is in line with the break values of the solubility curves. Moreover, NaI_2COSAN is significantly more efficient than NaCOSAN in terms of solubilization. Indeed, the slope in the solubility curve is increased of about 70% for NaI_2COSAN (with a slope around 175) compared to NaCOSAN. The more hydrophobic character (i.e., larger size and lower charge density) of NaI_2COSAN compared to NaCOSAN is likely the cause of this increased efficiency.

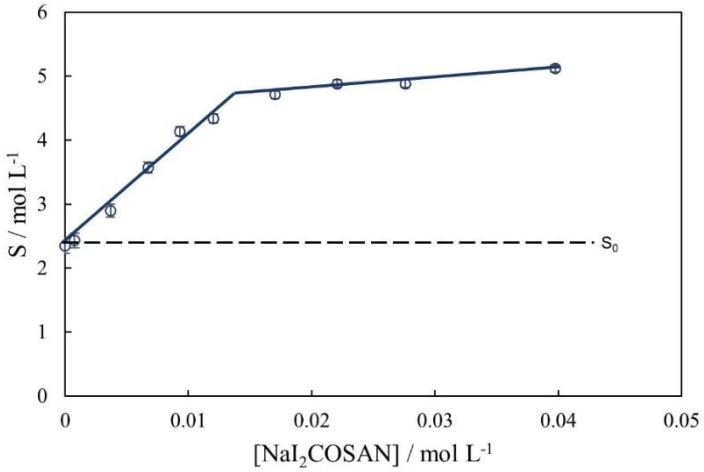

Figure 2.15. *Solubility of 2-BuOH in water (S in mol/L) at 22°C as a function of NaI_2COSAN concentration. The horizontal dark dashed line corresponds to the solubility value of 2-BuOH in water, S_0.*

The solubility of 1- BuOH, which has a slightly higher log *P* value (log *P* = 0.84) than 2- BuOH (log *P* = 0.68), was also investigated using NaCOSAN as a solubilizer (Figure 2.16). Compared to 2-BuOH (Figure 2.17), the slope of the1-butanol solubility increase is lesser (around 20), and there is no appearance of a saturation in the solubility curve. As a result, and as expected

from the first solubilization experiments (Figure 2.12), increasing the hydrophobic character leads to a decrease in solubilization efficiency by the NaCOSAN.

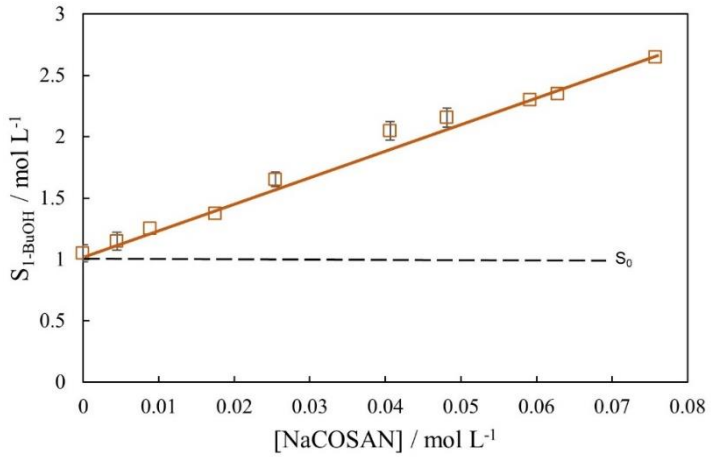

Figure 2.16. *Solubility of 1-BuOH in water (S in mol/L) at 22°C as a function of NaCOSAN concentration. The horizontal dark dashed line corresponds to the solubility value of 1-BuOH in water, S_0.*

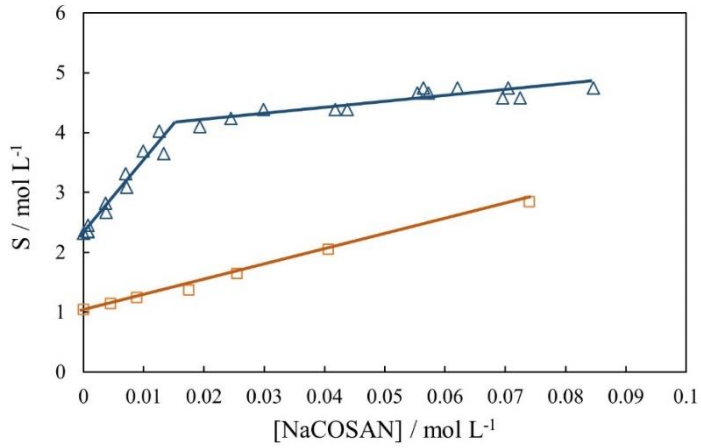

Figure 2.17. *Solubility of 2-BuOH (blue triangles) as a comparison with the solubility of 1-BuOH (orange squares) in water at 22°C as a function of NaCOSAN concentration.*

II.2.3 Molecular level: 2-BuOH solubility in the presence of COSAN (UV-Visible)

UV-Visible spectroscopy was used to investigate the solubilization mechanism at molecular level. As the concentration of 2-BuOH increases, up to the point where it reaches the solubility limit, a bathochromic shift (shown in Figure 2.18) occurs in the UV adsorption peak of NaCOSAN, shifting it from its λ_{max} in pure water, which is 281 nm, to 299 nm (see Figure 2.19). Remarkably, for 2-BuOH concentrations greater than the solubility limit in pure water, i.e., $S/S_0 > 1$, the λ_{max} of NaCOSAN is similar to the λ_{max} in pure 2-BuOH. This indicates that the local environment of NaCOSAN is comparable to that of pure 2-BuOH in this concentration range, where the volume fraction of water in the system is high, between 0.74 and 0.77.

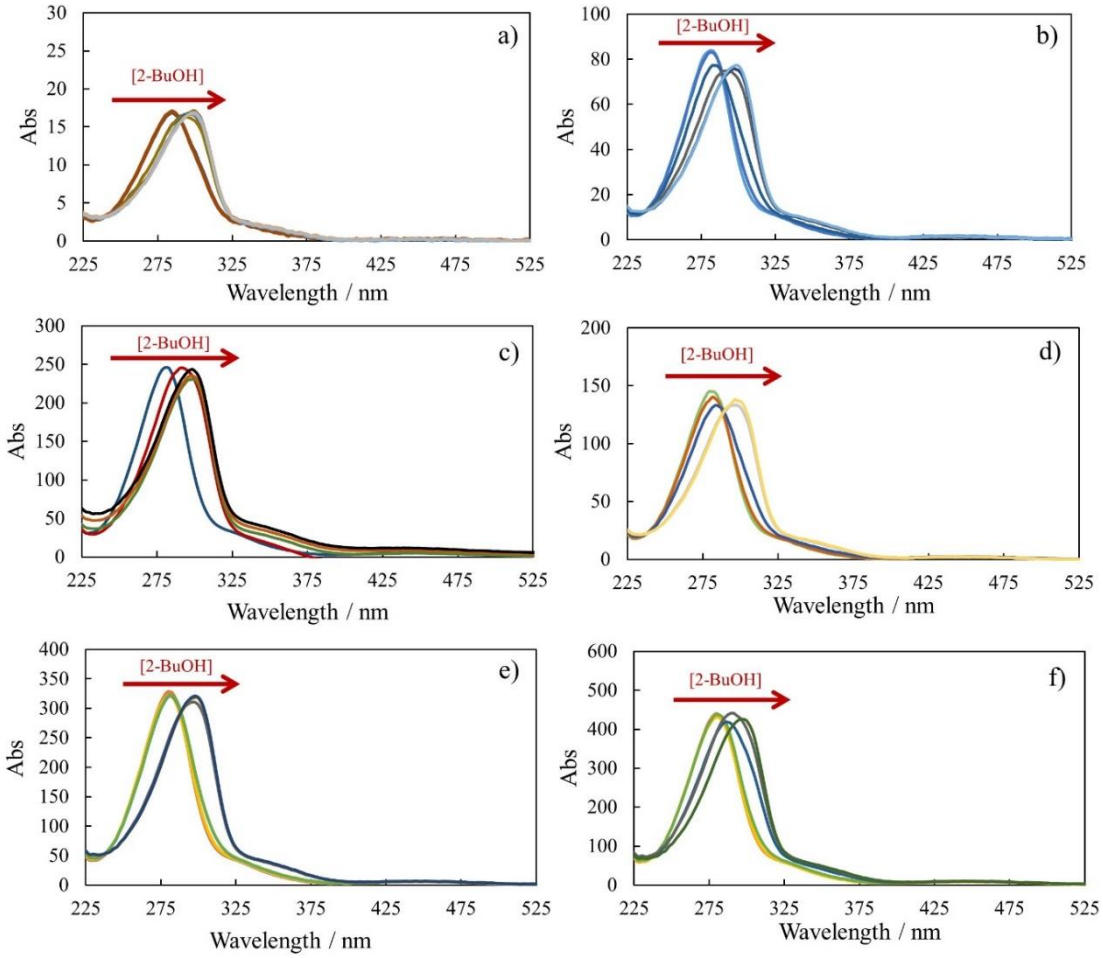

Figure 2.18. *UV-Visible spectra of a) 0.0008 mol L^{-1}, b) 0.004 mol L^{-1}, c) 0.007 mol L^{-1}, d) 0.01 mol L^{-1}, e) 0.013 mol L^{-1} and f) 0.020 mol L^{-1} NaCOSAN in the presence of different 2-BuOH concentrations.*

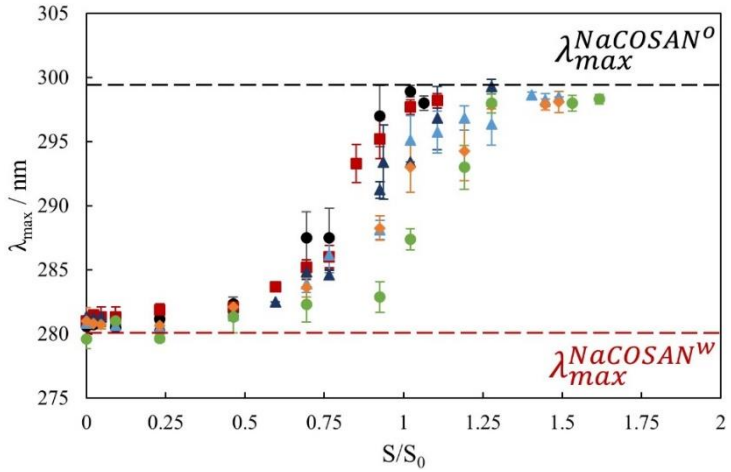

Figure 2.19. *λ_{max} evolution of NaCOSAN at different concentrations: 0.0008 mol L^{-1} (dark circles), 0.004 mol L^{-1} (red square), 0.007 mol L^{-1} (dark blue triangles), 0.01 mol L^{-1} (light blue triangles), 0.013 mol L^{-1} (orange rhombus) and 0.02 mol L^{-1} (green circles), as a function of 2-BuOH concentration expressed here as S/S$_0$. The red dashed line corresponds to λ_{max} of NaCOSAN in pure H$_2$O $\left(\lambda_{max}^{NaCOSAN^w}\right)$ and the dark dashed line is the λmax in 2-BuOH$\left(\lambda_{max}^{NaCOSAN^o}\right)$.*

Therefore, the shift in λ_{max}, that is observed upon increasing 2-BuOH can be attributed to the exchange of the hydration shell of NaCOSAN by a solvation shell of 2- BuOH (see Scheme 2.1).

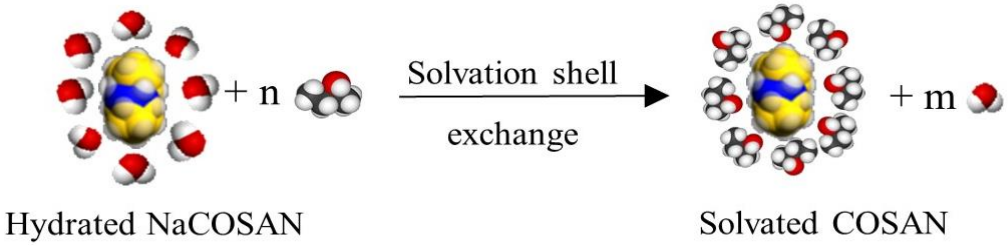

***Scheme 2.1**: Exchange of the hydration shell of NaCOSAN by a solvation shell of 2- BuOH.*

II.2.4 Supramolecular level: 2-BuOH and 1-BuOH solubility in the presence of NaCOSAN and its derivatives

II.2.4.1 Supramolecular level: 2-BuOH solubility in the presence of NaCOSAN

The solubilization mechanism of NaCOSAN at the molecular and supramolecular levels was investigated by using of small and wide-angle scattering (SWAXS). The SWAXS spectra show the scattered intensity I(q) as a function of the scattering angle expressed here as a wave vector q.

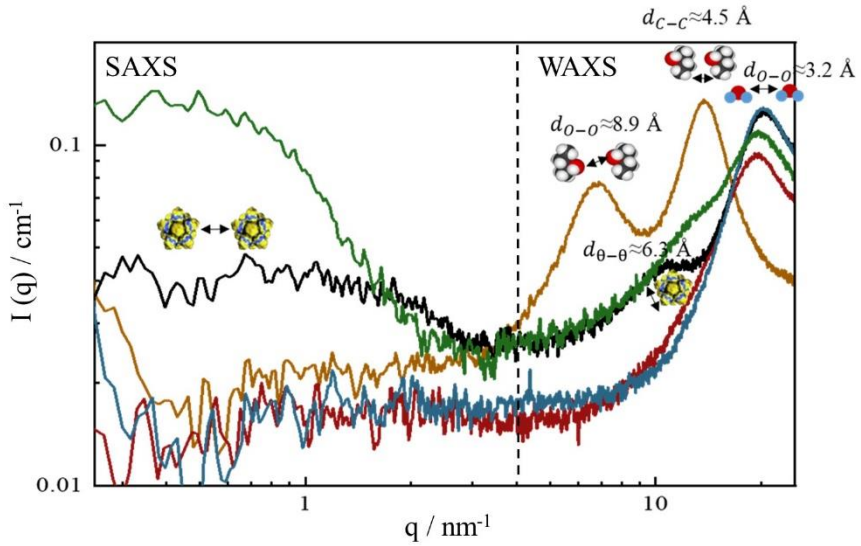

***Figure 2.20**. SWAXS spectra of water (blue), 2-BuOH (orange), 2 mol L^{-1} 2-BuOH (red), 0.09 mol L^{-1} NaCOSAN (dark) and 0.09 NaCOSAN in the presence of 4 mol L^{-1} 2-BuOH (green).*

The blue curve corresponds to the scattering curve of water which shows one distinctive peak at around 20 nm^{-1}which corresponds to the correlation between oxygen-oxygen (H-O···H-O) in liquid water with an average distance around 3.1 Å.[37] No signal is observed in the SAXS part as it does not have structure at large scale above 1 nm. The red curve corresponds to the scattering curve of 2 mol L^{-1} of 2-BuOH. On this latter curve, we can just see the correlation peaks of water molecules. The orange curve corresponds to the scattering curve of pure 2-BuOH which shows two distinctive broad peaks. The peak centered at around 14 nm^{-1} is characteristic of the carbon-carbon correlation typical of liquid alkanes with an average distance 4.5 Å. The peak centered at around 7 nm^{-1} is characteristic of the oxygen-oxygen correlation in pure 2-BuOH with an average distance 8.9 Å, corresponding to around the molecular size and characterizing the liquid order. The dark curve corresponds to 0.09 M of NaCOSAN in water. A broad peak is observed around 10 nm^{-1}, corresponding to the COSAN-COSAN inter-molecular correlations between neighboring COSAN molecules within COSAN micelles with an average distance of around 6.3 Å.[38] In the SAXS region, we see an excess scattering that corresponds to the scattering of the NaCOSAN micelles.
Finally, the green curve is the typical signature of the ternary system with an increase in the solubilization in water, which corresponds in this example to 0.09 mol L^{-1} NaCOSAN in the presence of 4 mol L^{-1} 2-BuOH. This scattering curve presents an excess of scattering intensity at low q and two correlation peaks at large q.

Subsequently, SWAXS measurements were performed on solutions at a fixed NaCOSAN concentration and varying the 2-BuOH concentrations, for the sake of clarity the SAXS and WAXS part are shown separately in Figure 2.21, top and bottom respectively. The wide-angle scattering (WAXS) part of the spectra in Figure 2.21 show three correlation peaks at q-values of around 10 nm^{-1}, 13 nm^{-1}, and 20 nm^{-1}. The peak centered at around 20 nm^{-1} is the structure peak of liquid water as we referred above. The peak centered at around 10 nm^{-1} corresponds to the COSAN-COSAN intermolecular correlations. This latter peak remains unaffected by 2-BuOH up to $S/S_0 \approx 1$ and then vanishes for $S/S_0 > 1$ while a peak centered at around 13 nm^{-1} appear. This peak corresponds in real space to a correlation distance of approximately 4.8 Å, which can be attributed to the average 2-BuOH-2BuOH distances within a suggested newly formed COSAN-2-BuOH hybrid co-assemblies (confirmed via the SAXS part analysis). It is worth mentioning at this point that pure 2-BuOH gives a correlation peak centered at around 14 nm^{-1} which is characteristic of the chain-chain distance (4.5 Å) in pure 2-BuOH (Figure 2.20).[38]

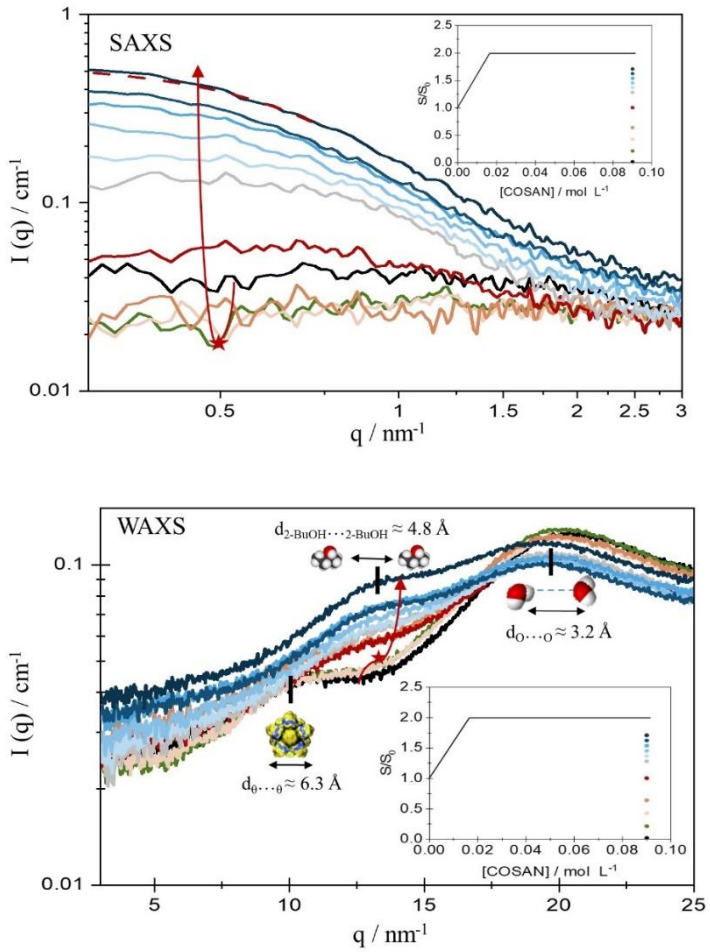

Figure 2.21. *SAXS (top) and WAXS (bottom) spectra of NaCOSAN in water (0.09 mol L^{-1}) increasing 2- BuOH concentration, as shown on the solubility phase diagram in the inset. In the upper graph, the red dashed line corresponds to a Guinier fit.*

The WAXS results are in full agreement with the UV-Vis results (Figure 2.19), which show that the hydration shell of COSAN is replaced by a 2-BuOH solvation shell upon the addition of 2-BuOH close to $S/S_0 \approx 1$.

The Figure 2.21 (top) shows the small-angle scattering (SAXS) part of the spectra. The spectrum of 0.09 mol L^{-1} NaCOSAN in water (dark curve), as it referred above, shows the typical signal of COSAN micelles[38] with a radius of around 1 nm, i.e., the scattered intensity levels off at low q and decreases at higher q. A decrease in the scattered intensity is observed, which corresponds to the disappearance of the signal of micelles. This implies that the addition of 2-BuOH at low concentrations causes the disassembly of NaCOSAN micelles, which is consistent with the increase in the CAC value of NaCOSAN from 0.01 mol/L in pure water[29] to 0.016 mol/L in the presence of 2-BuOH deduced from the solubility curve break (Figure 2.12). This increase in the CAC of NaCOSAN may originate from the association of 2-BuOH

and NaCOSAN monomer, which shifts the equilibrium between NaCOSAN monomer/micelles toward the monomer.

Further addition of 2-BuOH above the ratio of $S/S_0=1$ causes a significant increase in the scattered intensity (Figure 2.22). This increase is followed by the typical scattering pattern of globular objects with a finite size that is significantly larger than that of NaCOSAN micelles. This can be deduced from the fact that the scattered intensity remains constant at low q below approximately 0.5-0.7 nm^{-1}.

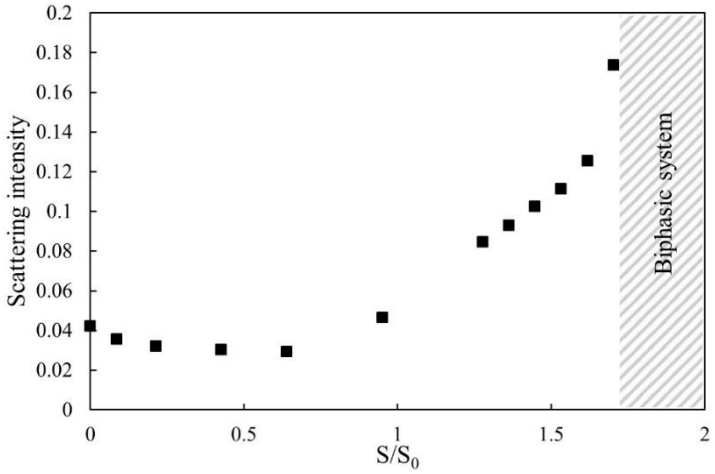

Figure 2.22. *The evolution of the scattered intensity at q = 1 nm^{-1}, increasing 2-BuOH concentration at a fixed NaCOSAN concentration*

Subsequently, SWAXS measurements were performed on solutions varying the NaCOSAN and the 2-BuOH concentrations (Figures S2.11 and S2.12), and we pre-analyzed the scattering upturn at low q using a Guinier approach for globular assemblies.

Indeed, Guinier fits of scattering spectra, as shown with the dashed red line in Figure 2.21 (top graph) and in detail in Figures 2.23 and S2.13, provide information on the overall size of the hybrid COSAN-2-BuOH co-assemblies. The radius of gyration of COSAN-2-BuOH co-assemblies ranges from 2.2 to 10 nm, as summarized in graph 2.24, by varying both the NaCOSAN and 2-BuOH concentrations (Figure S2.11).

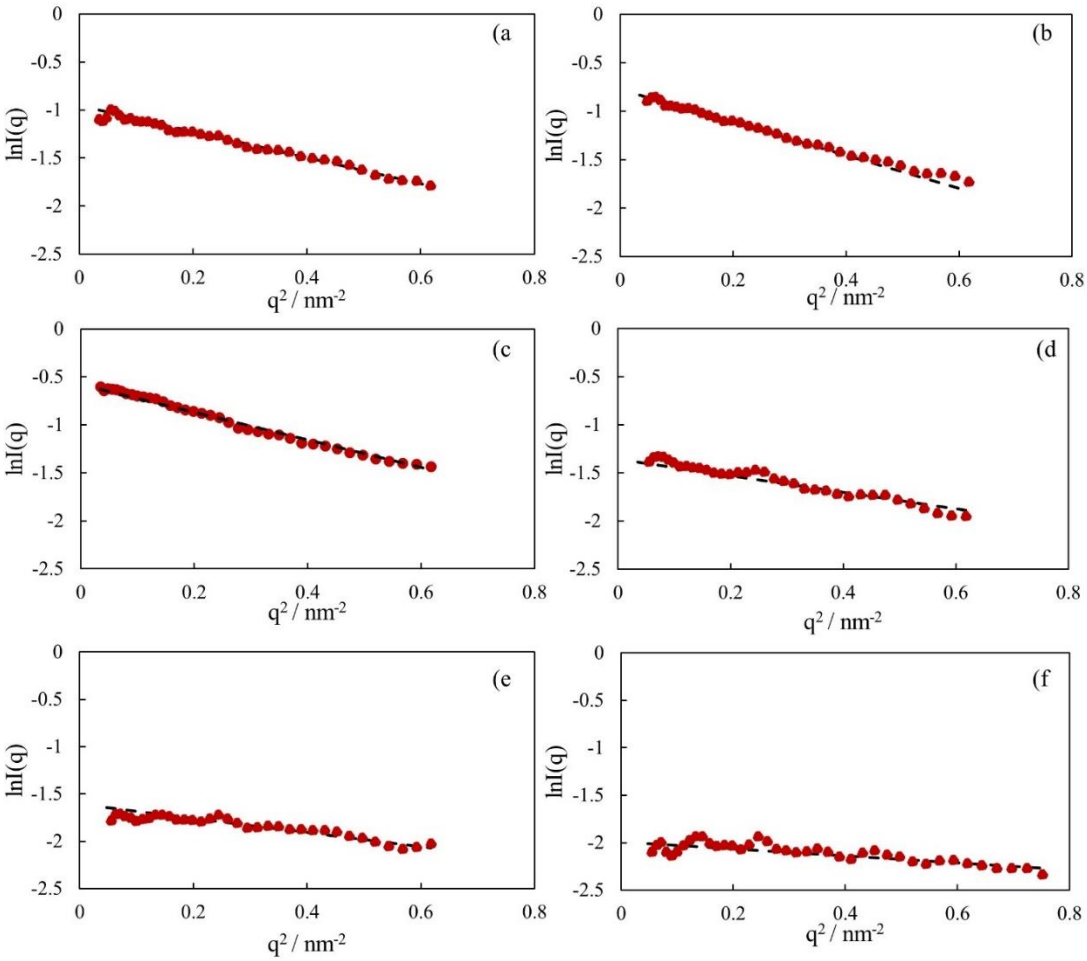

***Figure 2.23**. SAXS fit of 0.09 mol L^{-1} NaCOSAN concentration in the presence of (a) 4, (b) 3.8, (c) 3.6, (d) 3.4, (e) 3.2 and (f) 3 mol L^{-1} 2-BuOH. The red points correspond to the experimental data and the dark dashed line to the Guinier fit.*

We can conclude that the increase in the 2-BuOH and NaCOSAN concentrations leads respectively to a linear increase and decrease in the size of the co-assemblies, respectively. The results of Guinier fits are presented in Table 2.1 below, and some more examples of the fits are in Figure S2.11 and S2.12 in the Supporting information.

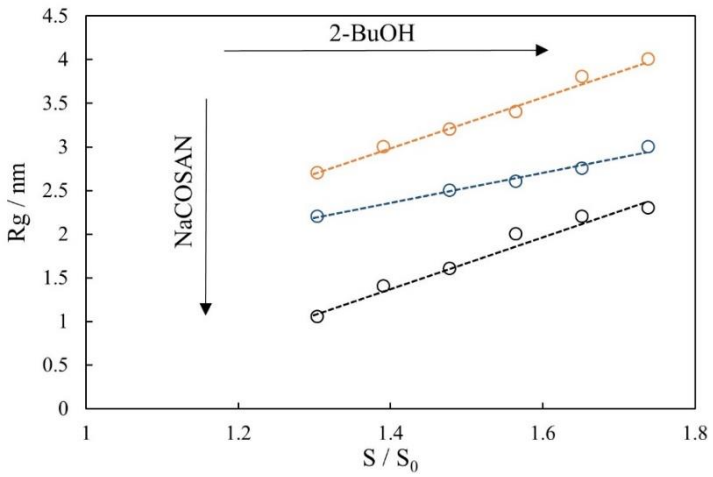

Figure 2.24. *Radius of gyration of hybrid co-assemblies of 0.024 mol L^{-1} (orange circles), 0.04 mol L^{-1} (light blue circles) and 0.09 mol L^{-1} (dark circles) NaCOSAN in the presence of different concentrations of 2-BuOH.*

Table 2.1: Radius of gyration of hybrid co-assemblies of NaCOSAN in the presence of different 2-BuOH concentrations.

[NaCOSAN] / M	**S/S_0**	**R_g / nm**
0.024	1.30	2.7
	1.39	3
	1.48	3.2
	1.57	3.4
	1.65	3.8
	1.74	4
0.04	1.30	2.2
	1.48	2.5
	1.57	2.6
	1.65	2.75
	1.74	3
0.09	1.74	2.3
	1.65	2.2
	1.57	2.0
	1.48	1.6
	1.39	1.4
	1.30	1.1

II.2.4.2 Supramolecular level: 2-BuOH solubility in the presence of NaI_2COSAN

Subsequently, SWAXS measurements were also performed on solutions at a fixed NaI_2COSAN concentration and varying the 2-BuOH concentrations (Figure 2.25 and Figure S2.14). A decrease in the scattered intensity was also observed upon the addition of 2-BuOH. This suggests a similar disassembly effect that was observed previously with NaCOSAN.

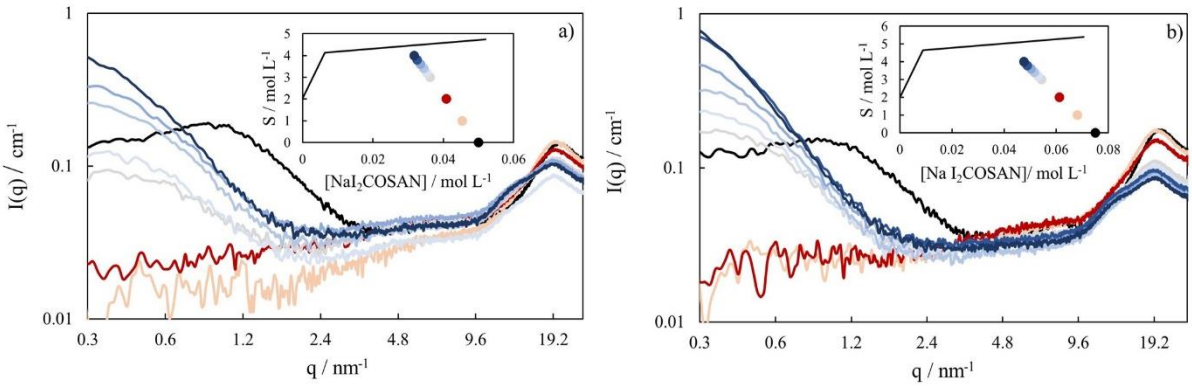

Figure 2.25. *SWAXS spectra of a) 0.075 mol L^{-1}, b) 0.050 mol L^{-1} NaI_2COSAN in aqueous solution in the presence of different 2-BuOH concentrations, as shown on the solubility phase diagram in the inset of a) and b).*

The evolution in the size of the hybrid assemblies (Figure 2.26) was similarly investigated by applying the Guinier model to the SAXS spectra of the co-assemblies NaI_2COSAN/2-BuOH. The results of Guinier fits are shown in Table 2.2. We can also conclude here that the increase in 2-BuOH concentrations leads to an apparently linear increase in the size of the co-assemblies. However, this variation has to be extrapolated to 0 at $S/S_0=1$ since no aggregate exists at this ratio and the SAXS intensity upturn when increasing S/S_0 between 1 and 1.3 was too weak to be analyzed and to extract the R_g.

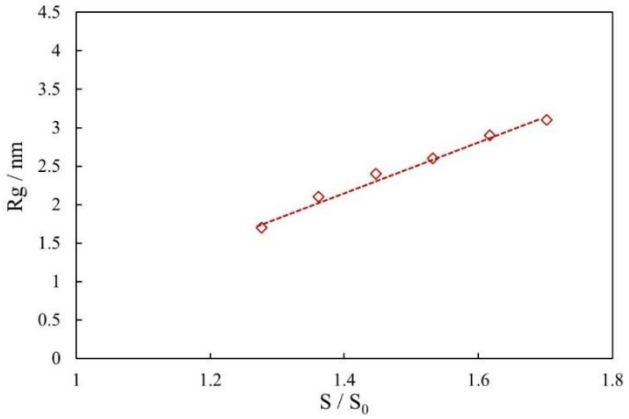

Figure 2.26. *Radius of gyration of hybrid co-assemblies of 0.04 mol L^{-1} NaI_2COSAN in the presence of different concentrations of 2-BuOH.*

Table 2.2: Radius of gyration of hybrid co-assemblies of NaI_2COSAN in the presence of different 2-BuOH concentrations.

[NaI_2COSAN] / mol L^{-1}	**S/S_0**	**R_g / nm**
0.04	1.70	3.1
	1.62	2.9
	1.53	2.6
	1.45	2.4
	1.36	2.1
	1.28	1.7

This first quantification using a Guinier fit only allows comparing the different systems. A more elaborate fitting procedure will be applied in the following sections.

II.2.4.3 Supramolecular level: 1-BuOH solubility in the presence of NaCOSAN

SWAXS measurements were performed on solutions of different NaCOSAN and 1-BuOH concentrations (Figure 2.27), to investigate if the spectra follow the same pattern as those for 2-BuOH, where co-assemblies form. As a conclusion here, the SWAXS spectra show the same scattering features as in the case of 2-BuOH. The advantage of 1-butanol is that it exists commercially in the deuterated form, which can be used for using small angle neutron scattering techniques and for contrast variation.

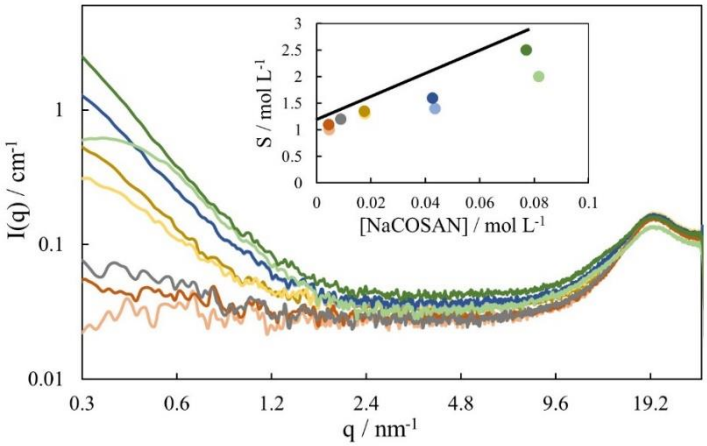

Figure 2.27. *SWAXS spectra of different NaCOSAN concentrations in the presence of different 1-BuOH concentrations, as shown on the solubility phase diagram in the inset.*

II.2.5 Size, shape and molecular distribution of 1-BuOH and 2-BuOH in the presence of NaCOSAN (SANS, ellipsoidal model)

The shape, size, interactions, and composition of the hybrid COSAN/alcohol co-assemblies were studied using small-angle neutron scattering (SANS) at the Institut Laue–Langevin (ILL) in Grenoble with contrast variation in conjunction with the e-contrast using SAXS. So the effect of NaCOSAN, water, and 1-BuOH co-assembly structures was investigated by recording SAXS and SANS (with two contrasts) for three different compositions. Figure 2.28 show the spectra of the three compositions 0.015 mol L^{-1} NaCOSAN with 1.3 mol L^{-1} 1-BuOH and 0.04 mol L^{-1} NaCOSAN with 1.3 and 1.6 mol L^{-1} 1-BuOH, respectively, the water being D_2O and the 1-butanol being in its deuterated form or not (1-BuOH and 1-BuOD).

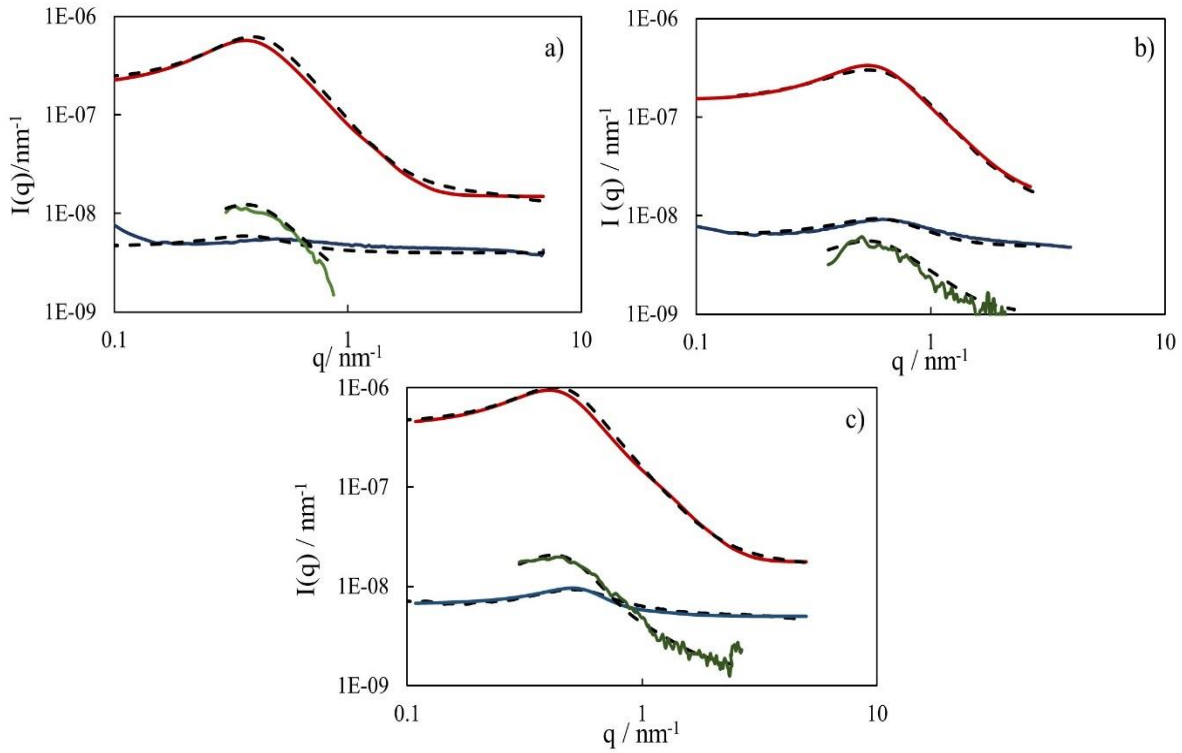

***Figure 2.28**. SANS spectra in absolute scattering unit of a) 0.015 mol L^{-1}, b) 0.04 mol L^{-1} NaCOSAN in D_2O in the presence of 1.3 mol L^{-1} and c) 1.6 M hydrogenated 1-butanol (BuOH, contrast I in red) and fully deuterated 1-butanol (BuOD, contrast II in blue). The sample with hydrogenated BuOH was also measured by SAXS (in green). Full lines represent simultaneous fits of the three scattering spectra (i.e. with same composition but with three different contrasts: two contrasts in SANS using deuterated and hydrogenated BuOH and the contrast in SAXS) using the same triaxial ellipsoid model, the details on the fitting procedure and parameters are listed below in the section II.2.6.*

The scattering length density of the different components, used to calculate the different contrasts through the equations 7 and 8 (Section II.2.8) and a sketch presenting the co-assemblies with the two contrasts in SANS is given in Figure 2.29.

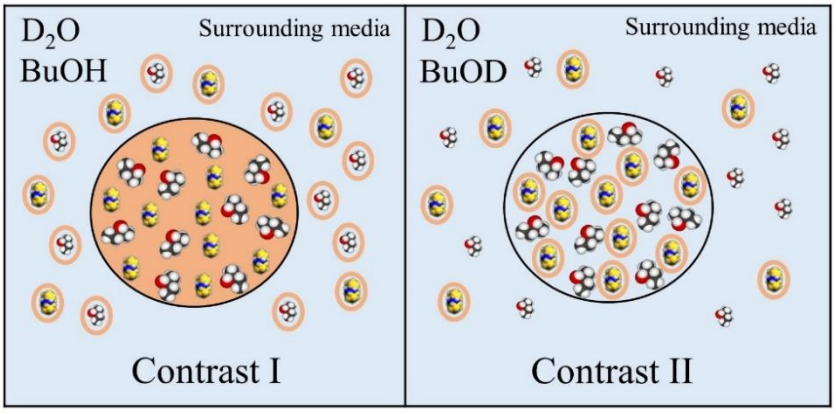

***Figure 2.29.** Sketch of the co-assemblies with the two contrasts in SANS with BuOH (left, contrast I) and with BuOD (right, contrast II) color coded with the scattering length densities of the different components. Deuterium-rich region in light blue and hydrogen-rich region in light orange.*

Therefore, the SANS contrast between the co-assemblies and the solvent (D_2O) is (i) mostly given between hydrogenated matter (1-BuOH, NaCOSAN) and deuterated solvent (D_2O) and (ii) it depends on the concentrations of NaCOSAN and butanol (H and D) in the co-assemblies and in the surrounding solvent (D_2O). A triaxial ellipsoid form factor model and an electrostatic structure factor (RMSA) were used to simultaneously fit the two SANS spectra and the SAXS spectra for each of the three compositions. The electrostatic structure factor was applied in order to take into consideration the inter-aggregate repulsions. The ellipsoid model produced the greatest results when attempting to characterize the hybrid co-assemblies when compared to the other form factor models that were tested. The spherical model did not work and was given up. Details are given in the modeling section II.2.8.

The SAXS spectra of hydrogenated and deuterated 1-butanol (Figure 2.30) was also measured in order to confirm that there is no difference between them.

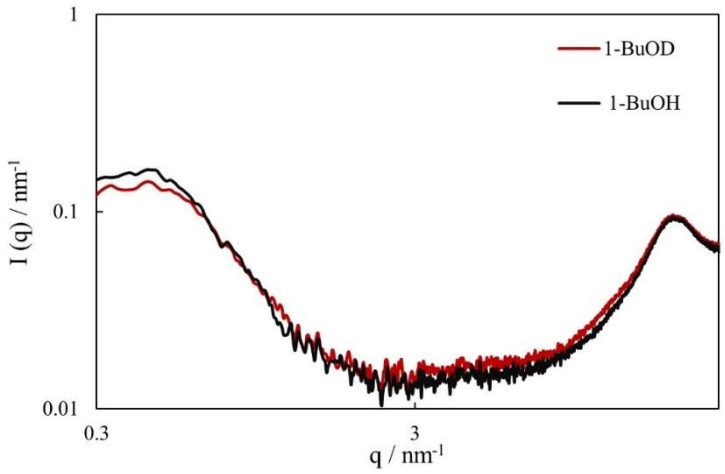

***Figure 2.30**. SWAXS spectra of 0.04 mol L^{-1} NaCOSAN in the presence of 1.6 mol L^{-1}deteurated 1-BuOH (red line) and 1.6 mol L^{-1} protonated 1-BuOH (dark line).*

The fitting results reveal that the co-assemblies are flattened (or discoid) with a concentration independent short semi-axis (a) of 1 nm which is approximately the length of a COSAN ion and two longer semi-axes (b) and (c) of 3 up to 4.8 nm upon decreasing NaCOSAN and increasing 1-BuOH concentrations (Table 2.3). According to the calculated scattering length density, all the excess solubilized 1-BuOH excess is found in the co-assemblies. Furthermore, the scattering length density of the assemblies is homogenous, indicating that no NaCOSAN accumulates at the surface of the co-assemblies, as expected for surface-active molecules. This result is in agreement with the thickness of the assemblies (thickness is $2a \approx 2$ nm), which is roughly twice the length of the COSAN (1 nm). Therefore, as the assembly thickness is close

to the molecular size, it is difficult to have an accumulation of NaCOSAN at the assembly surface. Furthermore, the 1-BuOH /NaCOSAN molecular ratios in the co-assemblies obtained from the fit (15 to 22, see Table 2.3) go in line with the value derived from the slope of the 1-BuOH solubility curve (1-butanol/NaCOSAN ≈ 20, Figure 2.16).

Table 2.3: Best fit parameters of the SANS-fits. Fixed parameters are shown with a grey background.

Parameters	Units	Contrast I Composition I 0.04 M COSAN 1.6 M 1-BuOH	Contrast II Composition I 0.04 M COSAN 1.6 M 1-BuOD	Contrast I Composition II 0.04 M COSAN 1.3 M 1-BuOH	Contrast II Composition II 0.04 M COSAN 1.3 M 1-BuOD	Contrast I Composition III 0.015 M COSAN 1.3 M 1-BuOH	Contrast II Composition III 0.015 M COSAN 1.3 M 1-BuOD
Background	cm^{-1}	0.15	0.5	0.15	0.5	0.15	0.5
a-semi axis of elliptical	nm	4.8	4.8	3	3	4.8	4.8
b-semi axis of elliptical	nm	1	1	1	1	1.2	1.2
c-semi axis of elliptical	nm	4.8	4.8	3	3	4.8	4.8
Number of the aggregates	None	0.00048	0.00048	0.328	0.328	0.000172	0.000172
SLD of aggreagates (ρ)	$10^{-6}Å^{-2}$	-0.183	5.64	-0.12	5.6	-0.23	6
SLD of solvent (ρ)	$10^{-6}Å^{-2}$	5.88	6.35	5.73	6.35	5.67	6.35
Hard sphere radius of aggregates (RHS)	nm	3.5	3.5	2.6	2.6	3.3	3.3
Charge (Z)	e	25	25	13	13	21	21
Volume fraction of aggregates	None	0.046	0.046	0.0328	0.0328	0.019	0.019
Salt concentration	M	0.015	0.015	0.01	0.01	0.005	0.005
1-BuOH concentration in the surrounding phase	M	1.15	1.15	1	1	1.1	1.1
Concentration of COSAN in the surrounding phase	M	0.02	0.02	0.02	0.02	0.009	0.009
Temperature (T)	K	295.15	295.15	295.15	295.15	295.15	295.15
Dielectric constant (ε)	None	72	72	72	72	72	72
$[BuOH]^{A}/[COSAN]^{A}$	-	22.5	22.5	15	15	≈22	≈22

* ^{A} is the abbreviation for the hybrid assemblies

Likewise, NaCOSAN/2-BuOH co-assemblies were studied using SANS (1 contrast), and the same fitting strategy was effectively applied to these co-assemblies (Figure 2.31). Three compositions were studied to evaluate the effect of the concentration of NaCOSAN and 2-BuOH on the structure of the assemblies: 0.015 mol L^{-1} NaCOSAN with 3 mol L^{-1} 2-BuOH, 0.04 mol L^{-1} NaCOSAN with 3 and 4 mol L^{-1} 2-BuOH. The results of the fits are shown in the Table 4. The fitting results indicate also that the assemblies are flattened (or disc-like) with a short semi-axis (a) of 0.6 nm that is independent of the concentration of NaCOSAN and 2-BuOH and two longer semi-axis radii (b) and (c) of 4.4 up to 6.2 nm upon decreasing NaCOSAN and increasing 2-BuOH concentrations. This result is comparable with the thickness of the assemblies (thickness is 2a ≈ 1 nm), which is roughly the length of the COSAN (1 nm), the length between its two poles. Moreover, the molecular ratios NaCOSAN/2-BuOH in the co-assemblies obtained from the fit (100 to 30, see Table 2.4) are of the same order of magnitude as the values obtained from the slopes of the 2-BuOH solubility curve (2-BuOH/NaCOSAN ≈ 120 and ≈ 10 respectively below and above C_{break}^{COSAN} the Figure 2.12). The fitted scattering length densities (see Table 2.7) suggest that all the excess solubilized 2-BuOH is located in the co-assemblies.

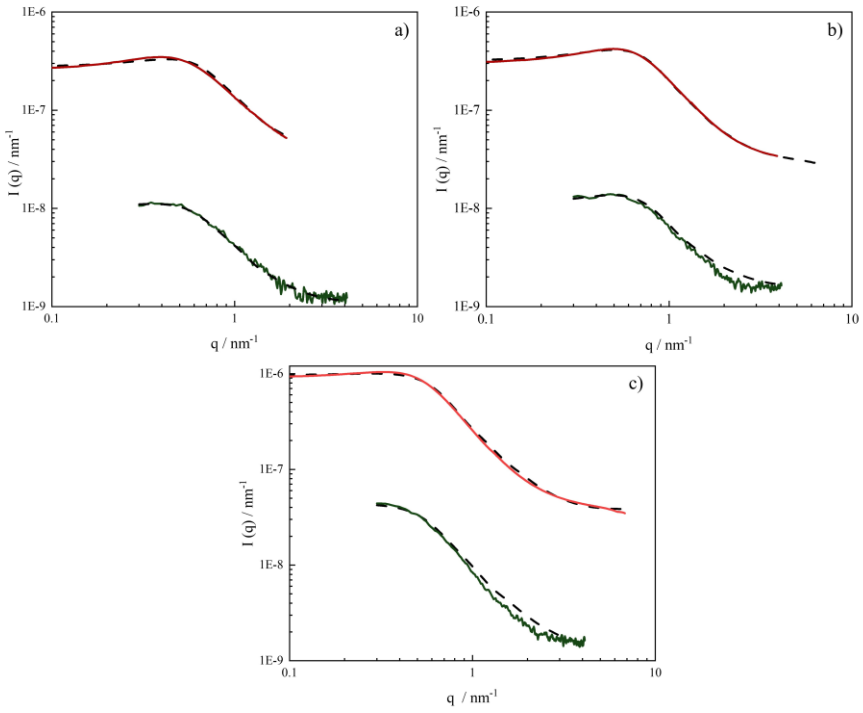

Figure 2.31. *SANS spectra of a) 0.015 mol L^{-1}, b) 0.04 mol L^{-1} NaCOSAN in D_2O in the presence of 3 mol L^{-1} hydrogenated 2-BuOH and c) 0.04 mol L^{-1} NaCOSAN in D_2O in the presence of 4 mol L^{-1} hydrogenated 2-BuOH. The sample with hydrogenated 2-BuOH was also measured by SAXS (in green). Full lines represent simultaneous fits of the scattering spectra using the same triaxial ellipsoid model, the details on the fitting procedure and parameters are listed below in the section II.2.6.*

Table 2.4: Fitting parameters obtained for the best fits of the SANS spectra in Fig.S16. Fixed parameters are shown with a grey background.

		Composition IV	Composition V	Composition VI
Parameters	Units	0.015 M COSAN 3 M 2-BuOH	0.04 M COSAN 3 M 2-BuOH	0.04 M COSAN 4 M 2-BuOH
a-semi axis of elliptical	nm	0.6	0.6	0.6
b-semi axis of elliptical	nm	5.3	4.4	6.1
c-semi axis of elliptical	nm	5.3	4.4	6.2
Number of the aggregates (N)	nm^{-3}	0.0008	0.001	0.0015
SLD of assemblies (ρ)	$10^{-6}Å^{-2}$	-0.29	-0.216	-0.26
SLD of surrounding solvent (ρ)	$10^{-6}Å^{-2}$	5.04	5.04	4.8
Hard sphere radius of aggregates (RHS)	nm	2.3	2.05	3.4
Charge (Z)	e	9	7	10
Volume fraction of aggregates	None	0.06	0.06	0.1
Salt concentration	M	0.01	0.01	0.02
$[2\text{-BuOH}]_{surrounding\ phase}$	M	2.4	2.4	2.4
$[COSAN]_{surrounding\ phase}$	M	0.009	0.02	0.02
Temperature (T)	K	295.15	295.15	295.15
Dielectric constant (ε)	None	72	72	72
$[BuOH]^A/[COSAN]^A$	-	100	30	80

At this point, it is worth mentioning that all the fittings (SAXS, SANS with 1-BuOH and 2-BuOH and SANS with 1-BuOD, the fully deuterated 1-BuOH) were carried out simultaneously with strong constraints imposed on the fixed parameters (as explained in detailed in the Supporting Information). All the values obtained are reasonable, i.e., with a physical meaning. Therefore, we conclude with a good robustness that flattened ellipsoid assemblies are formed.

As deuterated 2-butanol is not commercially available, SANS measurements with contrast variation were not possible. For this reason, only the SANS results of hydrogenated 2-BuOH were presented above. Although, after applying a proposal to the deuteration lab of Heinz Maier-Leibnitz Zentrum MLZ), Dr. Kuno Schwärzer from the Jülich Centre for Neutron Science (JCNS) synthesized deuterated 2-butanol. We recently performed SANS measurements at the Paul Scherrer Institut with deuterated 2-butanol. A rough analysis of the SANS data confirms all the conclusions that were made with 1-butanol.

To come back on the COSAN efficiency for the 2-BuOH solubilization and thus on the amount of alcohol molecules (of around 120) “associated” with COSAN, there exists a coherent view between the molecular and supramolecular analyses. A rough estimation of this number can be

obtained if we consider one or two solvation shells of BuOH around one COSAN molecule. The molecular volume of the COSAN molecule is 0.448 nm^3 and that of 2-BuOH is 0.152 nm^3. Let us first consider COSAN and BuOH as spherical molecules. The volume of either one spherical shell around COSAN with 0.669 nm thickness, the equivalent diameter for BuOH, or 1.338 nm for two solvation shells is respectively 5.88 and 24.5 nm^3. Dividing these shell volumes by the molecular volume of the 2-BuOH, we get about 40 alcohol molecules around COSAN in the first solvation layer and 160 in the first two layers. So, 120 molecules of alcohol for one COSAN molecule correspond to between one and two solvation shells. COSAN clusterizes alcohol molecules in water within alcohol-rich nano-assemblies with 2 and 3 layers of alcohol between COSAN molecules. These alcohol molecules are strongly correlated in position as observed through SWAXS data, with a chain-chain correlation signature that reminds those observed using SWAXS data in pure alcohol liquid phase. There is still the question of the asymmetry of the self-assemblies. Is it due to the presence of the charge carried by the COSAN that prevents an isotropic growth of the assembly? Is the isotropic growth of the assemblies going to tremendously increase the Born energy of the COSAN ion within the assemblies? Is it due to the asymmetrical structure of COSAN itself that induces an asymmetric solvation shell? We do not have the answer yet.

II.2.6 Solubilization of more hydrophobic compounds by NaCOSAN/2-BuOH co-assemblies

In this section, we investigated the solubilization efficiency of the NaCOSAN/2-BuOH co-assemblies of more hydrophobic compounds (log *P* from 1.1 to 6) with diverse chemical nature (aromatics, terpenoids, aldehydes, ketones, ethers) used as organic solvent, fragrance, pharmaceutical active ingredient, and dyes. Despite the fact that NaCOSAN alone has a limited efficiency in the solubilization of hydrophobic compounds, log $P < 1.5$, NaCOSAN/2-BuOH co-assemblies can efficiently solubilize a much larger number of hydrophobic compounds with log *P* up to 5.6 for Sudan I, dye (Figure 2.32).

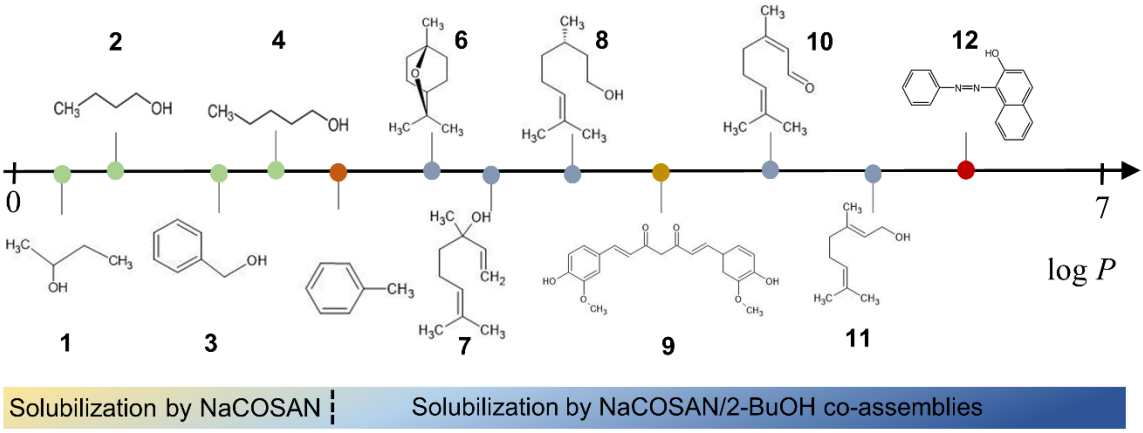

Figure 2.32. *The compounds that can be solubilized by COSAN (yellow region) and by the COSAN/2-BuOH co-assemblies (blue region) are shown on the logP scale, where 1 corresponds to 2-BuOH (LogP = 0.61), 2 1-BuOH (0.88), 3 benzyl alcohol (1.1), 4 1-pentanol (1.51), 5 toluene (2.73), 6 eucalyptol (2.74), 7 linalool (2.97), 8 b-citronellol (3.239), 9 curcumin (3.29), 10 citral (3.45), 11 geraniol (3.56) and 12 sudan I (5.6). The given logP values were taken from PubChem.*

TOC analysis was performed to assess the solubility of the different hydrophobic compounds in water and then compare it to their solubility in an aqueous solution containing NaCOSAN, 2-BuOH, and their co-assemblies. The theoretical solubility values in water of the hydrophobic compounds found in the literature and the experimental values determined by TOC are presented in the table below.

Table 2.5: Solubility values of the hydrophobic compounds in water.[36]

Hydrophobic compounds	Units	Theoritical solubility	Experimental solubility
2-butanol	mol L^{-1}	2.3	2.4
1-butanol	mol L^{-1}	0.92	1.5
Benzyl alcohol	mol L^{-1}	3.96	4.14
1-pentanol	mmol L^{-1}	0.25	0.20
Toluene	mmol L^{-1}	>5.65	5.5
Eucalyptol	mmol L^{-1}	>22.7	18.7
Linalool	mmol L^{-1}	10.3	11.6
b-citronellol	mmol L^{-1}	1.3	3.8
Citral	mmol L^{-1}	-	11.9
Geraniol	mmol L^{-1}	6	5

The evolution of the solubility of the hydrophobic compounds upon addition of NaCOSAN/2-BuOH co-assemblies is shown in Figure 2.33. The dark curves correspond to different 2- BuOH concentrations up to 2 mol L^{-1}, which is close to the solubility of 2-BuOH in water (S_0). The red curves correspond to 0.01 mol L^{-1} NaCOSAN in the presence of different 2-BuOH concentrations up to 3.4 mol L^{-1}, which is close to the solubility of NaCOSAN (see Figure 2.12 in Section II.6.2). The blue curves correspond to 0.02 mol L^{-1} NaCOSAN in the presence of different 2-BuOH concentrations up to 3.4 mol L^{-1}. As shown in Figure 2.33, all hydrophobic substances have bell-shaped solubilization curves. All hydrophobic compounds are significantly more soluble in co-assemblies than in aqueous solutions of NaCOSAN or 2-BuOH. The solubilization of hydrophobic substances by the NaCOSAN/2-BuOH co-assemblies was more efficient at 0.02 mol L^{-1} NaCOSAN, as expected from the evolution of the 2-BuOH solubility curve by NaCOSAN. The higher the NaCOSAN concentration, the higher the solubility of the hydrophobic compounds. The solubilization follows the same pattern for all the hydrophobic compounds. The first adjuncts of 2-BuOH in the aqueous solution of NaCOSAN lead to an increase in the solubility of the hydrophobic compounds, which increases significantly up to around the solubility of 2-BuOH in water. Upon further increase in the 2-BuOH concentration (S/S_0), the solubility increase is followed by a decrease in the solubility of the hydrophobic compounds, which is reasonable because more 2-BuOH is added to the system, causing more excess to be solubilized by the co-assemblies and less place for the hydrophobic compounds in the co-assemblies. The solubility efficiency of the hydrophobic compounds is not in the same order with the log *P* scale. The solubility efficiency follows the order Toluene < Benzyl alcohol < Eucalyptol < Citral < Geraniol < b-citronellol < linalool < Curcumin< Sudan I.

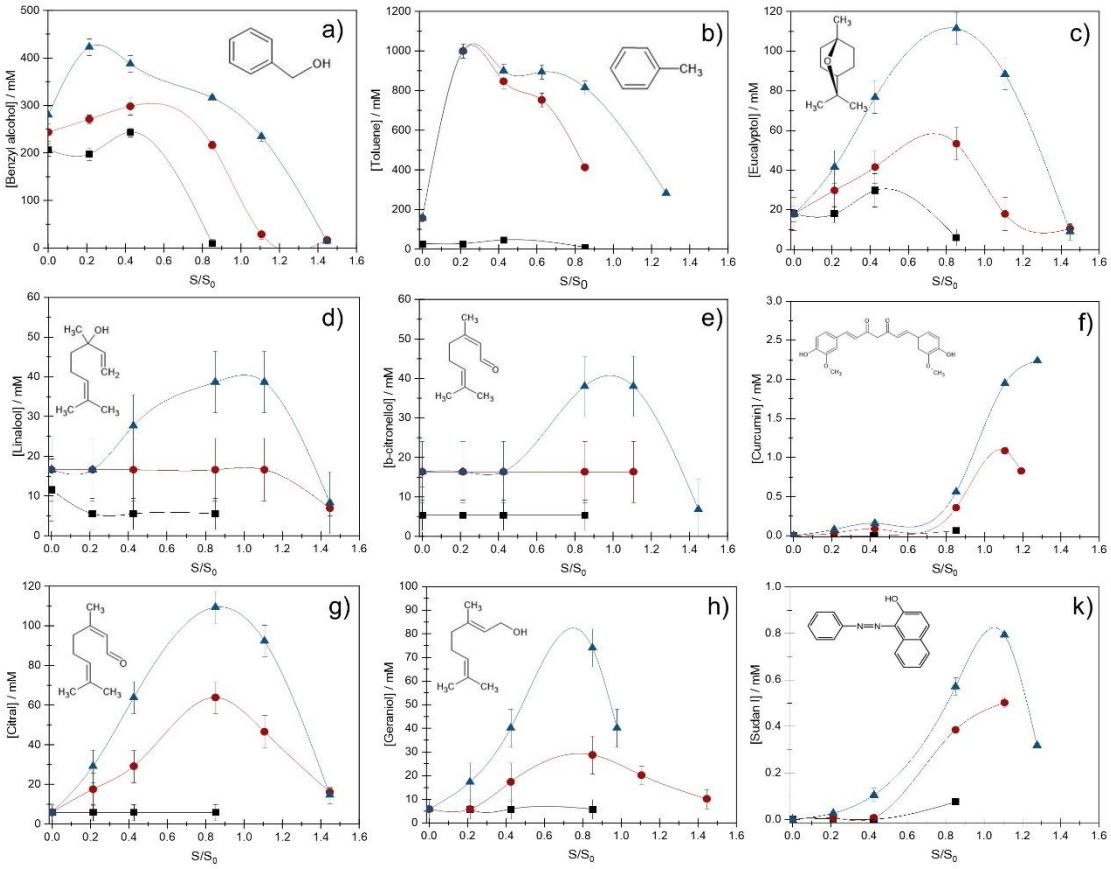

Figure 2.33. *Solubility of a) benzyl alcohol, b) toluene, c) eucalptol, d) linalool, e)b-citronellol, f) curcumin, g) citral, h) geraniol and k) sudan I as a function 2-BuOH concentration (S/S_0) and for different NaCOSAN concentrations: 0 (dark squares), 10 (red circles) and 20 mM NaCOSAN (blue triangles).*

II.2.6.1 Supramolecular level: Hydrophobic compounds solubility in the presence of COSAN/2-BuOH co-assemblies (SWAXS-SANS)

Figure 2.34 depicts the SWAXS spectra of different compositions of NaCOSAN/2-BuOH co-assemblies in the presence of different concentrations of eucalyptol and citral. SWAXS shows a significant increase in scattering intensity at low q values around 0.5 and 0.7 nm^{-1} as 2-BuOH and hydrophobic compound concentrations increase. We observed that the formation of NaCOSAN/2-BuOH co-assemblies in the presence of hydrophobic compounds occurs at S/S_0 that is significantly lower than in the absence of hydrophobic compounds. More specifically, the formation of NaCOSAN/2-BuOH co-assemblies form at $S/S_0 \approx 1$ and in the presence of hydrophobic compounds at $S/S_0 \approx 0.4$, which may suggest the re-organization of the co-assemblies or even the formation of new co-assemblies.

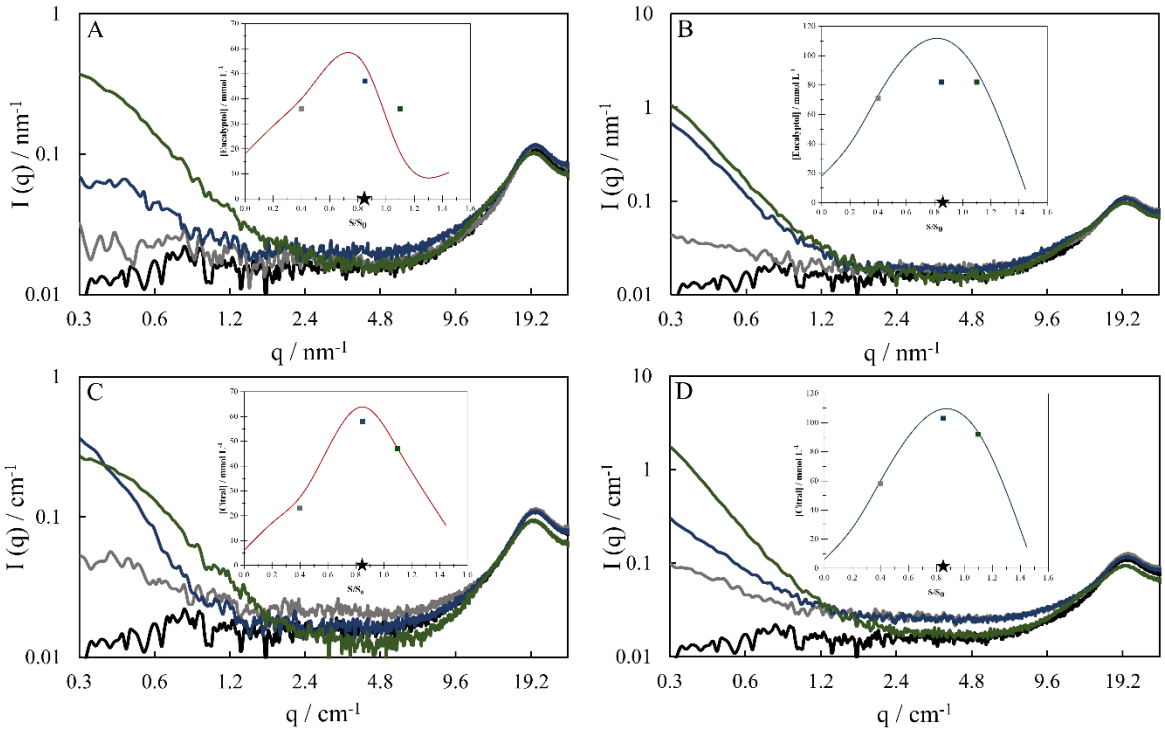

***Figure 2.34**. SWAXS spectra of different compositions of NaCOSAN/2-BuOH co-assemblies in the presence of different concentrations of (a), (b) eucalyptol **6** and (c), (d)citral **10**. The (a), (c) corresponds to 0.01 mol L^{-1} and the (b), (d) 0.02 mol L^{-1} NaCOSAN.*

We recently performed SANS measurements at the Paul Scherrer Institut in order to get more information about the solubilization of the hydrophobic compounds by the NaCOSAN/2-BuOH co-assemblies. In these experiments, we investigated different compositions of NaCOSAN/2-BuOH co-assemblies by varying either the concentration of NaCOSAN or the concentration of 2-BuOH at different concentrations of hydrophobic compounds or both. Figure 2.35 shows the SANS spectra of a composition of NaCOSAN/2-BuOH co-assemblies in the presence of different concentrations of eucalyptol and toluene.

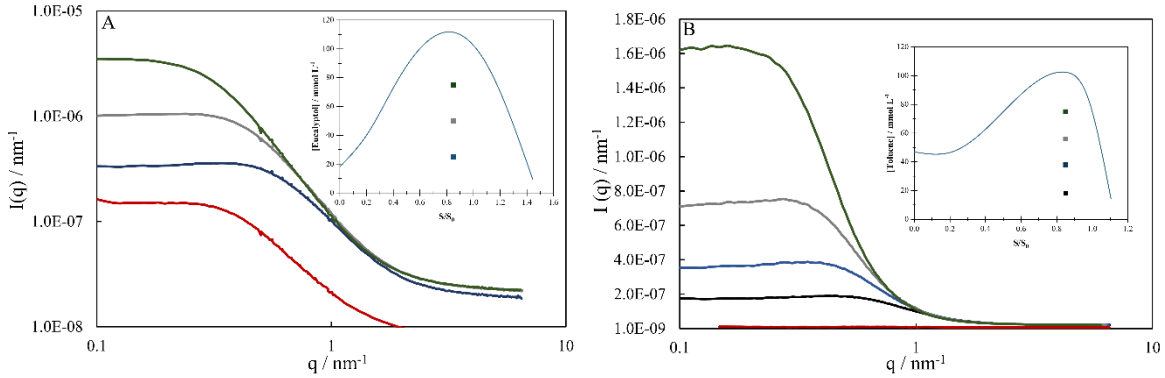

***Figure 2.35**. SANS spectra of NaCOSAN/2-BuOH co-assemblies (0.02 mol L^{-1}NaCOSAN and 2 mol L^{-1} 2-BuOH) in the presence of different concentrations of 25 (blue curve), 50 (grey curve) and 75 (green curve) mmol L^{-1}eucalyptol (left) and 18 (dark curve), 38 (blue curve), 56 (grey curve) and 75 (green curve) mmol L^{-1} toluene (right). The red curve corresponds to 25 mmol L^{-1}eucalyptol(left) and 18 mmol L^{-1}toluene in 2M 2-BuOD.*

It is worth mentioning that Figure 2.35 is just an example of two of the several hydrophobic compounds, which were studied. We observed that the increase in hydrophobic compound concentration leads to an increase in the size of the NaCOSAN/2-BuOH co-assemblies. Simulation of the SANS data is required to obtain more information about the solubilization mechanism of hydrophobic compounds by NaCOSAN/2-BuOH co-assembly.

II.2.7 Solubility of butanol in the presence of halogenated dodecaborate clusters

In this section, we investigated the ability of halogenated dodecaborate clusters ($B_{12}Cl_{12}^{2-}$, $B_{12}Br_{12}^{2-}$, $B_{12}I_{12}^{2-}$) to solubilize 2-BuOH in order to compare with the NaCOSAN/2-BuOH system, see Figure 2.36.

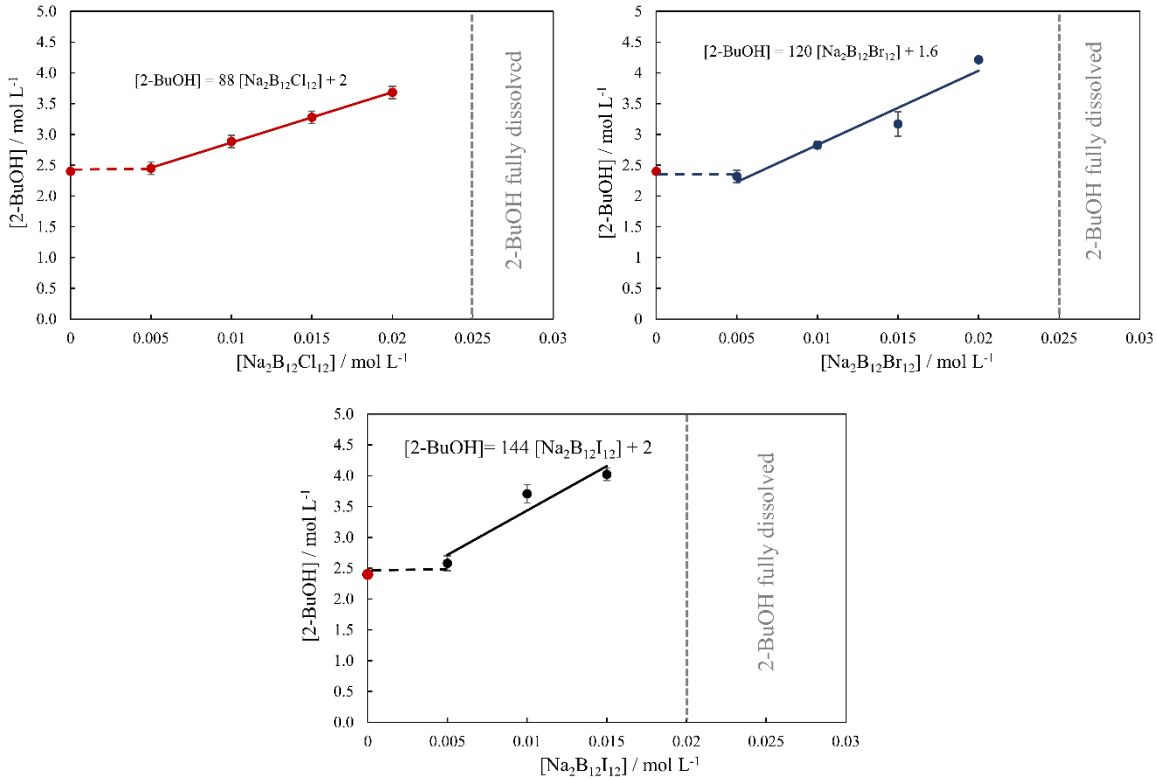

Figure 2.36. *Solubility of 2-BuOH in water (S in mol/L) at 22°C as a function of halogenated dodecaborate clusters concentration. The vertical dashed line corresponds to the increase of solubility value of 2-BuOH more concentrated halogenated dodecaborate cluster solutions.*

In Figure 2.36, we observe that the solubility of all investigated boron clusters increases abruptly above a concentration of approximately 0.005 mol L^{-1}. We also observed an increase in the solubility of 2-BuOH as the concentration of halogenated dodecaborate clusters increased up to the point where 2-BuOH was completely dissolved in the boron cluster solution. The slopes of the solubility curves of boron clusters increase with the superchaotropicity of the boron clusters $B_{12}Cl_{12}^{2-} < B_{12}Br_{12}^{2-} < B_{12}I_{12}^{2-}$. The value of each boron cluster slope corresponds

to the number of 2-BuOH molecules, which can be solubilized by one molecule of boron cluster.

In the next step, we roughly estimate the number of 2-BuOH molecules that can be "hosted" on the solvation shell of each boron cluster and compare this value to the slopes obtained from the solubility curves (Table 2.6). A rough estimation of this number can be obtained if we consider one or two solvation shells of 2-BuOH around one boron cluster molecule. As an example, the molecular volumes of $B_{12}I_{12}^{2-}$ and of 2-BuOH molecule are 0.5 nm^3 and 0.152 nm^3, respectively. We consider $B_{12}I_{12}^{2-}$ and 2-BuOH as spheres. Based on their molecular volumes this would correspond to spheres with equivalent diameters of 1 and 0.6 nm. The volumes of one and two spherical (solvation) shell(s), with a thickness of 0.6 and 1.2 nm, i.e. one and two times the 2-butanol diameter is respectively 5.6 and 20.6 nm^3. Dividing these shell volumes by the molecular volume of the 2-BuOH, we get about 37 alcohol molecules per $B_{12}I_{12}^{2-}$ in the first solvation layer and 137 in the first two solvation layers. Therefore, the value of 144 molecules of alcohol for one $B_{12}I_{12}^{2-}$ molecule seems to correspond to two solvation shells, which has physical meaning.

Table 2.6: Estimation of 2-BuOH molecules for the first and the second solvation shell in comparison with the slope values obtained from the solubility curves of the boron cluster.

Superchaotropic nano-ions	Slope of solubility curve	Range of 2-BuOH molecules of 1st and 2nd solvation shell
$Na_2B_{12}Cl_{12}$	88	30-120
$Na_2B_{12}Br_{12}$	120	33-128
$Na_2B_{12}I_{12}$	144	37-137
NaCOSAN	140	43-150

As a conclusion, boron clusters lead to clusterize alcohol molecules in water within alcohol-rich nano-assemblies with 2 and 3 layers of alcohol between boron cluster molecules.

Subsequently, the evolution of the solubility of the more hydrophobic compounds (HC: eucalyptol, citral, linalool, geraniol and b-citronellol) upon addition of 2-butanol (S/S_0) was investigated in the presence of a fixed concentration of $Na_2B_{12}I_{12}$ or $Na_2B_{12}Br_{12}$, see Figure 2.37. This set of experiment evaluates the solubilization ability of the $Na_2B_{12}I_{12}$ or $Na_2B_{12}Br_{12}$/2-BuOH co-assemblies. An increase in the solubility of HC, followed by a decrease

upon increasing 2-BuOH concentration (S/S_0), which might be followed by a second increase at higher 2-BuOH concentrations, was observed for most of the investigated HCs.

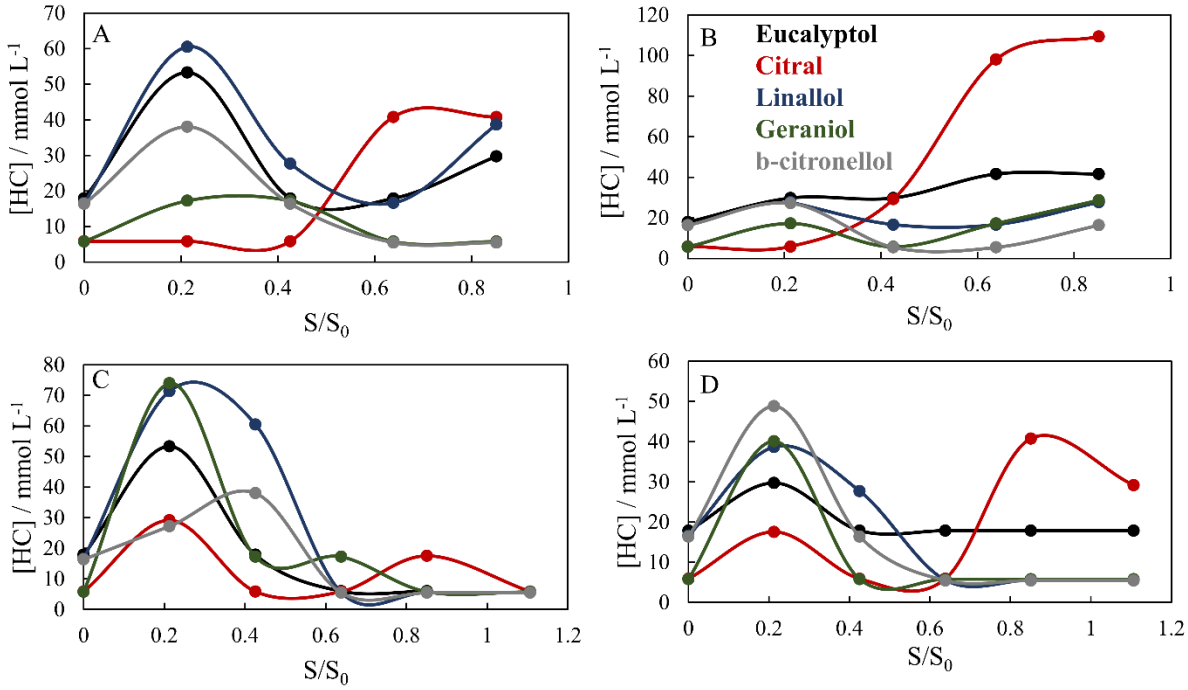

***Figure 2.37**. Solubility of hydrophobic compounds: eucalyptol (dark), citral (red), linalool (blue), geraniol (green) and b-citronellol (grey) a) 0.01 mol L^{-1} $Na_2B_{12}I_{12}$, b) 0.02 mol L^{-1} $Na_2B_{12}I_{12}$, c) 0.01 mol L^{-1} $Na_2B_{12}Br_{12}$ and d) 0.02 mol L^{-1} $Na_2B_{12}Br_{12}$ as a function of 2-BuOH concentration (S/S_0).*

The maximal solubility of the investigated hydrophobic compounds by $B_{12}I_{12}^{2-}$ or $B_{12}Br_{12}^{2-}$/2-BuOH co-assemblies shifted to a lower S/S_0 than that for NaCOSA/2-BuOH co-assemblies (see Figure 2.38).

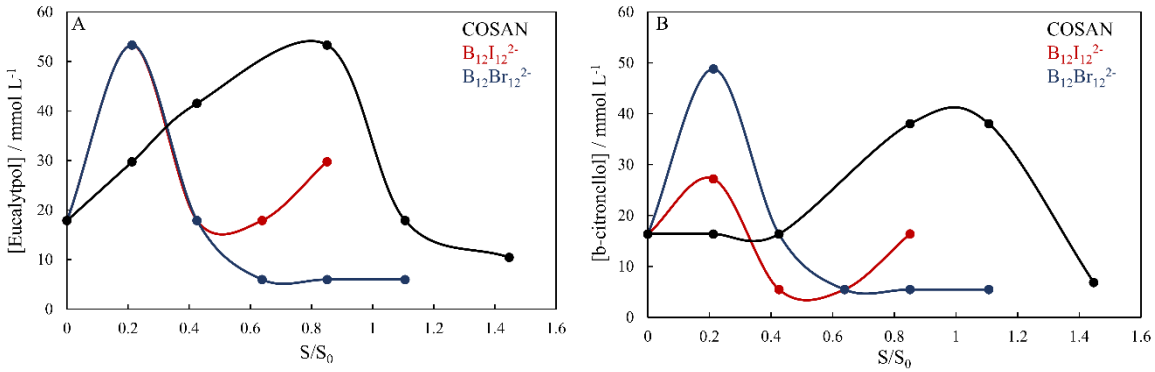

***Figure 2.38**. Solubility of (A) eucalyptol by 0.01 mol L^{-1} and (B) b-citronellol of 0.02 mol L^{-1} boron clusters as a function of 2-BuOH concentration S/S_0. The curves correspond to COSAN (dark), $B_{12}I_{12}^{2-}$ (red), and $B_{12}Br_{12}^{2-}$ (blue).*

To conclude, the NaCOSAN/2-BuOH co-assemblies efficiently solubilize hydrophobic compounds. The SAXS results revealed that the formation of co-assemblies occurs at much

lower 2-BuOH concentrations in the presence of hydrophobic compounds, which may suggest either the re-organization of the co-assemblies or the formation of new co-assemblies. We can also conclude that the solubility efficiency of alcohols, such as 2-BuOH, which has been extensively investigated, is increasing with the increase in the superchaotropic character of the boron clusters. However, the solubility efficiency of boron cluster/2-BuOH co-assemblies does not appear to increase with superchaotropicity.

II.2.8 SAXS- and SANS-fit parameters used in this chapter

Modeling of the SANS/SAXS data

All the combined SANS/SAXS data were fitted using the software SASfit 0.94.10 version. The SANS/SAXS intensity I (q) (cm^{-1} or nm^{-1}) for isotropically distributed scattering particles can be approximated as:

$$I(q) = N * V^2 * \Delta\rho^2 * P(q) * S(q) + I_b \quad (1)$$

where *N* is the number density, which is the concentration of co-assemblies, *V* is the volume of an individual scattering co-assembly, $\Delta\rho$ is the electron density difference (scattering contrast) between the co-assembly and the surrounding solution, P(q) and S(q) are the form and structure factors that takes into account respectively the size/shape of the aggregates and their interactions, I_b is the background scattering intensity.

The aggregate concentration can be expressed as a volume fraction of the aggregates, φ.

$$\varphi_A = n_A * V_A \quad (2)$$

The scattering length density difference Δρ (nm^{-1}) is expressed as

$$\Delta_\rho = \rho_{assemblies} - \rho_{surrounding\ phase} \quad (3)$$

Estimation of scattering length density (SLD or ρ)

The scattering length density for a pure compound in SAXS is:

$$\rho_{SAXS} = \frac{Z}{V_m} l_{Th} \quad (4)$$

where *Z* is the number of electrons, V_m is the molecular volume of the compound and l_{Th} is the Thomson length (b_{Th}= 2.83 10^{-13} cm) which calculated by:

The scattering length density for a pure compound in SANS is:

$$\rho_{SANS} = \frac{1}{V_m}\sum_j b_j \quad (5)$$

where b is the coherent scattering lengths of all the atoms j of the compound.

The volume of the compound can be calculated from its density, d (g/cm^3), by:

$$V_m = \frac{M_W}{dN_A} \quad (6)$$

where N_A is Avogadro's number, M_w is the molar mass (g/mol).

In Table 2.7, the physical data, which were used for the calculations of the molecular volume and scattering length density of all the compounds, are listed.

Table 2.7: Scattering Length Densities for X-rays

Substance	**Formula**	**Molar mass (g/mol)**	**Density (g/cm3)**	**Vm (10^{-22}cm^3)**	**Z**	**ρ_{SAXS} (10^{10}cm^{-2})**
Water	H_2O	18.01	0.99	0.30	10	9.43
Deuterium oxide	D_2O	20.03	1.1	0.30	11	10.30
Deuterated butanol	BuOD	84.12	0.92	1.52	43	8.01
Protonated butanol	BuOH	74.12	0.81	1.52	42	7.82
Cobalt-bis-dicarbollide	$(C_2B_9H_{11})_2Co$	346.74	-	4.48	16	10.36

The atomic scattering lengths, relevant here, are listed in Table 2.8.

Table 2.8: Scattering lengths of the relevant elements

Elements	**b (10^{12} cm)**[39,40]
^{1}H	-0.374
^{2}D	0.667
C	0.665
O	0.58
Co	0.249
B	0.53

Table 2.9 shows the relevant data for the calculations of the scattering length density in SANS.

Table 2.9: Scattering Length Densities for Neutrons

Substance	**Abbreviation**	**Formula**	**Σbj (10^{-12}cm)**	**Vm (10^{-22} cm^3)**	**ρ_{SANS} (10^{10} cm^{-2})**
Water	H_2O	H_2O	-0.17	0.30	-0.55
Deuterium oxide	D_2O	D_2O	1.92	0.30	6.33
Deuterated butanol	BuOD	$C_4D_{10}OD$	9.91	1.52	6.52
Protonated butanol	BuOH	$C_4H_{10}OH$	-0.50	1.52	-0.33
Cobalt-bis-dicarbollide	COSAN	$(C_2B_9H_{11})_2Co$	4.22	4.48	0.94

Calculation of the scattering length density difference, Δρ.

The scattering length densities of the assemblies and of the surrounding solvent can as

$$\rho_{assemblies} = \varphi^{A}_{BuOH}\rho_{BuOH} + \varphi^{A}_{COSAN}\rho_{COSAN} \quad (7)$$

$$\rho_{surrounding\ solvent} = \varphi^{ss}_{D2O}\rho_{D2O} + \varphi^{S_0}_{BuOH}\rho_{BuOH} \quad (8)$$

where φ^{A}_{BuOH} and φ^{A}_{COSAN} is the volume fraction respectively of BuOH and COSAN in the assemblies, φ^{ss} is the volume fraction of D_2O in the surrounding solvent and φ^{S_0} is the volume fraction of BuOH in the surrounding phase which is in the same range of the solubility of BuOH in water or slightly higher due to the presence of COSAN. Finally, with Eq. 9 we get the scattering contrast per mass.

By inserting the Eq. (7), (8) into Eq. (3), one gets

$$\Delta_\rho = \varphi^{A}_{BuOH}\rho_{BuOH} + \varphi^{A}_{COSAN}\rho_{COSAN} - \left(\varphi^{ss}_{D2O}\rho_{D2O} + \varphi^{S_0}_{BuOH}\rho_{BuOH}\right) \quad (9)$$

Note that:

$$\varphi^{A} + \varphi^{ss} = 1 \quad (10)$$

The volume fraction of the assemblies is given by:

$$\varphi^{A} = \frac{V_A}{V_T} \quad (11)$$

Where φ^A is the volume fraction of the assembly, V_A is the volume of the assembly and V_T the total volume defined as:

$$V_T = V_A + V_{SS} \tag{12}$$

where V_{SS} is the volume of the surrounding solvent phase.

In order to determine the volume fraction of the assemblies, the volume of the assemblies is needed and it is expressed as:

$$V_A = V^A_{COSAN} + V^A_{BuOH} + V^A_{D2O} \tag{13}$$

Eq. 13 can be written as:

$$V_A = C^A_{COSAN} * V^{COSAN}_m + C^A_{BuOH} * V^{BuOH}_m + C^A_{D2O} * V^{D2O}_m \tag{14}$$

The total concentration of each compound in the sample, which is known, is the sum of each concentrations of the compounds in the assemblies and in the surrounding solvent phase as described by the following equations:

$$C^T_{BuOH} = \varphi^A \varphi^A_{BuOH} C^A_{BuOH} + \varphi^{SS} \varphi^{SS}_{BuOH} C^{SS}_{BuOH} \tag{15}$$

$$C^T_{COSAN} = \varphi^A \varphi^A_{COSAN} C^A_{COSAN} + \varphi^{SS} \varphi^{SS}_{COSAN} C^{SS}_{COSAN} \tag{16}$$

$$C^T_{D2O} = \varphi^A \varphi^A_{D2O} C^A_{D2O} + \varphi^{SS} \varphi^{SS}_{D2O} C^{SS}_{D2O} \tag{17}$$

where φ^A_i and φ^{SS}_i are the volume fractions of the component *i* in the assemblies (*A*) and in the surrounding solvent phase (*SS*). In the assemblies φ^A_i are expressed as

$$\varphi^A_{BuOH} = \frac{C^A_{BuOH} * V^m_{BuOH}}{V_A} \tag{18}$$

$$\varphi^A_{COSAN} = \frac{C^A_{COSAN} * V^m_{COSAN}}{V_A} \tag{19}$$

$$\varphi^A_{D2O} = \frac{C^A_{D2O} * V_{D2O}}{V_A} \tag{20}$$

Similar equations can be expressed for the surrounding solvent phase.

Fitting procedure

At this point, it is worthwhile to recall Eq. 1.

$$I(q) = NV^2(\Delta\rho)^2 P(q)S(q) + I_b$$

The fitting of the SANS spectra was performed by separating the parameters in two groups: the fixed parameters and the fitting parameters.

I_b is the background scattering intensity, which was one of the fixed parameters.

Prefactor:

The total concentrations of C_{COSAN}^T, C_{BuOH}^T and C_{D2O}^T are determined experimentally from the chemical compositions.

The first assumption that we made is that there is no water in the aggregates, which means that we can write the Eq. 14 as:

$$V_A = C_{COSAN}^A * V_m^{COSAN} + C_{BuOH}^A * V_m^{BuOH} \quad (21)$$

This assumption is likely to be valid because we have previously shown for other nano-ions/organic assemblies (polyoxometalate/dipropyleneglycol propyl ether) built upon the superchoatropic effect in water that the presence of water in the assembly was negligible. [24]

The next assumption that we made is that the excess of butanol concentration (above its solubility in water) is in the droplet. This parameter is fixed at the initial stage of the fitting procedure since we know the solubility of butanol in the water, but it is fitted in the next step because it is possible that butanol partition differently between the surrounding solvent phase and the aggregate.

$$C_{BuOH}^A = \left(C_{BuOH}^T - C_{BuOH}^{S_0}\right) \quad (22)$$

From Eq. 22 we can write the Eq. 21 as:

$$V_A = C_{COSAN}^{A} * V_m^{COSAN} + \left(C_{BuOH}^{T} - C_{BuOH}^{S_0}\right) * V_m^{BuOH} \quad (23)$$

The C_{COSAN}^{A}, $C_{BuOH}^{S_0}$ are the parameters which were fitted here, and the volume of the aggregates were then calculated. The volume of the aggregates can be used to calculate the volume fraction of the butanol and COSAN aggregates through the Eq. 18 and 19, respectively. The next step is the calculation of the scattering length density through the Eq. 7 and 8. In Table 2.10, we summarize the fixed, the fitting, and the calculated parameters for the prefactor.

Table 2.10: Prefactor parameters

Fixed parameters	Fitting parameters	Calculated parameters
C_{COSAN}^{T}, C_{BuOH}^{T}, C_{D2O}^{T}, V_{BuOH}^{m}, V_{COSAN}^{m}, V_{D2O}^{m}	C_{COSAN}^{A}, $C_{BuOH}^{S_0}$	φ_{BuOH}^{A}, φ_{COSAN}^{A}, V_A, φ_{BuOH}^{SS}, φ_{COSAN}^{SS}, φ_{D2O}^{SS}, ρ_A, ρ_{SS}, C_{BuOH}^{A}

In the following table (Table 2.11) are given the results of the prefactor parameters in case of 0.04 M COSAN in the presence of 1.6 M 1-BuOH in D_2O.

Table 2.11: Example of results obtained for the prefactor calculation for 0.04 M COSAN and 1.6 M 1-BuOH in D_2O.

Parameter	Value	Units
C_{COSAN}^{T}	0.04	mol L^{-1}
C_{BuOH}^{T}	1.6	mol L^{-1}
C_{D2O}^{T}	50	mol L^{-1}
V_{BuOH}^{m}	91.48	cm^3
V_{COSAN}^{m}	269.70	cm^3
V_{D2O}^{m}	18.20	cm^3
C_{COSAN}^{A}	0.02 (best fit parameters)	mol L^{-1}
$C_{BuOH}^{S_0}$	1.15 (best fit parameters)	mol L^{-1}
C_{BuOH}^{A}	0.15	mol L^{-1}
φ_{BuOH}^{A}	0.88	-
φ_{COSAN}^{A}	0.12	-
φ_A	0.05	-
V_A	46.6	nm^3
φ_{BuOH}^{SS}	0.104	-
φ_{COSAN}^{SS}	0.12	-
φ_{D2O}^{SS}	0.89	-
ρ_A	-0.18	10^{-6} Å
ρ_{SS}	5.88	10^{-6} Å

Form factor:

Different form factors from the SASfit libraries, [41] have been tried to fit the SANS spectra:

Spherical Form factor

Spherical core-shell form factor

Disc form factor

Triaxial ellipsoid shell

The triaxial ellipsoid shell model from the SASfit library gave the best fit with the minimum of fitting parameters (i.e. the only model that enabled to fully fit the experimental data with a physical meaning and in absolute value). Note that there was no need to consider a shell to fit correctly the spectra.

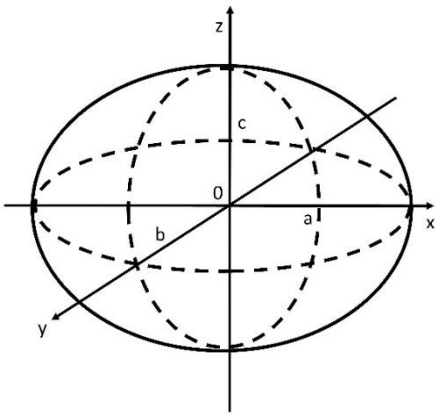

Figure 2.39. *A tri-axial ellipsoid in cartesian coordinates, a, b and c are the length of the ellipse semi-axis.*

Using a Cartesian coordinate system (x, y, z) in which the origin is the center of the ellipsoid and the coordinate axes of the ellipsoid (see Figure 2.39), the equation of the ellipsoid has the form:

$$\frac{x^2}{a^2}+\frac{y^2}{b^2}+\frac{z^2}{c^2}=1 \qquad (24)$$

with a, b and c are the length of the ellipse semi-axis.

Considering isotropic space distribution of the assemblies (ellipsoids) without a preferential orientation, the scattered intensity for one ellipsoid can be expressed as

$$I(q)=V_{ell}^2*(\Delta\rho)^2*\int_0^1\int_0^1\Phi^2(qr)\,dxdy \qquad (25)$$

where

$$\Phi(qr) = 3\frac{\sin qr - qr\cos qr}{(qr)^3} \tag{26}$$

$$r^2 = a^2e^2 + b^2f^2 + c^2g^2 \tag{27}$$

The e, f and g terms are the projections of the orientation vector on X, Y and Z respectively.

$$V_{ell} = \frac{4}{3}\pi abc \tag{28}$$

with V_{ell} the volume of the ellipsoid

The best fit was obtained with the three axial form factor, the three semi-axes of the ellipsoid (a,b,c). By fixing two semi-axes equal (here b and c) the quality of the fit remained as good as by taking into account the three semi axis. As a result, the triaxial shell ellipsoid model in SASfit was used as a triaxial ellipsoid model by applying the constraint, b = c, in the fit.

The scattered intensity was scaled by N, where N is the number density of the scattering objects, i.e., the co-assemblies. N, a and b are fitting parameters and N is simply related to the volume fraction,φ^A, of the scattering objects as

$$N = \frac{\varphi^A}{V_{ell}} \tag{29}$$

Structure factor:

To describe the shape of the aggregates the ellipsoid form factor, $P_A^{ellipsoid}$ (expressed in Eq. 25-28) was used, and the electrostatic inter-aggregate repulsions were modelled by using a Hayter Penfold Rescaled Mean Sphere Approximation (RMSA) structure factor, S_A^{RMSA}. The input parameters for this model is RHS: the hard sphere radius in nm, Z is the charge in units of the charge of an electron, and φ^A is the volume fraction of the assemblies, T is the temperature in Kelvin, *S* is the salt concentration in M, e_r is the relative dielectric constant of the solvent (here water). The salt concentration is used to compute the ionic strength of the solution, which in turn is used to compute the Debye screening length. All the parameters were fixed besides the radius of the hard sphere that was fitted.

II.3 Conclusions of chapter II

As a conclusion, alcohols (1 or 2-BuOH) at low concentrations bind to NaCOSAN monomer leading to the disassembly of the NaCOSAN micelle-like aggregates. Further addition of alcohols, at concentrations close to their solubility limit in pure water, provokes the formation of larger hybrid alcohol-COSAN co-assemblies, at the origin of the increased alcohol solubility. The formation of these larger assemblies is concomitant with the exchange of the hydration shell of NaCOSAN for a solvation shell of alcohol, as concluded from UV-Vis and WAXS results. The size evolution of the assemblies with changing NaCOSAN or butanol concentrations is characterized by an anisotropic growth that is certainly controlled by the presence of ionic species within these organic/inorganic assemblies, which still contain some water molecules but have a significantly lower dielectric permittivity. Such a solubilization mechanism based on organic-inorganic co-assemblies that grow in 2D has, to the best of our knowledge, never been reported in the literature. It strongly differs from classical micellar solubilization, i.e., solubilization within the hydrophobic micellar core leading to a 3D swelling of micelles, or from co-solvency, hydrotropy, and host-guest complexation approaches. Other types of inorganic superchaotropic nano-ions, as shown here with NaI_2COSAN, and halogenated dodecaborate clusters: $B_{12}Cl_{12}^{2-}$, $B_{12}Br_{12}^{2-}$, $B_{12}I_{12}^{2-}$, act also as solubilizers with a comparable solubilization mechanism but varying efficiencies that depend on their position on the Hofmeister series. We have shown that the formulation of these boron nano-ions with short-chain alcohols can be used to solubilize more hydrophobic compounds ($0.5 < \log P < 6$) and open new prospects for aqueous formulations across a wide range of application domains.

References

[1] C.A. Miller, K.H. Raney, Solubilization-emulsification mechanisms of detergency, Colloids Surfaces A Physicochem. Eng. Asp. 74 (1993) 169–215. https://doi.org/10.1016/0927-7757(93)80263-E.

[2] J.Y. Kim, S. Kim, M. Papp, K. Park, R. Pinal, Hydrotropic solubilization of poorly water-soluble drugs, J. Pharm. Sci. 99 (2010) 3953–3965. https://doi.org/10.1002/jps.22241.

[3] B.C. Stephenson, C.O. Rangel-Yagui, A. Pessoa, L.C. Tavares, K. Beers, D. Blankschtein, Experimental and theoretical investigation of the micellar-assisted solubilization of ibuprofen in aqueous media, Langmuir. 22 (2006) 1514–1525. https://doi.org/10.1021/la052530k.

[4] A. Dahan, J.M. Miller, A. Hoffman, G.E. Amidon, G.L. Amidon, The Solubility – Permeability Interplay in Using Cyclodextrins as Pharmaceutical Solubilizers : Mechanistic Modeling and Application to Progesterone, J. Pharm. Sci. 99 (2010) 2739–2749. https://doi.org/10.1002/jps.22033.

[5] R. Tekade, Dosage from Design Considerations, Academic Press, Cambridge, MA, USA, 2018. https://doi.org/https://doi.org/10.1016/C2017-0-01072-8.

[6] M.H. Uddin, N. Kanei, H. Kunieda, Solubilization and emulsification of perfume in discontinuous cubic phase, Langmuir. 16 (2000) 6891–6897. https://doi.org/10.1021/la000327d.

[7] J. Labows, J. Bahms, R. Cagan, Surfactants in Cosmetics, Second, CRC Press, New York, 1997. https://doi.org/https://doi.org/10.1201/9780203737743.

[8] E.T. Alori, B.R. Glick, O.O. Babalola, Microbial phosphorus solubilization and its potential for use in sustainable agriculture, Front. Microbiol. 8 (2017) 1–8. https://doi.org/10.3389/fmicb.2017.00971.

[9] P. Bauduin, A. Renoncourt, A. Kopf, D. Touraud, W. Kunz, Unified concept of solubilization in water by hydrotropes and cosolvents, Langmuir. 21 (2005) 6769–6775. https://doi.org/10.1021/la050554l.

[10] Y. Chevalier, T. Zemb, The structure of micelles and microemulsions, Reports Prog. Phys. 53 (1990) 279–371. https://doi.org/10.1088/0034-4885/53/3/002.

[11] Robert J. Hunter, Introduction to Modern Colloid Science, Oxford Science Publications, 1993.

[12] S.H.. Yalkowsky, Solubility and Solubilization in Aqueous Media, Oxford University Press, New York, 1999.

[13] H. Wennerström, Thermodynamic theory of surfactant phases, Curr. Opin. Colloid Interface Sci. 1 (1996) 370–375. https://doi.org/10.1016/s1359-0294(96)80136-1.

[14] W.L. Hinze, Organized Surfactant Assemblies in Separation Science, (1987) 2–82. https://doi.org/10.1021/bk-1987-0342.ch001.

[15] T.N.C. Dantas, V.C. Santanna, T.T.C. Souza, C.R.S. Lucas, A.A. Dantas Neto, P.T.P. Aum, Microemulsions and Nanoemulsions Applied To Well Stimulation and Enhanced Oil Recovery (Eor), Brazilian J. Pet. Gas. 12 (2019) 251–265. https://doi.org/10.5419/bjpg2018-0023.

[16] J.N. Israelachvili, D.J. Mitchell, B.W. Ninham, Theory of self-assembly of hydrocarbon amphiphiles into micelles and bilayers, J. Chem. Soc. Faraday Trans. 2 Mol. Chem. Phys. 72 (1976) 1525–1568. https://doi.org/10.1039/F29767201525.

[17] W. Kunz, F. Testard, T. Zemb, Correspondence between curvature, packing parameter, and hydrophilic-lipophilic deviation scales around the phase-inversion temperature, Langmuir. 25 (2009) 112–115. https://doi.org/10.1021/la8028879.

[18] M.A.-F. and J.C.M. Gonzalo Astray Dopazo, Cecilia Martínez-Castillo, Modeling the

Behavior of Amphiphilic Aqueous Solutions, 2020.

[19] S. Shimizu, N. Matubayasi, Cooperativity in micellar solubilization, Phys. Chem. Chem. Phys. 23 (2021) 8705–8716. https://doi.org/10.1039/d0cp06479c.

[20] O. Glatter, S. Salentinig, Inverting structures: from micelles via emulsions to internally self-assembled water and oil continuous nanocarriers, Curr. Opin. Colloid Interface Sci. 49 (2020) 82–93. https://doi.org/10.1016/j.cocis.2020.05.003.

[21] Robert G. Laughlin, The aqueous phase behavior of surfactants, Academic P, London, 1994.

[22] J.W. McBain, G.C. Brock, R.D. Vold, M.J. Vold, Phase Rule Studies of Soap. II. The System Sodium Laurate-Sodium Chloride-Water, J. Am. Chem. Soc. 60 (1938) 1870–1876. https://doi.org/10.1021/ja01275a042.

[23] W. Kunz, K. Holmberg, T. Zemb, Hydrotropes, Curr. Opin. Colloid Interface Sci. 22 (2016) 99–107. https://doi.org/10.1016/j.cocis.2016.03.005.

[24] P. Schmid, T. Buchecker, A. Khoshsima, D. Touraud, O. Diat, W. Kunz, A. Pfitzner, P. Bauduin, Self-assembly of a short amphiphile in water controlled by superchaotropic polyoxometalates: H4SiW12O40 vs. H3PW12O40, J. Colloid Interface Sci. 587 (2021) 347–357. https://doi.org/10.1016/j.jcis.2020.12.003.

[25] A. El Maangar, P. Degot, V. Huber, J. Causse, P. Berthault, D. Touraud, W. Kunz, T. Zemb, Pre-nucleation cluster formation upon ethyl acetate addition to an aqueous solution of an anionic hydrotrope, J. Mol. Liq. 310 (2020) 113240. https://doi.org/10.1016/j.molliq.2020.113240.

[26] J.A.P. Coutinho, D.O. Abranches, J. Benfica, S. Shimizu, The perspective of cooperative hydrotropy on the solubility in aqueous solutions of cyrene, Ind. Eng. Chem. Res. 59 (2020) 18649–18658. https://doi.org/10.1021/acs.iecr.0c02346.

[27] Millard, F.A. Alvarez-Núñez, S.H. Yalkowsky, Solubilization by cosolvents: Establishing useful constants for the log-linear model, Int. J. Pharm. 245 (2002) 153–166. https://doi.org/10.1016/S0378-5173(02)00334-4.

[28] P. Saokham, C. Muankaew, P. Jansook, T. Loftsson, Solubility of cyclodextrins and drug/cyclodextrin complexes, Molecules. 23 (2018) 1–15. https://doi.org/10.3390/molecules23051161.

[29] P.M. Gassin, L. Girard, G. Martin-Gassin, D. Brusselle, A. Jonchère, O. Diat, C. Viñas, F. Teixidor, P. Bauduin, Surface activity and molecular organization of metallacarboranes at the air-water interface revealed by nonlinear optics, Langmuir. 31 (2015) 2297–2303. https://doi.org/10.1021/acs.langmuir.5b00125.

[30] Ž. Medoš, B. Hleli, Z. Tošner, P. Ogrin, T. Urbič, K. Kogej, M. Bešter-Rogač, P. Matějíček, Counterion-Induced Aggregation of Metallacarboranes, J. Phys. Chem. C. 126 (2022) 5735–5742. https://doi.org/10.1021/ACS.JPCC.2C00107/SUPPL_FILE/JP2C00107_SI_001.PDF.

[31] P. Merhi, Tania; Alban, Jonchère; Girard, Luc;Diat, Olivier; Nuez, Miquel; Viñas, Clara;Bauduin, Highlights on the Binding of Cobalta-Bis- (Dicarbollide) with Glucose Units Accepted Article Accepted Article, Chem. - A Eur. J. 26 (2020) 13935–13947. https://doi.org/10.1002/chem.202002123.

[32] P. Bauduin, A. Renoncourt, A. Kopf, D. Touraud, W. Kunz, Unified Concept of Solubilization in Water by Hydrotropes and Cosolvents, (2005). https://doi.org/10.1021/la050554l.

[33] P. Bauduin, A. Basse, D. Touraud, W. Kunz, Effect of short non-ionic amphiphiles derived from ethylene and propylene glycol alkyl ethers on the CMC of SDS, Colloids Surfaces A Physicochem. Eng. Asp. 270–271 (2005) 8–12. https://doi.org/10.1016/j.colsurfa.2005.05.030.

[34] J.N. Israelachvili, Intermolecular and Surface Forces, Second Edi, Academic Press,

1991.
[35] R.K. Birdwhistell, D.B. Alger, textbook forum edited by The Water Solubility of 2-Butanol: A Widespread Error, n.d. https://pubs.acs.org/sharingguidelines.
[36] P. Yalkowsky, Samuel; He, Yan; Jain, Aqueous Solubility Data, Second Edi, CRC Press, 2010. https://doi.org/https://doi.org/10.1201/EBK1439802458.
[37] O. Diat, M.L. Klossek, D. Touraud, B. Deme, research papers Octanol-rich and water-rich domains in dynamic equilibrium in the pre-ouzo region of ternary systems containing a hydrotrope 1 research papers, (2014) 1665–1670. https://doi.org/10.1107/S002188981302606X.
[38] P. Bauduin, S. Prevost, P. Farràs, F. Teixidor, O. Diat, T. Zemb, A theta-shaped amphiphilic cobaltabisdicarbollide anion: Transition from monolayer vesicles to micelles, Angew. Chemie - Int. Ed. 50 (2011) 5298–5300. https://doi.org/10.1002/anie.201100410.
[39] Otto Glatter, Scattering Methods and their Application in Colloid and Interface Science, 2018.
[40] Varley F. Sears, Neutron scattering lengths and cross sections, Taylors &, 1992.
[41] I. Breßler, J. Kohlbrecher, A.F. Thünemann, SASfit: A tool for small-angle scattering data analysis using a library of analytical expressions, J. Appl. Crystallogr. 48 (2015) 1587–1598. https://doi.org/10.1107/S1600576715016544.

Supporting Information of Chapter II

II.2.1 Solubilization of hydrophobic compounds by NaCOSAN

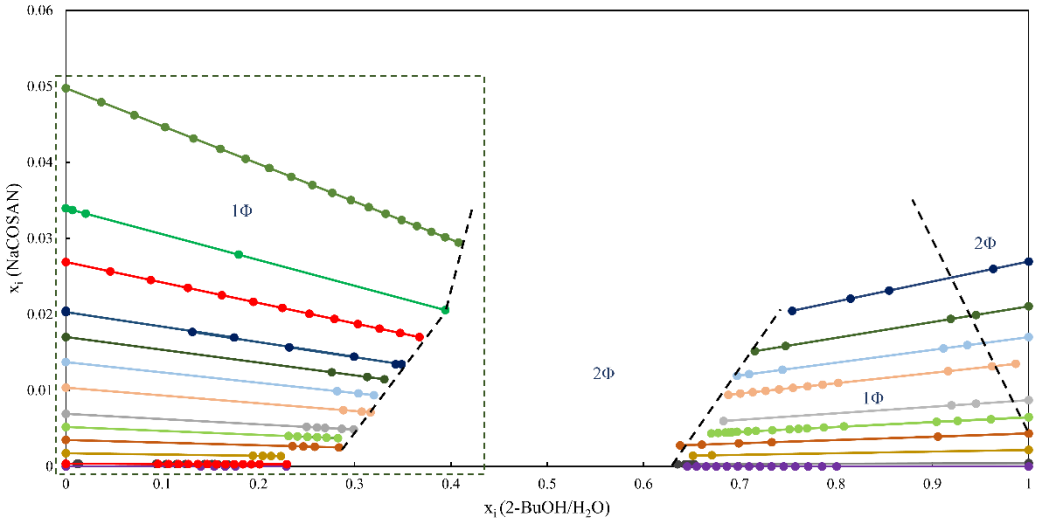

Figure S2.1. *Solubility lines of NaCOSAN in the presence of 2-butanol.*

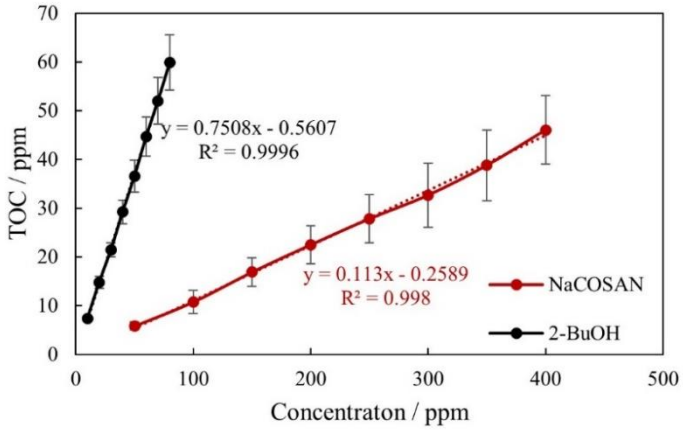

Figure S2.2. *TOC calibration curve for NaCOSAN (red) and 2-butanol (black) concentration.*

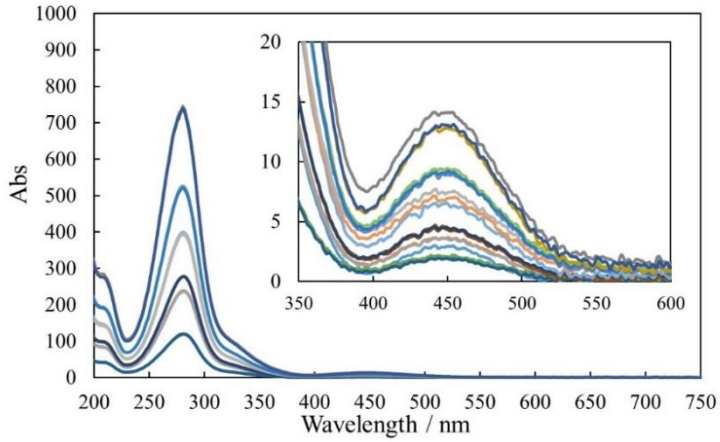

Figure S2.3. *UV-Vis spectra of different NaCOSAN concentrations in H_2O. The inset shows a zoom-in of the visible range.*

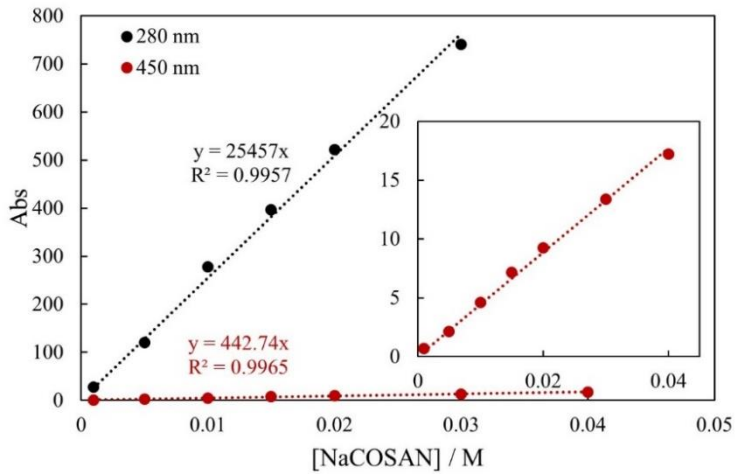

Figure S2.4. *The calibration curve of NaCOSAN obtained from UV-vis spectra are plotted in Figure S3.*



Figure S2.5. *Samples of the biphasic system NaCOSAN/2-BuOH/water.*

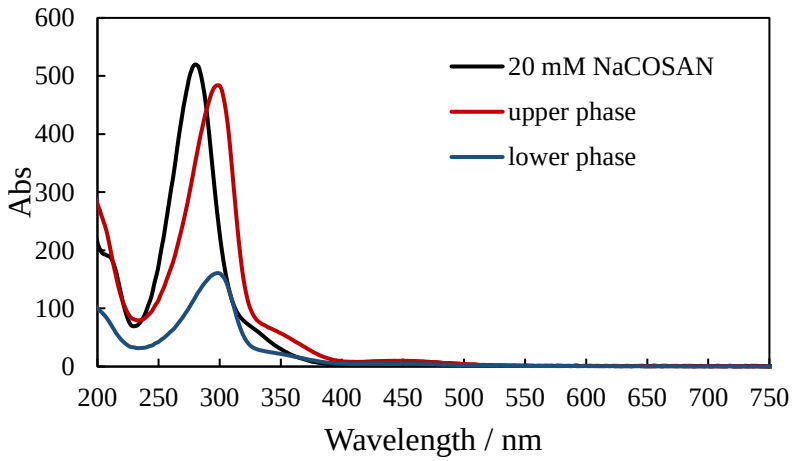

Figure S2.6. *Example of UV-Vis spectra of 20 mM NaCOSAN in H_2O (dark), in the upper alcohol-rich phase (red) and in the lower water-rich phase (blue) of the biphasic system of NaCOSAN/2-BuOH/water.*

Table S2.1: Concentration of NaCOSAN in each phase of the biphasic system NaCOSAN/2-BuOH/water.

NaCOSAN/2-BuOH/water biphasic system	[NaCOSAN] / mmol L^{-1}	Error / mmol L^{-1}
≈9 mmol L^{-1} NaCOSAN upper phase	6.3	0.07
≈9 mmol L^{-1} NaCOSAN lower phase	1.9	0.13
≈12.5 mmol L^{-1} NaCOSAN upper phase	8.8	0.74
≈12.5 mmol L^{-1} NaCOSAN lower phase	3.6	0.12
≈17 mmol L^{-1} NaCOSAN upper phase	12.6	0.61
≈17 mmol L^{-1} NaCOSAN lower phase	4.7	0.03
≈22 mmol L^{-1} NaCOSAN upper phase	13.9	0.95
≈22 mmol L^{-1} NaCOSAN lower phase	4.7	0.03
≈27 mmol L^{-1} NaCOSAN upper phase	20.3	0.33
≈27 mmol L^{-1} NaCOSAN lower phase	6.3	0.62

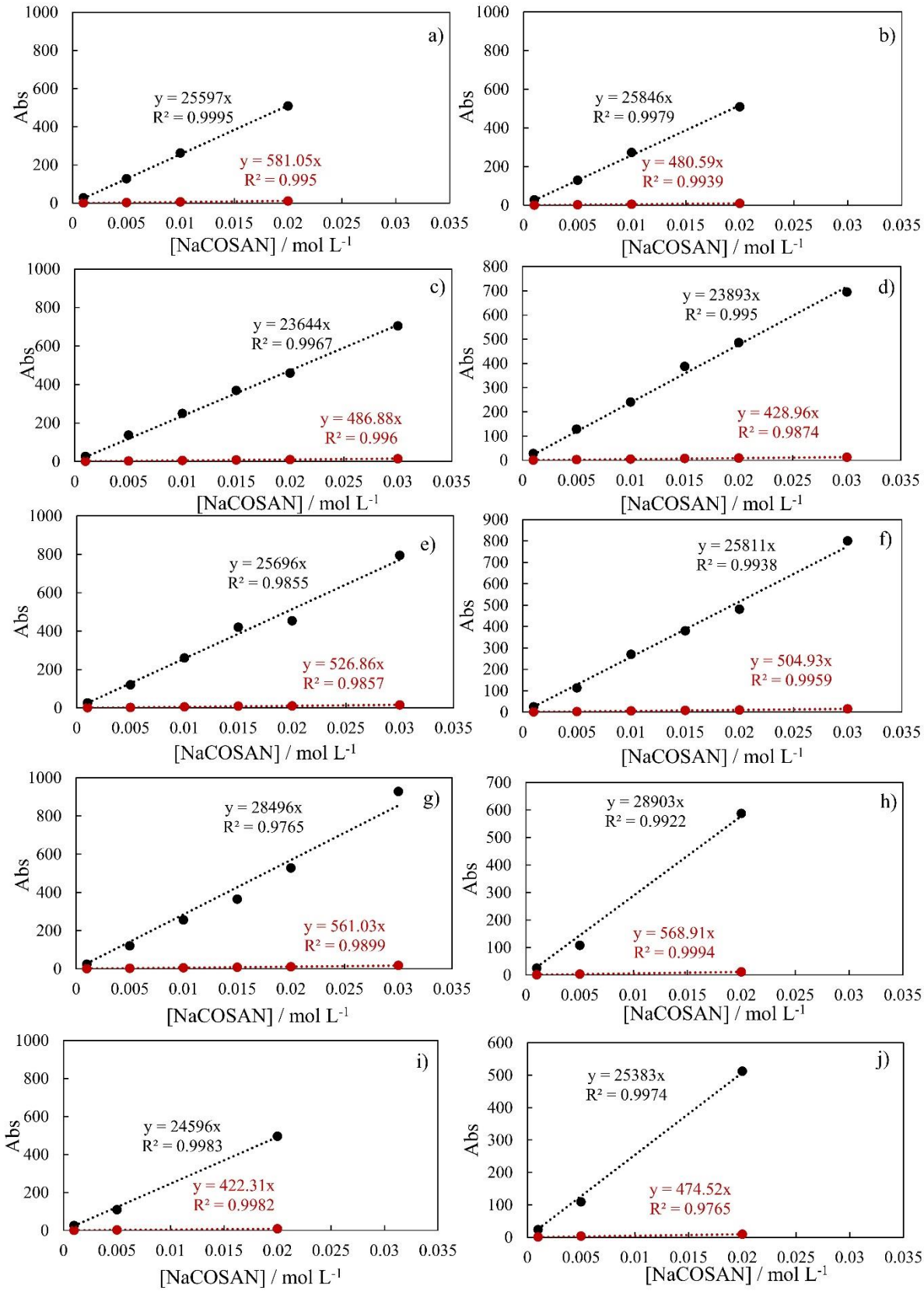

Figure S2.7. *Calibration curve of NaCOSAN in the presence of different percentages of 2-BuOH a) 0.5%, b) 1%, c) 2%, d) 5%, e) 10%, f) 15%, g) 20%, h) 80%, i) 85% and j) 90%.*

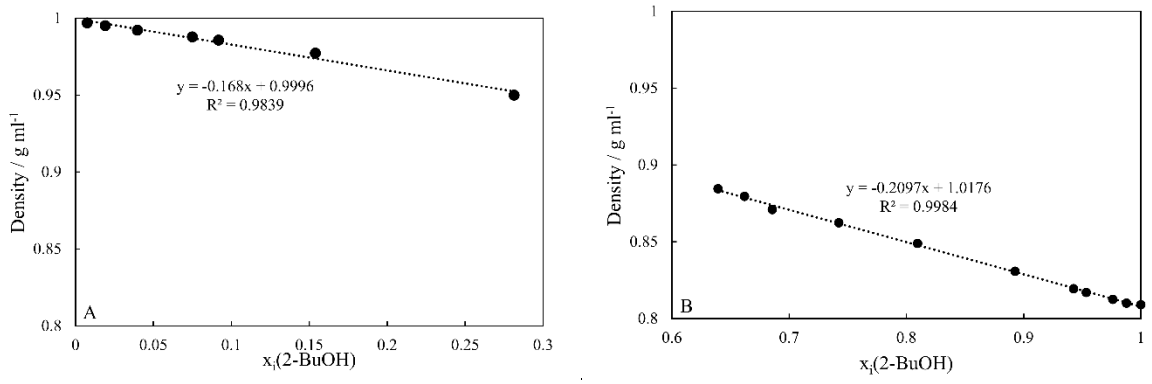

Figure S2.8. *The density of successive additions of 2-butanol in water (left) and water in 2-butanol (right) as a function of 2-butanol mass fraction.*

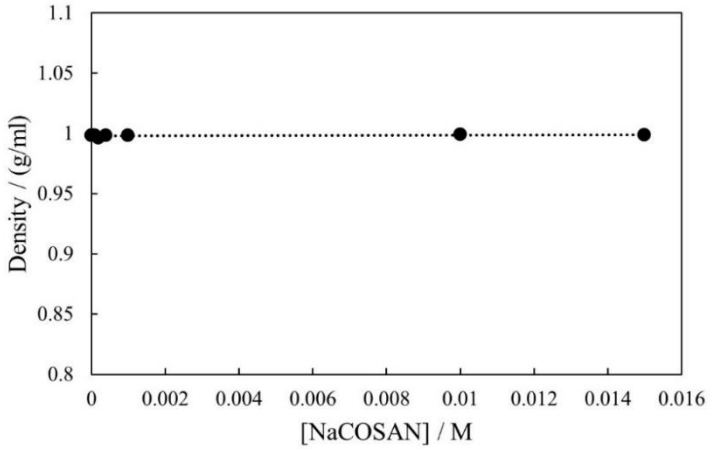

Figure S2.9. *The density of water upon the addition of NaCOSAN as a function of NaCOSAN concentration.*

Table S2.2: Karl Fischer titration results

NaCOSAN/2-BuOH/water biphasic system	% H_2O (w/w)
≈9 mmol L^{-1} NaCOSAN upper phase	72
≈12.5 mmol L^{-1} NaCOSAN upper phase	78
≈17 mmol L^{-1} NaCOSAN upper phase	76
≈22 mmol L^{-1} NaCOSAN upper phase	85
≈27 mmol L^{-1} NaCOSAN upper phase	76
2-BuOH	2

II.2.2 Solubility of butanol in the presence of NaCOSAN

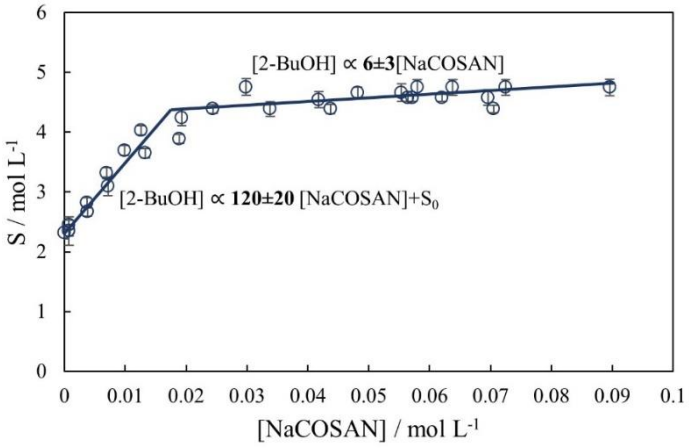

Figure S2.10. *Solubility of 2-BuOH in water (S in mmol L^{-1}) at 22°C as a function of NaCOSAN concentration.*

II.2.4 Supramolecular level: 2-BuOH and 1-BuOH solubility in the presence of NaCOSAN and its derivatives

II.2.4.1 Supramolecular level: 2-BuOH solubility in the presence of NaCOSAN

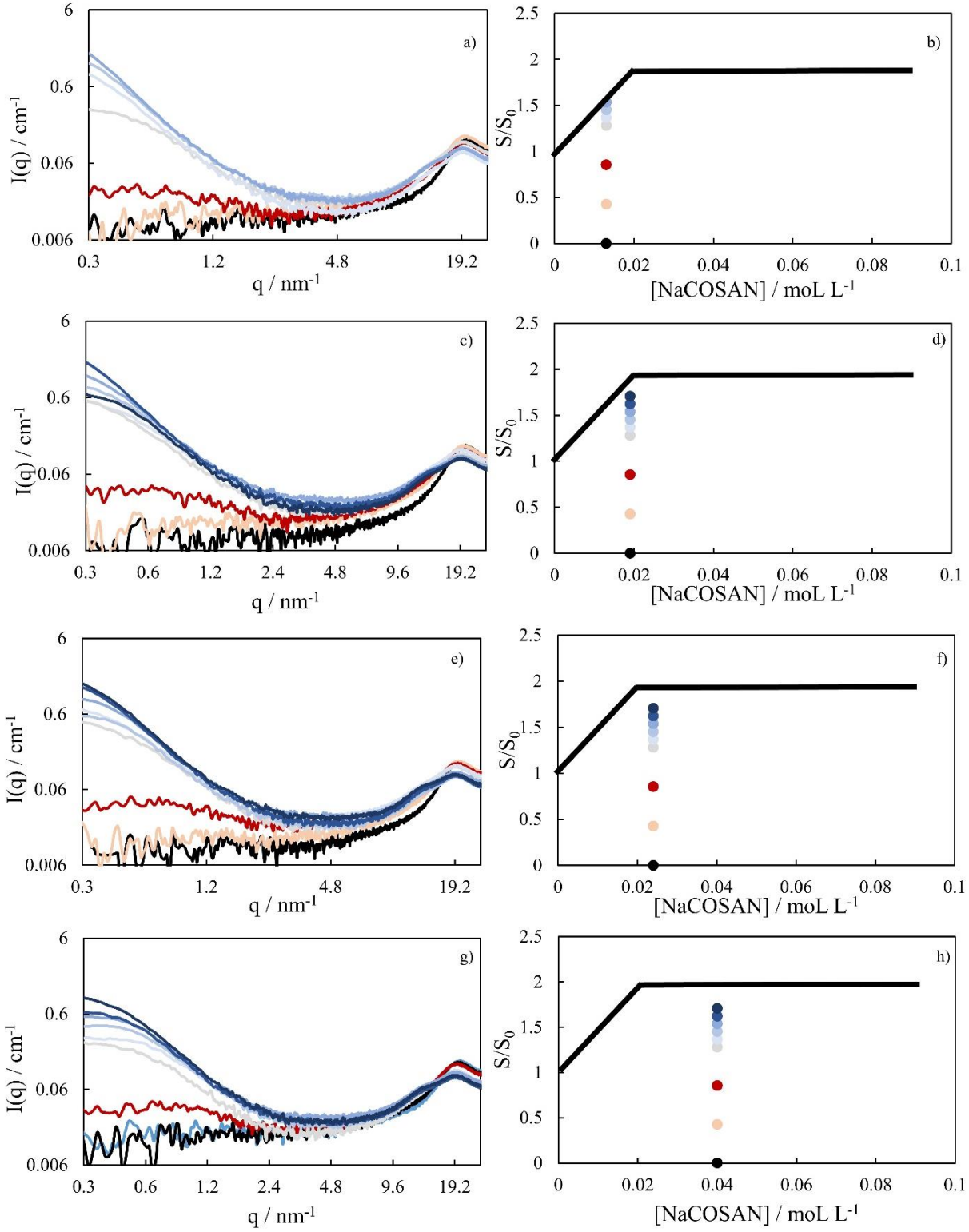

Figure S2.11. *SWAXS spectra of (a) 0.013 mmol L^{-1}, (c) 0.02 mmol L^{-1}, (e) 0.024 mmol L^{-1}, (g) 0.04 mmol L^{-1} NaCOSAN in aqueous solution in the presence of different 2-BuOH concentrations, as shown on the solubility curve (b), (d), (f), (g).*

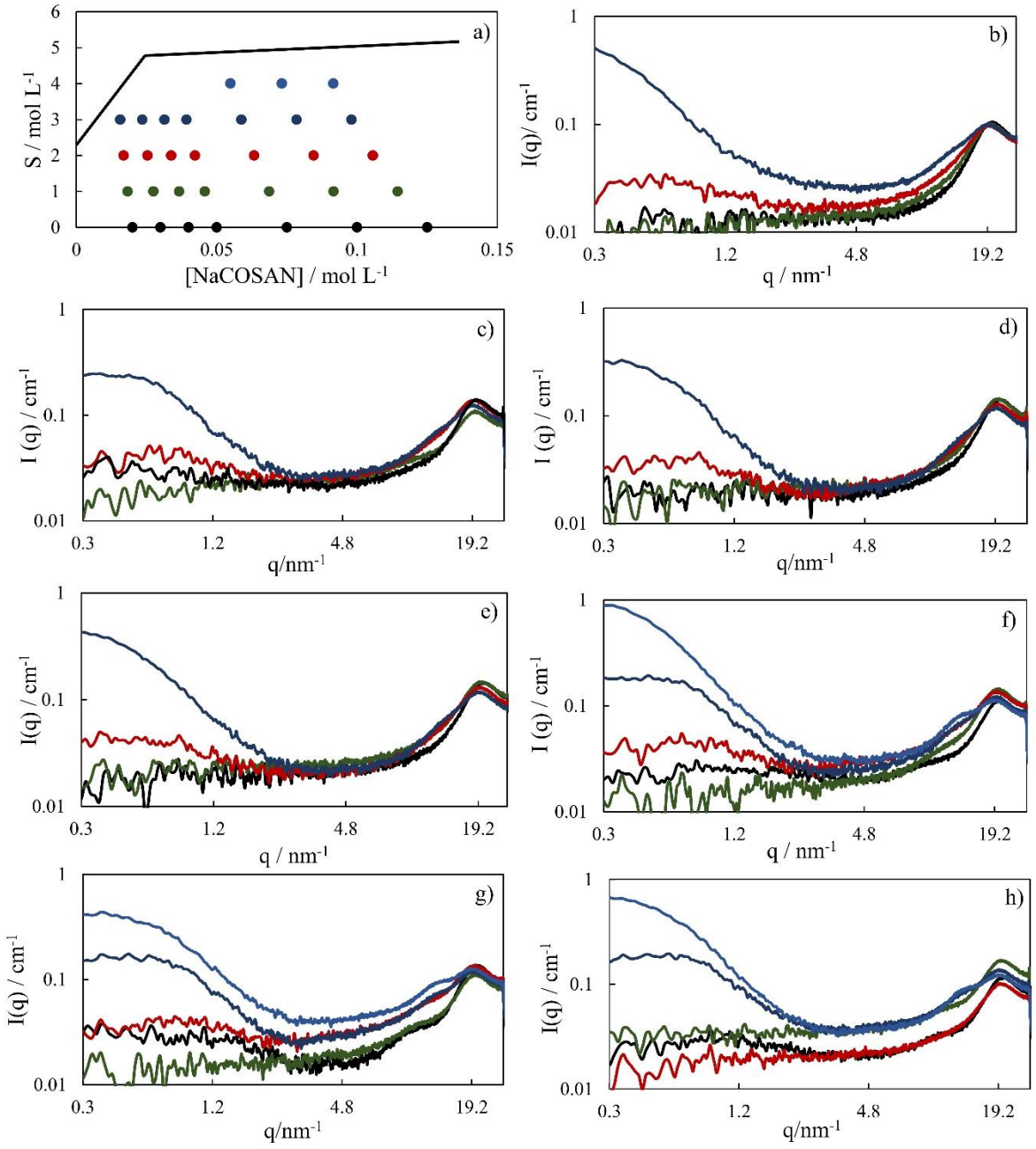

Figure S2.12. *SWAXS spectra of (b) 0.02 mmol L^{-1}, (c) 0.03 mmol L^{-1}, (d) 0.04 mmol L^{-1}, (e) 0.05 mmol L^{-1}, (f) 0.04 mmol L^{-1}, (g) 0.075 mmol L^{-1} (e) 0.1 mmol L^{-1} and (h) 0.125 mmol L^{-1} NaCOSAN in aqueous solution in the presence of different 2-BuOH concentrations, as shown on the solubility curve (a).*

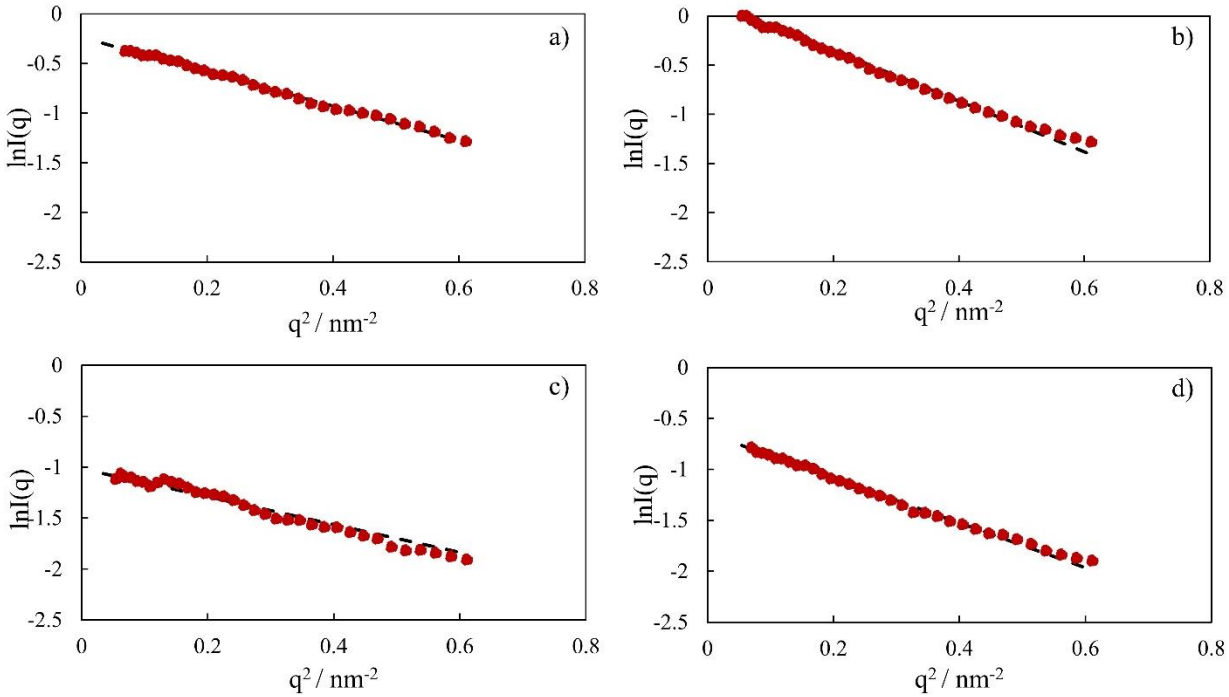

Figure S2.13. *SAXS fit of a) 0.075 mmol L^{-1}, b) 0.055 mmol L^{-1}, c) 0.03 mmol L^{-1} and d) 0.022 mmol L^{-1} NaCOSAN concentration in the presence of 4 M 2-butanol concentration. The red points corresponds to the experimental data and the dark dashed line to the Guinier fit.*

II.2.4.2 Supramolecular level: 2-BuOH solubility in the presence of NaI_2COSAN

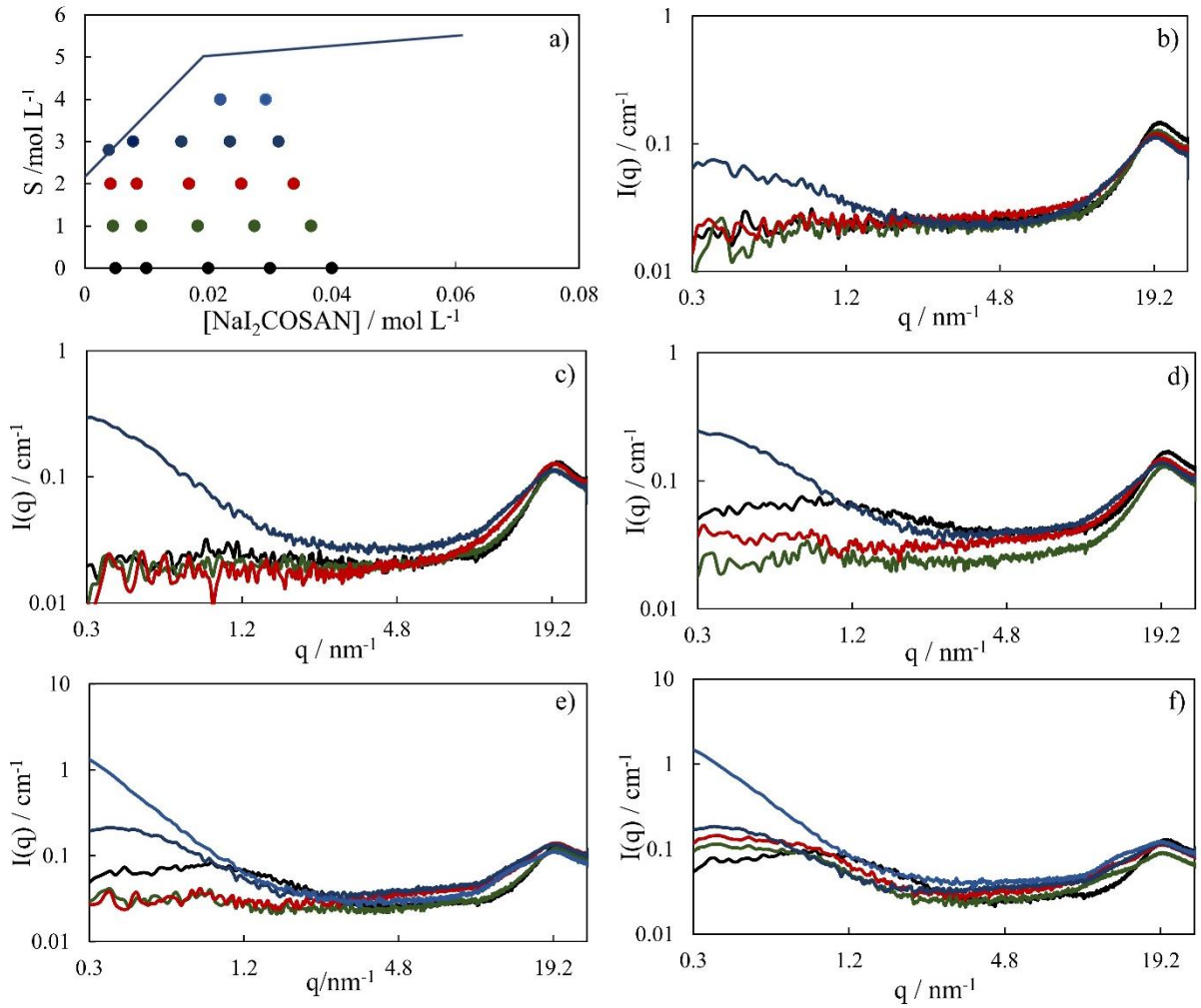

Figure S2.14. *SWAXS spectra of (b) 0.005 mmol L^{-1}, (c) 0.01 mmol L^{-1}, (d) 0.02 mmol L^{-1}, (e) 0.03 mmol L^{-1} and (f) 0.04 mmol L^{-1} NaI_2COSAN in aqueous solution in the presence of different 2-BuOH concentrations, as shown on the solubility curve (a).*

Chapter III: Specific interactions of boron clusters with proteins

As mentioned in Chapter I, the specific ion effect can be diminished in various systems, including biological, colloidal, polymer, surfactant, and crystallization systems. In biological systems, such as proteins, liposomes, and cells, these effects have been found to have an impact, for example, on the enzymes stability and activity,[1,2] on cell membrane permeability,[3–5] on proteins folding and stability,[6,7] on drugs binding to their target receptors.[8] This chapter focuses on the specific "nano-ion" effect on proteins, which are the fundamental building blocks of biological systems that are involved in all cellular functions.

The protein surface consists of three layers: (i) the solvation layer, which is immediately adjacent to the protein surface; (ii) the transition layer; and the third layer, designated as the bulk surface.[9] The different hydration levels of the proteins have an impact on the specific ion effect. The addition of chaotropic ions (weakly hydrated ions) to a protein aqueous solution increases protein solubility, which occurs when ions bind to proteins and increase their net charge (the salting-in effect). Whereas the addition of kosmotropic ions (strongly hydrated ions) to a protein aqueous solution decreases protein solubility, which results from interfacial effects of anions (strongly hydrated) close to the surface of proteins (salting-out). [9,10] Ions that are strongly hydrated are in competition with water molecules in the second layer of hydration of a protein, which prevents them to "help out" the first hydration layer in solvating the protein's polar surface. This results in the bulk solution being a less effective solvent, which causes the protein to reduce its surface area that is accessible to the solvent and forms crystal contacts. On the other hand, weakly hydrated ions release the second layer of water molecules, which helps the first hydration layer become more hydrated, resulting in protein unfolding by increasing the solvent-exposed surface area. [9]

Proteins are an interesting model of colloids because they have a wide variety of surfaces chemistry. They can appear negative or positive in a patchy surface distribution but also locally hydrophobic surface groups or even with accessible hydrophobic pockets. However, they cannot be considered as simply hard sphere colloids because they are macromolecular species with a 3D conformation depends on intra-molecular and inter-molecular interactions. H-bond, van de Waals, ionic and hydrophobic interactions, all compete to keep a native cohesion in the formation of secondary (such as alpha helices and beta sheets), super-secondary (domains) and tertiary structures of the protein in global topology that can be more complex and dynamic than a hard sphere.

Proteins, as previously described, have a complex colloidal structure, which makes it challenging to understand the salting-in and salting-out effects on them. Vrbka et al. investigated how certain ions were distributed around two different proteins using molecular dynamic simulation. Despite the proteins being distinct from each other, they found that the distribution of ions around them was remarkably alike.[11] The study of Vrbka et al. is an instance of the complexity of the impact of specific ion effects on proteins.

Recently, specific ion effects with nanometric-sized ions have been studied (the extended Hofmeister series). A demonstration was given by Assaf et al. that characterized the binding strength (or energy) of boron clusters to the hydrophobic pockets of macrocycle molecules such as cyclodextrin at millimolar concentrations.[12–14] This study reinforces our group to classify these nano-ions characterized by a low charge density as superchaotropic within the Hofmeister series via the study of their adsorption onto neutral and hydrated surfaces of self-assembly systems.[15–17]

As already mentioned, nano-ions, and more specifically boron clusters, are able to bind to classic macrocyclic hosts (CDs), but they also have the ability to form host-guest complexes with biomolecules such as proteins, DNA, and polysaccharides.[18–20] The driving force behind these interactions of boron clusters with all aforementioned hosts is the superchaotropic effect or a non-classical hydrophobic effect.[14,21]

Several examples can be found in the literature, without always considering the superchaotropic feature of these nanometer-sized ions. Goszczyński et al. investigated the interaction between serum albumin (SA), a major plasma protein, and different boron clusters such as metallocarboranes, carboranes and dodecaborate anion. It was shown that metallacarboranes have the strongest interaction with albumin among the tested clusters. There was no significant difference between the affinity constants of FESAN and COSAN, showing that the type of metal sandwiched between carbollide ligands does not influence the strength of binding. The fluorescence results show that the presence of boron clusters in the environment of BSA quenches the fluorescence of its tryptophan residues, which are located in hydrophobic pockets. The quenching constant was found on the order of 10^4 to 10^5 mol L^{-1}. On the basis of thermodynamic calculations, it was demonstrated that metallocarboranes have a specific interaction with BSA by binding to its hydrophobic pockets through hydrophobic interactions under low stoichiometry conditions, while under high stoichiometry conditions the interactions are non-specific.[19]

Prior to the study described above, Rak et al. correlated the strength of the interaction with BSA with the lipophilicity of metallacarborane derivatives, suggesting the hydrophobic nature of the interaction. [22] Rak et al. also reported a non-specific interaction of metallacarborane derivatives with HSA for complexes with high stoichiometry.[23]

Goszczyński et al. also investigated the interaction between bovine serum albumin (BSA) and different boron clusters such as COSAN and $[B_{12}H_{12}]^{2-}$ by DLS. The hydrodynamic diameter of BSA was independent of the $[B_{12}H_{12}]^{2-}$ concentration, whereas with COSAN the increase was significant: for a COSAN/BSA molar ratio greater than 10, the hydrodynamic diameter appeared to increase up to 9.5 nm. Then, beyond a threshold ratio, no size evolution was observed. However, it was found that when the molar ratio is over 100, the hydrodynamic dimension starts to grow again, suggesting non-specific interactions with the protein surface.[19]

In addition, enzyme pockets were found to interact with COSAN-based inhibitors of HIV-1 protease and carbonic anhydrase IX. [24,25] HIV protease is a prime target for rational drug design, and protease inhibitors (PI) are highly effective antiviral drug. The majority of the current PIs are pseudopeptide compounds with limited bioavailability and stability, and their use is problematic due to their high costs, side effects, and emergence of resistant strains.[24] Therefore, a class of nonpeptidic PIs is needed. Cigler et al. studied the icosahedral metallocarboranes as potential candidates for a novel class of non-peptidic protease inhibitors. The most active compound was a COSAN derivative, which appears to have an inhibition constant in the nmol range and no toxicity in μmol. The parent compound of COSAN was shown to bind to the hydrophobic pockets that are formed by the side chains of protease residues in a ratio of 2:1.[24] Kožíšek et al. shown that COSAN holds the flaps of HIV protease in a semi-open conformation where two COSAN molecules bind asymmetrically into the symmetrical active site of HIV protease.[26]

Grüner et al. showed that COSAN derivatives substituted at the boron or carbon sites by alkylsulfamide groups are highly specific and selective inhibitors of carbonic anhydrase IX (CAIX). Carbonic anhydrase IX (CAIX) is a transmembrane enzyme that regulates pH in hypoxic tumors and promotes tumor cell survival and its expression has been linked to metastasis and a poor prognosis. The inhibition efficacy and selectivity of COSAN compounds for CAIX originate from their space-filling property, which introduces additional interactions with the enzyme active site. [27] The inhibition efficiency of COSAN compounds is 2-3 orders

of magnitude higher than that of other metallocene-sulfamides [28] and the inhibition (K_i) values (nanomolar to subnanomolar) are several orders of magnitude lower than those for corresponding alkylsulfamidodicarbaboranes. [29]

Fink et al. studied the capability to enhance the activity of therapeutic peptides, specifically thymosin β4 (Tβ4).[30,31] This peptide promotes tissue healing and regeneration through its influence on cell survival, angiogenesis, and inflammation. [32,33] They found that $[B_{12}H_{12}]^{2-}$ and COSAN were successfully conjugated to the peptide thymosin β4. More specifically, Tβ4-COSAN derivatives or Tβ4-$[B_{12}H_{12}]^{2-}$ bind to human serum albumin (HSA) which results in the prolongation of the half-life of Tβ4 in the blood circulation.

Kaniowski et al. investigated the nucleolytic stability of DNA oligonucleotides labeled with FESAN against snake venom phosphodiesterase.[20] They found that snake venom phosphodiesterase (svPDE) can hydrolyze oligonucleotides much faster in the presence of FESAN, either when it is conjugated to oligonucleotides or when FESAN is free in solution.[20,33]

COSAN and its derivatives, such as I_2COSAN can pass through synthetic lipid membranes and those of living cells without causing breakdown of membrane barrier properties.[34,35] Membranes establish the boundary between the living cells and the external environment and form barriers between internal cell compartments and organelles. Tarrés et al. show that COSAN induces a variety of biological effects, including altered cell morphology, inhibition of cell growth, and, in some instances, apoptosis. It emerged that COSAN has no immediate effect on cell viability (not the cases where apoptosis occurs) and those cells entirely recovered after being exposed to it for a few hours to several days if COSAN was washed out. No immediate effect on cell viability means that after rinsing out COSAN, some cells recovered and began to grow and proliferate normally. It was also found that in all the cases described above, the effect of I_2COSAN was stronger than that of COSAN. [34]

Later, Fuentes et al. found that COSAN, which displays high uptake by cancer cells, accumulates mainly in membranes and the nucleus with no cytotoxicity even after long incubation times. Due to this property, COSAN could act as a suitable compound for further development as a boron neutron capture therapy (BNCT) agent that requires the accumulation of boron near or in the nucleus to increase its efficiency.[18]

Recently, Barba-Bon et al. demonstrated that globular dodecaborate clusters, and prominently $[B_{12}Br_{12}]^{2-}$, can function as anionic inorganic membrane carriers for a broad range of

hydrophilic cargo molecules. It was found that $[B_{12}Br_{12}]^{2-}$ is able to translocate many types of cargo molecules that are positively charged, zwitterionic, or completely lack charge. The size of the molecules that $[B_{12}Br_{12}]^{2-}$ can translocate is very broad and spans from very small molecules, such as acetylcholine (146 Da), to larger polypeptides, such as protamine (4500 Da). The presence of $[B_{12}Br_{12}]^{2-}$ increased, in vitro, the membrane permeability of the antineoplastic drug monomethyl auristatin F (MMAF), as the viability of HeLa cells was significantly reduced in its presence. Additionally, it was demonstrated that $[B_{12}Br_{12}]^{2-}$ has potential antibacterial activity against the Escherichia coli Top10 strain. [36]

To conclude, boron clusters form complexes with a wide variety of hosts, from classic macrocycles to biomolecules, as described in these cited studies. As a result, boron clusters are extremely versatile building blocks, as they can connect to other commonly used building blocks. Boron clusters were also used to modify the biological activity of other molecules by conjugating them with their physiochemical properties.[33]

The nanometric-sized boron clusters have attracted attention for their potential applications in biological systems. Proteins, as mentioned above, are one of the main constituents in biological systems and effectors that participate in every process within the cells. The study of the effect of the boron cluster with proteins, molecules with a wide range of physical and chemical features, and the understanding of their mechanism piqued our interest, and it is the topic that will be investigated in this chapter.

III.1 Proteins under investigation

The investigations in this chapter were based on the final chapter of Merhi's thesis, "Interactions of COSAN Anions with Proteins." The study was based on a strategy related to the hypothesis that when COSAN interacts with a protein, the protein's overall charge must be altered. This change in the overall charge induces changes in the isoelectric point of the protein, which can be observed by isoelectric focusing electrophoresis (IEF), a method in which proteins migrate with an electric field in a pH gradient gel. This hypothesis was confirmed by studying the interaction of NaCOSAN with the proteome of Hela cells. Results from isoelectric focusing electrophoresis migration of proteomes pre-incubated with or without NaCOSAN, followed by a mass spectrometry analysis of selected bands, confirmed that some proteins change their pI in the presence of NaCOSAN. The electrophoresis gel revealed some trends, with some proteins precipitating at the beginning of the well, others having little impact, and others still showing a shift in pI of 2 or even 3 pH units. To simplify the above-described investigation, the same strategy was applied to a mixture of nine standard proteins (Table 3.1), which also allowed for the study of the impact of COSAN on these proteins.

Table 3.1: Proteins of the isoelectric focusing (IEF) marker 3-10, SERVA Liquid Mix.

Protein Components	**pl**
Cytochrome C (porcine, heart)	10.7
Ribonuclease A (bovine, pancreas)	9.5
Lectin (lens culinaris)	8.3, 8.0, 7.8
Myoglobin (horse, muscle)	7.4, 6.9
Carbonic anhydrase (bovine erythrocytes)	6.0
β-Lactoglobulin (bovine, milk)	5.3, 5.2
Trypsin inhibitor (soybean)	4.5
Glucose oxidase (Aspergillus niger)	4.2
Amyloglucosidase (Aspergillus niger)	3.5

The effect of interactions of proteins with boron clusters were investigated in this chapter. Isoelectric focusing (IEF) was used to investigate the charge modifications of each of these

proteins (Table 3.1) upon interaction with NaCOSAN. Isoelectric focusing is a technique used to separate proteins based on their isoelectric point (pI). The pI is the pH at which the net charge of the protein is zero. At this point, the protein has equal numbers of positively charged and negatively charged groups. In IEF, a protein sample, in this case the mixture of nine standard proteins, is loaded into the pre-casted gel with a pH gradient from 10 to 3, inducing modulations of the protein's global charge and enabling protein migration. The global charge of the protein comes from the sum of the positive and negative charges at a given pH.

An electric field is applied across the gel, which leads the proteins to migrate from the cathode (negative) to the anode (positive). As the proteins migrate along the pH gradient gel, they become concentrated at the pH value that corresponds to their pI (neutral global charge). Figure 3.1 demonstrates the gel of the isoelectric focusing marker, which consists of nine native proteins in the pI range of 3.5 to 10.7 (13 isoforms).

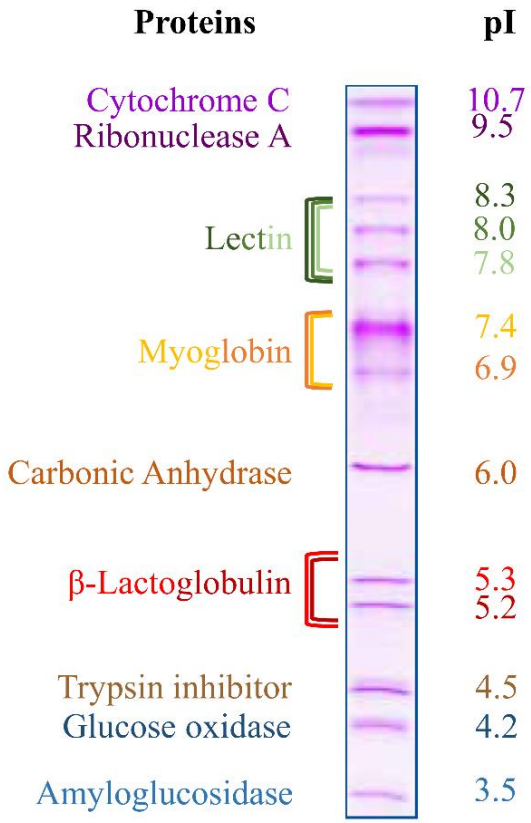

Figure 3.1. *IEF marker 3-10, SERVA Liquid Mix.*

Proteins that migrate to their pI in the gel should migrate to a new isoelectric point as a result of their binding with NaCOSAN, which modifies their global charge. Thus, if the interaction

is an ion adsorption onto the protein rather than merely a screening effect, we expect that the negative charge of proteins increases with the number of interacting NaCOSAN molecules, leading to a longer migration as compared to the migration of the protein that does not bind NaCOSAN. Gel migration in the presence of NaCOSAN enables the identification of the proteins that interact most with NaCOSAN. The gel migration of the standard protein in the presence of NaCOSAN (4 mmol L^{-1}) is shown in Figure 3.2. We can observe that a dark band appeared at the top of the gel in the well indicating that precipitation of some proteins occurred in the presence of NaCOSAN, probably preventing the migration. Myoglobin and carbonic anhydrase bands changed their position in the presence of NaCOSAN. According to mass spectrometry, the band that appeared in the middle of the gel consists mainly of myoglobin and carbonic anhydrase, both of which have a pI of approximately 6.5. Therefore, myoglobin and carbonic anhydrase are strongly affected by the presence of COSAN. Mass spectroscopy also indicated that the coagulated protein in the well is mostly composed of myoglobin. The presence of NaCOSAN on the trypsin inhibitor appears to have a slight impact on its migration around pH=4. In this chapter, the interaction of NaCOSAN with these three proteins—myoglobin (Mb), carbonic anhydrase (BCA), and trypsin inhibitor (SKTI)—was investigated in greater detail. Apart from the interaction with the NaCOSAN monitored by IEF, these three proteins were also selected due to their different features, i.e., three-dimensional structure, composition, etc. Some general feature on these three proteins are given in Table 3.2.

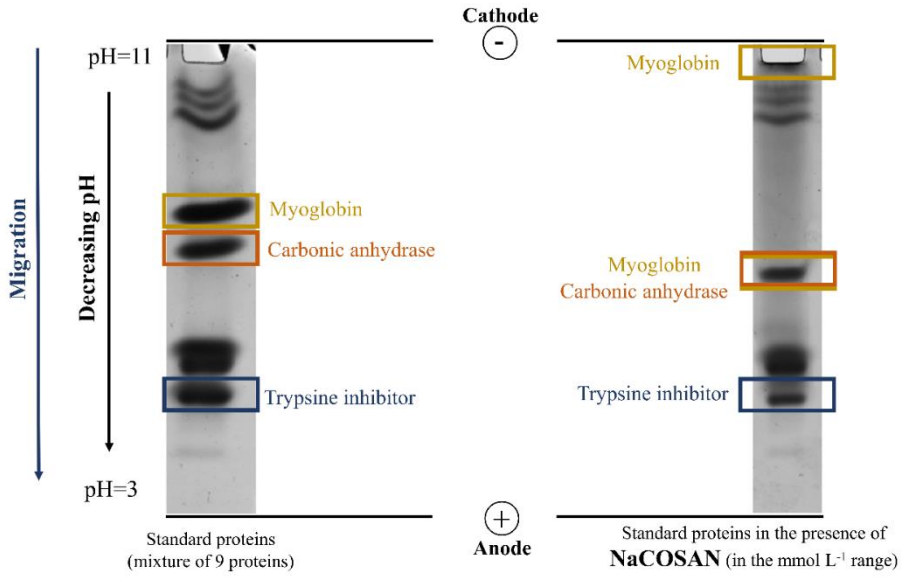

***Figure 3.2**. Mixture of nine standard proteins of isoelectric focusing marker (left) and mixture of nine standard proteins in the presence of 4 mmol L^{-1} NaCOSAN (right).The identification of the proteins on the gel bands is made by mass spectrometry.*

Table 3.2: Features of proteins under investigation.

Proteins	Myoglobin (from equine skeletal muscles)	Carbonic anhydrase (from bovine)	Trypsin inhibitor (from soybean)
Structure		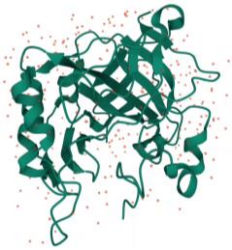	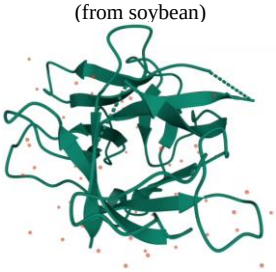
Molecular weight	17400 g mol^{-1}	30000 g mol^{-1}	21500 g mol^{-1}
Length	154 amino acids	260 amino acids	181 amino acids
Isoelectric point	7.4	6.0	4.5
Alpha helix	72%	7.4%	-
Beta strand	-	27%	39%

Amino acids are the chemical building blocks that form the residues that make up proteins. Each amino acid has the same fundamental structure, which consists of a central carbon atom, also known as the alpha (α) carbon, bonded to an amino group (NH_2), a carboxyl group (COOH), and a hydrogen atom. In the aqueous environment, the amino group and the carboxyl group are ionized under physiological conditions, as are the structures $-NH_3^+$ and $-COO^-$, respectively. Every amino acid also has another atom or group of atoms bonded to the central atom, known as the R group.

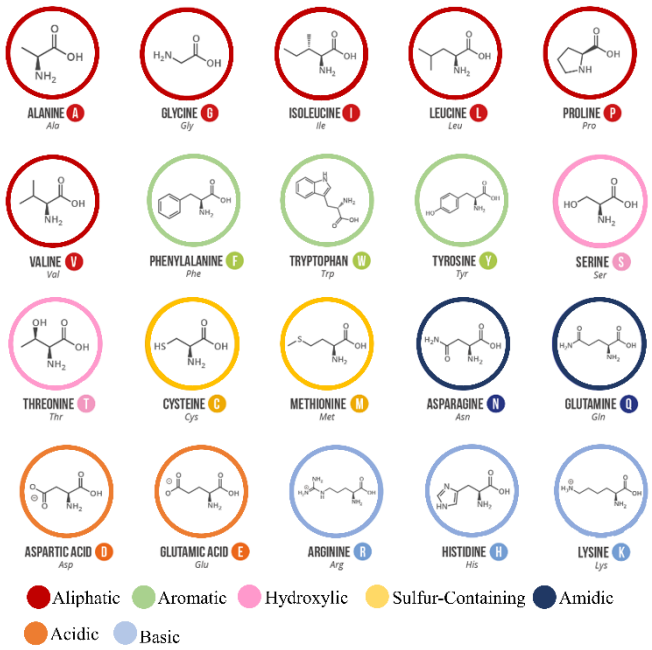

Figure 3.3. *The 20 types of amino acids. The figure was modified from Explorations of everyday chemical compounds Ci.[68]*

This R group, or side chain, gives each amino acid protein specific characteristics, including size, polarity, and pH. The 20 types of amino acids are listed in Figure 3.3.

Among the 20 amino acids, Arginine, Histidine, Tyrosine, Cysteine, Lysine (N-terminal), Aspartic Acid (C-terminal), and Glutamic Acid (C-terminal) have a side chain that can be charged (see Figure 3.4). The three basic amino acids, arginine, lysine, and histidine, are positive when the pH is below their pKa whereas the two acidic amino acids, aspartate and glutamate, are negative above their pKa. The pKa is the pH at which a molecule's ionized and unionized forms of a functional group are present in equal amounts. When pH is varied above or below the pKa, the concentrations of the ionized and unionized forms will also shift, favoring one form over the other.

Figure 3.4 shows the unionized and ionized states of various R-groups and their preferred states, depending on whether the pH is above or below their respective pKa values.

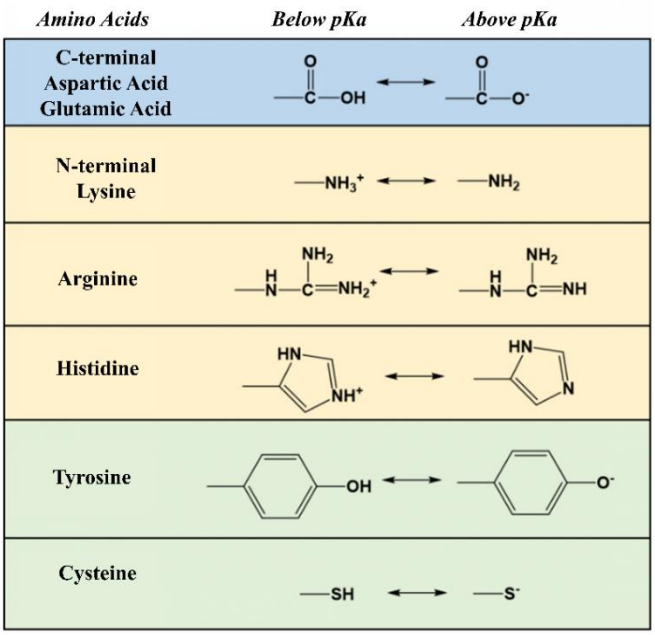

Figure 3.4. *Ionizable Functional Groups in Common Amino Acids. The functional group's favored states are shown either above or below their respective pK$_a$ values. The figure was modified from [69].*

Our objective was to investigate how NaCOSAN binds to proteins with a focus on the superchaotropic effect, so we attempted to minimize the electrostatic attractions between COSAN (which has a negative charge) and the positively charged residues. To accomplish this, we conducted our experiments under alkaline conditions with a pH of 10 at which the lysine are the only amino acid charged positively. We use myoglobin as an example to show how we estimated the charged residues of proteins at pH 10. The number of amino acid residues in

myoglobin is provided in Table 3.3, and the charges of myoglobin residues charged at pH = 10 are listed in Table 3.4.

Table 3.3: Number of amino acid residues of myoglobin.

Myoglobin (from equine skeletal muscles)	**pI=7.47**	**Tridimensional structure of Myoglobin and amino acid features**
Residue	Number	
Alanine	18	
Arginine	2	
Asparagine	4	
Aspartate	8	
Glutamine	4	
Glutamate	13	
Glycine	13	
Histidine	13	
Isoleucine	6	
Leucine	17	
Lysine	18	
Methionine	4	
Phenylalanine	7	
Proline	3	
Serine	6	
Threonine	5	
Tyrosine	2	
Valine	9	
Tryptophan	2	
Cysteine	0	

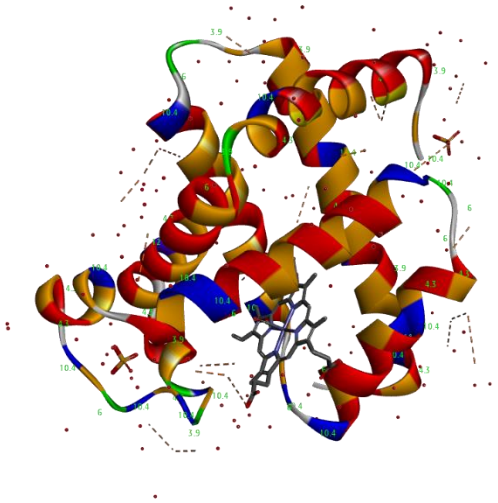

Table 3.4: Charges of residue in myoglobin expected in buffer at pH=7 and pH=10. $N_{residue}$ is the number of residues in myoglobin.

Residue	$N_{residue}$	a-COOH	a-NH_2	RH^+	Charge at pH=7	Charge at pH=10
Aspartic Acid	8	2.1	9.8	3.9	-8	-8
Glutamic Acid	13	2.2	9.7	4.3	-13	-13
Lysine	18	2.2	9.0	10.5	+18	No charge
Arginine	2	2.2	9.0	12.5	+2	+2
Histidine	13	1.8	9.2	6.0	No charge	No charge
Tyrosine	2	2.2	9.1	10.1	No charge	-2
Cysteine	0	1.7	10.8	8.3	-	-
Total					-1	-21

Using the same procedure, the total charges of BCA and SKTI were calculated (Table S3.2) using the composition in residues of each protein listed in Table S3.1.

In the next step, we studied the interaction of the three selected proteins individually with NaCOSAN by IEF. In order to carry out the experiment, the concentration of the three proteins in the mixture of the nine standard proteins was calculated through the abundance of each protein. The relative abundance of each protein in the marker is assessed by mass spectrometry through the number of spectral counts (Table 3.5). The concentrations were calculated by taking into account both the furnisher concentration and the relative abundance assessed by mass spectrometry.

Table 3.5: The results of mass spectrometry on selected proteins from the mixture.

Total Spectral Counts of Marker	Spectral Count of Myoglobin	Spectral Count of Carbonic Anhydrase	Spectral Count of Trypsin inhibitor
9437	2749	1061	237
	29.13%	11.24%	2.5%

The concentrations were obtained 0.17, 0.04 and 0.01 mmol L^{-1} for myoglobin, carbonic anhydrase and trypsin inhibitor, respectively. Then, we attempted to establish our working conditions according to these values, varying the NaCOSAN/protein ratio from 0 to 100. Figures S1-3 in the supporting part of this chapter show the impact of various NaCOSAN/protein ratios on individual protein migration within the gel and along the pH gradient.

Zeta potential measurements were carried out in order to investigate the evolution of the surface of proteins potential upon addition of NaCOSAN (see Figure 3.5). The zeta potential of the three proteins in the absence of NaCOSAN at pH = 10 ranges between -15 and -10 mV. The three proteins are then, as expected from the pka values and composition (Table 3.4), globally negatively charged. By increasing NaCOSAN concentration in the protein solutions, a more negative zeta potential was determined (see Figure 3.5), which certainly reflects an adsorption of the NaCOSAN onto the proteins. The increased zeta potential is pronounced for Mb and BCA and is moderated for SKTI, where it is only observed for the highest NaCOSAN/SKTI ratio. This evolution is fully in line with the results obtained from the IEF measurement (Figure 3.2).

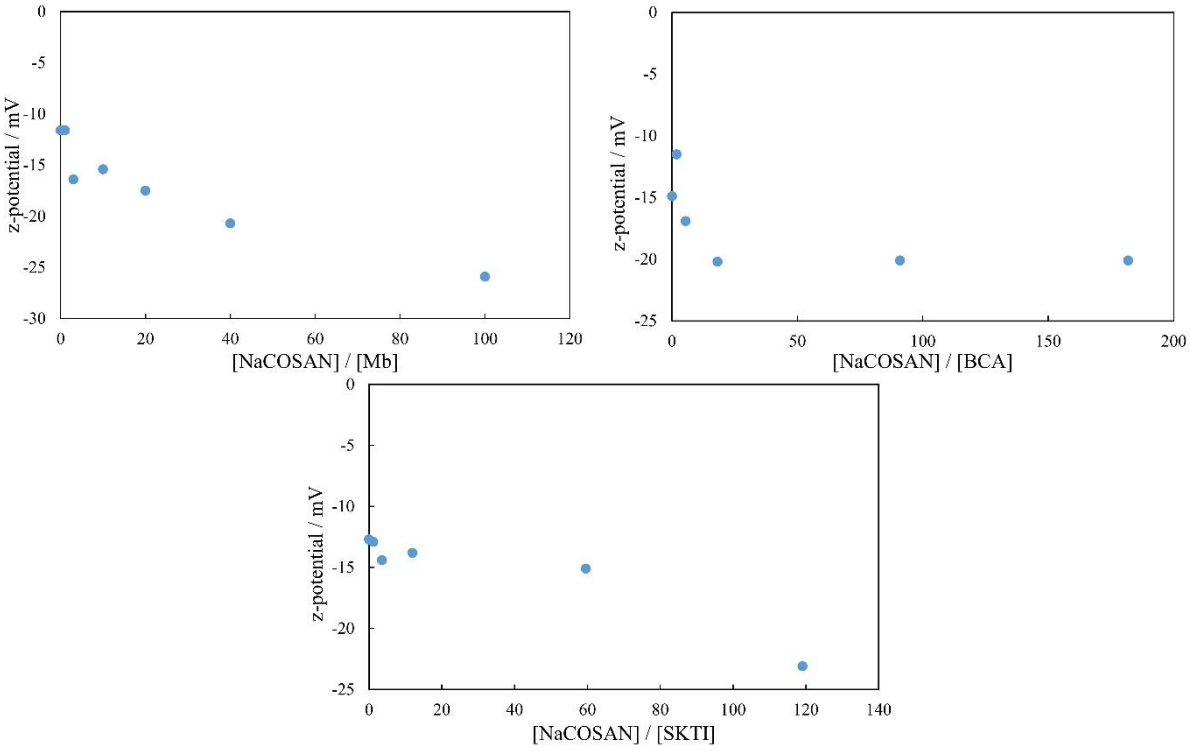

***Figure 3.5**. zeta-potential of (A) 0.01 mmol L^{-1} Mb, (B) 0.0055 mmol L^{-1} and (C) 0.0084 mmol L^{-1} in the presence of different NaCOSAN concentrations in PBS at pH=10.*

In the previous chapter, we demonstrated how interesting it was to use various techniques probing the molecular and supramolecular scales in order to investigate the interactions of boron clusters with hydrophobic compounds. Here, we use a similar procedure using complementary techniques, combining a set of spectroscopic and scattering techniques, in order to understand how NaCOSAN interacts with the proteins, which are more complex than hydrophobic compounds, and what the impact is on possible protein denaturation as expected with superchaotropic anions. UV-Vis and circular dichroism were used to obtain information on the local environment of nano-ions as well as the protein secondary structure, folding, and interactions. Circular dichroism is especially suitable to follow the denaturation process. Dynamic light scattering (DLS) and static small-angle X-ray (SAXS), and neutron (SANS) scattering techniques were used to obtain information on protein 3D conformation and potential aggregation (if charge screening effects are detectable). A brief description of the sections following is given below.

Initially, we studied the interactions of NaCOSAN with myoglobin (Mb) in subchapter III.2, and then we studied the interactions of two other proteins, carbonic anhydrase and trypsin inhibitor, with NaCOSAN in subchapter III.3. Subsequently, a comparative analysis was

performed to evaluate the “super”chaotropic effects of NaCOSAN versus more classical chaotropic salts (subchapter II.4.1), versus other superchaotropic ions (subchapter III.4.2), and versus classical surfactants (III.4.3) on these three selected proteins. Finally, we present (in subchapter III.5) results at a pH close to 7 that are more reliable for biological investigations.

In the following section, we examined the interactions of NaCOSAN with myoglobin (Mb), which is a monomeric (only one polypeptidic chain) protein that traps the oxygen storage heme molecule and is a fundamental model protein extensively used in molecular design. Horse Mb consists of 153 amino acids with eight α-helices and seven non-helical segments. The heme, which is a porphyrin cycle within which is coordinated an atom of Fe II or III in its center, is embedded in the polypeptidic chain (within an hydrophobic pocket) and coordinated by Histidine (His93 and His64) via a hydrogen bond with the bound dioxygen, which is itself coordinated to the iron atom (see Figure 3.6).

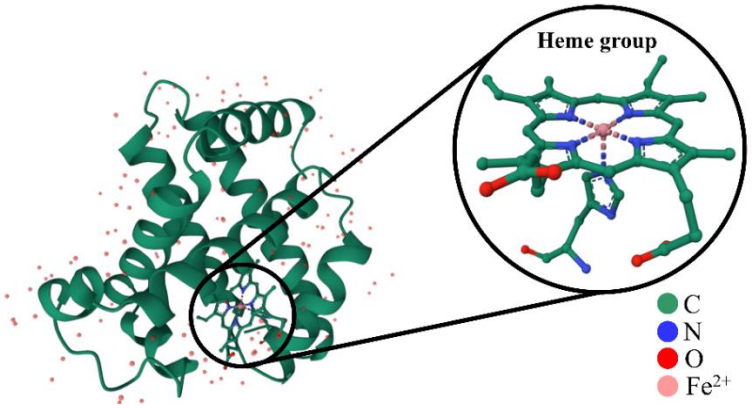

***Figure 3.6**. Heme group of Mb.*

III.2 NaCOSAN in interaction with myoglobin (Mb)

III.2.1 Interaction between NaCOSAN and Mb followed by UV-Vis

The absorption spectra of native Mb in phosphate-buffered saline (PBS) at pH=7.4 contain two strong bands in the ultraviolet region and several weaker bands in the visible region. [37] The peak in the Mb absorbance spectrum centered at 280 nm is linked to the presence of the aromatic residues, tryptophan and tyrosine, as well as the presence of the heme. The peak centered at 410 nm is entirely due to the heme and corresponds to the Soret band. This narrow, intense band is characteristic of all hemoproteins and is commonly referred to as the Soret band. This adsorption in the UV-vis spectrum originates from an electronic dipole movement

that allows a π-π* transition, common in porphyrins.[38] The UV-Vis spectra of Mb in the absence and in the presence of NaCOSAN were recorded from 200 to 800nm. The peak of Mb, centered at 280 nm, is overlapped by the intense peak of NaCOSAN.

Thus, the UV-vis spectra were presented from 300 to 800 nm. Figure 3.7 shows the absorbance spectra as a function of Mb at 0.01 mmol L^{-1} for different NaCOSAN/Mb ratios from 0 up to 16 in PBS at pH = 10. NaCOSAN has a second peak at 450 nm, which is much less intense than the peak at 280 nm. In order to eliminate the signal contribution of NaCOSAN from the different spectra, a subtraction of the NaCOSAN contribution in solution at an equivalent concentration was applied (Figure 3.7). The unsubtracted raw data were presented in the supporting information for this chapter (Figure S3.4). It is then clear that the intensity of the Soret band is decreased upon the addition of NaCOSAN, whereas an increase is observed around 280, 360 and between 500 and 700 nm.

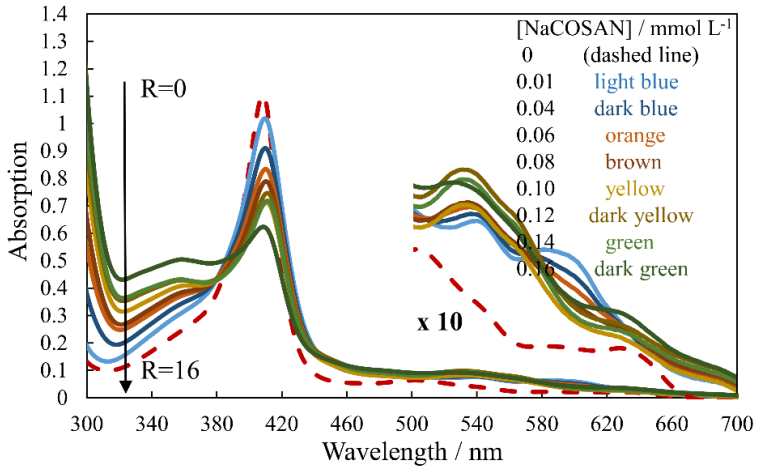

Figure 3.7. *(a) Subtracted UV-Vis spectra of 0.01 mmol L^{-1} Mb in PBS at pH=10 in the presence of different NaCOSAN concentrations (Ratio: [NaCOSAN]/[Mb]=0-16).*

The absorption spectra are typical of metmyoglobin, which differs from oxymyoglobin and deoxymyoglobin by the disappearance of the absorption band at 575 nm. The state of the iron determines the three types of myoglobin. For metmyoglobin, the iron is in the ferric state (Fe^{3+}), and for oxymyoglobin and deoxymyoglobin, it is in the ferrous state (Fe^{2+}). After NaCOSAN interaction, the decrease in Soret band absorption is clearly observed with the increase in NaCOSAN concentration. A new absorption band appears with a maximum around 360 nm, which is known to be related to the disruption of the heme iron-proximal histidine bond after unfolding of deoxymyoglobin.[39] We observed an effect on the evolution of the spectra in the Q region between the wavelengths of 500 and 750 nm.[40]

In Q region, the UV visible spectra of the myoglobin alone indicates that the state of the iron in the heme is ferric according to the bands at 504, 535, and 634 nm. The interaction with NaCOSAN induces the appearance and disappearance of the Q-band region, which indicates that the charge localization of the porphyrin as well as the heme coordination state change with the NaCOSAN concentration. This analysis is consistent with the aforementioned decrease in Soret band intensity and suggests that NaCOSAN interacts with the heme group or in its surrounding environment. This could be due to either (i) the electrostatic nature of the interaction between the NaCOSAN anion and the positive iron complex, or (ii) to the NaCOSAN interacting with the periphery of the hydrophobic pocket in which is embedded the heme as the COSAN interacts with the internal part of the sugar cycle of the cyclodextrin.[12] To determine whether NaCOSAN interacts specifically with the heme group or not, we studied hemin, which is the heme group only without the peptidic sequence of Mb, under similar physical-chemical conditions.

III.2.2 Interaction of NaCOSAN/Hemin followed by UV-Vis

As already mentioned, heme is essential for binding oxygen in the blood, while in the hemin, the iron cation interacts with chlorine. Figure 3.8 shows the absorption spectra of Hemin in the absence (dark) and in the presence of NaCOSAN in PBS at pH = 10.

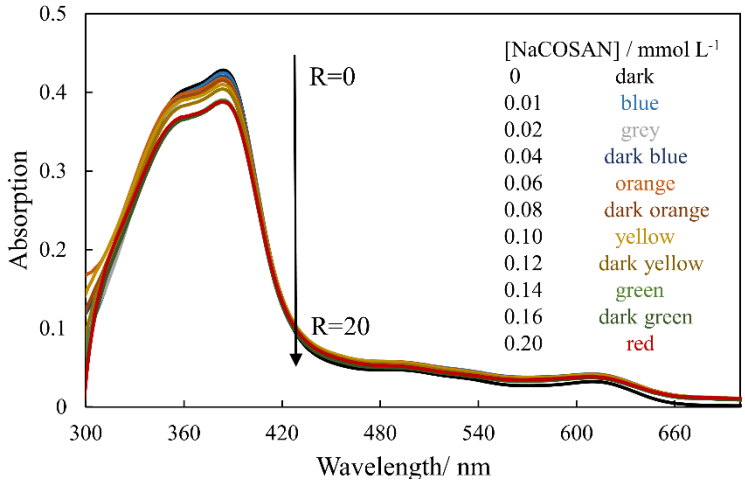

Figure 3.8. *UV-Vis spectra of 0.01 mmol L^{-1} Hemin in the presence of different NaCOSAN concentrations (Ratio: [NaCOSAN]/[Hemin]=0-20).*

Hemin showed a decrease in the absorption of the Soret band by increasing the NaCOSAN concentration, which was significantly less pronounced than that of Mb. Figure 3.9 presents the evolution of the Soret band intensity variation of the heme in Mb and of the hemin as a function of NaCOSAN concentrations. It shows clearly that the evolution of the Soret band is

nearly unaffected for the Hemin compared to the Mb. We can conclude here that the interactions between heme and NaCOSAN require the presence of the hydrophobic environment within the Mb. NaCOSAN appears to have a preferential interaction with heme when it is in the hydrophobic pocket of Mb. This suggests that hemin is maybe too "hydrophilic" to interact with NaCOSAN.

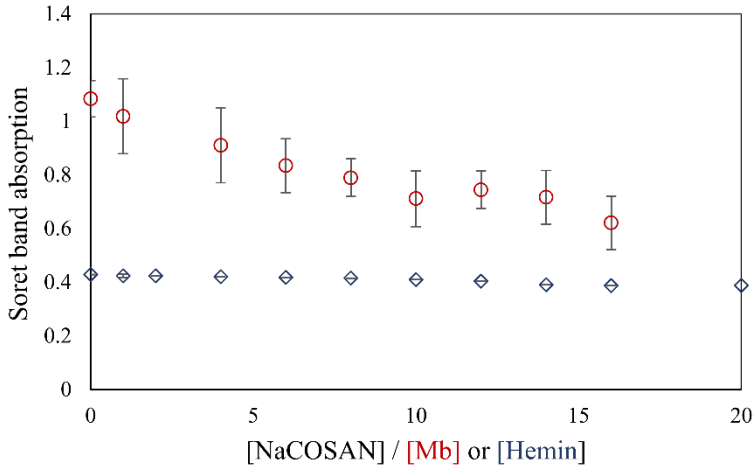

Figure 3.9. *The evolution of heme absorption in Mb at 410 nm and 'in' Hemin at 395 nm as a function of NaCOSAN concentration, expressed here as [NaCOSAN]/[protein].*

III.2.3 Interaction of NaCOSAN/Mb followed by fluorescence technique.

Fluorescence was used to obtain structural information about the interaction of NaCOSAN with Mb. The fluorescence of Mb comes from tryptophan (Trp), tyrosine (Tyr) and phenylalanine (Phe) residues. The aromatic residues are sensitive fluorescent probes for studying conformational transitions.[41]

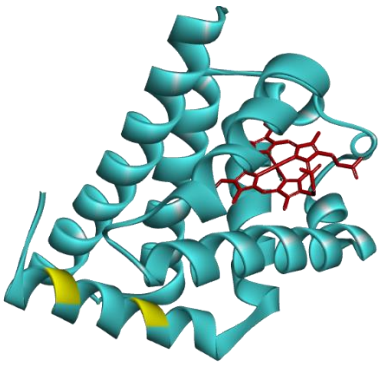

Figure 3.10*. 3D structure of Mb, where the tryptophan residues are highlighted.*

The Trp residue has the strongest fluorescence intensity and is the most sensitive to changes in the microenvironment of the protein. Two tryptophan residues are present in the sequence of

Mb and are located at positions 7 and 14 (Figure 3.10). These Trp residues are present on the alpha-helix of Mb near the N-terminus of the protein, with the distances from the heme cofactor being ~21 and ~15 Å for Trp 7 and Trp 14, respectively.[42]

In these steady-state fluorescence experiments, the concentration of Mb was kept constant at 0.01 mmol L^{-1}, while the concentration of NaCOSAN was increased stepwise from 0 to 0.4 mmol L^{-1}, i.e., COSAN/Mb ratios ranging from 0 up to 40 (Figure 3.10). The fluorescence spectra of 0.01 mmol L^{-1} Mb (tryptophan) in the absence and presence of NaCOSAN are plotted in Figure 3.11A. Similar to the Soret band, an increase in NaCOSAN concentration results in a significant decrease in fluorescence intensity. A slight shift to higher wavelengths was also observed above ratio 5. The quenching of the fluorescence intensity due to the presence of NaCOSAN could result from either a direct or indirect interaction with the tryptophan.

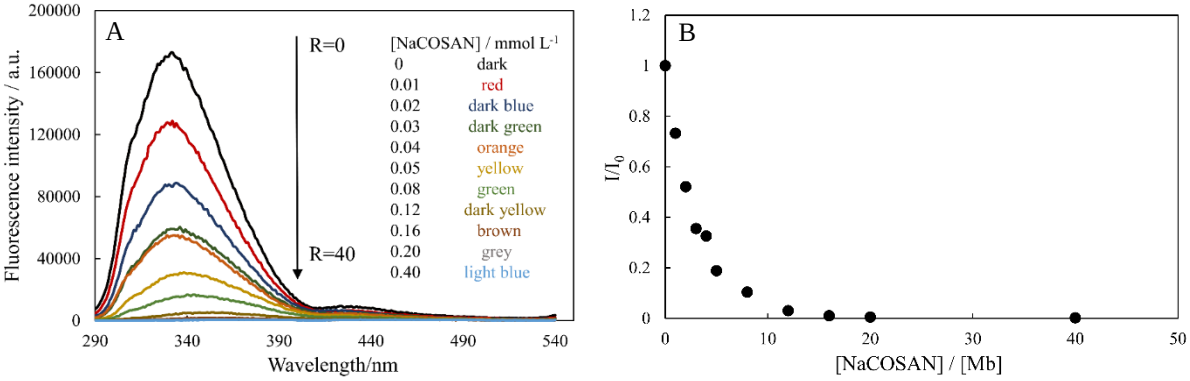

Figure 3.11. *(A) Emission fluorescence spectra of Myoglobin (Tryptophan) in the absence (dark) and in the presence of NaCOSAN ([Mb]=0.01 mmol L^{-1}). The excitation wavelength of the spectra was 275 nm and the band pass was 5 nm. From top to bottom, the concentration of NaCOSAN increased stepwise from 0 to 0.4 mmol L^{-1}. (B)Normalized fluorescence intensity as a function of [NaCOSAN]/[Mb] ratio.*

If we postulate a direct interaction, the intensity decrease can be described by a binding constant with a given stoichiometry. The principle of binding constant in fluorescence refers to the relationship between the concentration of a fluorescent molecule and the strength of the binding between this molecule and its binding partner. The binding constant can be calculated from the decrease in fluorescence intensity along with the concentration of NaCOSAN (the quencher) between the fluorescent molecule (Mb) and its binding partner (NaCOSAN) using the following Stern-Volmer equation[19]:

$$log\frac{(I_0 - I)}{I} = \log K_q + n\log[Q] \quad (1)$$

where I_0 is the fluorescence intensity of the protein before the addition of the quencher, I the fluorescence in the presence of the quencher and [Q] the concentration of the quencher. The

main advantage of using Eq. 1 is the possibility of extracting the quenching constant Kq and the number of bound molecules (stoichiometry) n to Mb. Figure 3.12 shows the Stern-Volmer plot, from which n, the number of NaCOSAN molecules bound to Mb, was estimated to be approximately around 2, and the quenching constant, *Kq*, was found to be 5.6 x 10^6 mol L^{-1}. The Mb quenching constant found in the presence of NaCOSAN is of the same order as that described in the literature.[20,43]

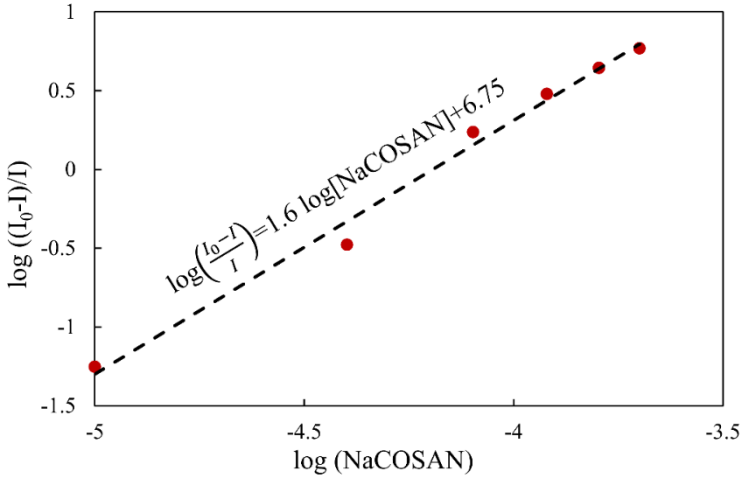

***Figure 3.12**. The plot of the derived Stern-Volmer equation is given with (R^2=0.98). From the plot, n and Kq were calculated to be 1.6 and 5.6 x 10^6 mol L^{-1}, respectively.*

The distribution of interparticle distances and scattering phenomena play an important role in the fluorescence quenching resulting from electron transfer and Förster resonance energy transfer (FRET).[44] Stoica et al. have already established that COSAN interacts with tryptophan from BSA through the unconventional di-hydrogen bonds.[45] This kind of interaction could induce the quenching effect of the tryptophan fluorescence. However, the Stern-Volmer plot in Figure 3.12 is linear, indicating that there is no quenching effect saturation even at the higher NaCOSAN concentration. A second hypothesis, according to which the decrease in fluorescence could be due to a protein unfolding process, is therefore conceivable and could be proportional to the number of NaCOSAN molecules inducing the progressive unfolding of the protein. This hypothesis is consistent with the decrease of the Soret band absorption observed in UV-VIS spectroscopy at 410 nm (Figure 3.7) which was found to be proportional to the NaCOSAN concentration.

III.2.4 Interaction of NaCOSAN/ApoMb followed by fluorescence

As described in the previous section, NaCOSAN interacts with myoglobin, altering both the heme and tryptophan's chemical environment. Moreover, it was found that NaCOSAN binds

with Mb through its heme and that the heme (Hemin) alone does not bind with NaCOSAN. So we conclude that the hydrophobic environment (hydrophobic pocket) where the heme is inserted in the Mb 3D structure is necessary for the NaCOSAN to bind to the heme. In the next step, we investigate the interaction of NaCOSAN with apomyoglobin (ApoMb), which is Mb (an alpha-helix globular protein) lacking the heme.

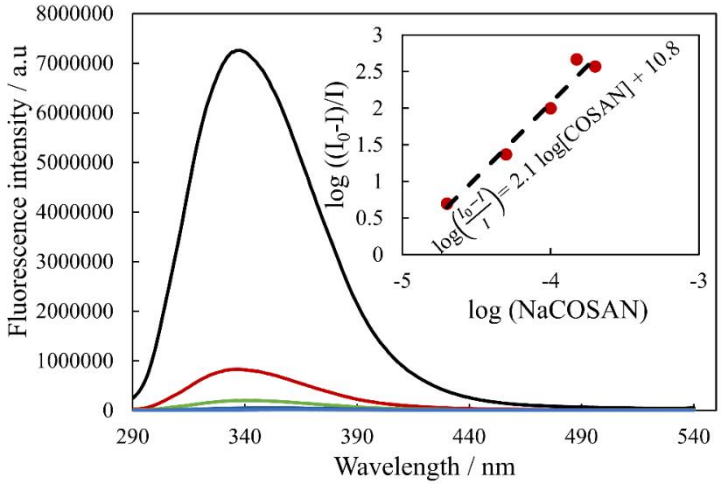

Figure 3.13. *Emission fluorescence spectra of ApoMb in the absence and in the presence of NaCOSAN ([ApoMb] = 0.01 mmol L^{-1}). From top to the bottom, the concentration of NaCOSAN increased stepwise from 0 to 0.2 mM. The excitation wavelength of the spectra was 275 nm and the band pass was 5 nm. In the inset, the plot of the derived Stern-Volmer equation is given with (R^2=0.96). From the plot, n and Kq were calculated to be 2 and 6.3 x 10^{10} $mmol^{-1}$ L^{-1}, respectively.*

Figure 3.13 depicts the fluorescence spectra of ApoMb as a function of NaCOSAN concentration. It is important to recall that, as Mb, apomyoglobin contains two tryptophan residues. The quenching of fluorescence quenching is also observed. A similar analysis using the Stern-Volmer equation revealed that the number of NaCOSAN molecules bound to ApoMb is approximately 2, and the quenching constant is equal to 6.3 x 10^{10} mol L^{-1}. The binding constant of ApoMb is much higher than that of Mb. This may be due to the lack of heme in ApoMb, which makes the protein more flexible and might make the tryptophan residues more exposed to the solution. The hydrophobic pocket of ApoMb is a highly favorable (hydrophobic) environment for COSAN binding, similar to what was previously observed with HIV protease, where it was demonstrated that COSAN binds to the hydrophobic pocket.

III.2.5 Interaction of NaCOSAN/Mb followed by circular dichroism (CD)

Circular Dichroism (CD) spectroscopy is a powerful tool for studying the secondary structure of proteins and other chiral biomolecules. Proteins adopt specific conformations or secondary

structures, including α-helices, β-sheets, and random coils, which can be identified and quantified using CD spectroscopy.

CD data are reported through an ellipticity (θ) parameter, in mdeg. The relationship between the ellipticity (θ) and the absorbance (A) in CD spectroscopy is given by the following equation:

$$\theta = A / (c \ l \ f)$$

where c is the concentration of the sample in g/mL, l is the path length of the cuvette in cm, and f is the factor that relates the number of photons to the amount of light absorbed by the sample. The factor f is a constant and equal to 32.98.

Circular dichroism (CD) spectra of Mb exhibit two significant negative and broad bands in the ultraviolet region at 209 and 222 nm, which are characteristic for α-helical structure of proteins. Figure 3.14 shows that the increase of NaCOSAN concentration leads to a slight decrease in the CD signal of Mb from -65 to -50 mdeg approximately. Above the ratio [NaCOSAN]/[Mb] = 20, a saturation effect was observed (Figure 3.14B).

As a point of comparison, in Figure S3.6, the myoglobin CD evolution by increasing temperature is plotted and shows the signature of a significant decrease in secondary structure content (the disappearance of the two negative bands). Indeed, the CD signal of the denaturated form of Mb at 90 °C varied from -27 mdeg (208 nm) to -20 mdeg (222 nm), indicating that the presence of NaCOSAN did not significantly alter the tertiary structure of Mb at room temperature, with the CD signal remaining stabilized at -50 mdeg.

K2D3 software is a tool for analyzing the CD spectrum of a protein and predicting the percentages of alpha helix and beta strand content. In K2D3 analysis, the input CD values can be expressed either in differential absorption units (Δε) or in mean residue ellipticity units [Θ] and over any wavelength range in the interval 190–240 nm.[46] Figure 3.15 shows two examples with experimental data as input (dark line) and the predicted (red dashed line), which were used to calculate the percentage of the a-helix of Mb in the presence of NaCOSAN (Figure 3.16).

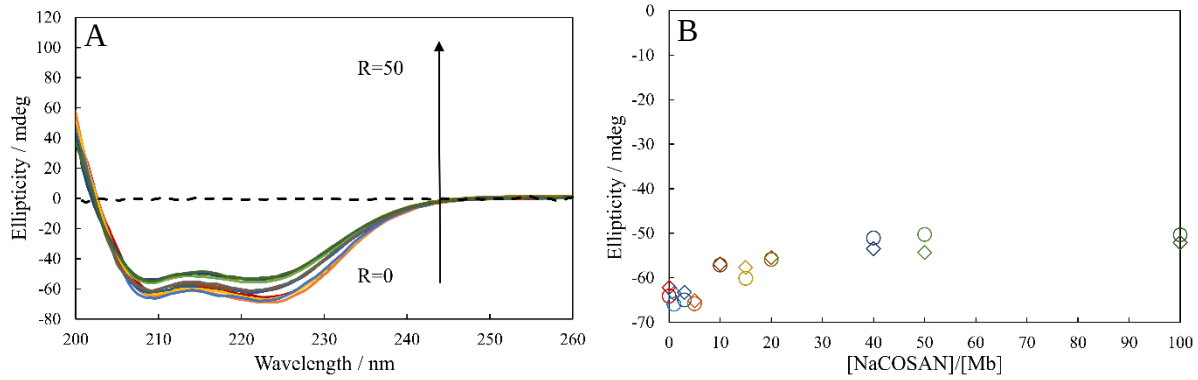

***Figure 3.14**. (A) Far-UV CD spectrum of Mb in the absence and presence of NaCOSAN at pH=10 and 298 K. The dark dashed line corresponds to 1 mmol L^{-1} NaCOSAN in PBS at pH=10. (B) NaCOSAN-induced partial unfolding of Mb in PBS at 25 °C. The unfolding transition curve monitored by the CD ellipticity at 208 (triangles) and 222 (circles) nm as a function of [NaCOSAN]/[Mb].*

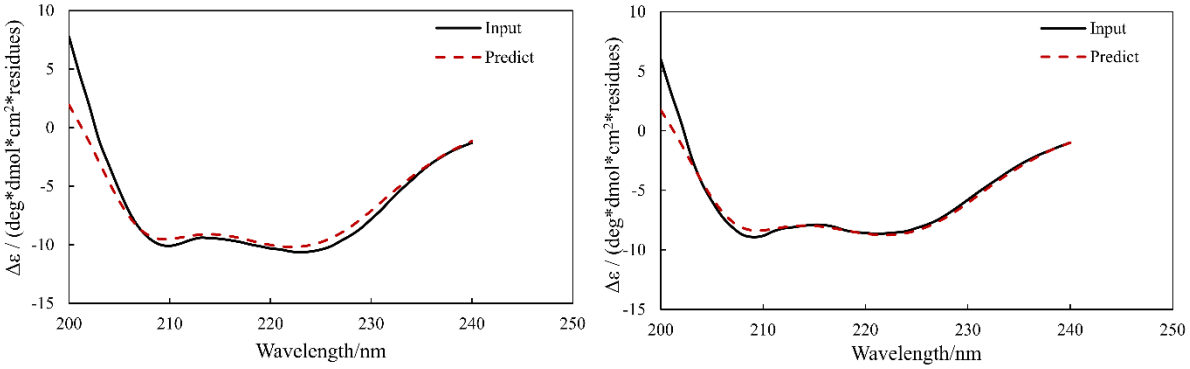

***Figure 3.15.** Molar ellipticity of 0.01 mmol L^{-1} Mb in the absence (left) and in the presence of 0.5 mmol L^{-1} NaCOSAN (right). The dark lines correspond to the experimental spectra and the red dashed lines to the predicted spectra, as fitted by K2D3 analysis.*

The evolution of this percentage is given in Table 3.6 and shows abrupt variation when COSAN is added and then a saturation of the evolution as qualitatively observed (Figure 3.14) above the ratio [NaCOSAN]/[Mb] = 20.

Table 3.6: Percentages of a-helixes

NaCOSAN/Mb	α-helix (%)
0	89.71
1	89.4
3	88.85
10	80.93
20	78.74
40	78.87
50	78.64
100	76.55

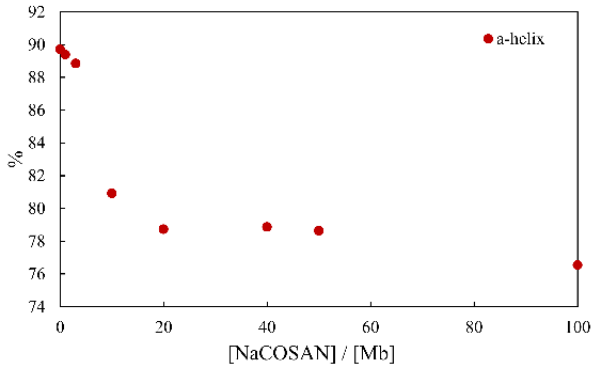

***Figure 3.16**. Percentage of a-helixes of 0.01 mmol L^{-1} Mb in the presence of NaCOSAN as a function of NaCOSAN/Mb ratio.*

This evolution will be discussed further in the chapter when the interaction between SDS and the protein is compared.

In the next step, we investigated how NaCOSAN affects the stability of Mb secondary structure when varying the temperature. Figure 3.17 shows the ellipticity of 0.01 mmol L^{-1} Mb at 208 nm in the absence and in the presence of different NaCOSAN concentrations as a function of temperature, which were extracted from Figure S3.7.

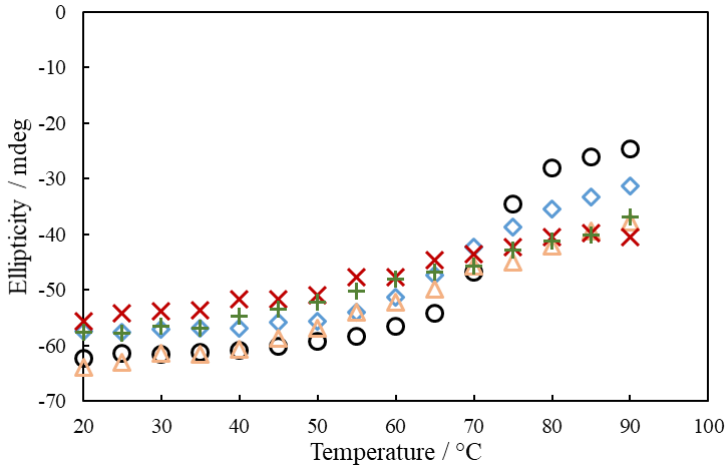

Figure 3.17. *Evolution of the ellipticity at 208 nm of 0.01 mmol L^{-1} Mb for various NaCOSAN/Mb ratios, 0 (dark circles), 5 (blue rhombus), 10 (orange triangle), 20 (red cross) and 30 (green cross) as a function of temperature.*

The effect of temperature on the CD signal evolution of Mb is much less pronounced in the presence of NaCOSAN (Figure 3.17). There is a slight change in the secondary structure of Mb upon increasing the NaCOSAN concentration at ambient temperature. Moreover, it seems that NaCOSAN prevents or limits the temperature denaturation of Mb, as seen with the ellipticity that achieves -40 mdeg at most at 90°C (compared to -25 mdeg for Mb without NaCOSAN).

Subsequently, for comparison, we analyzed the evolution of the CD signal of ApoMb in interaction with NaCOSAN. The ApoMb native state has a distinct tertiary structure, and it has packing of a-helices that is looser than that of myoglobin, as revealed by the scattering profiles at a wide scattering angle.[47] Apomyoglobin gives a visually comparable shape to the CD spectra of Mb (Figure 3.18A), but with a lower amplitude of the bands (Figure S3.8), which is representative of a lower percentage of a-helices of about 30% for ApoMb compared to Mb. By increasing the NaCOSAN/ApoMb ratio, the evolution of the ellipticity is slightly distorted by the addition of NaCOSAN at low ratios and then quasi-unaffected at much higher ratios.

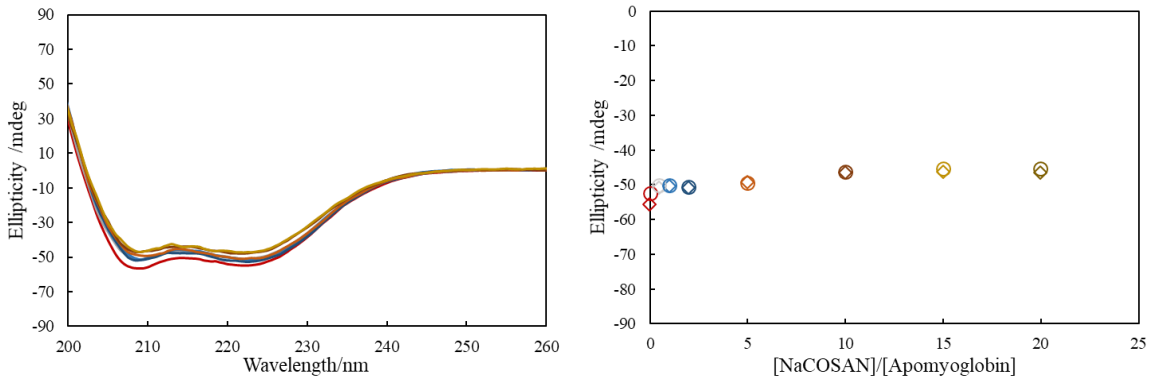

***Figure 3.18**. (A) Far-UV CD spectrum of ApoMb in the absence and presence of NaCOSAN at pH=10 and 298 K. (B) NaCOSAN-induced slight changes to the unfolding of ApoMb in PBS at 25 °C. The unfolding transition curve monitored by the CD ellipticity at 208 (triangles) and 222 (circles) nm as a function of [NaCOSAN]/[ApoMb].*

In the next step, we investigated how the different temperatures affect the secondary structure of ApoMb. Figure 3.19 shows the ellipticity of 0.01 mmol L^{-1} ApoMb at 208 nm in the absence (dark) and in the presence of 0.2 mmol L^{-1} NaCOSAN concentration as a function of temperature, which were extracted from Figure S3.9. The ellipticity of ApoMb upon temperature denaturation is in the same range as that of Mb, from -65 mdeg at room temperature to -25 at 90°C. The presence of NaCOSAN appears to prevent temperature denaturation of ApoMb (ellipticity from -25 mdeg to -40 mdeg at 90°C) like Mb in the presence of NaCOSAN, but the stabilization effect is in this case much less pronounced than that of Mb. This might be due to the plasticity of the molten globule-like character known for ApoMb, which comes from the lack of heme (compared to Mb).

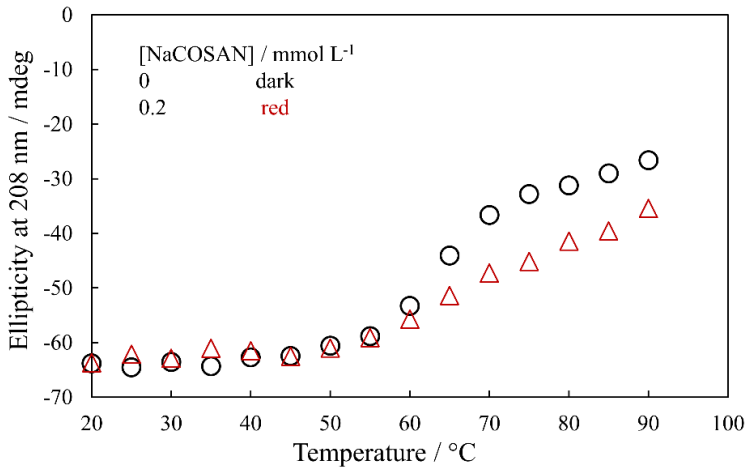

***Figure 3.19**. Ellipticity at 208 nm of 0.01 mmol L^{-1} ApoMb in the absence (dark circles) and at a ratio NaCOSAN/ApoMb=20 (red triangles) as a function of temperature.*

Indeed, the denaturation of myoglobin occurs at 65 °C, whereas it starts at 55°C for ApoMb, indicating its lower stability. The temperature of denaturation does not change with NaCOSAN, and that is true for both of the two proteins.

The reversibility of all these transformations would be interesting to further investigate; this revealed a lot about the type of interactions between NaCOSAN and the protein. Furthermore, time-resolved fluorescence or CD kinetics could inform us about the various steps of this interaction and secondary structural modifications.

III.2.6 Interaction of NaCOSAN/Mb followed by dynamic light scattering (DLS)

As a continuation of the investigation at the molecular scale, we have performed new experiments to probe the interactions of NaCOSAN with Mb at the supramolecular scale. Dynamic light scattering was first used to investigate the NaCOSAN/Mb system as a function of the molar ratio. The native hydrodynamic diameter of the Mb is about 4 nm.[48] A change in the secondary structure should impact the tertiary structure and thus the hydrodynamic diameter. Figure 3.20 presents a continuous increase in the diameter from 4 to 15 nm upon addition of NaCOSAN. Such a significant increase in size cannot be explained by simple unfolding of the protein, but rather by the formation of protein aggregates. Fuentes et al. have suggested that NaCOSAN provides a robust coating by forming a shell around the protein.[49]

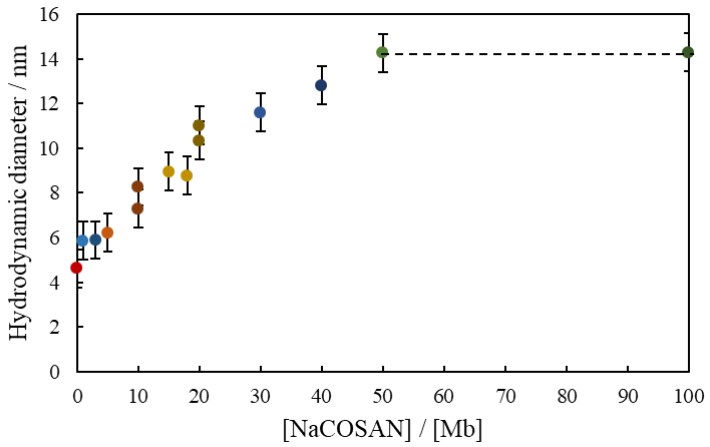

***Figure 3.20**. Hydrodynamic diameter of 0.01 mmol L^{-1} Mb in PBS at pH=10 in the presence of different NaCOSAN concentrations as a function of [NaCOSAN]/[Mb].*

However, the size increase is too small to be explained only by the formation of a COSAN shell around the protein, and this hypothesis was not verified experimentally. From our

observation of the low NaCOSAN/protein ratio and the amplitude of the diameter variation, we lean towards some protein's association. It seems that this increase in hydrodynamic diameter is followed by a leveling up of the size above ratio 50, but more data points are required between ratio 50 and 100 to support this observation.

III.2.7 Supramolecular level: Interaction of NaCOSAN/Mb followed by small angle X-ray scattering

Small-angle X-ray scattering (SAXS) was then performed on a synchrotron (SOLEIL, SWING beamline) to investigate deeply the possible NaCOSAN/Mb assemblies at the supramolecular levels. The SAXS spectra of solutions at a constant Mb concentration and varying the NaCOSAN concentrations are shown in Figure 3.21. The scattering curve of 0.1 mol L^{-1} Mb in PBS (red curve) shows the signal of Mb monomers (Figure 3.21) and the signal adjusted (dashed line) with a form factor of a tri-axial ellipsoid with dimensions of around 4.6 nm x 4.6 nm x 4.4 nm, which are in the same order of magnitude as the dimensions described in the literature.[50]

By increasing the NaCOSAN/Mb ratio, we observe an increase in the scattering excess at low scattering vectors q, indicating the formation of large aggregates (much larger than protein monomers). This suggests that the addition of NaCOSAN provokes the formation of NaCOSAN/Mb assemblies, which is in agreement with the increase of the hydrodynamic radius which observed by DLS.

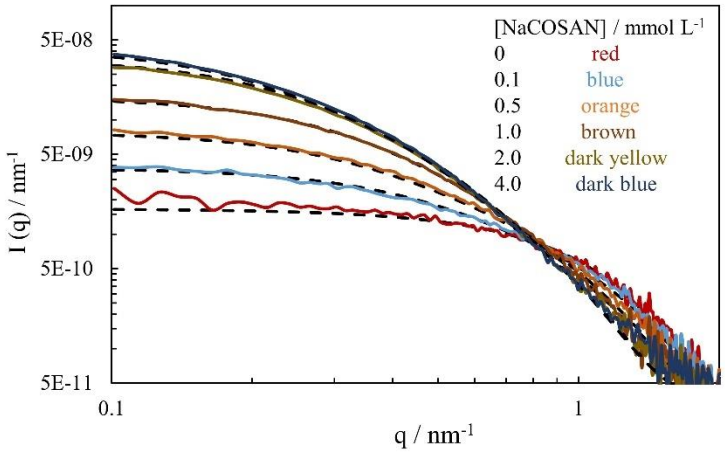

Figure 3.21. *SAXS spectra of 0.1 mmol L^{-1} Mb in PBS at pH=10 increasing the NaCOSAN concentrations. Dashed lines represent simultaneous data adjustment with parameters listed in SI. The spectra were recorded at Soleil.*

SAXS has a restricted window in this range (q = 0.1-1 nm^{-1}); the constant scattered intensity observed in the low q range below around 0.2 nm^{-1} informs on the formation of NaCOSAN/Mb assemblies of finite size.

The scattering of COSAN in PBS is negligible compared to the scattering of the protein; therefore, it was assumed with good confidence that the scattering of the assemblies only arises from the protein. The model based on a tri-axial ellipsoid form factor (dashed lines in Figure 3.21) gave a good fit to the experimental data. It has allowed us to deduce the global size of the assemblies and the number of aggregations, considering an assembly of proteins. Details of the fitting procedure are given in the SAXS modeling section in the supporting information section of this chapter. The fitting results are listed in Table 3.7 below.

Table 3.7: Aggregation number of flattened assemblies and dimensions (fittings were made on data were collected at Soleil / SWING and at ESRF / ID02).

[NaCOSAN]/[Mb]	<Nag>	a-semi axis	b-semi axis	c-semi axis
0	1	2.3	2.3	2.2
0.5	0.9±0.04	3.2	2.3	1.5
1	2±0.2	6.9	2	1.7
2	2±0.01	6.9	1.9	1.7
5	4±0.4	9.5	3	1.7
10	6±1.2	10	4.4	1.8
20	16±3.3	13.8	5.5	2.3
40	18±4	16	6	2.3
50	37±7	23	4.8	2.9

As shown on the Table 3.7, when the NaCOSAN/Mb ratio is less than one, the scattering curve reflects an average between protein alone and protein in interaction with NaCOSAN. At a ratio equal to 1, Mb forms dimers (Nagg = 2). Upon further increase in the NaCOSAN/Mb ratio, larger multimers are formed, up to Nagg = 37 for NaCOSAN/Mb =50. The greater variation observed at the a-semi axis indicates that, once dimers are formed, the addition of NaCOSAN

can be associated with the formation of longer chains and, consequently, larger scattering objects.

Complementary SANS measurements were also performed at the Paul Scherrer Institut Paul on several compositions of NaCOSAN/Mb (see Figure S3.10). Although the scattering intensity was weaker due to the low concentration of proteins in deuterated solution (deuterated PBS at pH=10), SANS curves show an increase in the scattered intensity upon addition of NaCOSAN, in agreement with the observation in SAXS.

A rough schematic representation of the self-assembly process can be proposed to summarize the observations made at supramolecular scales using DLS and SAXS/SANS techniques. Upon addition of NaCOSAN in a solution of Mb at a high pH to minimize the positive charge at the surface of the protein while still maintaining the structural integrity of the protein in terms of secondary and tertiary structure, we observed first a light impact on the 3D structure of the globular protein and the association of proteins by pairs, either considering the NaCOSAN as a sticky molecule or considering the energy of solvation of the NaCOSAN/protein system increases and thus induce an association by pairing to minimize this energy. Then the reason why the self-assembly evolved toward an elongated structure remains unknown at this stage.

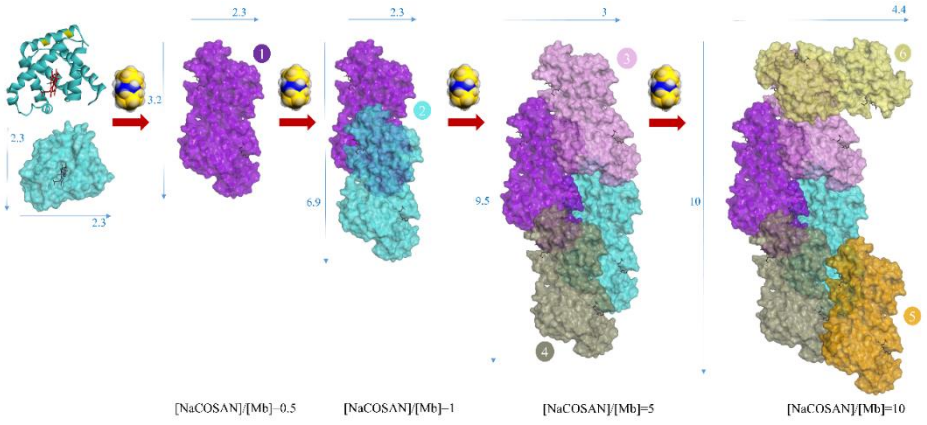

***Figure 3.22**. Representation of NaCOSAN/Mb assemblies, which are elongated in 2D, forming flattened assemblies.*

III.2.8 Interaction of NaCOSAN/Mb followed by small angle X-ray scattering at different temperatures

In the next step, we investigate the reversibility of the NaCOSAN/Mb assemblies with temperature. The temperature was increased stepwise from 25 °C to 60 °C, which is the maximum temperature that the sample could be heated before denaturation occurs at around 65 °C, and then decrease to 25 °C. The assemblies were followed by SAXS, which were

recorded at ESRF. Figure 3.23 shows the scattering intensity of 0.1 mmol L^{-1} Mb in PBS at pH = 10 in the presence of 0.2 mmol L^{-1} ([NaCOSAN]/[Mb] = 2) and 1 mmol L^{-1} NaCOSAN concentrations ([NaCOSAN]/[Mb] = 10), increasing the temperature. Instead of a decrease in this signal, which would indicate a dissociation at low ratio, we observed an increase in the SAXS signal at low q, which appears to be the signature of an assembly lengthening. At higher ratios, however, there was no discernible change in the scattering curve, indicating that NaCOSAN and proteins are tightly associated to form the assemblies. To attempt to separate the nano-ion/protein complexes, a different approach is required.

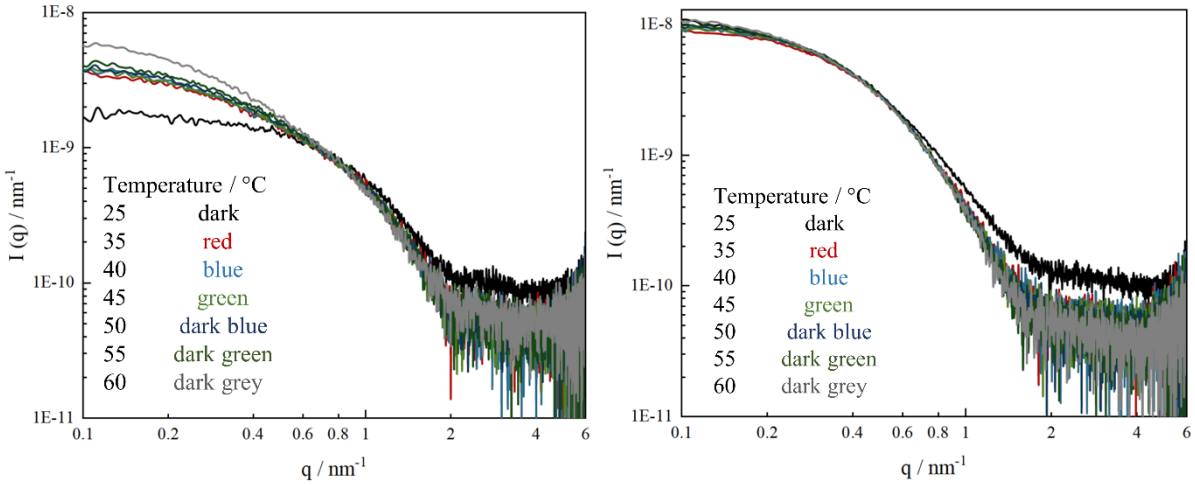

Figure 3.23. *SAXS spectra of 0.1 mmol L^{-1} Mb in PBS at pH=10 in the presence of (A) 0.2 mmol L^{-1} and (B) 1 mmol L^{-1} NaCOSAN concentrations at different temperatures. The spectra were recorded at the beamline ID02 at ESRF.*

III.3 NaCOSAN in interaction with two other proteins: carbonic anhydrase or trypsin inhibitor

In the following section, we examined the interactions of NaCOSAN with Bovine carbonic anhydrase (BCA) and soybean Kunitz trypsin inhibitor (SKTI). The results will be compared with those obtain on Mb and still at pH=10. BCA is a protein found in almost all animals and photosynthesizing organisms.[51] Aside from its biological and scientific significance, BCA has a 10-stranded twisted β-sheet with a few small helices,[51] and its actual size is ~6 × 4 × 4 nm. [52] SKTI is a small, monomeric and non-glycosylated protein containing 181 residues. Sweet et al.[53] first reported its crystal structure, which was later refined by Song et al.,[54] who found that the overall structure of SKTI is spherical with a diameter of 3–5 nm. SKTI consists of 12 crisscrossing antiparallel beta-strands, largely stabilized by hydrophobic side chains.[55]

III.3.1 Interaction of NaCOSAN/BCA and NaCOSAN/SKTI followed by fluorescence

Seven tryptophan residues are located at positions 4, 15, 96, 122, 190, 207, and 243 in the sequence of BCA, whereas two tryptophan residues are located at positions 93 and 117 in the sequence of SKTI. Figure 3.24 depicts the derived Stern-Volmer equation (extracted from fluorescence spectra, Figure S11), from which it was determined that the number of NaCOSAN molecules bound is 2.2 for BCA and 3.3 for SKTI.

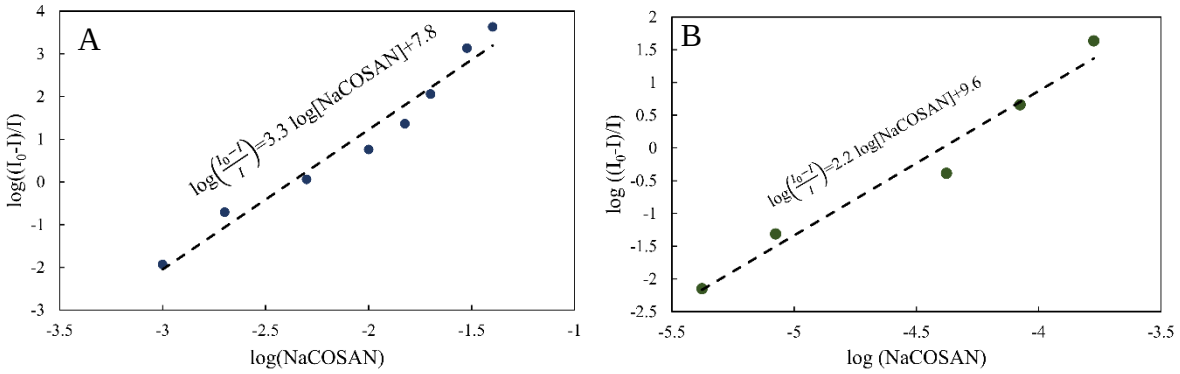

Figure 3.24*. The plot of the derived Stern-Volmer equation for BCA (left) and SKTI (right) as a function of NaCOSAN concentration. From the plot, n and Kq were calculated to be 3.3 and 6.3 x 10^7 for BCA and 2.2 and 3.9 x 10^9 mol^{-1} L for SKTI.*

Comparing the various Kq for the different proteins reveals that NaCOSAN has increased affinity in the order Mb < BCA < SKTI. The number of tryptophan that bound to nano-ions, as estimated by the Stern-Volmer equation, increases with the amount of tryptophan contained in the protein. BCA contains seven tryptophan residues in its amino acid sequence, three of which are not involved in hydrogen bonding and are therefore well exposed for interaction. Mb and SKTI each have two tryptophan residues in the first a-helix that are free of hydrogen bonds. However, the binding constants differ from protein to protein. Considering that NaCOSAN forms non-conventional di-hydrogen bonds with tryptophan, *Kq* reflects the nature of these bonds.

III.3.2 Interaction of NaCOSAN/BCA and NaCOSAN/SKTI followed by circular dichroism (CD)

Circular dichroism (CD) spectra of BCA exhibit one significant negative bands in the ultraviolet region at 215 nm, which are characteristic for β-strand structure of proteins. Figure 25 shows that the increase in NaCOSAN concentration does not affect the secondary structure content of the protein until the NaCOSAN/BCA ratio reaches 15. With an increase in NaCOSAN concentration, there is an increase in ellipticity above this ratio 15 (Figure 3.25 B).

This increase in CD signal suggests an increase in β-strand content, which Rana et al. also observed. [51] K2D3 analysis was applied in order to calculate the percentage of β-strand in the BCA. Figure 3.26 shows two examples of input (dark line) experimental data and the predicted (red dashed line), which were used to calculate the percentage of the β-strand of BCA in the presence of NaCOSAN (Figure 3.27).

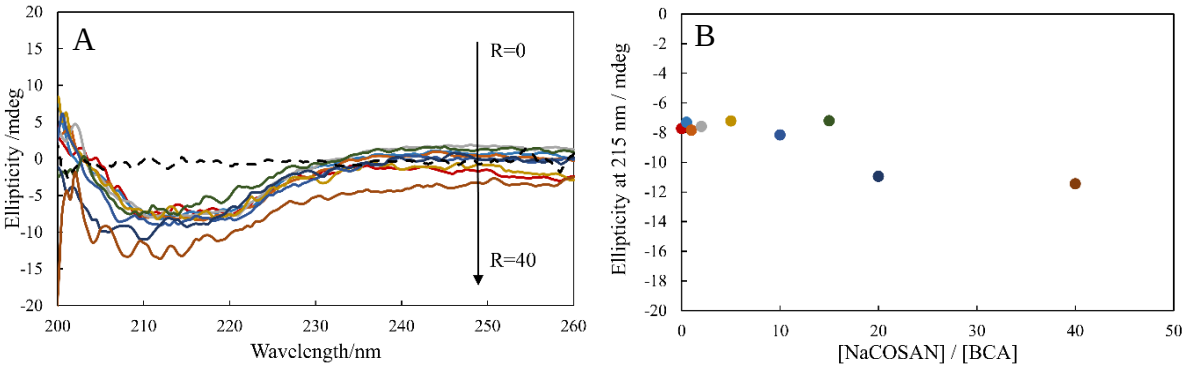

***Figure 3.25**. (A) Far-UV CD spectrum of BCA in the absence and presence of NaCOSAN at pH=10 and 298 K. The dark dashed line corresponds to 1 mmol L^{-1} NaCOSAN in PBS at pH=10. (B) The transition curve monitored by the CD ellipticity at 215 nm as a function of [NaCOSAN]/[BCA].*

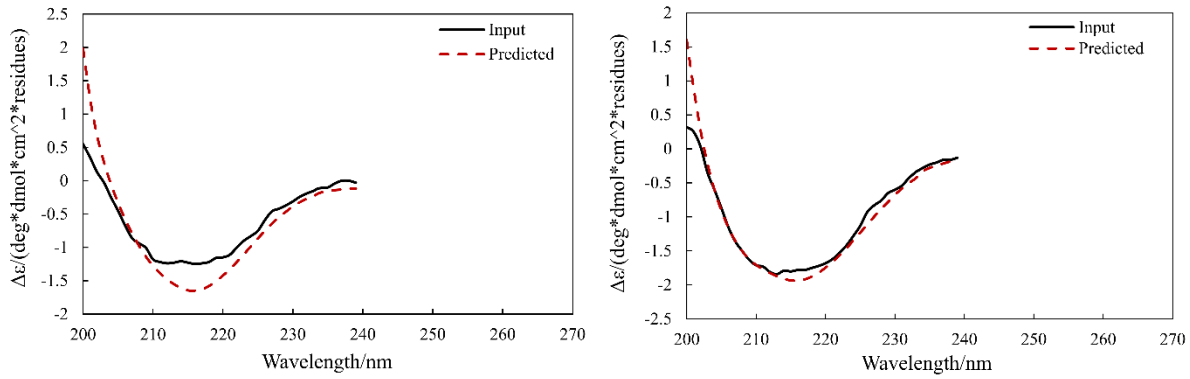

***Figure 3.26.** Molar ellipticity of 0.0055 mmol L^{-1} BCA in the absence (left) and in the presence of 0.01 mmol L^{-1} NaCOSAN (right). The dark lines correspond to the experimental spectra and the red dashed lines to the predicted spectra, as fitted using a K2D3-type analysis.*

Table 3.8: Percentages of b-strand

NaCOSAN/BCA	b-strand (%)
0	43.8
2	39.6
5.5	40.6
18	39.2

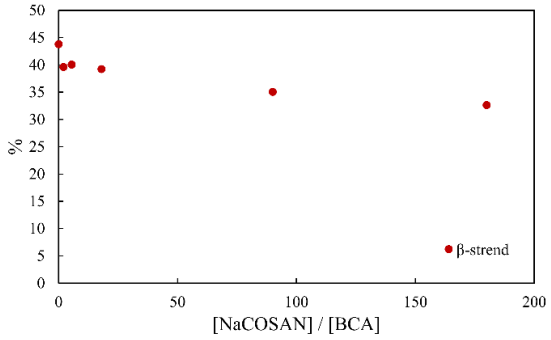

***Figure 3.27.** Percentage of β-strand of 0.055 mmol L^{-1} BCA in the presence of NaCOSAN as a function of NaCOSAN/BCA concentrations.*

In contrast to the Mb-case and its corresponding CD evolution as a function of NaCOSAN/protein ratio, the variation for BCA is initially unaffected by the first addition of NaCOSAN and then varies in a more gradual manner above a ratio of 15. In the case of SKTI, circular dichroism (CD) spectra presents a minimum ellipticity at about 200 nm and a slight positive shoulder at 225 nm, which is characteristic for the class of β_{II}-proteins (β-sheet content in β_{I}-proteins is generally higher than that in β_{II}-proteins[56]).[55] Figure 3.28 shows the CD spectra of SKTI in the absence and in the presence of different NaCOSAN concentrations. The backbone structure of SKTI in the presence of NaCOSAN does not undergo a major overall change, especially in comparison with the temperature denaturation of the protein (Figure S3.13 A). The ellipticity of SKTI at 225 nm (Figure 3.28B) is practically constant upon addition of NaCOSAN, indicating that the secondary structure of SKTI is not affected by NaCOSAN.

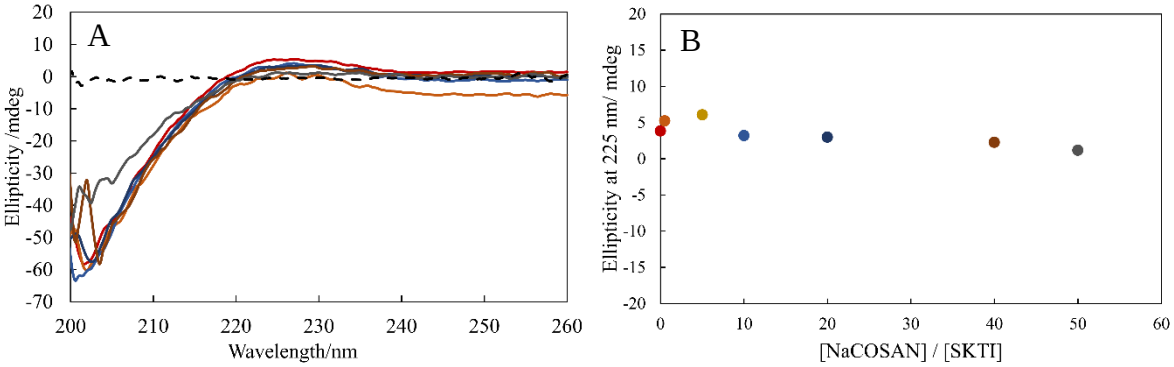

***Figure 3.28**. (A) Far-UV CD spectrum of SKTI in the absence and presence of NaCOSAN at pH=10 and 298 K. The dark dashed line corresponds to 1 mmol L^{-1} NaCOSAN in PBS at pH=10. (B) The transition curve monitored by the CD ellipticity at 225 nm as a function of [NaCOSAN]/[SKTI].*

In the next step, we investigated how the presence of NaCOSAN affects the secondary structure of BCA and SKTI at different temperatures. Figure 3.29A shows the ellipticity variation of 0.0055 mmol L^{-1} BCA at 215 nm in the absence and in the presence of different NaCOSAN concentrations as a function of temperature, which were extracted from Figure S3.12.

Similarly, Figure 3.29B shows the ellipticity variation of 0.0084 mmol L^{-1} SKTI at 225 nm in the absence and in the presence of different NaCOSAN concentrations as a function of temperature, which were extracted from Figure S3.13. It was found that the effect of temperature on the CD signals of SKTI and BCA in the presence of NaCOSAN is opposite to that observed for Mb. The temperature-induced denaturation appears to be shifted to lower

temperatures in both cases when the NaCOSAN/protein ratio increases, resulting in a greater absolute value for the ellipticity.

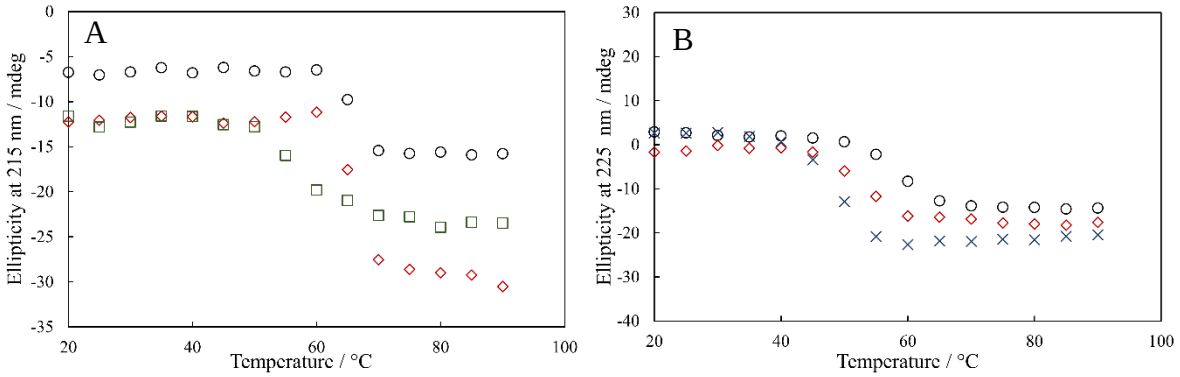

***Figure 3.29**. (A)Evolution of the ellipticity at 215 nm of 0.0055 mmol L^{-1} BCA for various NaCOSAN/BCA ratios, 0 (dark circles), 2.4 (red rhombus) and 5.5(green squares) as a function of temperature. (B)Evolution of the ellipticity at 225 nm of 0.0084 mmol L^{-1} SKTI for various NaCOSAN/SKTI ratios, 0 (dark circles), 1 (red rhombus) and 70 (blue crosses) as a function of temperature.*

III.3.3 Formation of NaCOSAN/BCA fibrils followed by fluorescence

As previously demonstrated, small, globular proteins are likely to form disordered amorphous aggregates under destabilizing physicochemical conditions.[51,57] It was found that BCA, when incubated in mildly denaturing conditions, causes the partially unfolded conformers to assemble together and forms ordered amyloid aggregates.[51] The increase in β-sheet content of BCA in the presence of NaCOSAN could suggest the formation of amyloid aggregates. In order to confirm the formation of amyloid aggregates in the presence of NaCOSAN, we studied the fluorescence intensity of thioflavin T (ThT), which binds specifically to amyloids, in the presence of the NaCOSAN/BCA system. The fluorescence intensity of ThT at 482 nm increases when the formation of amyloid aggregates occurs.[58] The orange curve in Figure 3.30 represents the reference intensity of ThT fluorescence at 482 nm. In the presence of BCA, the intensity of this band increases, indicating the possible formation of amyloid aggregates (green curve). However, the addition of NaCOSAN causes a shift in the BCA/ThT curve due to the interaction between NaCOSAN and ThT. Thus, the presence of NaCOSAN interferes with the detection of amyloid aggregates in BCA, making it impossible to detect the amyloid aggregates in BCA.

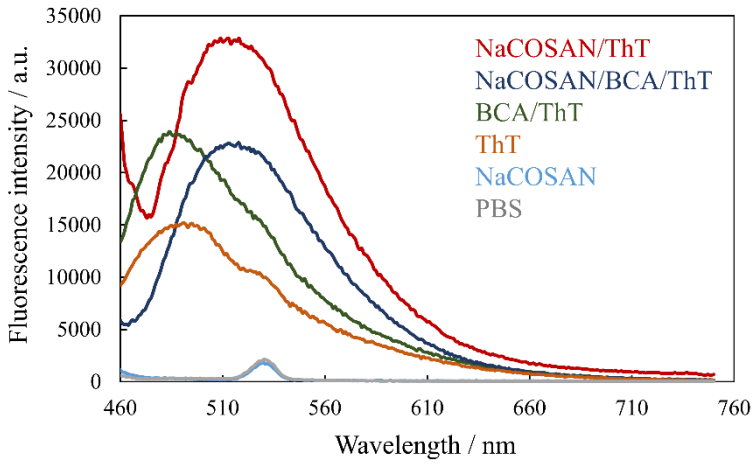

Figure 3.30. *Emission fluorescence spectra of 0.3 mmol L^{-1} NaCOSAN (light blue), 0.09 mmol L^{-1} Thioflavin T (orange), 0.018 mmol L^{-1} BCA in the presence of 0.3 mmol L^{-1} NaCOSAN and 0.09 mmol L^{-1} Thioflavin T (dark blue), 0.3 mmol L^{-1} NaCOSAN in the presence of 0.09 mmol L^{-1} Thioflavin T (red). The excitation wavelength was 450 nm.*

III.3.4 Interaction of NaCOSAN/BCA and NaCOSAN/SKTI followed by dynamic light scattering (DLS)

As a continuation of the investigation at the molecular scale, we investigate BCA and SKTI in interaction with NaCOSAN at the supramolecular scale. Figure 3.31 presents the hydrodynamic diameter of BCA or SKTI in the absence and in the presence of NaCOSAN.

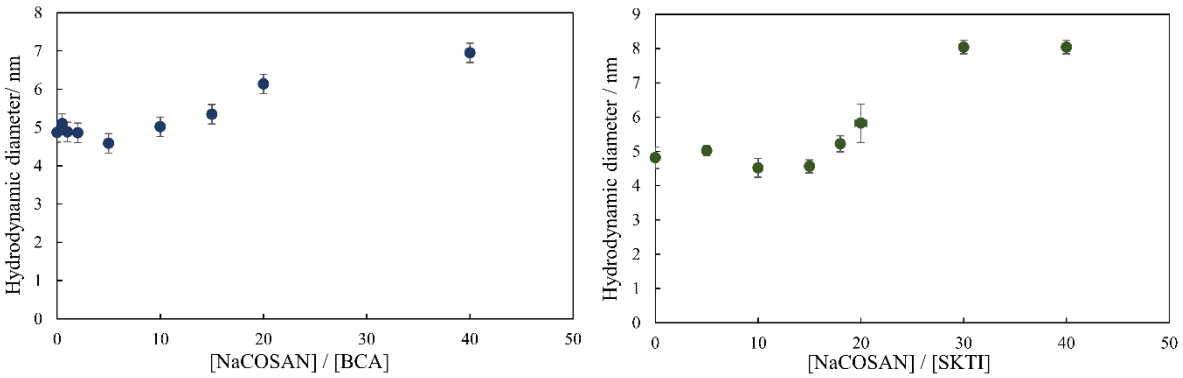

Figure 3.31. *Hydrodynamic diameter of 0.055 mmol L^{-1} BCA (left) and 0.0084 mmol L^{-1} SKTI (right) in PBS at pH=10 in the presence of different NaCOSAN concentrations as a function of [NaCOSAN]/[BCA] or [NaCOSAN]/[SKTI].*

The addition of NaCOSAN had no effect on the hydrodynamic diameter of NaCOSAN/BCA assemblies until approximately a ratio of 10. Similar to the CD experiment, there may be a NaCOSAN/protein threshold at which the effect can be measured (a threshold that was not observed for Mb). We also observed that, until the ratio of 15 is reached, NaCOSAN has no effect on the hydrodynamic diameter of NaCOSAN/SKTI assemblies. In contrast to Mb in the presence of NaCOSAN, where an immediate increase in hydrodynamic diameter was observed

upon the addition of NaCOSAN, BCA and SKTI show that their hydrodynamic diameter begins to be affected above a molar ratio threshold that increases depending on the protein.

III.3.5 Supramolecular level: Interaction of NaCOSAN/BCA and NaCOSAN/SKTI followed by small angle X-ray scattering

The SAXS spectra of a constant BCA concentration and varying the NaCOSAN concentrations are shown in Figure 3.32. The SAXS curve of 0.055 mol L^{-1} BCA in PBS (red curve on Figure 3.32) corresponds to the signal of BCA monomers with fitted dimensions of around 5.2 nm x 1.9 nm x 2 nm, which are in the same order of magnitude as the dimensions of the native protein described in the literature.[52] The increase in scattered intensity suggests that NaCOSAN/BCA assemblies are forming. We observed that a low NaCOSAN concentration corresponding to [NaCOSAN]/[BCA] = 1 does not affect the scattering intensity, whereas at a higher [NaCOSAN]/[BCA] ratio above 10, the scattering intensity increases, which is fully in agreement with the evolution of the hydrodynamic radius determined by DLS.

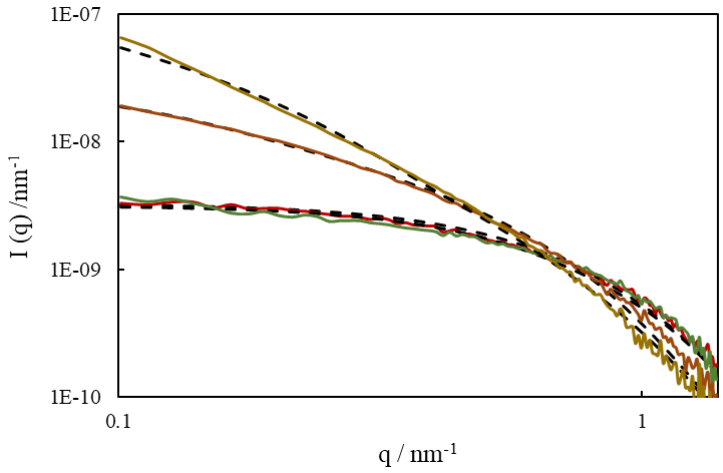

***Figure 3.32**. SAXS spectra of 0.055 mmol L^{-1} BCA (red curve) in PBS at pH=10 increasing the NaCOSAN concentrations. The NaCOSAN concentrations were recorded in the presence of BCA were 0.055 mmol L^{-1}(green curve), 0.5mmol L^{-1}(dark orange) and 1.1 mmol L^{-1}(dark yellow). Dashed lines represent simultaneous data adjustment with parameters listed in SI. The spectra were recorded at ESRF.*

The SAXS spectra of the NaCOSAN/BCA system were simultaneously fitted using a tri-axial ellipsoid form factor model, like in the case of the NaCOSAN/Mb system. As mentioned previously, the fitting results indicate that without NaCOSAN, BCA is present in its monomeric state and has an ellipsoid shape. Above the ratio [NaCOSAN]/[BCA] = 10, BCA starts to aggregate by forming dimers. The assemblies then elongate in 2D, forming flattened aggregates with one dimension being increased more than twice as much as the other (Table 3.9).

Table 3.9: Aggregation number of flattened [NaCOSAN]/[BCA] aggregates and dimensions (fittings were made on data were collected at Soleil/SWING and ESRF/ID02).

[NaCOSAN]/[BCA]	<Nag>	a-semi axis	b-semi axis	c-semi axis
0	1	5.2	1.9	2
1	1±0.09	5.5	1.8	2
10	2±0.02	9.3	2.1	2.3
15	2.5±0.02	10	2.3	2.1
20	8±0.1	23	3.7	1.9
40	52±0.14	52	10.3	1.9

Figure 3.33 depicts the SAXS spectra of a constant SKTI concentration and varying the NaCOSAN concentrations. The spectrum of 0.084 mol L^{-1} SKTI in PBS (red curve) shows in SAXS (Figure 3.32) corresponds to the signal of SKTI monomers with dimensions of around 3.9 nm x 1.6 nm x 1.8 nm, which are in the same order of magnitude as the dimensions described in the literature.[55] The increase in scattered intensity suggests that NaCOSAN/SKTI assemblies are forming by adding NaCOSAN to the SKTI solutions.

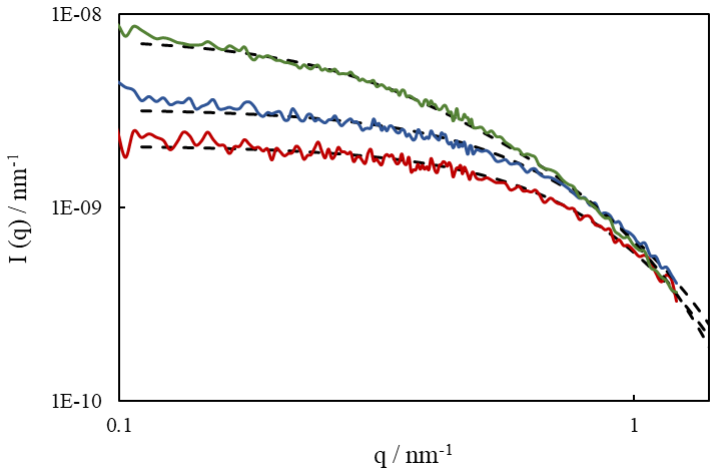

Figure 3.33. *SAXS spectra of 0.084 mmol L^{-1} SKTI in PBS at pH=10 increasing the NaCOSAN concentrations. Dashed lines represent simultaneous data adjustment with parameters listed in SI. The spectra were recorded at ESRF.*

The SAXS spectra of the NaCOSAN/SKTI system were simultaneously fitted using a tri-axial ellipsoid form factor model, like the case of the two other proteins/NaCOSAN systems. The fitting results indicate that without NaCOSAN, SKTI is present in monomeric state, and it has

a near spherical shape with a diameter of around 4 nm. Upon addition of NaCOSAN (at a molar ratio of 5), SKTI starts to form assemblies that can be attributed to trimers.

Table 3.10: Aggregation number of flattened [NaCOSAN]/[SKTI] aggregates and dimensions.

[NaCOSAN]/[SKTI]	<Nag>	a-semi axis	b-semi axis	c-semi axis
0	1	3.9	1.6	1.8
1	1±0.15	4.9	1.7	1.7
5	3±0.28	9.4	2.1	1.8

Figure 3.34 depicts the variation of the aggregation number of the protein assemblies as a function of the NaCOSAN/protein ratio for each of the three proteins. We observed a smooth increase for Mb, a sharper increase above a given threshold for BCA, and perhaps a much sharper increase for STKI that was not possible to detect because it was too sharp and then induced precipitation as observed through the clouded solution.

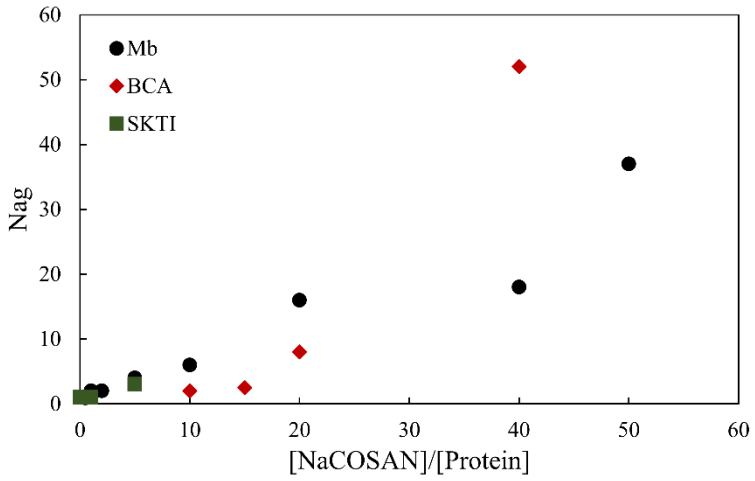

Figure 3.34. *Aggregation number of the protein assemblies as a function of the NaCOSAN/protein ratio for each of Mb (dark circles), BCA (red rhombus) and SKTI (green squares).*

The conclusion here is that we can control the assembly of three proteins. The ratio of NaCOSAN to protein that will take place during the controlled assembly varies between the three proteins due to their different features. As referred to in Chapter I, chaotropic ions increase the solubility of protein in aqueous solutions while inducing denaturation. Surprisingly, NaCOSAN, as a super-chaotropic ion, acts as molecular glue and forms protein assemblies in aqueous solutions. This can be associated with a different approach of solubilizing proteins while avoiding total denaturation. In the following section, we compared

the interactions of Mb in the presence of a classical chaotropic ion, NaSCN, to those of NaCOSAN.

III.4 Chaotropic salt in interaction with myoglobin-comparison at pH=10

III.4.1 Classical chaotropic (NaSCN) in the presence of Mb-comparison with NaCOSAN

We studied the interactions of Mb with NaSCN at the molecular scale in order to compare the observed effect to that of NaCOSAN. According to UV-Vis (Figure 3.35A and S3.14), fluorescent (Figure 3.35B and S3.15), and CD results (Figure 3.35C and S3.16), we observed that NaSCN does not affect the heme group, the tryptophan fluorescence signal, or the secondary structure content of Mb, regardless its investigated concentration. We also did not observe any difference in the hydrodynamic diameter of Mb with increasing NaSCN concentration (Figure 3.35D).

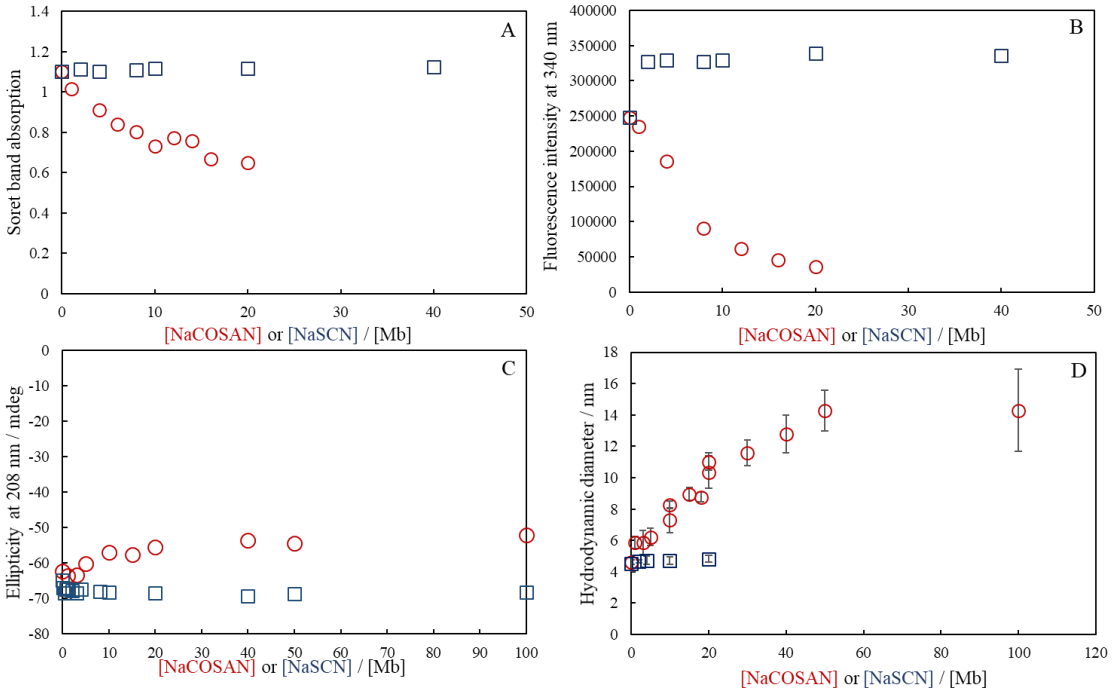

Figure 3.35. *(A) Soret band absorption, (B) fluorescence intensity at 340 nm, (C) ellipticity at 208 nm and (D) hydrodynamic diameter as a function of the ratio NaCOSAN(red) and NaSCN (blue) with Mb.*

In the next step, we investigated the effect on the secondary structure of Mb in the presence of NaSCN at different temperatures. Figure 3.36 shows the ellipticity of 0.01 mmol L^{-1} Mb at 208 nm in the absence (dark curve) and in the presence of 0.1 mmol L^{-1} NaCOSAN (red curve) or

NaSCN (green curve, extracted from Figure S3.17) as a function of temperature. We observed that, unlike NaCOSAN, NaSCN does not prevent temperature denaturation.

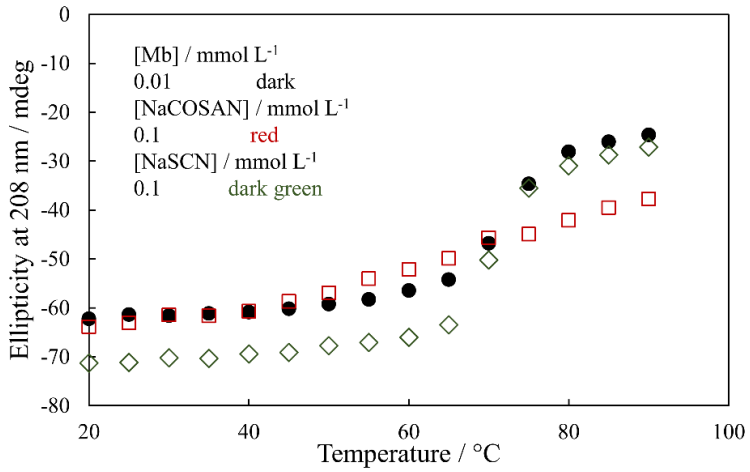

***Figure 3.36**. Ellipticity of 0.01 mmol L^{-1} Mb in the absence (dark circles) and in the presence of 0.1 mmol L^{-1} (red squares) NaCOSAN and 0.1 mmol L^{-1}NaSCN (green rhombus) at 208 nm as a function of temperature.*

III.4.2 NaCOSAN in comparison with dodecaborates ($Na_2B_{12}X_{12}$) in the presence of Mb

In this section, we investigate the interactions of Mb with other boron clusters that are less superchaotropes than NaCOSAN, such as $Na_2B_{12}H_{12}$, $Na_2B_{12}Cl_{12}$, $Na_2B_{12}Br_{12}$, and $Na_2B_{12}I_{12}$.The charge densities of the used boron clusters are listed in Table 3.11.

Table 3.11: Volumes, charges and charge densities of the used dodecaborates $B_{12}X_{12}^{2-}$ in comparison to NaCOSAN

Boron cluster	Charge (q_e)	Ionic volume (nm^3)	Charge density [q_e/nm^3]
$B_{12}I_{12}^{2-}$	2	0.52[59]	3.9
$B_{12}Br_{12}^{2-}$	2	0.42[59]	4.8
$B_{12}Cl_{12}^{2-}$	2	0.33[59]	6.0
$B_{12}H_{12}^{2-}$	2	0.15[59]	13.2
[3,3- $Co(1,2\text{-}C_2B_9H_{11})_2]^-$	1	0.45[60]	2.2

Initially, we study at the molecular scale the interactions of Mb with $Na_2B_{12}H_{12}$, which is the smallest and least chaotropic in the extended Hofmeister series, and $Na_2B_{12}I_{12}$, which is the largest and most chaotropic one after NaCOSAN. We observed that $Na_2B_{12}H_{12}$ did not show any effect on hydrodynamic diameter and the secondary structure content of Mb upon its

addition (Figure 3.37 C and D). Although a slight increase in fluorescence intensity and the Soret band's absorption was observed (Figure 3.37 A and B). On the other hand, $Na_2B_{12}I_{12}$ shows to affect the Soret band absorption, the hydrodynamic diameter, and the secondary structure content of Mb in a similar way to NaCOSAN. The results of Figure 3.37 were extracted from Figures S3.18-S3.20.

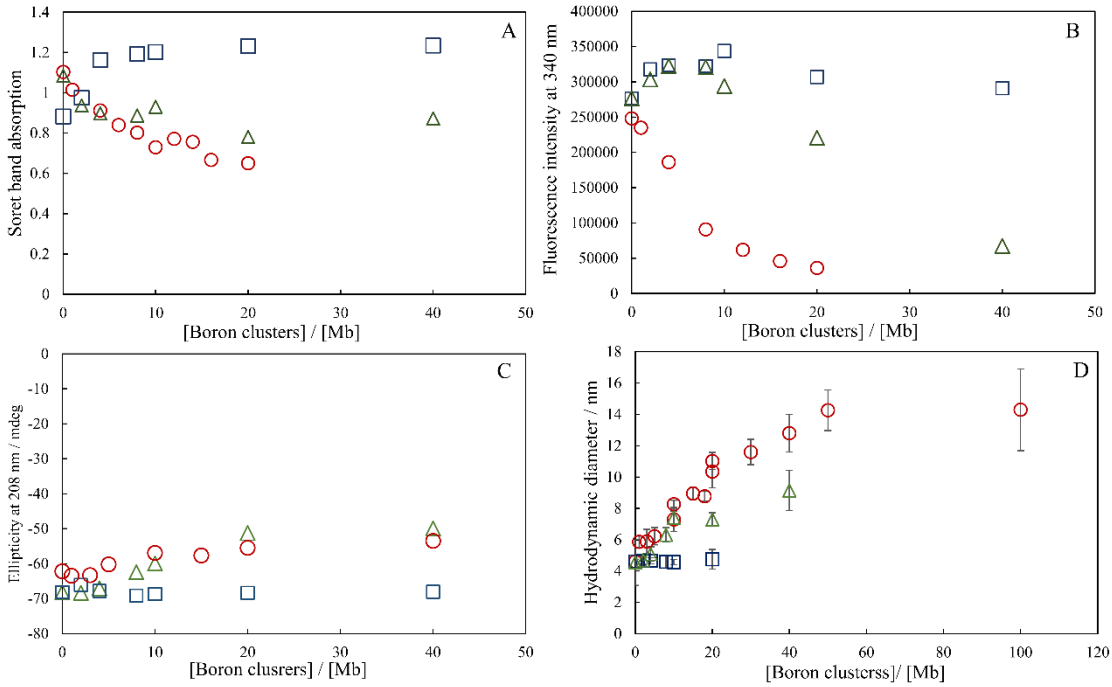

Figure 3.37. *(A) Soret band absorption, (B) fluorescence intensity at 340 nm, (C) ellipticity at 208 nm and (D) hydrodynamic diameter as a function of the ratio NaCOSAN(red), $Na_2B_{12}H_{12}$ (blue) and $Na_2B_{12}I_{12}$ (green) with Mb.*

In the next step, we study the effect of $Na_2B_{12}Cl_{12}$ and $Na_2B_{12}I_{12}$ on Mb at the supramolecular level by SANS and SAXS. Figure 3.38 illustrates the SANS spectra of 0.1 mmol L^{-1} Mb in PBS at pH=10 in the absence and in the presence of different concentrations of $Na_2B_{12}I_{12}$. We observed that the increase in $Na_2B_{12}I_{12}$ concentration leads to an increase in scattered intensity, which can be attributed to the formation of $Na_2B_{12}I_{12}$/Mb assemblies.

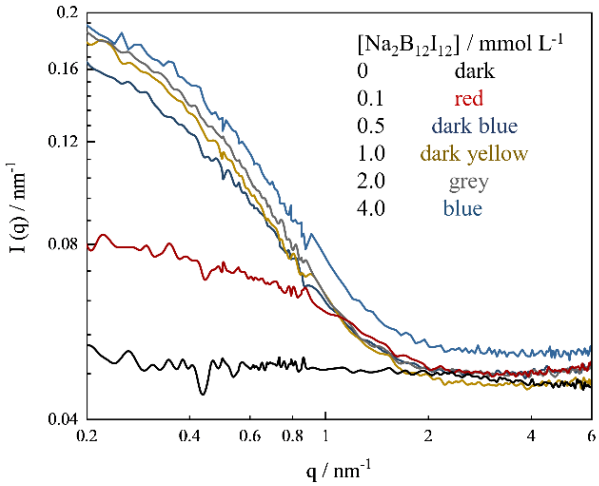

Figure 3.38. *SANS spectra of 0.1 mmol L^{-1} Mb in PBS at pH=10 in the absence and in the presence of different concentrations of $Na_2B_{12}I_{12}$. The spectra were recorded at PSI.*

Figure 3.39 illustrates the SAXS spectra of 0.1 mmol L^{-1} Mb in PBS at pH=10 in the absence and in the presence of different concentrations of $Na_2B_{12}I_{12}$. We also found that increasing the concentration of iodinated dodecaborate causes a rise in scattering intensity, as revealed by SAXS, which entails the controlled assembly of $Na_2B_{12}I_{12}$/Mb assemblies. Then, we studied the effect on Mb in the presence of the chlorinated dodecaborate cluster, $Na_2B_{12}Cl_{12}$, which is one of the intermediaries in size and chaotropicity. The chlorinated dodecaborate cluster did not show any effect on the scattering intensity (Figure 3.39B).

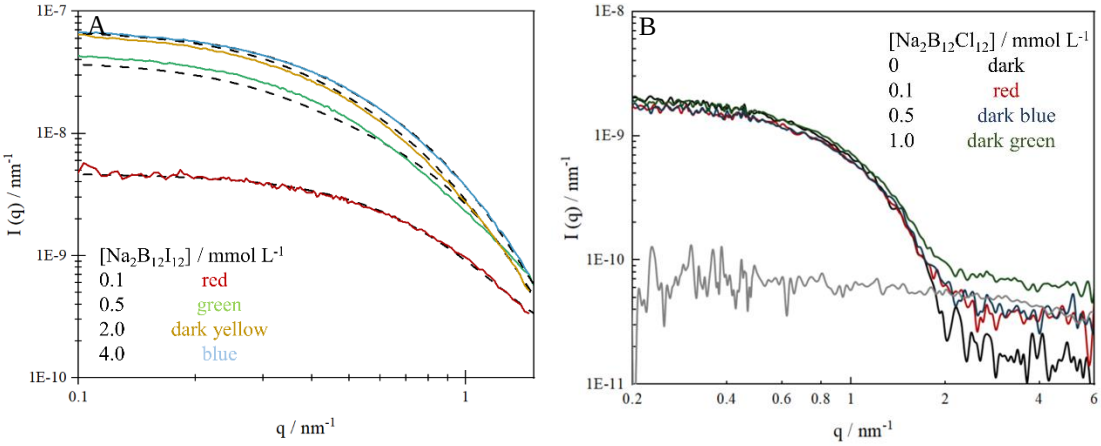

Figure 3.39. *SAXS spectra of 0.1 mmol L^{-1} Mb in PBS at pH=10 in the absence and in the presence of different concentrations of (A) $Na_2B_{12}I_{12}$ and (B) $Na_2B_{12}Cl_{12}$. The grey curve corresponds to 4 mmol L^{-1} $Na_2B_{12}Cl_{12}$ in the absence of Mb. The spectra were recorded at ESRF.*

The SAXS spectra of the $Na_2B_{12}I_{12}$/Mb system were simultaneously fitted using a tri-axial ellipsoid form factor model, like the case of Mb/NaCOSAN systems. The fitting results indicate that upon addition of $Na_2B_{12}I_{12}$, Mb starts to aggregate by forming trimers.

Table 3.12: Results of the SAXS fits (Figure 3.39).

[$Na_2B_{12}I_{12}$]/[Mb]	<Nag>	a-semi axis	b-semi axis	c-semi axis
0	1	2.5	2.2	2.1
1	1±0.36	4.9	2.1	2.1
5	3±0.56	10	2.6	1.7
10	5±0.98	9	3.7	1.8
20	4±2	8.2	3.3	1.7

III.4.2.1 NaCOSAN in comparison with dodecaborates ($Na_2B_{12}X_{12}$) in the presence of BCA or SKTI

Figure 3.40 presents the hydrodynamic diameter of BCA or SKTI in the absence and in the presence of $Na_2B_{12}I_{12}$. We observed that the addition of $Na_2B_{12}I_{12}$ does not affect the hydrodynamic diameter of $Na_2B_{12}I_{12}$/BCA assemblies until ratio 10, like in the case of NaCOSAN/BCA. We also observed that the addition of $Na_2B_{12}I_{12}$ does not affect the hydrodynamic diameter of the $Na_2B_{12}I_{12}$/SKTI system, which is not the case for NaCOSAN/SKTI assemblies.

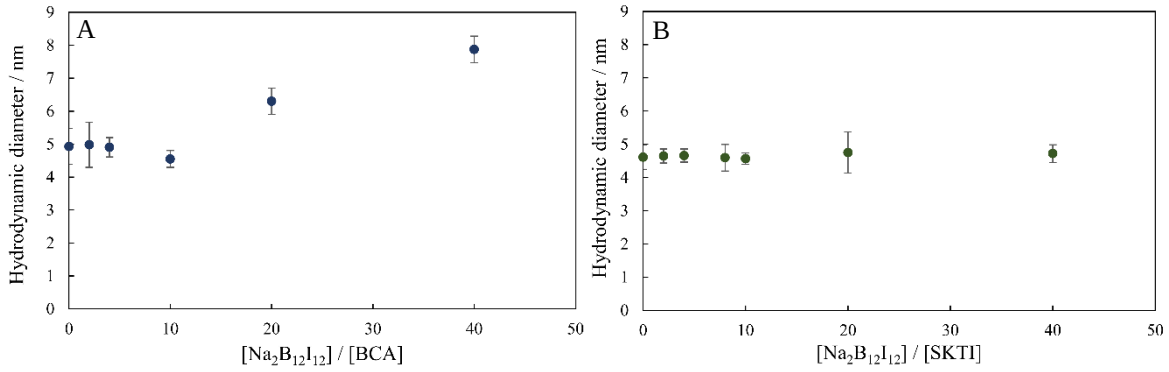

Figure 3.40. *Hydrodynamic diameter of (A) 0.055 mmol L^{-1} BCA and (B) 0.084 mmol L^{-1} SKTI in the absence and in the presence of different $Na_2B_{12}I_{12}$ concentrations.*

In the next step, we studied the effect of the interactions of BCA and SKTI with $Na_2B_{12}I_{12}$ by SANS and SAXS. Figure 3.41 illustrates the SANS spectra of (A) 0.055 mmol L^{-1} BCA and (B) 0.084 mmol L^{-1} SKTI in PBS at pH=10 in the absence (red curve) and in the presence of different concentrations of $Na_2B_{12}I_{12}$. We observed that the increase in $Na_2B_{12}I_{12}$ concentration

leads to an increase in scattered intensity, which can be attributed to the formation of $Na_2B_{12}I_{12}$/BCA or $Na_2B_{12}I_{12}$/SKTI assemblies.

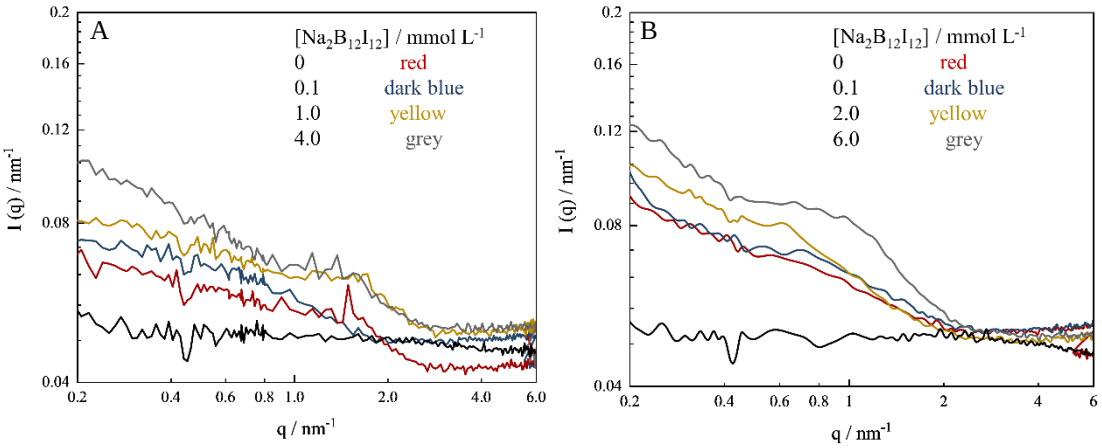

Figure 3.41. *SANS spectra of (A) 0.055 mmol L^{-1} BCA and (B) 0.084 mmol L^{-1} SKTI in PBS at pH=10 in the absence and in the presence of different concentrations of $Na_2B_{12}I_{12}$. The dark line corresponds to 10 mmol L^{-1} $Na_2B_{12}I_{12}$ in PBS at pH=10 in the absence of BCA or SKTI. The spectra were recorded at PSI.*

Figure 3.42 illustrates the SAXS spectra of (A) 0.055 mmol L^{-1} BCA and (B) 0.084 mmol L^{-1} SKTI in PBS at pH=10 in the absence and in the presence of different concentrations of $Na_2B_{12}I_{12}$. We also found that increasing the concentration of $Na_2B_{12}I_{12}$ causes a rise in scattering intensity, as revealed by SAXS, which entails the controlled assembly of $Na_2B_{12}I_{12}$/BCA and $Na_2B_{12}I_{12}$/SKTI assemblies.

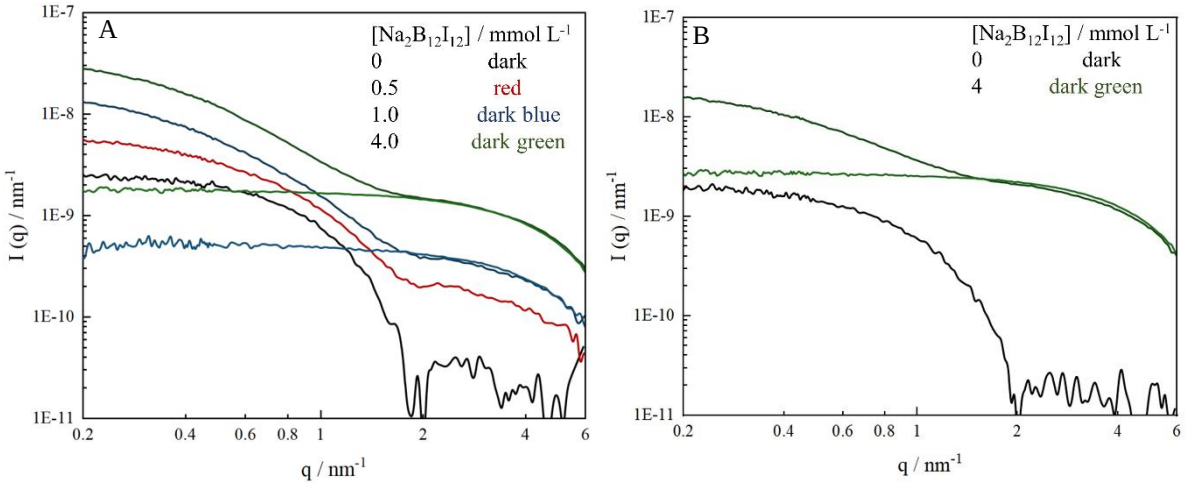

Figure 3.42. *SAXS spectra of (A) 0.055 mmol L^{-1} BCA and (B) 0.084 mmol L^{-1} SKTI in PBS at pH=10 in the absence and in the presence of different concentrations of $Na_2B_{12}I_{12}$. The curves colored by light shades of (A) blue and green correspond to 1 and 4 mmol L^{-1} $Na_2B_{12}I_{12}$, respectively, and (B) green correspond to 1 and 4 mmol L^{-1} $Na_2B_{12}I_{12}$ in the absence of BCA or SKTI. The spectra were recorded at ESRF.*

Subsequently, we studied the effect on BCA and SKTI in the presence of $Na_2B_{12}Cl_{12}$. Figure 3.43 did not show any effect on the scattering intensity of the BCA or SKTI in the presence of $Na_2B_{12}Cl_{12}$.

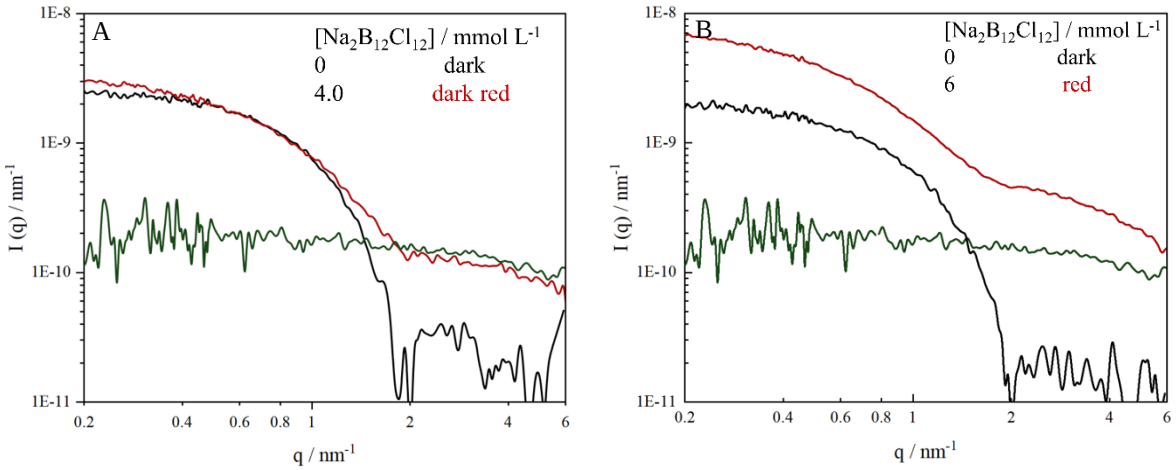

***Figure 3.43**. SAXS spectra of (A) 0.055 mmol L^{-1} BCA and (B) 0.084 mmol L^{-1} SKTI in PBS at pH=10 in the absence and in the presence of different concentrations of $Na_2B_{12}Cl_{12}$. The green line corresponds to 4 mmol L^{-1} $Na_2B_{12}Cl_{12}$ in PBS at pH=10 in the absence of BCA or SKTI.*

III.4.3 Effect of the classical surfactant (SDS) on Mb and comparison to NaCOSAN

Despite the large number of articles devoted to the characterization of Mb/surfactant complexes, in this section we studied the interactions of a classical surfactant, such as SDS, with Mb in order to compare, under the same conditions (PBS at pH=10), the effects of SDS and NaCOSAN on Mb. We chose SDS in order to compare the effect of a conventional surfactant on Mb with the effect of NaCOSAN on Mb, which is a molecule with surfactant properties but does not have the classical amphiphilic structure—no conventional surfactant. Figure 3.44A shows the Soret band absorption, which was extracted from the UV-Vis spectra (Figure S3.21), as a function of SDS concentration. We observed that there is a slight decrease in the signal of the Soret band absorption, which is much less pronounced than that of NaCOSAN. Figure S3.22 shows representative fluorescence spectra of Mb at increasing SDS concentration. The effect of adding SDS is a large increase in the fluorescence intensity, as shown in Figure 3.44B, and is opposite that of adding NaCOSAN. This indicates that the tryptophan residues have moved away from the heme and have become more exposed to the solvent, as Tofani et al. described. [41] Figure 3.44C shows the ellipticity of Mb in the presence of different SDS concentrations, which was extracted from the CD spectra (Figure S3.23). We observed that there is a slight decrease in the ellipticity, which suggests a decrease in the a-helixes content. However, this decrease is much less pronounced than that of NaCOSAN. Figure 3.44D depicts the hydrodynamic diameter of the [SDS]/[Mb] system as a function of

[SDS] concentration. A slight increase in the hydrodynamic diameter was observed from 4.6 to 6.2 by increasing the SDS.

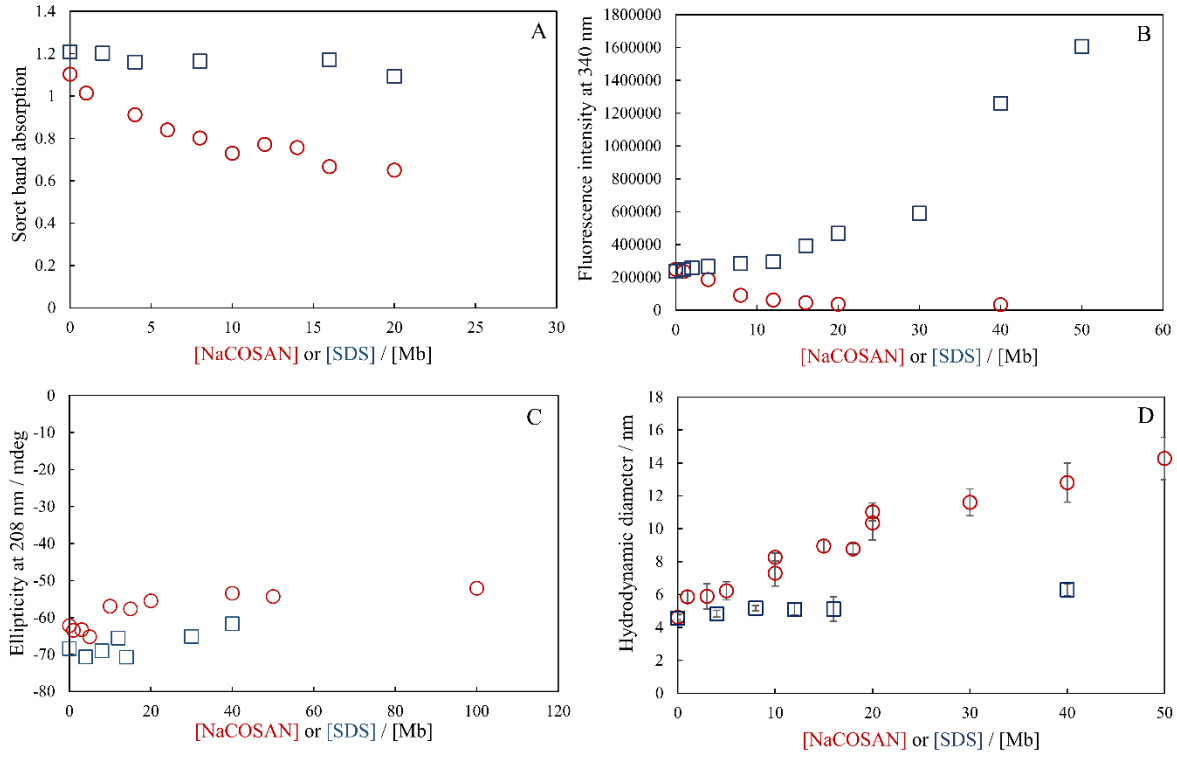

Figure 3.44. *(A) Soret band absorption, (B) fluorescence intensity at 340 nm, (C) ellipticity at 208 nm (D) hydrodynamic diameter as a function of the ratio NaCOSAN(red), SDS (blue) with Mb.*

III.4.3.1 NaCOSAN in comparison with a classical surfactant (SDS) in the presence of BCA or SKTI

In the next step, we studied the interactions of SDS in the presence of BCA and SKTI in PBS at pH 10. Figure 3.45 shows (A) the ellipticity and (B) the hydrodynamic diameter of BCA with increasing SDS concentration. We observed that the ellipticity and the hydrodynamic diameter of BCA are practically unaffected by the presence of SDS. Figure 3.45 shows (C) the ellipticity and (D) the hydrodynamic diameter of SKTI with increasing SDS concentration. We observed a slight increase in the hydrodynamic diameter of SKTI from 5.5 to 6.6 nm with increasing SDS concentration. The presence of SDS barely changes the ellipticity of SKTI at 225 nm, but the ellipticity at 205 nm seems to change at high SDS concentrations (Figure S3.25).

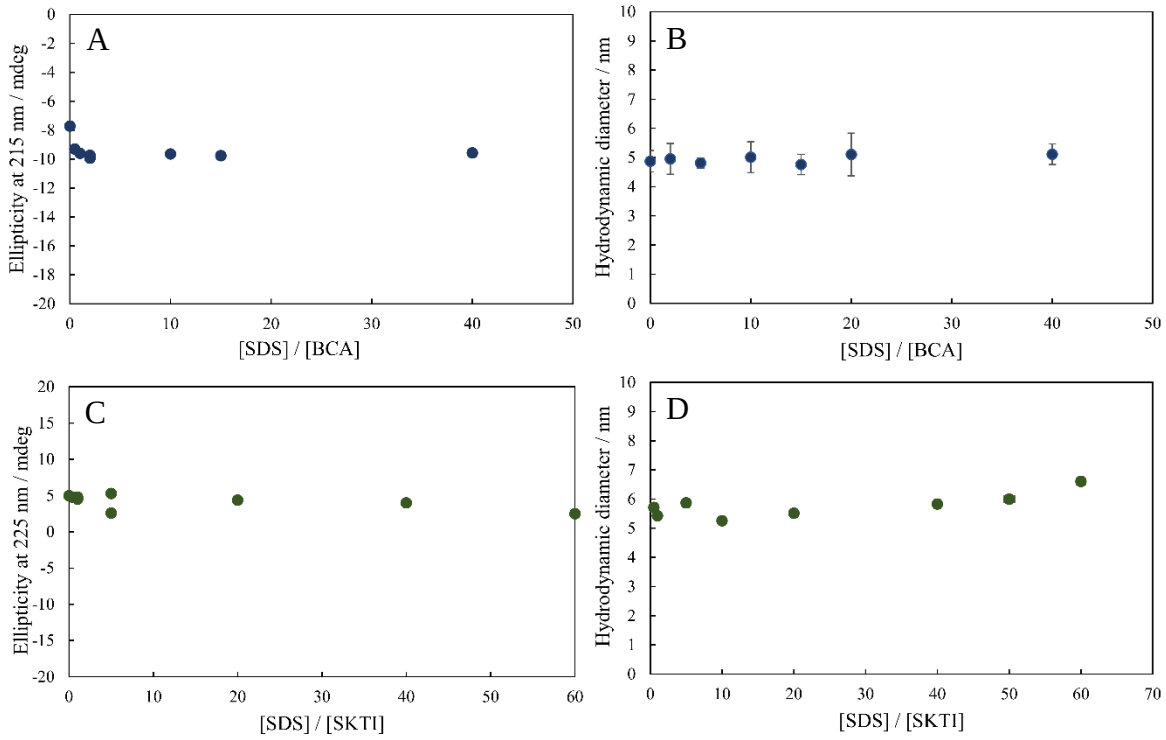

Figure 3.45. *(A) Ellipticity at 215 nm and (B) hydrodynamic diameter of BCA in the absence and in the presence of different SDS concentrations as a function of the ratio SDS/BCA. (C) Ellipticity at 225 nm and (D) hydrodynamic diameter of SKTI in the absence and in the presence of different SDS concentrations as a function of the ratio SDS/SKTI.*

III.5 pH effect

In this section, we investigate the interactions of Mb with NaCOSAN at pH = 7. We worked at pH=7 and pH=10, in order to study how the modification of the pH affects the interactions between Mb and NaCOSAN. As mentioned in section II.1, Mb at pH=10 has more negatively charged amino acid residues, which reduces the electrostatic interaction between Mb and NaCOSAN, which is also negatively charged. However, this is not the case for Mb at pH=7, which is also close to the isoelectric point of Mb.

III.5.1 Mb in the presence of NaCOSAN at two different pH.

Figure 3.46A illustrates the Soret band absorption of Mb in the presence of different NaCOSAN concentrations at pH=7 and at pH=10. We observed that the increase in NaCOSAN concentration leads to a decrease in Soret band absorption for both pH = 7 and pH = 10, the results we extracted from the Mb UV-Vis spectra analysis in the presence of different NaCOSAN concentrations (Figure S3.26). Figure 3.46B depicts the derived Stern-Volmer equation (extracted from fluorescence spectra, Figure S3.27), from which it was not possible

to determine the number of NaCOSAN molecules that bind to Mb at pH = 7 (due to the variation of the experimental points), even though quenching of the fluorescence intensity was observed for pH = 7 and pH = 10. Figure 3.46C shows that the increase of NaCOSAN concentration leads to a slight decrease in the CD signal of Mb at pH=7 from -68 to -61 mdeg approximately. This decrease is much less pronounced than that of Mb at pH=10. As a point of comparison, Figure S3.28 shows the CD of Mb in PBS at pH=7 with increasing temperature, which results in a significant decrease in secondary structure content. The CD signal of the denaturated form of Mb at 90 °C indicates that the presence of NaCOSAN did not significantly alter the tertiary structure of Mb at room temperature and at pH = 7, as was the case at pH = 10. Figure 3.46D shows the hydrodynamic diameter of Mb in the presence of different NaCOSAN concentrations at pH = 7 in comparison with pH = 10. We observed that above a ratio 10 large aggregates (100-1000 nm) exist in the solution at pH=7 which suggests the precipitation of Mb/NaCOSAN system.

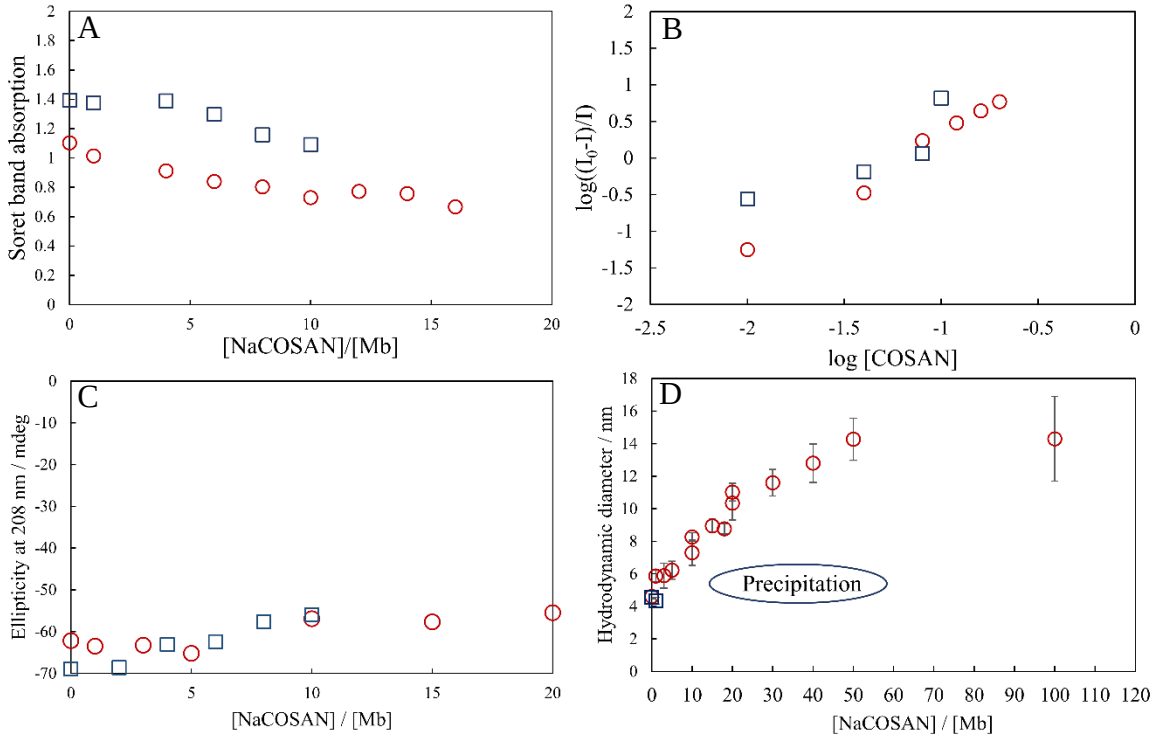

Figure 3.46. *(A) Soret band absorption, (B) fluorescence intensity at 340 nm derived by Stern-Volmer equation, (C) ellipticity at 208 nm (D) hydrodynamic diameter as a function of the ratio NaCOSAN/Mb at pH=10 (red) and at pH=7 (blue).*

Figure 3.47 shows the ellipticity of 0.01 mmol L^{-1} Mb at 208 nm in PBS at pH=7 and at pH=10 as a function of temperature. The temperature at which the denaturation of the secondary structure starts is common for pH=7 and pH=10.

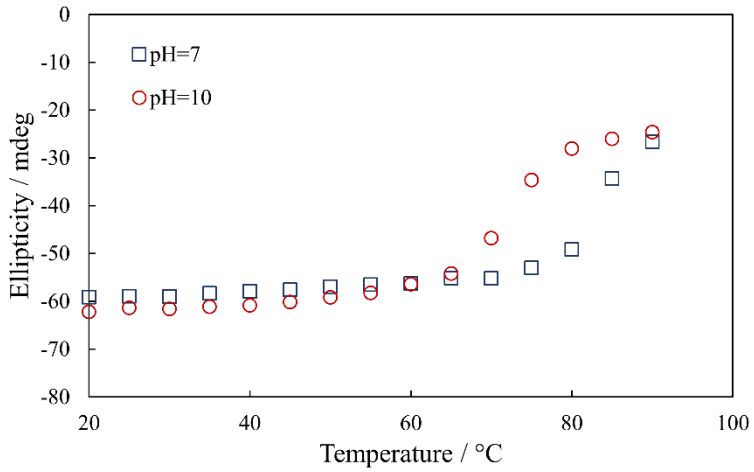

***Figure 3.47**. Ellipticity of 0.01 mmol L^{-1} Mb in PBS at pH=7 (blue squares) and pH=10 (red circles) at 208 nm as a function of temperature.*

In the next step, we studied the interaction of Mb with NaCOSAN at pH = 7 at the supramolecular scale by SAXS. Figure 3.48 depicts the SAXS spectra of 0.1 mmol L^{-1} Mb in PBS at pH=7 in the absence (dark curve) and in the presence of different NaCOSAN concentrations. The SAXS spectra for all the compositions were simultaneously fitted using a tri-axial ellipsoid form factor model. The fitting results indicate that without NaCOSAN, Mb has an ellipsoid shape with a diameter of around 8 nm, which is almost two times that which was calculated for Mb at pH = 10. This suggests that Mb is not in its monomeric state in the solution at pH = 7. The increase in scattered intensity observed as NaCOSAN concentrations increased suggests that NaCOSAN/Mb assemblies are forming (Table 3.13).

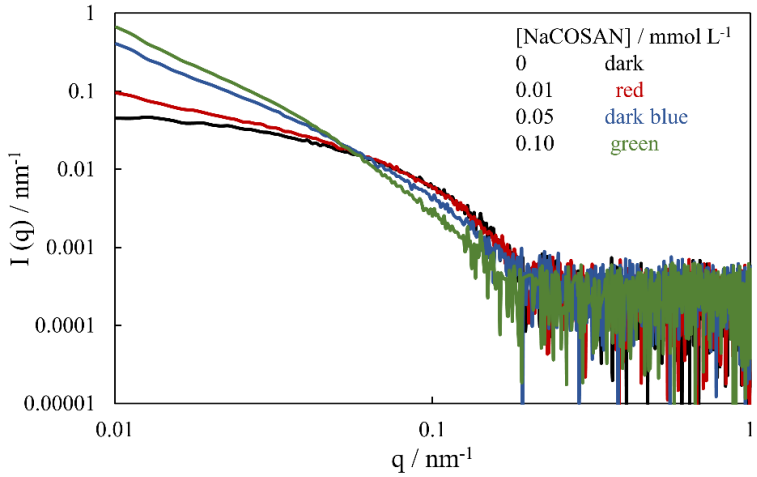

***Figure 3.48.** SAXS spectra of 0.1 mmol L^{-1} Mb in PBS at pH=7 increasing the NaCOSAN concentrations. The spectra were recorded at Soleil.*

Table 3.13: Aggregation number of flattened [NaCOSAN]/[Mb] aggregates and dimensions.

[NaCOSAN]/[Mb]	<Nag>	a-semi axis	b-semi axis	c-semi axis
0	1	4.1	4.1	0.6
1	1.3±0.3	7.8	3.3	0.5
5	3.6±1.4	16.2	5.6	0.4
10	8±3.3	29	8.9	0.32

III.5.2 BCA or SKTI in the presence of NaCOSAN at two different pH.

In the next step, we studied the interactions of NaCOSAN on BCA and SKTI at pH = 7 at the molecular and supramolecular levels. Figure 3.49 depicts the derived Stern-Volmer equation (extracted from fluorescence spectra, Figure S3.29), from which it was determined that the number of NaCOSAN molecules bound to SKTI is 2.2 for pH = 10 and 3.1 for pH = 7. The quenching constant differs significantly for the two different pHs.

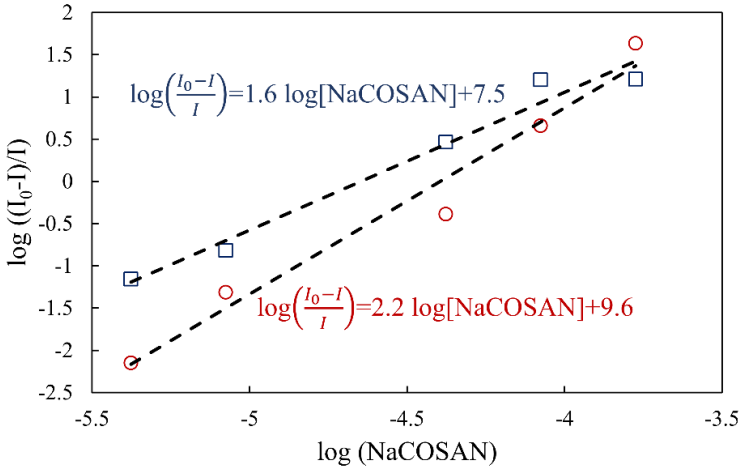

Figure 3.49. *The plot of the derived Stern-Volmer equation for 0.0084 mmol L^{-1} SKTI in PBS at pH=7 (blue) and pH=10 (red) as a function of NaCOSAN concentration. From the plot, n and Kq were calculated to be 2.2 and 3.9 x 10^{9} for pH=10 and 1.6 and 3.1 x 10^{7} mol^{-1} L for pH=7.*

Subsequently, we studied the ellipticity of BCA in the presence of different NaCOSAN concentrations at pH=7 (Figure 3.50A). The ellipticity of BCA is practically unaffected (Figure S3.30) by the increase in NaCOSAN concentration which is not the case at pH=10. Figure 3.50B shows the ellipticity of 0.0055 mmol L^{-1} BCA upon increasing temperature at pH=7 and at pH=10. The temperature at which the denaturation of the secondary structure of BCA starts at 65 °C and is common for pH=7 and pH=10 but not at the same level. However, at

temperatures above this, there is a noticeable difference in the ellipticity of Mb for pH=7 and pH=10.

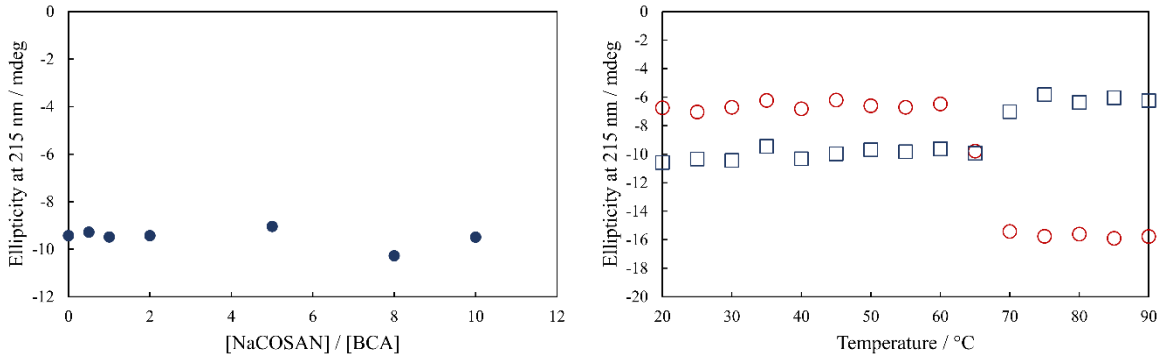

Figure 3.50. *(A) The transition curve of 0.0055 mmol L^{-1} BCA in PBS at pH=7 in the absence of NaCOSAN monitored by the CD ellipticity at 215 nm as a function of [NaCOSAN]/[BCA]. (B) Ellipticity of 0.0055 mmol L^{-1} BCA in PBS at pH=7 (blue squares) and pH=10 (red circles) at 215 nm as a function of temperature.*

In the next step, we studied the effect of the interactions of NaCOSAN with BCA and SKTI at pH=7 and at the supramolecular level by DLS. Figure 3.51A depicts the hydrodynamic diameter of BCA, which increases with the increase of NaCOSAN concentration above ratio 5, as in the case of BCA in the presence of NaCOSAN at pH = 10. Figure 3.51B shows the hydrodynamic diameter of BCA, which increases with the increase of NaCOSAN concentration until ratio 10, and then bigger aggregates appear in the solution, which suggests precipitation of the NaCOSAN/SKTI system.

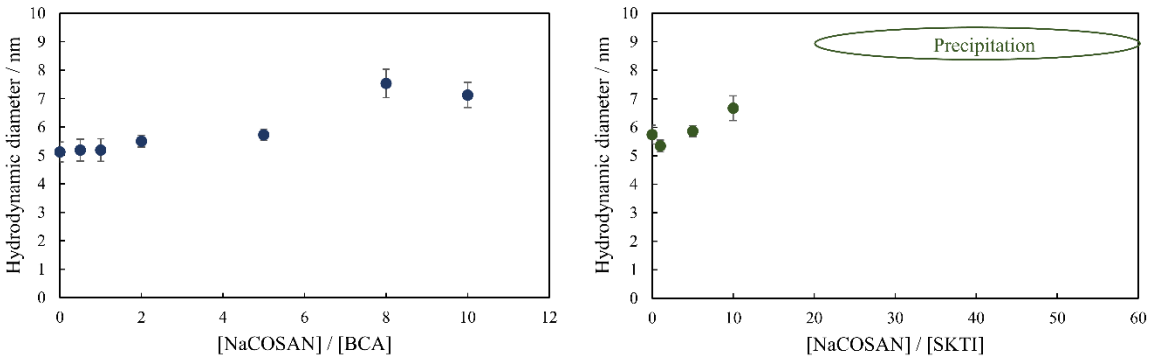

Figure 3.51. *Hydrodynamic diameter of 0.055 mol L^{-1} BCA (left) and 0.0084 mol L^{-1} SKTI (right) in PBS at pH=7 in the presence of different NaCOSAN concentrations as a function of [NaCOSAN]/[BCA] or [NaCOSAN]/[SKTI].*

III.5.3 Mb in the presence of NaSCN at two different pH.

In this section, we study the effect the chaotropic salt, NaSCN, at pH = 7 on Mb. Figure 3.52A shows the ellipticity (extracted from the CD spectra, Figure S3.31) of Mb in the presence of

NaSCN at pH = 7 and pH = 10. The secondary structure content of Mb is not affected by the presence of NaSCN, neither at pH 7 nor at pH 10. Figure 3.52B shows the ellipticity of Mb in the presence of NaSCN at pH = 7 and pH = 10 as a function of temperature. The temperature at which the denaturation of the secondary structure of Mb in the presence of NaSCN starts at 65°C and is common for pH=7 and pH=10 but above this temperature the ellipticity differs significantly for the pH=7 and pH=10.

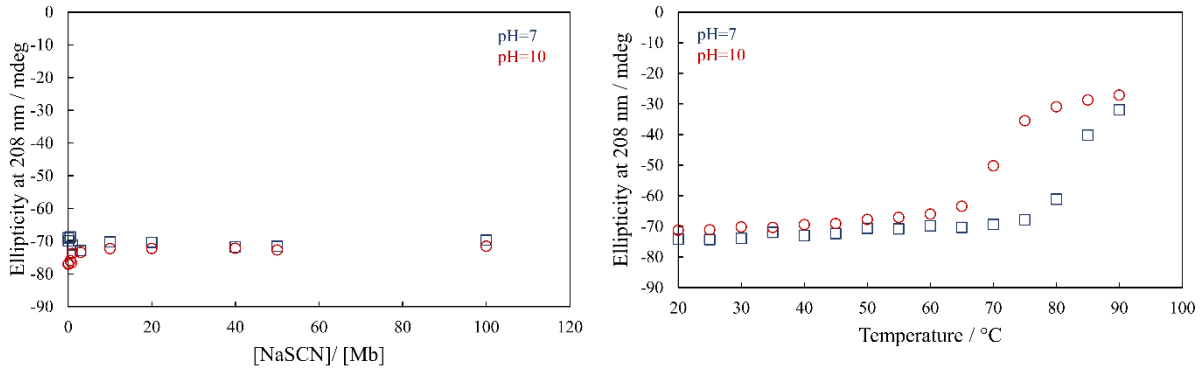

Figure 3.52. *(A) The transition curve of 0.01 mol L^{-1} Mb in PBS at pH=7 (blue squares) and pH=10 (red squares) in the absence and in the presence of NaSCN monitored by the CD ellipticity at 208 nm as a function of [NaSCN]/[Mb]. (B) Ellipticity of 0.01 mmol L^{-1} Mb in the presence of 0.1 mmol L^{-1} NaSCN in PBS at pH=7 (blue squares) and pH=10 (red circles) at 208 nm as a function of temperature.*

III.5.4 Mb in the presence of SDS at two different pH.

In this section we studied the interactions of Mb with SDS at pH =7 at the molecular level. Figure 3.53A illustrates the Soret band absorption of Mb in the presence of different SDS concentrations at pH=7 and at pH=10. We observed that the increase in SDS concentration leads to a decrease in Soret band absorption for both pH = 7 and pH = 10, the results we extracted from the UV-Vis spectra of Mb in the presence of different SDS concentrations (Figure S3.33A).

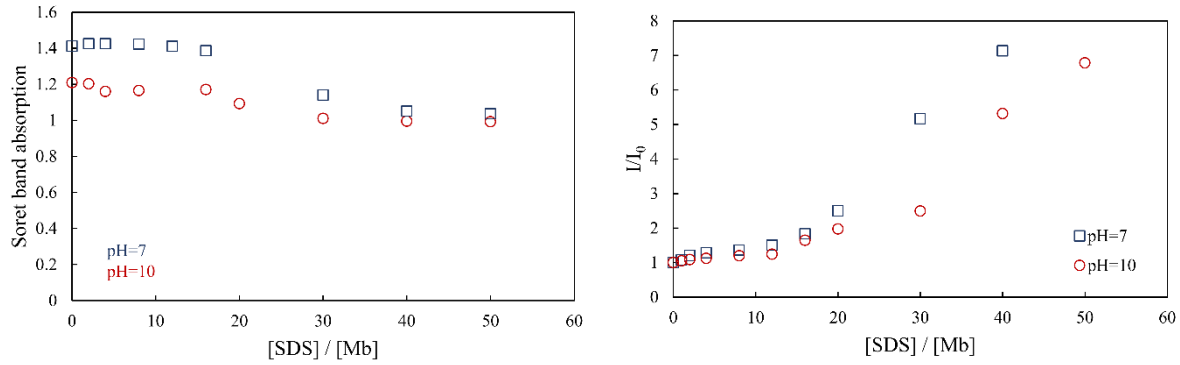

Figure 3.53. *(A) Soret band absorption and (B) fluorescence intensity at 340 nm as a function of the ratio SDS/Mb at pH=10 (red circles) and at pH=7 (blue squares).*

Figure 3.53B depicts the normalized fluorescence intensity of Mb in the presence of SDS (extracted from fluorescence spectra, Figure S3.33 B). The effect of adding SDS is a large increase in the fluorescence intensity at pH=7 and pH=10 until ratio 20. Above this ratio, the normalized intensity of Mb in the presence of SDS appears to increase more sharply in comparison to that at pH=10.

III.6 SAXS-fit parameters used in this chapter

All the combined SAXS data were fitted using the software SASfit 0.94.10 version. The SAXS intensity I (q) in absolute unit, cm^{-1} or nm^{-1} for isotropically distributed scattering particles can be described as in the modelling procedure presented in the supporting information of Chapter II.

Estimation of scattering length density (SLD or ρ)

The scattering length density was calculated by following the equations that were also described in the modelling procedure in the supporting information of Chapter II. We can see in Table 3.14 that the scattering length density (ρ_{SAXS}) for water and COSAN is very close and that the ρ_{SAXS} for protein is much lower. Therefore, the contrast (Δρ), is mainly produced by the protein. This was verified experimentally by comparing the scattering curves of COSAN in water and Mb in water.

Table 3.14: Scattering length Densities for X-rays

Substance	**Formula**	**Molar mass (g/mol)**	**Density (g/cm3)**	**Vm ($10^{-22}cm^3$)**	**Z**	**ρ_{SAXS} ($10^{10}cm^{-2}$)**
Water	H_2O	18.01	0.99	0.30	10	9.43
Cobalt-bis-dicarbollide	$(C_2B_9H_{11})_2Co$	346.74	-	4.48	16	10.36
Protein	-	-	-	0.15[61]	-	1.8[62,63]

Fitting procedure

The scattered intensity for isotropically distributed scatterers in space can be expressed as:

$$I(q) = NV^2(\Delta\rho)^2P(q)S(q) + I_b$$

The contrast (Δρ), which is directly related to the electron density difference between the protein assemblies and the surrounding solution, in this case PBS, was one of the fixed parameters, and tabulated value were used (Table S3.14). The I_b is the background scattering intensity, which was also one of the fixed parameters, taken from the constant intensity at high q. The structure factor, S(q), was not applied because it was assumed that electrostatic inter-aggregate repulsions were negligible, as the proteins are used at low concentrations.

Form factor:

Different form factors from the SASfit libraries, [64] have been tried to fit the SAXS spectra such as: spherical form factor, spherical core-shell form factor, disc form factor and triaxial ellipsoid shell.

The triaxial ellipsoid shell model from the SASfit library gave the best fit with the minimum of fitting parameters (i.e., the only model that enabled to fully fit the experimental data with a physical meaning and in absolute value). The tri-axial ellipsoid was also used to fit the SANS data in Chapter II, where a detailed description of the model is provided.

The scattered intensity was scaled by N, where N is the number density of the scattering objects, i.e., the NaCOSAN/protein assemblies. N, a, b and c are fitting parameters.

Table 3.15: Some examples of the best-fitting parameters for the SAXS data of NaCOSAN/Mb assemblies. Fixed parameters are shown with a grey background.

		R*	R*	R*	R*	R*
Parameters	Units	0	1	5	10	40
Background	cm^{-1}	0.0002	0.0002	0.0002	0.0002	0.0002
a-semi axis of elliptical	nm	2.3	6.9	9.5	10	16
b-semi axis of elliptical	nm	2.3	2	3	4.4	6
c-semi axis of elliptical	nm	2.3	1.7	1.7	1.8	2.3
$V_{ellipsoid}$	nm^3	50	98	202	331	924
Number of the aggregates (N)	None	0.0000605	0.000035	0.000017	0.000012	0.0000045
$\rho_{protein}$	10^{-6} Å^{-2}	1.8	1.8	1.8	1.8	1.8
ρ_{PBS}	10^{-6} Å^{-2}	9.43	9.43	9.43	9.43	9.43
V_{ell}/V_{Mb} (Nag)	None	1	1.9	3.9	6.5	18
N/N_{Mb} (Nag)	None	1	1.7	3.6	5	13

*R= Ratio of [NaCOSAN]/[Mb]

III.7 Conclusions of Chapter III

In this chapter, we studied the interactions of boron clusters on three different proteins with different features at the molecular and supramolecular scales.

The increase in NaCOSAN concentration leads to a decrease in the intensity of the Soret band, which suggests that NaCOSAN interacts with the heme group, as expected by the opposite charges of NaCOSAN and of the heme. No change in the position of Soret band, indicates that the heme moiety does not exposes from inner hydrophobic pocket to the outer part of the subunit. To determine whether NaCOSAN interacts specifically with the heme group or not, we studied hemin. We observe here only a very slight decrease in the intensity of the Soret band upon addition of NaCOSAN. We conclude here that NaCOSAN interacts stronger with heme when it is inserted into the hydrophobic pocket of Mb.

The presence of NaCOSAN quenched the fluorescence spectrum of Mb, which suggests that the structure of Mb has been modified in the presence of NaCOSAN. When tryptophan is buried under the core, it is in a hydrophobic environment, and therefore higher fluorescence intensity is observed. On the other hand, when tryptophan is in a hydrophilic environment, it is exposed to the solvent, and due to this, lower fluorescence intensities are observed. We can conclude here that the tryptophan has become more exposed to the solvent in the presence of NaCOSAN.

CD results confirm the slight modifications in the secondary structure content of Mb in the presence of NaCOSAN. We also found from CD results that NaCOSAN prevents partially the temperature denaturation of Mb at high temperatures ($T > 65 - 90$ °C).

In the next step, the study at the supramolecular scales reveals the formation of NaCOSAN/Mb assemblies. DLS results shows an immediate increase in the hydrodynamic diameter upon addition of NaCOSAN from 4 to 15 nm which suggest protein assemblies. Then, SAXS and SANS confirm the formation of NaCOSAN/Mb assemblies. Upon addition of NaCOSAN, Mb starts to aggregate by forming dimers. Then by further addition of NaCOSAN the aggregates elongate in 2D forming flattened aggregates with one of the dimension being increased more than two times than the other. At this point, it is worth highlighting that the fluorescence quenching could be due to the direct effect of NaCOSAN to tryptophan or indirect effect due to the association between the proteins. We can conclude that NaCOSAN play the role of the glue for the formation of the controlled NaCOSAN/Mb assemblies.

Subsequently, we compare the effects of NaCOSAN on Mb with two other proteins, the BCA and the SKTI. The two proteins differ from Mb in terms of secondary structure content and the absence of a heme group. The presence of NaCOSAN quenched the fluorescence spectrum of BCA and SKTI, which suggests that the structure of BCA and SKTI has been modified in the presence of NaCOSAN. CD results confirm the slight modifications in the secondary structure content of BCA and SKTI in the presence of NaCOSAN. DLS results show an increase in the hydrodynamic diameter of BCA and SKTI upon addition of NaCOSAN, which suggests protein assemblies. However, this increase was not immediate like in the case of Mb. The increase in the hydrodynamic diameter was observed at ratios of 10 and 15 for BCA and SKTI, respectively. Then, SAXS revealed that NaCOSAN acts as glue for the formation of controlled NaCOSAN/BCA or NaCOSAN/SKTI assemblies.

Subsequently, the interactions of NaSCN with Mb were investigated at the molecular and supramolecular scales. NaSCN is a classical chaotropic ion of Hofmeister series. The interactions between Mb and NaSCN are negligible compared to the interactions with NaCOSAN. The increase in NaSCN concentration does not affect either the secondary structure content or the hydrodynamic diameter of Mb, which is not the case for NaCOSAN. The absorption spectra of the heme reveal that the interaction between Mb and NaCOSAN is not solely electrostatic, as there is no variation in absorption spectra in the presence of NaSCN.

In the next step, we investigate the interactions of the three proteins with other boron clusters that are less superchaotropes than NaCOSAN, such as $Na_2B_{12}H_{12}$, $Na_2B_{12}Cl_{12}$, and $Na_2B_{12}I_{12}$. The studies at the molecular and supramolecular scales shows that $Na_2B_{12}I_{12}$, the largest and most chaotropic one after NaCOSAN, interacts with the proteins and forms assemblies as in the case of NaCOSAN. Following then, we study the effect on the three proteins in the presence of the $Na_2B_{12}Cl_{12}$, which is one of the intermediaries in size and chaotropicity. We found that $Na_2B_{12}Cl_{12}$ did not interact with the proteins and therefore did not form assemblies like the more superchaotropic ions. Similarly, the $Na_2B_{12}H_{12,}$ which is the smallest and least chaotropic in this series, did not show any effect on Mb at the molecular scale. These observations indicates that the (super-)chaotropicity plays an important role on the formation of controlled boron cluster/proteins assemblies. The lesser is the (super-) chaotropicity of the boron clusters the less interactions between boron clusters and proteins leads to lack of the ability to form controlled proteins assemblies.

Subsequently, the interactions of SDS with the three proteins were investigated at the molecular and supramolecular scales. The conclusion that arises from this part of the study is that the interactions between Mb and SDS are much less pronounced than those between Mb and NaCOSAN. The two other proteins, BCA and SDS, are practically unaffected by the presence of SDS, as revealed by CD and DLS.

To conclude, regardless of the three investigated proteins, we observed an aggregation process with a finite size and molar ratio dependence. The observed ratio at which the aggregate forms decrease with increasing (super)chaotropicity ($Na_2B_{12}H_{12}$ < $Na_2B_{12}Cl_{12}$ < $Na_2B_{12}I_{12}$ < NaCOSAN). Working at high pH values, always beyond their isoelectric point where the proteins are mainly negative, we demonstrated that the superchaotropic and/or hydrophobic feature of the ions is essential and acts at a relatively low concentration (1–100 mmol L^{-1} of salt).

These mixed assemblies appear to have an anisotropic form, flattened assemblies. The aggregation phenomenon was unexpected in and of itself, with the nano-ions acting as molecular glue and the proteins within these assemblies being only partially denaturated, contrary to what we anticipated when using chaotropic salts! At this point, it is worth highlighting that protein assembly is a significant phenomenon,[65–67] and here we discovered that nano-ions can promote and control protein assembly. This general process applies to different proteins. The formation of nano-ions/proteins assemblies results from the versatile interaction between nano-ions and proteins, combining electrostatic interaction, dihydrogen bonds, hydrophobicity, and the superchaotropic effect.

These studies suggest that the hydrophobic subdomains appear to be more exposed to the aqueous solution depending on the strength of the interaction between the nano-ions and the protein, which may be a mechanism at the onset of aggregation. It appears that the effect of the interaction between superchaotropic nano-ions and proteins is not specific, but rather dependent on many binding sites (hydrophobic pockets, tryptophan, etc.). A comprehensive analysis of the spectral responses is required for full comprehension.

References

[1] J. Zeng, X. Gao, Z. Dai, B. Tang, X.F. Tang, Effects of metal ions on stability and activity of hyperthermophilic pyrolysin and further stabilization of this enzyme by modification of a Ca2+-binding site, Appl. Environ. Microbiol. 80 (2014) 2763–2772. https://doi.org/10.1128/AEM.00006-14.

[2] H. Zhao, Protein Stabilization and Enzyme Activation in Ionic Liquids: Specific Ion Effects, J. Chem. Technol. Biotechnol. 91 (2016) 25–50. https://doi.org/10.1002/jctb.4837.

[3] M.L. Berkowitz, R. Vácha, Aqueous solutions at the interface with phospholipid bilayers, Acc. Chem. Res. 45 (2012) 74–82. https://doi.org/10.1021/ar200079x.

[4] H.I. Petrache, T. Zemb, L. Belloni, V.A. Parsegian, Salt screening and specific ion adsorption determine neutral-lipid membrane interactions, Proc. Natl. Acad. Sci. U. S. A. 103 (2006) 7982–7987. https://doi.org/10.1073/pnas.0509967103.

[5] H.C. Visser, D.M. Rudkevich, W. Verboom, F. Jong, D.N. Reinhoudt, Anion carrieer mediated membrane transport of phosphate: selectivity of H2PO4- over Cl-, J. Am. Chem. Soc. 116 (1994) 11554–11555.

[6] M. Boström, D.R.M. Williams, B.W. Ninham, Specific ion effects: Why the properties of lysozyme in salt solutions follow a hofmeister series, Biophys. J. 85 (2003) 686–694. https://doi.org/10.1016/S0006-3495(03)74512-3.

[7] J. Kozuch, C. Steinem, P. Hildebrandt, D. Millo, Combined electrochemistry and surface-enhanced infrared absorption spectroscopy of gramicidin A incorporated into tethered bilayer lipid membranes, Angew. Chemie - Int. Ed. 51 (2012) 8114–8117. https://doi.org/10.1002/anie.201203214.

[8] R. Holm, C. Schönbeck, P. Somprasirt, P. Westh, H. Mu, A study of salt effects on the complexation between β-cyclodextrins and bile salts based on the Hofmeister series, J. Incl. Phenom. Macrocycl. Chem. 80 (2014) 243–251. https://doi.org/10.1007/s10847-014-0383-9.

[9] K.D. Collins, Ions from the Hofmeister series and osmolytes: Effects on proteins in solution and in the crystallization process, Methods. 34 (2004) 300–311. https://doi.org/10.1016/j.ymeth.2004.03.021.

[10] T. Arakawa, S.N. Timasheff, Preferential Interactions of Proteins with Salts in Concentrated Solutions1" It seemed of interest, therefore, to in, Biochem. Timasheff Inoue Gekko Timasheff. 21 (1982) 6545–6552.

[11] L. Vrbka, P. Jungwirth, P. Bauduin, D. Touraud, W. Kunz, Specific ion effects at protein surfaces: A molecular dynamics study of bovine pancreatic trypsin inhibitor and horseradish peroxidase in selected salt solutions, J. Phys. Chem. B. 110 (2006) 7036–7043. https://doi.org/10.1021/jp0567624.

[12] K.I. Assaf, B. Begaj, A. Frank, M. Nilam, A.S. Mougharbel, U. Kortz, J. Nekvinda, B. Grüner, D. Gabel, W.M. Nau, High-Affinity Binding of Metallacarborane Cobalt Bis(dicarbollide) Anions to Cyclodextrins and Application to Membrane

Translocation, J. Org. Chem. 84 (2019) 11790–11798. https://doi.org/10.1021/acs.joc.9b01688.

[13] J. Warneke, C. Jenne, J. Bernarding, V.A. Azov, M. Plaumann, Evidence for an intrinsic binding force between dodecaborate dianions and receptors with hydrophobic binding pockets, Chem. Commun. 52 (2016) 6300–6303. https://doi.org/10.1039/c6cc01233g.

[14] K.I. Assaf, W.M. Nau, The Chaotropic Effect as an Assembly Motif in Chemistry, Angew. Chemie - Int. Ed. 57 (2018) 13968–13981. https://doi.org/10.1002/anie.201804597.

[15] B. Naskar, O. Diat, V. Nardello-Rataj, P. Bauduin, Nanometer-Size Polyoxometalate Anions Adsorb Strongly on Neutral Soft Surfaces, J. Phys. Chem. C. 119 (2015) 20985–20992. https://doi.org/10.1021/acs.jpcc.5b06273.

[16] T. Buchecker, P. Schmid, S. Renaudineau, O. Diat, A. Proust, A. Pfitzner, P. Bauduin, Polyoxometalates in the Hofmeister series, Chem. Commun. 54 (2018) 1833–1836. https://doi.org/10.1039/c7cc09113c.

[17] M. Hohenschutz, I. Grillo, O. Diat, P. Bauduin, How Nano-Ions Act Like Ionic Surfactants, Angew. Chemie Int. Ed. 59 (2020) 8084–8088. https://doi.org/10.1002/anie.201916193.

[18] I. Fuentes, T. García-Mendiola, S. Sato, M. Pita, H. Nakamura, E. Lorenzo, F. Teixidor, F. Marques, C. Viñas, Metallacarboranes on the Road to Anticancer Therapies: Cellular Uptake, DNA Interaction, and Biological Evaluation of Cobaltabisdicarbollide [COSAN]−, Chem. - A Eur. J. 24 (2018) 17239–17254. https://doi.org/10.1002/chem.201803178.

[19] T.M. Goszczyński, K. Fink, K. Kowalski, Z.J. Leśnikowski, J. Boratyński, Interactions of Boron Clusters and their Derivatives with Serum Albumin, Sci. Rep. 7 (2017) 1–12. https://doi.org/10.1038/s41598-017-10314-0.

[20] D. Kaniowski, K. Kulik, K. Ebenryter-Olbińska, E. Wielgus, Z. Leśnikowski, B. Nawrot, Metallacarborane complex boosts the rate of dna oligonucleotide hydrolysis in the reaction catalyzed by snake venom phosphodiesterase, Biomolecules. 10 (2020). https://doi.org/10.3390/biom10050718.

[21] R. Fernandez-Alvarez, V. Ďorďovič, M. Uchman, P. Matějíček, Amphiphiles without Head-and-Tail Design: Nanostructures Based on the Self-Assembly of Anionic Boron Cluster Compounds, Langmuir. 34 (2018) 3541–3554. https://doi.org/10.1021/acs.langmuir.7b03306.

[22] J. Rak, M. Jakubek, R. Kaplánek, P. Matějíček, V. Král, Cobalt bis(dicarbollide) derivatives: Solubilization and self-assembly suppression, Eur. J. Med. Chem. 46 (2011) 1140–1146. https://doi.org/10.1016/j.ejmech.2011.01.032.

[23] J. Rak, B. Dejlová, H. Lampová, R. Kaplánek, P. Matějíček, P. Cígler, V. Král, On the solubility and lipophilicity of metallacarborane pharmacophores, Mol. Pharm. 10 (2013) 1751–1759. https://doi.org/10.1021/mp300565z.

[24] P. Cígler, M. Kožíšek, P. Řezáčová, J. Brynda, Z. Otwinowski, J. Pokorná, J. Plešek,

B. Grüner, L. Dolečková-Marešová, M. Máša, J. Sedláček, J. Bodem, H.G. Kräusslich, V. Král, J. Konvalinka, From nonpeptide toward noncarbon protease inhibitors: Metallacarboranes as specific and potent inhibitors of HIV protease, Proc. Natl. Acad. Sci. U. S. A. 102 (2005) 15394–15399. https://doi.org/10.1073/pnas.0507577102.

[25] B. Grüner, M. Kugler, S. El Anwar, J. Holub, J. Nekvinda, D. Bavol, Z. Růžičková, K. Pospíšilová, M. Fábry, V. Král, J. Brynda, P. Řezáčová, Cobalt Bis(dicarbollide) Alkylsulfonamides: Potent and Highly Selective Inhibitors of Tumor Specific Carbonic Anhydrase IX, Chempluschem. 86 (2021) 352–363. https://doi.org/10.1002/cplu.202000574.

[26] M. Kožíšek, P. Cígler, M. Lepšík, J. Fanfrlík, P. Řezáčová, J. Brynda, J. Pokorná, J. Plešek, B. Grüner, K.G. Šašková, J. Václavíková, V. Král, J. Konvalinka, Inorganic polyhedral metallacarborane inhibitors of HIV protease: A new approach to overcoming antiviral resistance, J. Med. Chem. 51 (2008) 4839–4843. https://doi.org/10.1021/jm8002334.

[27] J. Brynda, P. Mader, V. Šícha, M. Fábry, K. Poncová, M. Bakardiev, B. Grüner, P. Cígler, P. Řezáčová, Carborane-based carbonic anhydrase inhibitors, Angew. Chemie - Int. Ed. 52 (2013) 13760–13763. https://doi.org/10.1002/anie.201307583.

[28] A.J. Salmon, M.L. Williams, Q.K. Wu, J. Morizzi, D. Gregg, S.A. Charman, D. Vullo, C.T. Supuran, S. Poulsen, S. Fiorentino, Metallocene-Based Inhibitors of Cancer-Associated Carbonic Anhydrase Enzymes IX and XII, (2012).

[29] B. Grüner, J. Brynda, V. Das, V. Šícha, J. Štěpánková, J. Nekvinda, J. Holub, K. Pospíšilová, M. Fábry, P. Pachl, V. Král, M. Kugler, V. Mašek, M. Medvedíková, S. Matějková, A. Nová, B. Lišková, S. Gurská, P. Džubák, M. Hajdúch, P. Řezáčová, Metallacarborane Sulfamides: Unconventional, Specific, and Highly Selective Inhibitors of Carbonic Anhydrase IX, J. Med. Chem. 62 (2019) 9560–9575. https://doi.org/10.1021/acs.jmedchem.9b00945.

[30] K. Fink, K. Kobak, M. Kasztura, Synthesis and Biological Activity of Thymosin β 4-Anionic Boron Cluster Conjugates , (2018) 4–10. https://doi.org/10.1021/acs.bioconjchem.8b00646.

[31] K. Fink, J. Boraty, Metallacarboranes as a tool for enhancing the activity of therapeutic peptides, 1457 (2019) 128–141. https://doi.org/10.1111/nyas.14201.

[32] M. Gozzi, B. Schwarze, E. Hey-Hawkins, Preparing (Metalla)carboranes for Nanomedicine, ChemMedChem. 16 (2021) 1533–1565. https://doi.org/10.1002/cmdc.202000983.

[33] J. Cebula, K. Fink, J. Boratyński, T.M. Goszczyński, Supramolecular chemistry of anionic boron clusters and its applications in biology, Coord. Chem. Rev. 477 (2023). https://doi.org/10.1016/j.ccr.2022.214940.

[34] M. Tarrés, E. Canetta, E. Paul, J. Forbes, K. Azzouni, C. Viñas, F. Teixidor, A.J. Harwood, Biological interaction of living cells with COSAN-based synthetic vesicles, Sci. Rep. 5 (2015) 1–8. https://doi.org/10.1038/srep07804.

[35] C. Verdiá-Báguena, A. Alcaraz, V.M. Aguilella, A.M. Cioran, S. Tachikawa, H. Nakamura, F. Teixidor, C. Viñas, Amphiphilic COSAN and I2-COSAN crossing

synthetic lipid membranes: Planar bilayers and liposomes, Chem. Commun. 50 (2014) 6700–6703. https://doi.org/10.1039/c4cc01283f.

[36] A. Barba-Bon, G. Salluce, I. Lostalé-Seijo, K.I. Assaf, A. Hennig, J. Montenegro, W.M. Nau, Boron clusters as broadband membrane carriers, Nat. |. 603 (2022) 637. https://doi.org/10.1038/s41586-022-04413-w.

[37] A.B. Anderson, C.R. Robertson, Absorption spectra indicate conformational alteration of myoglobin adsorbed on polydimethylsiloxane, Biophys. J. 68 (1995) 2091–2097. https://doi.org/10.1016/S0006-3495(95)80388-7.

[38] F.A. Lima, T.J. Penfold, R.M. Van Der Veen, M. Reinhard, R. Abela, I. Tavernelli, U. Rothlisberger, M. Benfatto, C.J. Milne, M. Chergui, Probing the electronic and geometric structure of ferric and ferrous myoglobins in physiological solutions by Fe K-edge absorption spectroscopy, Phys. Chem. Chem. Phys. 16 (2014) 1617–1631. https://doi.org/10.1039/c3cp53683a.

[39] J. Kundu, U. Kar, S. Gautam, S. Karmakar, P.K. Chowdhury, Unusual effects of crowders on heme retention in myoglobin, FEBS Lett. 589 (2015) 3807–3815. https://doi.org/10.1016/j.febslet.2015.11.015.

[40] J. Uddin, Macro To Nano Spectroscopy, IntechOpen, 2012.

[41] L. Tofani, A. Feis, R.E. Snoke, D. Berti, P. Baglioni, G. Smulevich, Spectroscopic and interfacial properties of myoglobin/surfactant complexes, Biophys. J. 87 (2004) 1186–1195. https://doi.org/10.1529/biophysj.104.041731.

[42] A. Kumar, P. Venkatesu, A comparative study of myoglobin stability in the presence of Hofmeister anions of ionic liquids and ionic salts, Process Biochem. 49 (2014) 2158–2169. https://doi.org/10.1016/j.procbio.2014.09.014.

[43] M. V. Kuperman, M.Y. Losytskyy, A.Y. Bykov, S.M. Yarmoluk, K.Y. Zhizhin, N.T. Kuznetsov, O.A. Varzatskii, E. Gumienna-Kontecka, V.B. Kovalska, Effective binding of perhalogenated closo-borates to serum albumins revealed by spectroscopic and ITC studies, J. Mol. Struct. 1141 (2017) 75–80. https://doi.org/10.1016/j.molstruc.2017.03.059.

[44] J.R. Lakowicz, Principles of Fluorescence Spectroscopy, 3rd ed., Springer, New York, 2006.

[45] A.I. Stoica, C. Viñas, F. Teixidor, Cobaltabisdicarbollide anion receptor for enantiomer-selective membrane electrodes, Chem. Commun. (2009) 4988–4990. https://doi.org/10.1039/b910645f.

[46] C. Louis-Jeune, M.A. Andrade-Navarro, C. Perez-Iratxeta, Prediction of protein secondary structure from circular dichroism using theoretically derived spectra, Proteins Struct. Funct. Bioinforma. 80 (2012) 374–381. https://doi.org/10.1002/prot.23188.

[47] M. Kataoka, I. Nishii, T. Fujisawa, T. Ueki, F. Tokunaga, Y. Goto, Structural characterization of the molten globule and native states of apomyoglobin by solution x-ray scattering, J. Mol. Biol. 249 (1995) 215–228. https://doi.org/10.1006/jmbi.1995.0290.

[48] S. Ali, H. Farooqi, R. Prasad, M. Naime, I. Routray, S. Yadav, F. Ahmad, Boron stabilizes peroxide mediated changes in the structure of heme proteins, Int. J. Biol. Macromol. 47 (2010) 109–115. https://doi.org/10.1016/j.ijbiomac.2010.05.013.

[49] I. Fuentes, J. Pujols, C. Viñas, S. Ventura, F. Teixidor, Dual Binding Mode of Metallacarborane Produces a Robust Shield on Proteins, Chem. - A Eur. J. 25 (2019) 12820–12829. https://doi.org/10.1002/chem.201902796.

[50] H. Essa, E. Magner, J. Cooney, B.K. Hodnett, Influence of pH and ionic strength on the adsorption, leaching and activity of myoglobin immobilized onto ordered mesoporous silicates, J. Mol. Catal. B Enzym. 49 (2007) 61–68. https://doi.org/10.1016/j.molcatb.2007.07.005.

[51] A. Rana, T.P. Gupta, S. Bansal, B. Kundu, Formation of amyloid fibrils by bovine carbonic anhydrase, Biochim. Biophys. Acta - Proteins Proteomics. 1784 (2008) 930–935. https://doi.org/10.1016/j.bbapap.2008.02.020.

[52] R. Afrin, M.T. Alam, A. Ikai, Pretransition and progressive softening of bovine carbonic anhydrase II as probed by single molecule atomic force microscopy, Protein Sci. 14 (2009) 1447–1457. https://doi.org/10.1110/ps.041282305.

[53] R.M. Sweet, D.M. Blow, H.T. Wright, J. Janin, C.H. Chothia, Crystal structure of the complex of porcine trypsin with soybean trypsin inhibitor (kunitz) at 2.6 Å resolution, Biochemistry. 13 (1974) 4212–4228. https://doi.org/10.1021/bi00717a024.

[54] H.K. Song, S.W. Suh, Kunitz-type soybean trypsin inhibitor revisited: Refined structure of its complex with porcine trypsin reveals an insight into the interaction between a homologous inhibitor from Erythrina caffra and tissue-type plasminogen activator, J. Mol. Biol. 275 (1998) 347–363. https://doi.org/10.1006/jmbi.1997.1469.

[55] R. Roychaudhuri, G. Sarath, M. Zeece, J. Markwell, Stability of the allergenic soybean Kunitz trypsin inhibitor, Biochim. Biophys. Acta - Proteins Proteomics. 1699 (2004) 207–212. https://doi.org/10.1016/j.bbapap.2004.02.014.

[56] R.W. Woody, Structural composition of β_I- and β_{II}- proteins, (2003) 384–388. https://doi.org/10.1110/ps.0235003.The.

[57] B. Kundu, P. Guptasarma, Use of a hydrophobic dye to indirectly probe the structural organization and conformational plasticity of molecules in amorphous aggregates of carbonic anhydrase, 293 (2002) 572–577.

[58] R. Eisert, L. Felau, L.R. Brown, Methods for enhancing the accuracy and reproducibility of Congo red and thio X avin T assays, 353 (2006) 144–146. https://doi.org/10.1016/j.ab.2006.03.015.

[59] K.I. Assaf, D. Gabel, W. Zimmermann, W.M. Nau, High-affinity host-guest chemistry of large-ring cyclodextrins, Org. Biomol. Chem. 14 (2016) 7702–7706. https://doi.org/10.1039/c6ob01161f.

[60] P. Bauduin, S. Prevost, P. Farràs, F. Teixidor, O. Diat, T. Zemb, A theta-shaped amphiphilic cobaltabisdicarbollide anion: Transition from monolayer vesicles to micelles, Angew. Chemie - Int. Ed. 50 (2011) 5298–5300. https://doi.org/10.1002/anie.201100410.

[61] N.S.K. Gunda, S.K. Mitra, Modeling of dielectrophoretic transport of myoglobin molecules in microchannels, Biomicrofluidics. 4 (2010) 1–20. https://doi.org/10.1063/1.3339773.

[62] S. Longeville, W. Doster, G. Kali, Myoglobin in crowded solutions: Structure and diffusion, Chem. Phys. 292 (2003) 413–424. https://doi.org/10.1016/S0301-0104(03)00292-1.

[63] K. Ibel, H.B. Stuhrmann, Comparison of neutron and X-ray scattering of dilute myoglobin solutions, J. Mol. Biol. 93 (1975) 255–265. https://doi.org/10.1016/0022-2836(75)90131-X.

[64] I. Breßler, J. Kohlbrecher, A.F. Thünemann, SASfit: A tool for small-angle scattering data analysis using a library of analytical expressions, J. Appl. Crystallogr. 48 (2015) 1587–1598. https://doi.org/10.1107/S1600576715016544.

[65] J. Zhu, N. Avakyan, A. Kakkis, A.M. Ho, K. Han, Y. Li, Z. Zhang, T.S. Choi, Y. Na, C. Yu, F.A. Tezcan, Protein Assembly by Design, (2021). https://doi.org/10.1021/acs.chemrev.1c00308.

[66] M. Garzoni, K. Okuro, N. Ishii, T. Aida, G.M. Pavan, Structure and shape effects of molecular glue on supramolecular tubulin assemblies, ACS Nano. 8 (2014) 904–914. https://doi.org/10.1021/nn405653k.

[67] N. Uchida, K. Okuro, Y. Niitani, X. Ling, T. Ariga, M. Tomishige, T. Aida, Photoclickable dendritic molecular glue: Noncovalent-to-covalent photochemical transformation of protein hybrids, J. Am. Chem. Soc. 135 (2013) 4684–4687. https://doi.org/10.1021/ja401059w.

Online websites

[68] https://www.compoundchem.com/2014/09/16/aminoacids/

[69] https://wou.edu/chemistry/courses/online-chemistry-textbooks/ch450-and-ch451-biochemistry-defining-life-at-the-molecular-level/chapter-2-protein-structure/

Supporting information of Chapter III

Table S3.1. Number of amino acid residues of carbonic anhydrase and trypsin inhibitor

Carbonic anhydrase		**Trypsine inhibitor**	
Residue	Number	Residue	Number
Alanine	17	Alanine	13
Arginine	9	Arginine	9
Asparagine	13	Asparagine	9
Aspartate	19	Aspartate	12
Glutamine	12	Glutamine	7
Glutamate	11	Glutamate	11
Glycine	20	Glycine	14
Histidine	11	Histidine	2
Isoleucine	5	Isoleucine	14
Leucine	26	Leucine	18
Lysine	18	Lysine	13
Methionine	4	Methionine	4
Phenylalanine	11	Phenylalanine	13
Proline	19	Proline	11
Serine	16	Serine	13
Threonine	14	Threonine	11
Tyrosine	8	Tyrosine	7
Valine	20	Valine	16
Tryptophane	7	Tryptophane	2
Cysteine	0	Cysteine	5

Table S3.2: Charges of residue in BCA and SKTI expected in buffer at pH=7 and pH=10. $N_{residue}$ is the number of residue in BCA and SKTI .

BCA Residue	$N_{residue}$	a-COOH	a-NH_2	RH^+	Charge at pH=7	Charge at pH=10
Aspartic Acid	19	2.1	9.8	3.9	-19	-19
Glutamic Acid	11	2.2	9.7	4.3	-11	-11
Lysine	18	2.2	9.0	10.5	+18	No charge
Arginine	9	2.2	9.0	12.5	+9	+9
Cysteine	0	1.7	10.8	8.3	-	-
Total					-3	-21

SKTI Residue	$N_{residue}$	a-COOH	a-NH_2	RH^+	Charge at pH=7	Charge at pH=10
Aspartic Acid	12	2.1	9.8	3.9	-12	-12
Glutamic Acid	11	2.2	9.7	4.3	-11	-1
Lysine	13	2.2	9.0	10.5	+13	No charge
Arginine	9	2.2	9.0	12.5	+9	+9
Cysteine	0	1.7	10.8	8.3	No charge	-5
Total					-1	-9

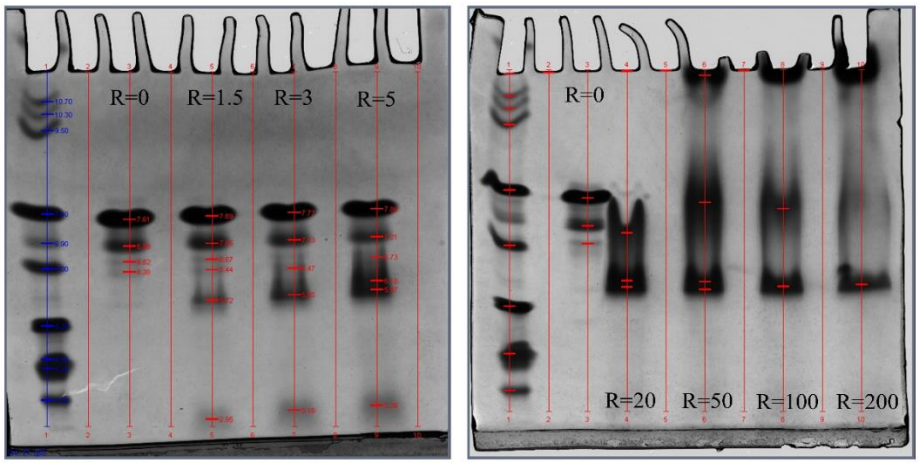

Figure S3.1. *Bands on isoelectric focusing electrophoresis gels. The first bands corresponds to the mixture of nine standard proteins (marker) and the other bands corresponds to 0.12 mmol L^{-1} Mb in the absence and in the presence of different NaCOSAN concentrations.*

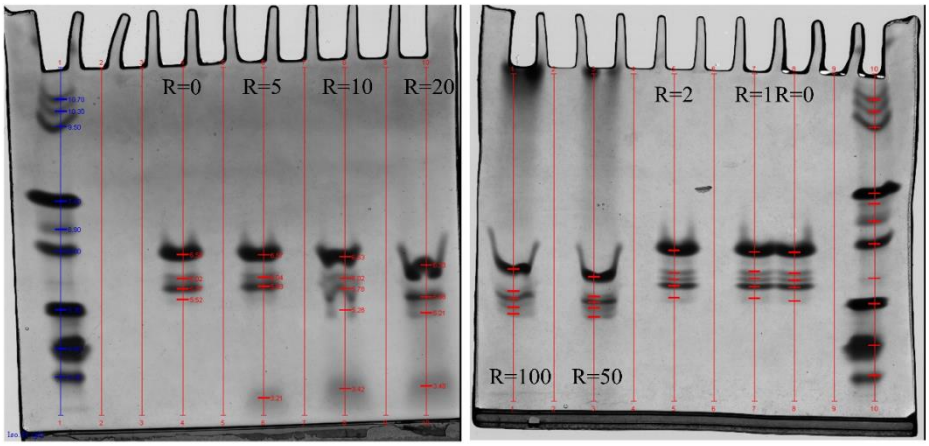

Figure S3.2. *Bands on isoelectric focusing electrophoresis gels. The first band of the first gel and the last band of the second gel corresponds to the mixture of nine standard proteins (marker) and the other bands corresponds to 0.036 mmol L^{-1} BCA in the absence and in the presence of different NaCOSAN concentrations.*

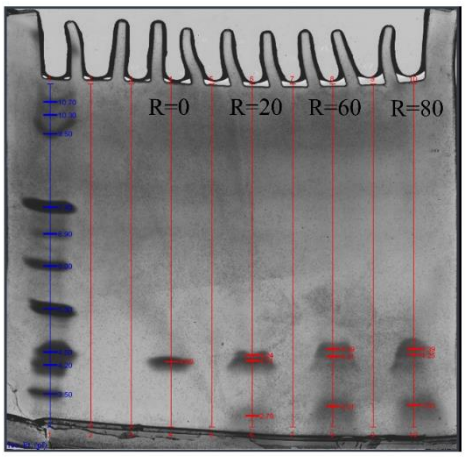

Figure S3.3. *Bands on isoelectric focusing electrophoresis gels. The first band of the gel corresponds to the mixture of nine standard proteins (marker) and the other bands corresponds to 0.015 mmol L^{-1} SKTI in the absence and in the presence of different NaCOSAN concentrations.*

III.2.1 Interaction of NaCOSAN/Mb followed by UV-Vis

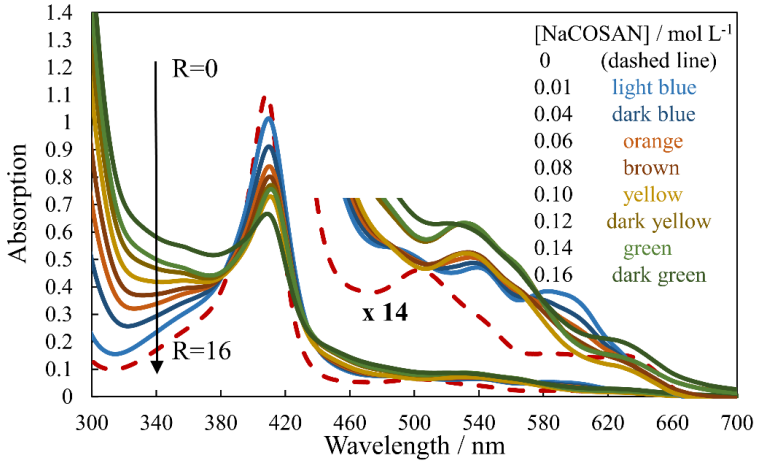

Figure S3.4. *UV-Vis spectra of 0.01 mmol L^{-1} Mb in PBS at pH=10 in the presence of different NaCOSAN concentrations (unsubtracted spectra).*

III.2.2 Interaction of NaCOSAN/Hemin followed by UV-Vis

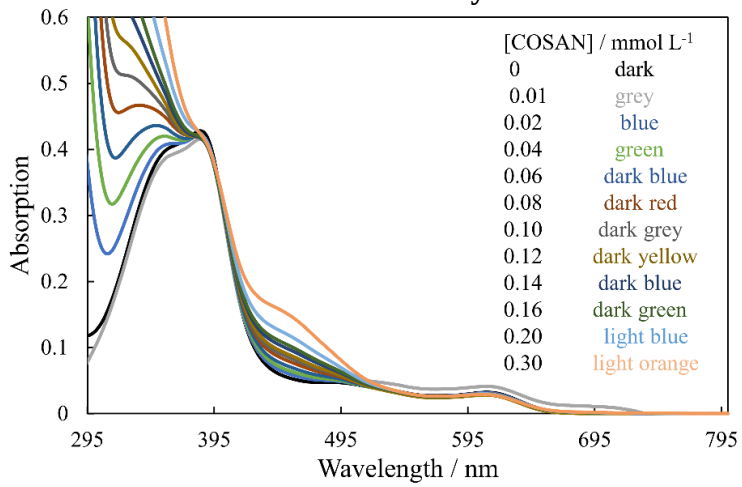

Figure S3.5. *UV-Vis spectra of 0.01 mmol L^{-1} Hemin in PBS at pH=10 in the presence of different NaCOSAN concentrations (unsubtracted spectra).*

III.2.5 Interaction of NaCOSAN/Mb followed by circular dichroism (CD)

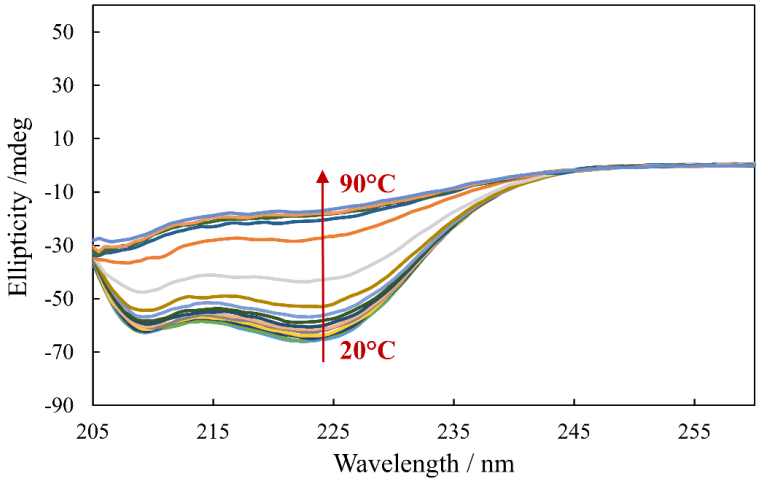

Figure S3.6*. Far-UV CD spectrum of 0.01 mol L^{-1} Mb in PBS at pH=10 by increasing temperature.*

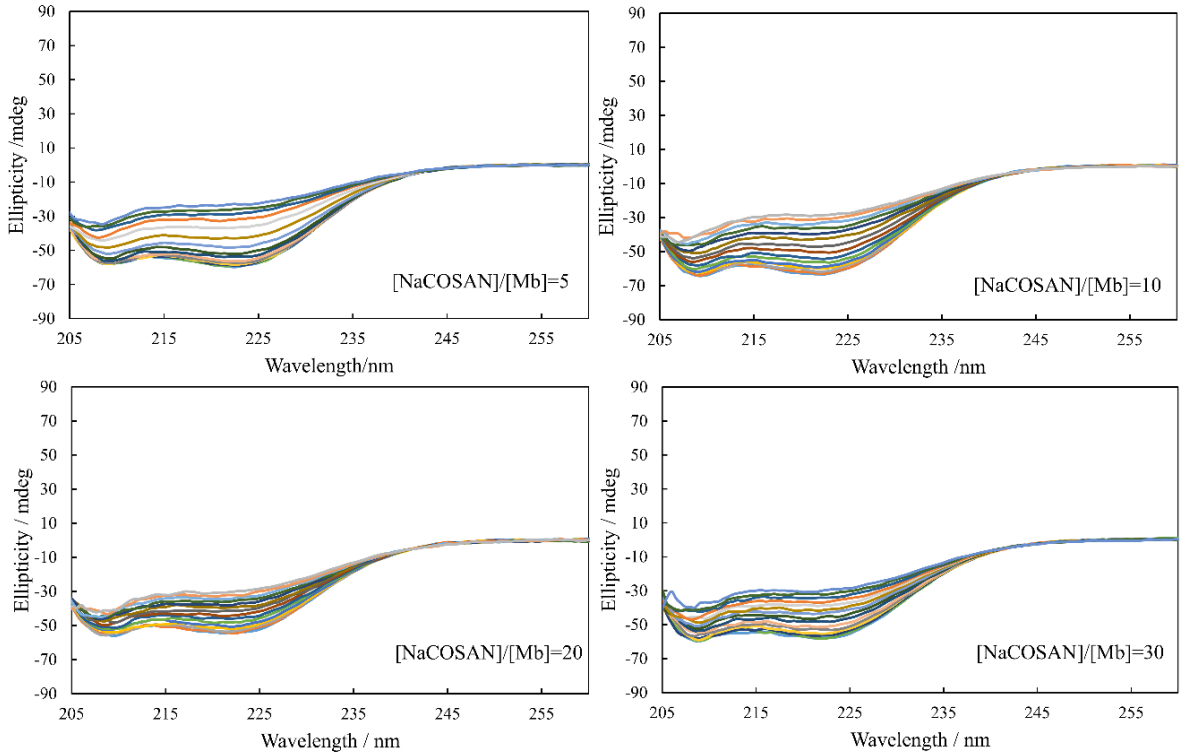

Figure S3.7. *Far-UV CD spectrum of Mb in the presence of different NaCOSAN concentrations in PBS at pH=10 at different temperatures.*

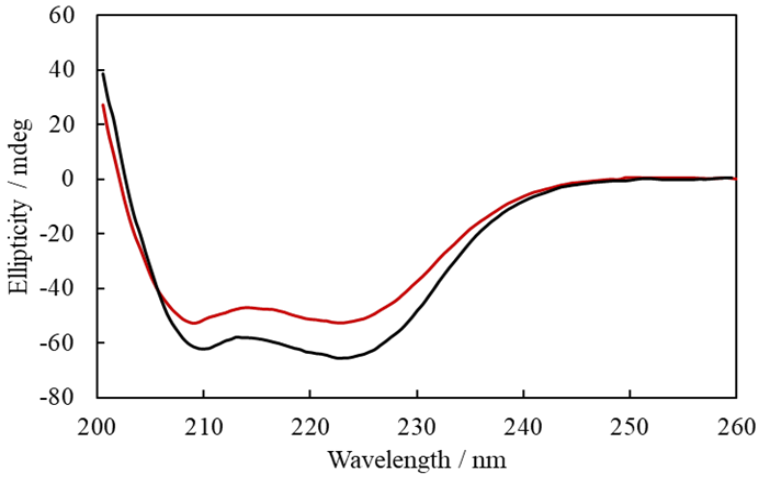

Figure S3.8. *Far-UV CD spectrum of Mb (dark) and ApoMb (red) in PBS at pH=10 and 298 K.*

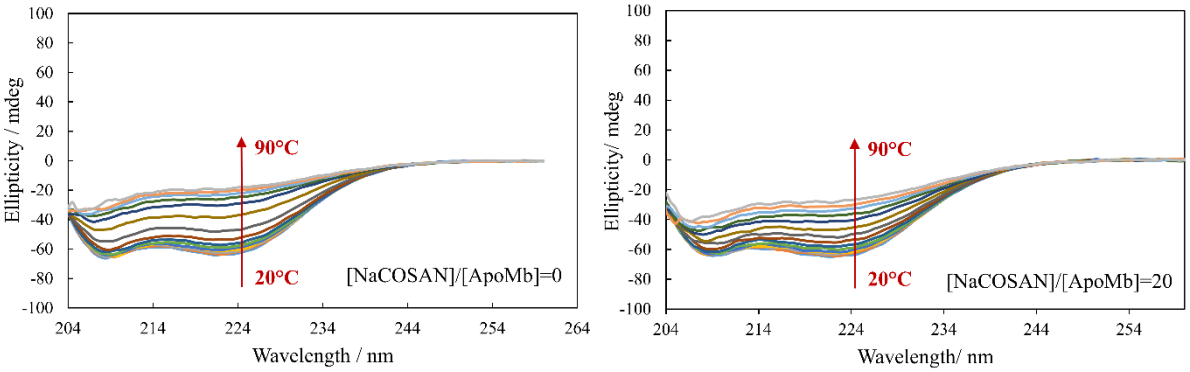

***Figure S3.9**. Far-UV CD spectrum of 0.01 mmol L^{-1} ApoMb in the absence and in the presence of 0.2 mmol L^{-1} NaCOSAN concentrations in PBS at pH=10 at different temperatures.*

III.2.7 Supramolecular level: Interaction of NaCOSAN/Mb followed by small angle X-ray scattering

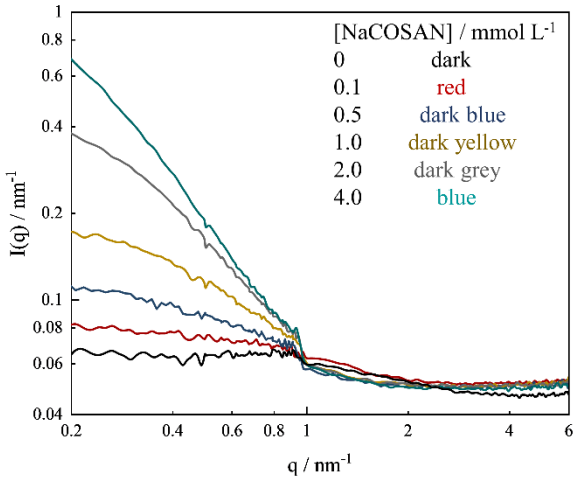

***Figure S3.10**. SAXS spectra of 0.1 mmol L^{-1} Mb in PBS at pH=10 increasing the NaCOSAN concentrations. The spectra were recorded at PSI.*

III.3.1 Interaction of NaCOSAN/BCA and NaCOSAN/SKTI followed by fluorescence

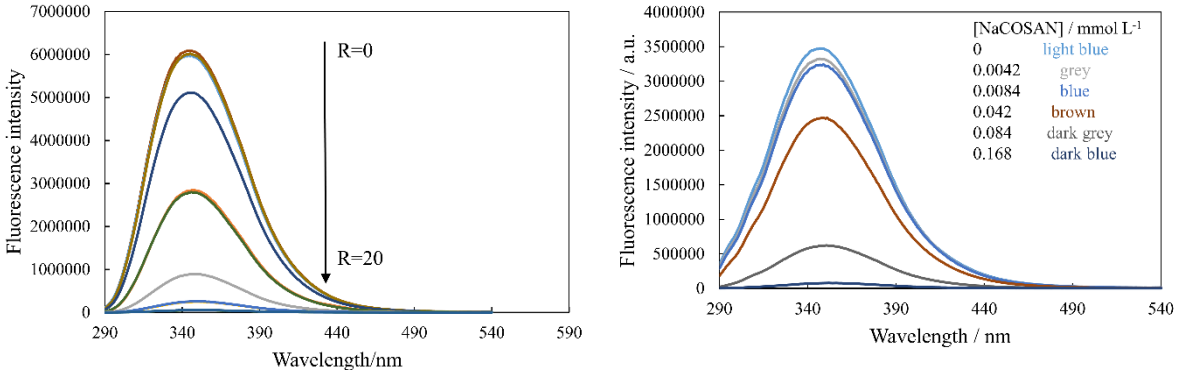

***Figure S3.11**. Emission fluorescence spectra of 0.055 mmol L^{-1} carbonic anhydrase (left) and 0.084 mmol L^{-1} trypsin inhibitor (right) in the absence and in the presence of NaCOSAN. From top to the bottom, the concentration of NaCOSAN increased stepwise from 0 to 0.2 mmol L^{-1}.*

III.3.2 Interaction of NaCOSAN/BCA and NaCOSAN/SKTI followed by circular dichroism (CD)

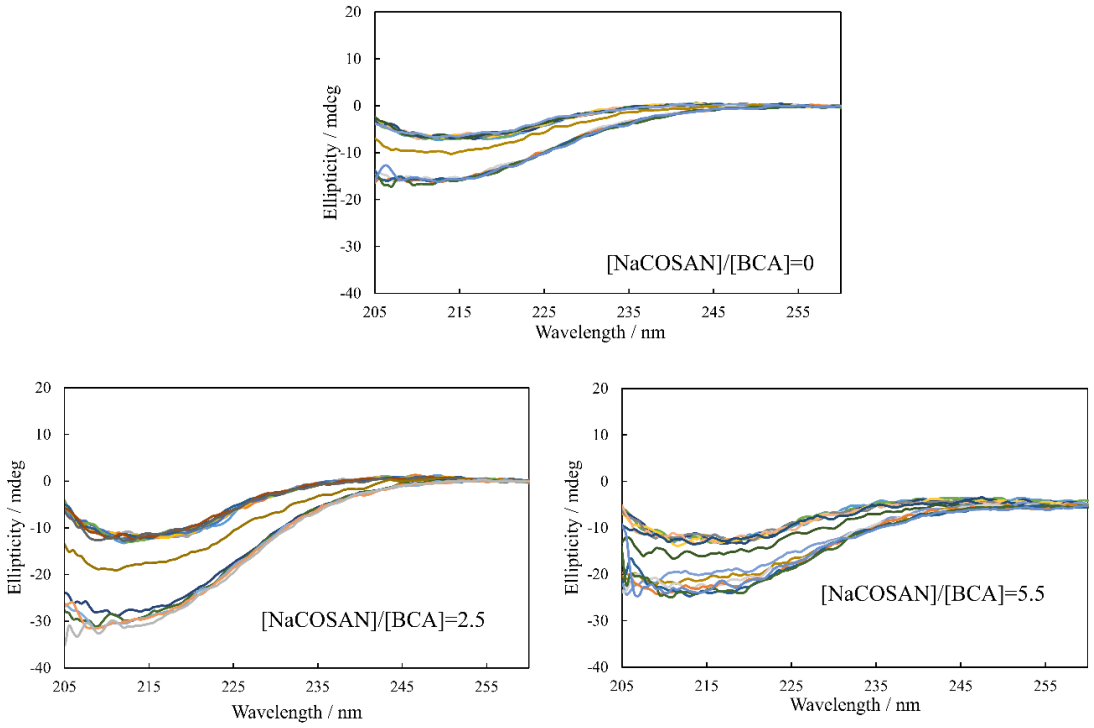

***Figure S3.12**. Far-UV CD spectrum of BCA in the presence of different NaCOSAN concentrations in PBS at pH=10 at different temperatures.*

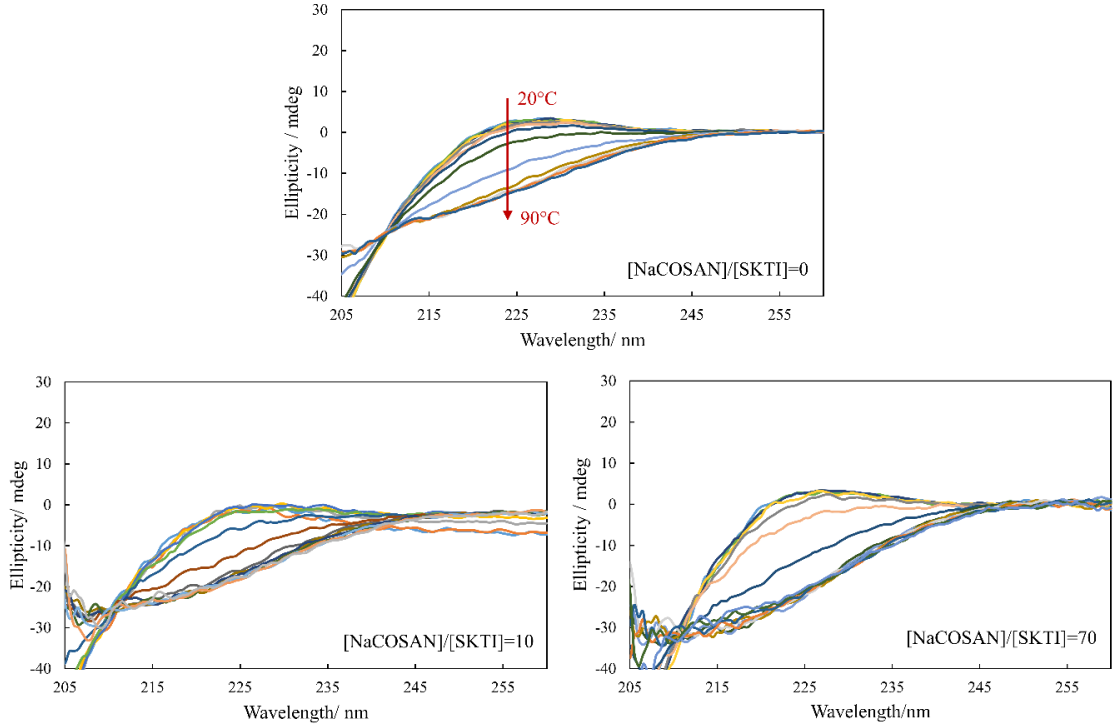

***Figure S3.13**. Far-UV CD spectrum of SKTI in the presence of different NaCOSAN concentrations in PBS at pH=10 at different temperatures.*

III.4.1 NaCOSAN in comparison with a classical chaotropic (NaSCN) in the presence of Mb

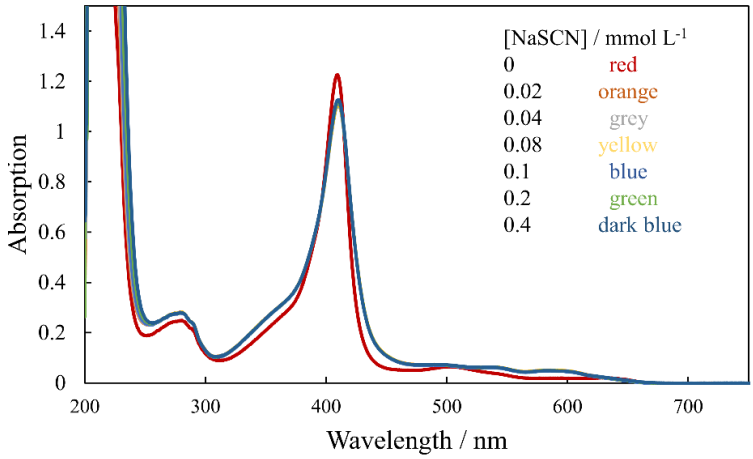

Figure S3.14. *UV-Vis spectra of 0.01 mol L^{-1} Mb in the presence of different NaSCN concentrations at pH=10 in PBS.*

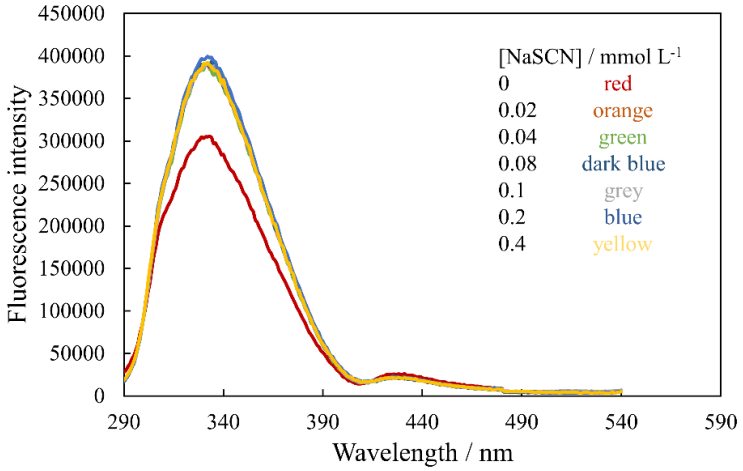

Figure S3.15*. Emission fluorescence spectra of 0.01 mmol L^{-1} Mb in the absence and in the presence of NaSCN at pH=10 in PBS.*

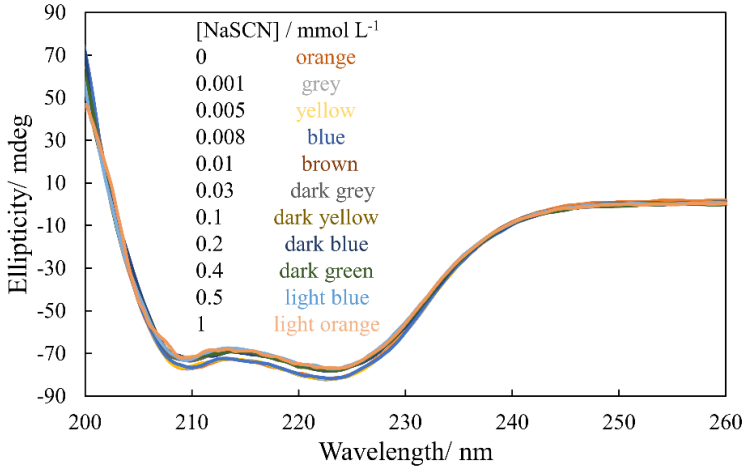

Figure S3.16*. Far-UV CD spectrum of Mb in the absence and presence of NaSCN at pH=10 and 298 K.*

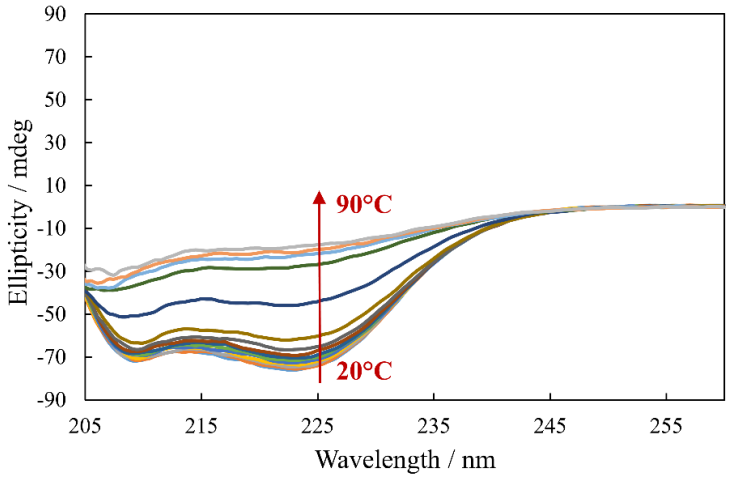

Figure S3.17. *Far-UV CD spectrum of 0.01 mmol L^{-1} Mb in the presence of 0.1 mmol L^{-1} NaSCN concentration in PBS at pH=10 at different temperatures.*

III.4.2 NaCOSAN in comparison with dodecaborates ($Na_2B_{12}X_{12}$) in the presence of Mb

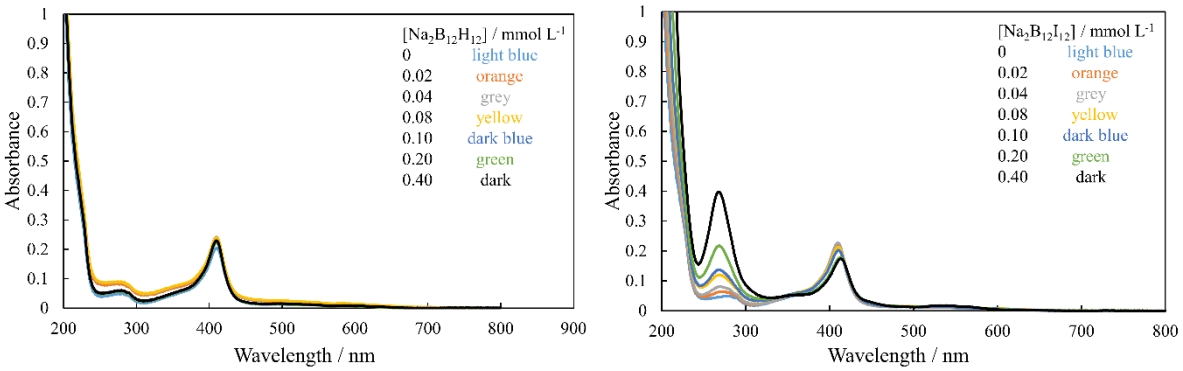

Figure S3.18. *UV-Vis spectra of 0.01 mol L^{-1} Mb in the absence and in the presence of different $Na_2B_{12}H_{12}$ (left) and $Na_2B_{12}I_{12}$ (right) concentrations at pH=10 in PBS.*

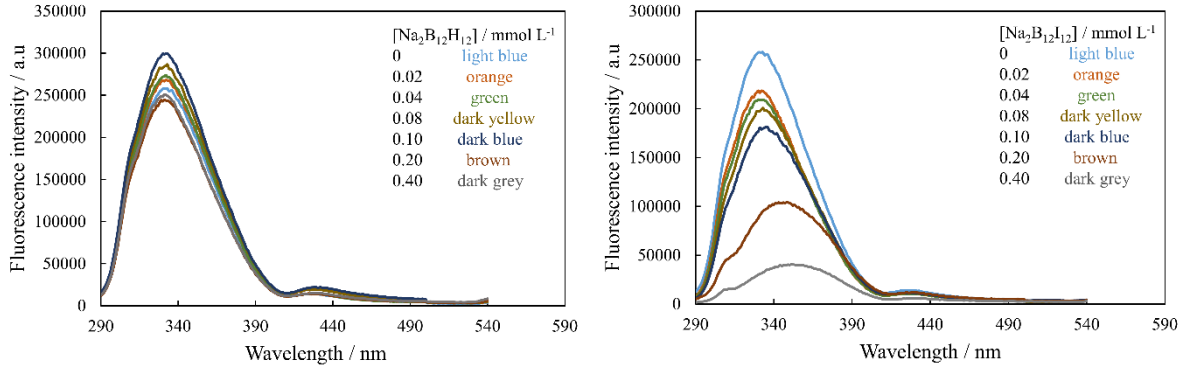

Figure S3.19. *Emission fluorescence spectra of 0.01 mmol L^{-1} Mb in the absence and in the presence of different $Na_2B_{12}H_{12}$ (left) and $Na_2B_{12}I_{12}$ (right) concentrations at pH=10 in PBS.*

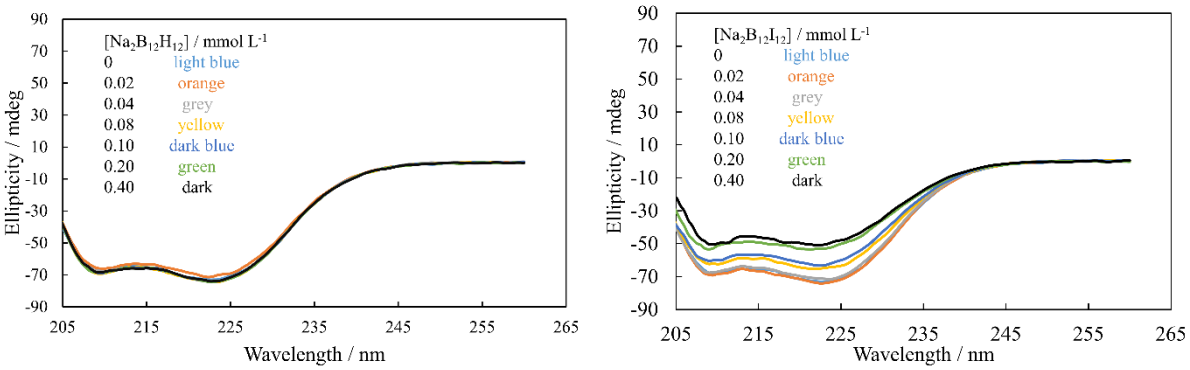

Figure S3.20. *Far-UV CD spectrum of 0.01 mmol L^{-1}Mb in the absence and in the presence of different $Na_2B_{12}H_{12}$ (left) and $Na_2B_{12}I_{12}$ (right) concentrations at pH=10 in PBS.*

III.4.3 NaCOSAN in comparison with a classical surfactant (SDS) in the presence of Mb

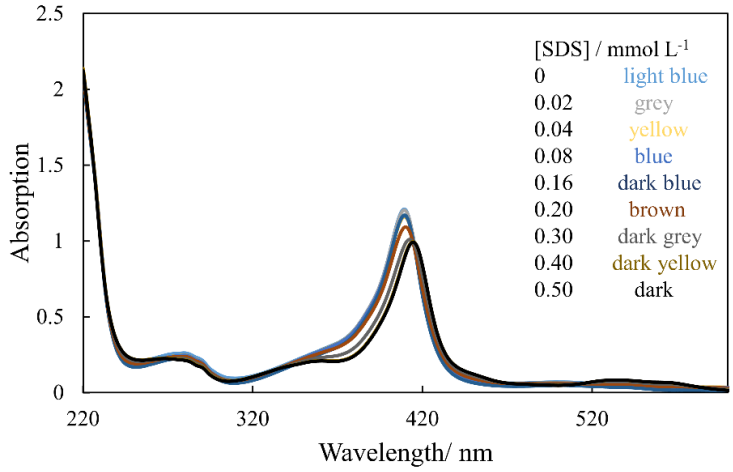

Figure S3.21. *UV-Vis spectra of 0.01 mol L^{-1} Mb in the presence of different SDS concentrations at pH=10 in PBS.*

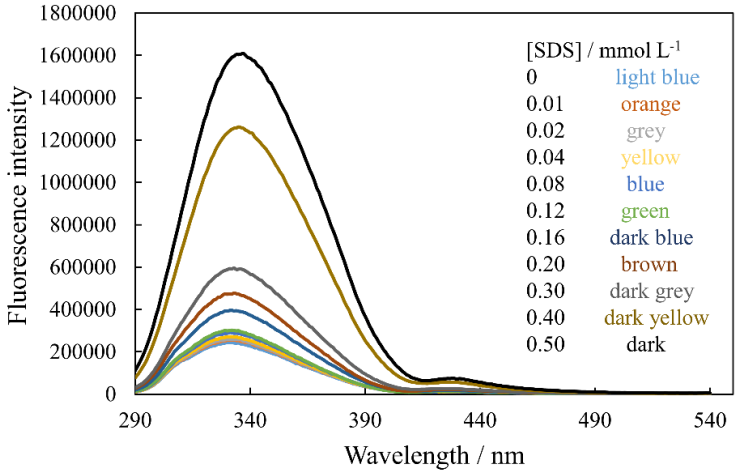

Figure S3.22. *Emission fluorescence spectra of 0.01 mmol L^{-1} Mb in the absence and in the presence of SDS at pH=10 in PBS.*

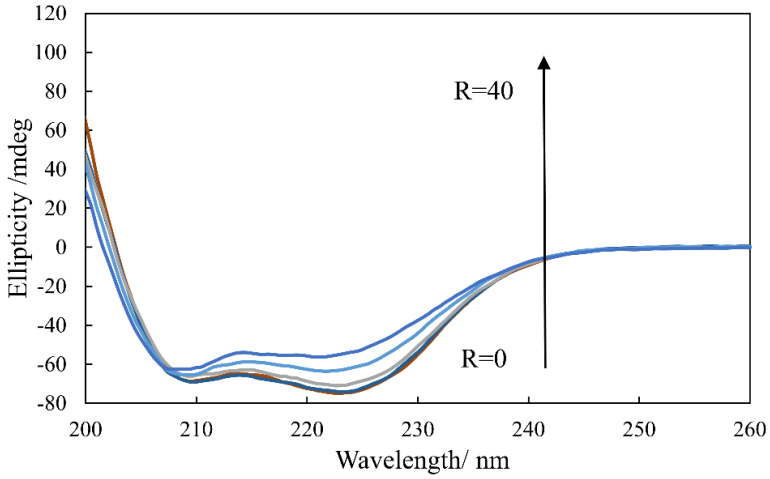

Figure S3.23. *Far-UV CD spectrum of Mb in the absence and presence of SDS at pH=10 and 298 K.*

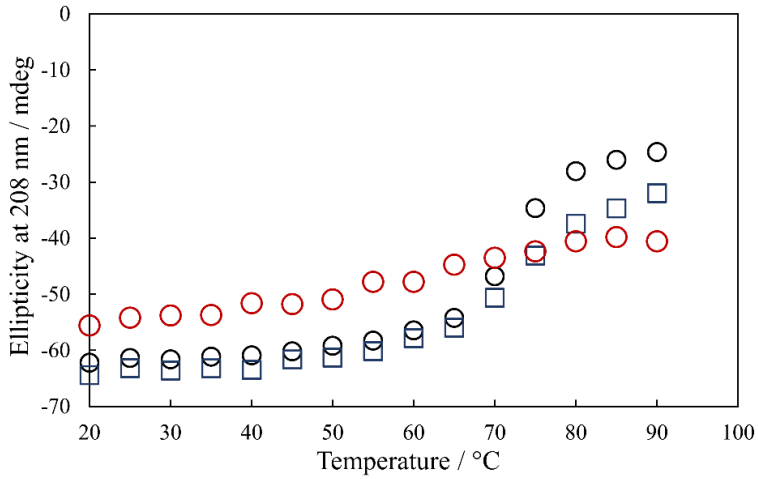

Figure S3.24. *Ellipticity of 0.01 mmol L^{-1} Mb in the absence (dark circles) and in the presence of 0.2 mmol L^{-1} SDS (blue squares) or 0.2 mmol L^{-1} NaCOSAN (red circles) at 208 nm as a function of temperature.*

III.4.3.1 NaCOSAN in comparison with a classical surfactant (SDS) in the presence of BCA or SKTI

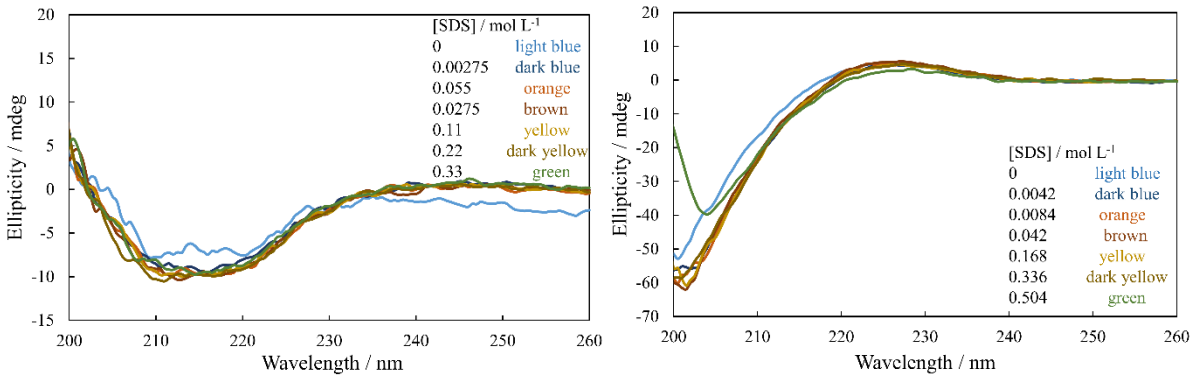

Figure S3.25. *Far-UV CD spectrum of BCA (left) and SKTI (right) in the absence and presence of SDS at pH=10 and 298 K.*

III.5.1 Mb in the presence of NaCOSAN at two different pH.

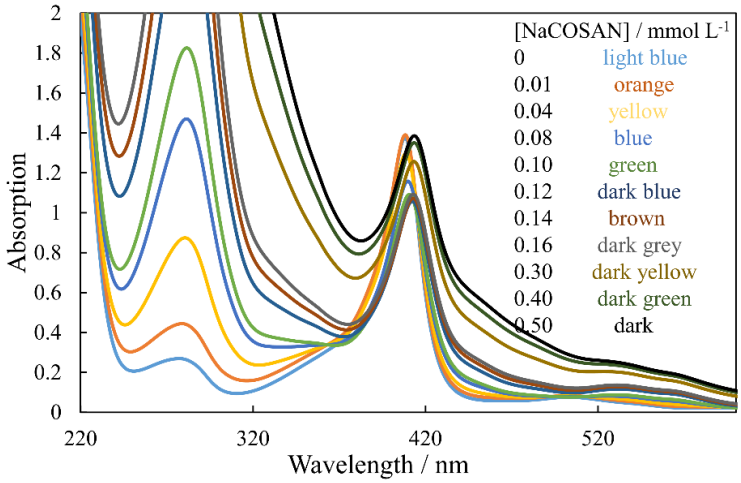

Figure S3.26. *UV-Vis spectra of 0.01 mmol L^{-1} Mb in PBS at pH=7 in the presence of different NaCOSAN concentrations (unsubtracted spectra).*

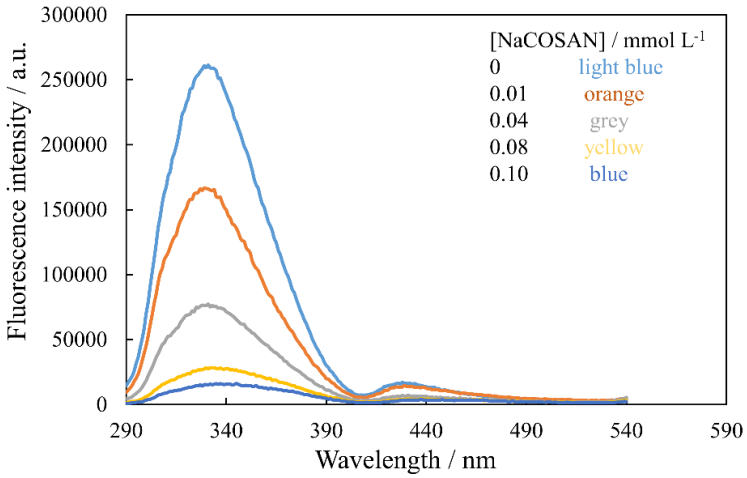

Figure S3.27. *Emission fluorescence spectra of 0.01 mmol L^{-1} Mb in the absence and in the presence of NaCOSAN at pH=7 in PBS.*

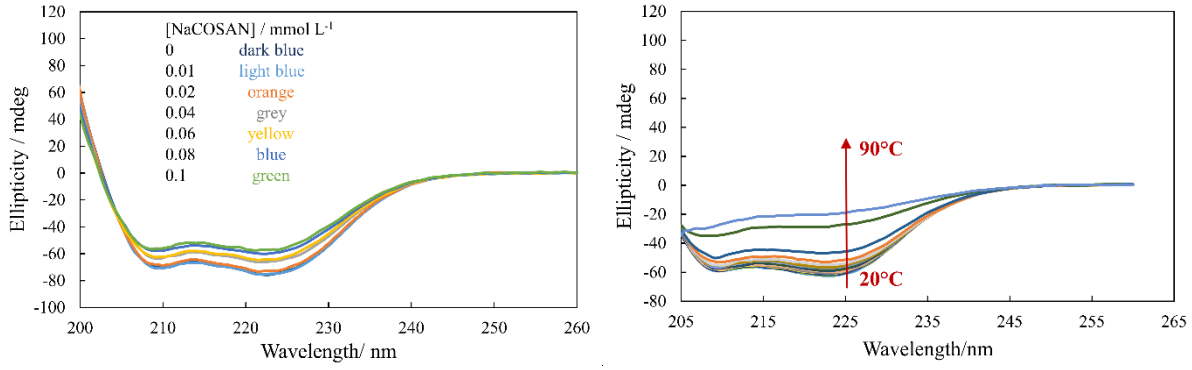

Figure S3.28. *Far-UV CD spectrum of 0.01 mol L^{-1} Mb in PBS at pH=7(A) in the presence of different NaCOSAN concentrations at 298 K and (B) in the absence of NaCOSAN at different temperatures.*

III.5.2 BCA or SKTI in the presence of NaCOSAN at two different pH.

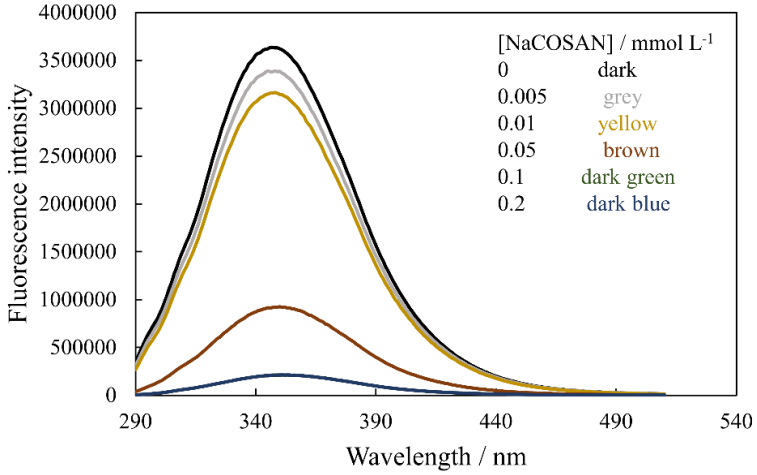

Figure S3.29. *Emission fluorescence spectra of 0.0084 mmol L^{-1} SKTI in the absence and in the presence of NaCOSAN at pH=7 in PBS.*

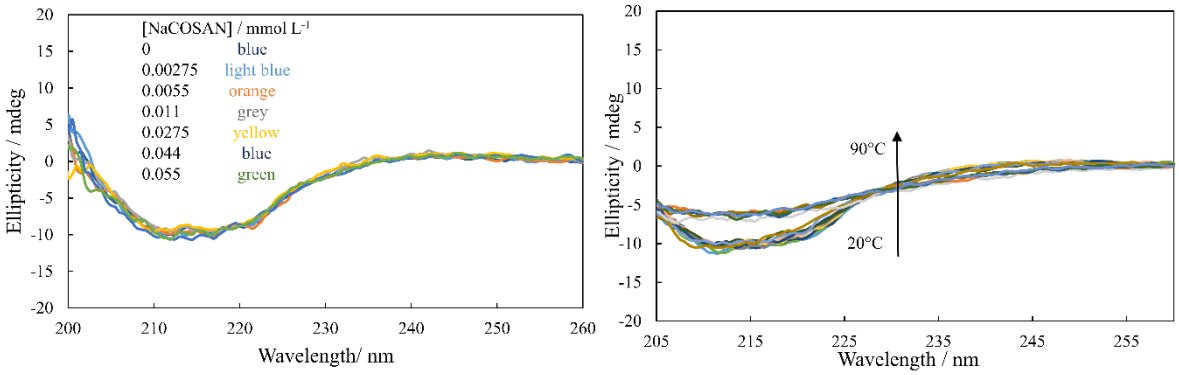

Figure S3.30. *Far-UV CD spectrum of 0.0055 mol L^{-1} BCA in PBS at pH=7(A) in the presence of NaCOSAN at 298 K and (B) in the absence of NaCOSAN at different temperatures.*

III.5.3 Mb in the presence of NaSCN at two different pH.

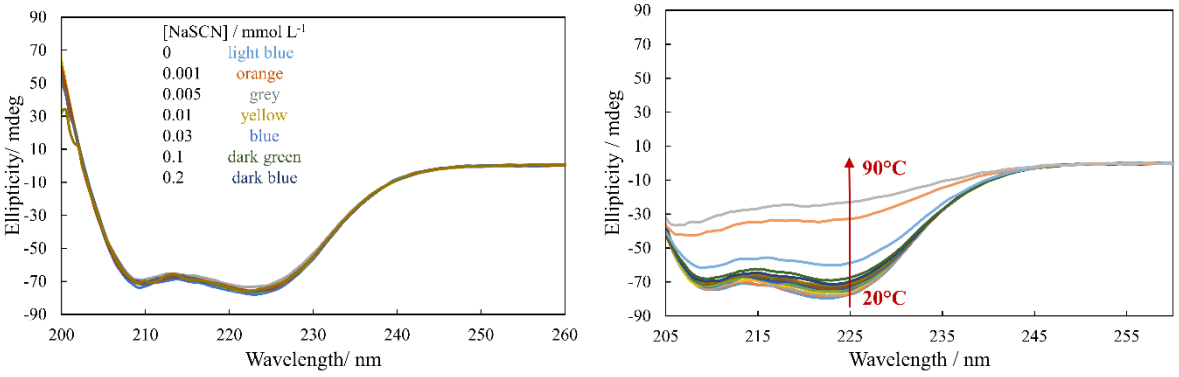

Figure S3.31. *Far-UV CD spectrum of 0.01 mol L^{-1} Mb in PBS at pH=7(A) in the presence of NaSCN at 298 K and (B) in the absence of NaSCN at different temperatures.*

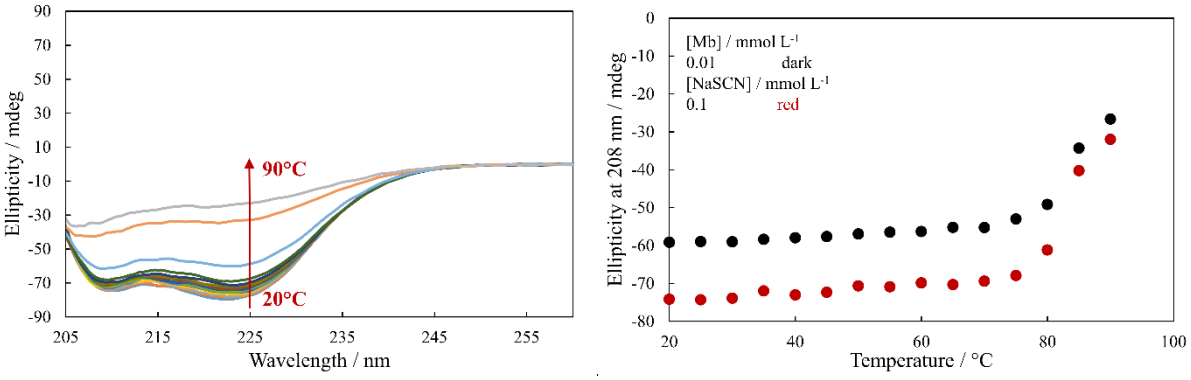

Figure S3.32*. (A)Far-UV CD spectrum of 0.01 mmol L^{-1} Mb in the presence of 0.1 mmol L^{-1} NaSCN concentration in PBS at pH=7 at different temperatures. (B)Ellipticity of 0.01 mmol L^{-1} Mb in the absence (dark circles) and in the presence of 0.1 mmol L^{-1} NaSCN (red circles) at pH=7 at 208 nm as a function of temperature.*

III.5.4 Mb in the presence of SDS at two different pH.

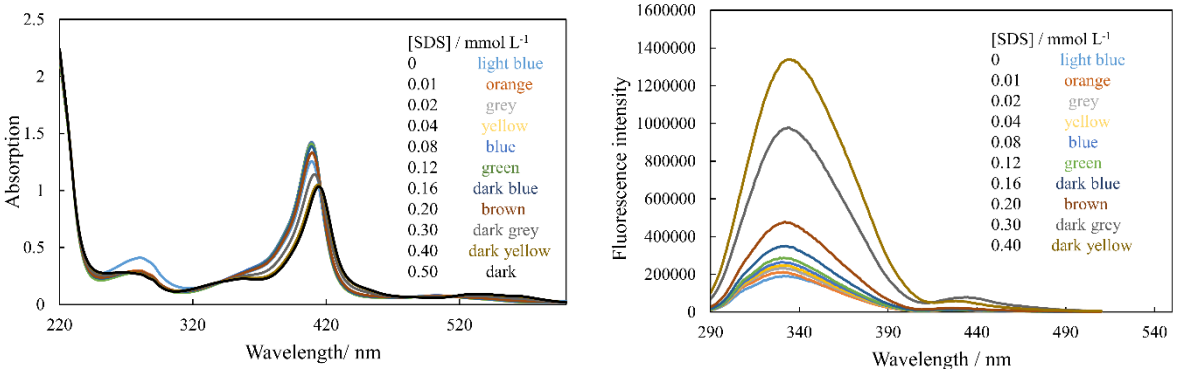

Figure S3.33. *(A) UV-Vis spectra of 0.01 mmol L^{-1} Mb in PBS at pH=7 in the presence of different SDS concentrations (B) Emission fluorescence spectra of 0.01 mmol L^{-1} Mb in the absence and in the presence of SDS at pH=7 in PBS.*

Chapter IV: Photophysical investigation of cobalta-bis dicarbollides

The photophysics of NaCOSAN and its derivatives in aqueous solutions have not been thoroughly investigated so far.[1] It was shown that NaCOSAN has interesting redox properties and can therefore be used as a photocatalyst.[1,2] Indeed, the particular structure of the COSAN anion is composed of a cobalt cation in oxidation state +III sandwiched by two heteropolyhedral half-cages composed of boron and carbon. This particular structure of COSAN allows different rotation conformers or rotamers (transoid, gauche, and cisoid) to be stabilized according to the redox of the cation, the chemical grafting on the boron atoms, or the interactions of the anion with its environment.[3–6] The distribution of charges on this mobile structure generates multiple electronic states and provides a wealth of spectral information that can be more or less sensitive to the anion's environment.

Moreover, the formation of supramolecular assemblies may significantly influence electron transfer processes, and thus photocatalytic efficiency.[7,8] We have examined the influence of the self-assembly of NaCOSAN on its photophysical properties in aqueous and organic solutions, as observed and studied in Chapter II, using steady state and time-resolved fluorescence spectroscopy.

IV.1 Steady state absorption of NaCOSAN

Before presenting the fluorescence signal, UV-visible spectra of NaCOSAN were recorded in H_2O by a NanoDrop UV-vis spectrophotometer (Figure 4.1). The NanoDrop UV-vis spectrometer can measure much higher absorptions than conventional UV-vis spectrometers, extending the concentration measurement range by a factor of 100. The maximum absorbance at 280 nm for NaCOSAN should be less than 550 A, which is approximately 20 mmol L^{-1}. In Figure 4.1, the two absorption bands at 280 nm and the weaker one at 450 nm were observed. Increasing COSAN concentration results in a linear increase in absorption. The extinction coefficients and the λmax values (ε =26353 L mol^{-1} cm^{-1} at λmax = 280 nm and ε=442.74 L mol^{-1} cm^{-1} at λmax = 450 nm) were comparable to those previously determined for HCOSAN in water by D. Brusselle, (ε =25763 L mol^{-1} cm^{-1} at λmax = 287 nm and ε=355.4 L mol^{-1} cm^{-1} at λmax = 455 nm) or for CsCOSAN in methanol in previous investigations (ε =30980 L mol^{-1} cm^{-1} at λmax = 287 nm and ε=445 L mol^{-1} cm^{-1} at λmax = 455 nm).[4,9] It is interesting to note that micellization of COSAN, appearing above the critical aggregation concentration (between 10 and 20 mmol L^{-1} depending on the technique[10,11]), does not affect the

adsorption of the UV light (i.e., linear dependence of the absorption vs. concentration curve). Remarkably, the extinction coefficient of NaCOSAN up to such high concentrations, particularly the peak in the UV region, which is sensitive to the hydration shell as mentioned in Chapter II, has never been reported.

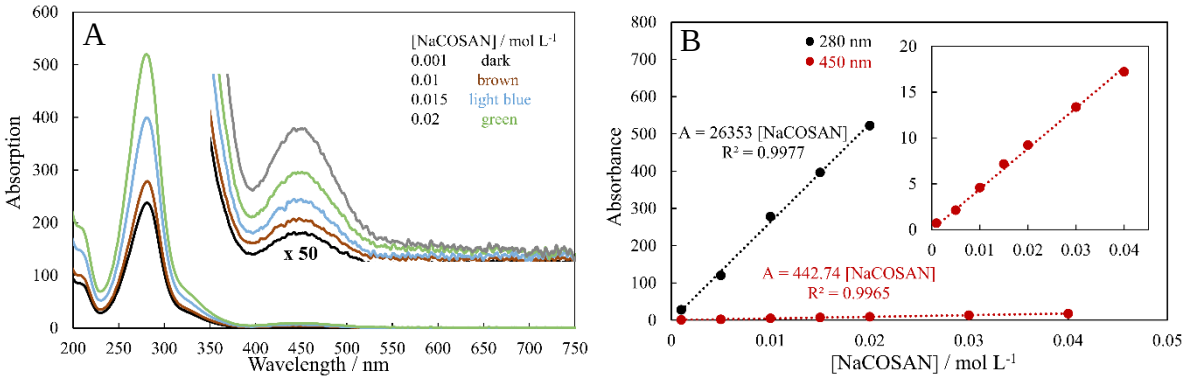

***Figure 4.1**. (A) UV-Vis spectra of different NaCOSAN concentrations in H_2O. The inset shows a zoom-in of the visible range. (B) Calibration curve of NaCOSAN obtained by UV-VIS data of (A).*

In contrast to absorption spectroscopy, which tracks transitions from the ground state to the excited state, fluorescence spectroscopy focuses on the transitions of electrons from the excited state to the ground state.[12] Fluorescence spectroscopy is more sensitive (nanomolar range) than UV-vis spectroscopy, which typically has detection limits in the micromolar to millimolar range. The fluorescent signal is amplified using a high-intensity excitation light source. In the next section, we investigate the fluorescence of NaCOSAN, which has never been studied so far. Despite the fact that the existing literature suggests that COSAN does not exhibit fluorescence[1], a thorough investigation will be conducted.

IV.2 Fluorescence of NaCOSAN in H_2O

The study of NaCOSAN fluorescence has been carried out using the fluorospectrometer FluoroMax4 from Horiba Scientific. Spectra were recorded running the FluorEssence software under Origin. The excitation wavelength ranged between 200 nm and 400 nm, and the emission wavelength was recorded in the range of 300 nm and 700 nm. The bandwidth was 5 and 4 nm for the excitation and emission wavelengths, respectively.

Initially, the 2D emission spectra of NaCOSAN in H_2O at different concentrations were recorded (Figure 4.2 and Figure S4.1-4.4), from which the 1D spectra were extracted at a given excited wavelength. Surprisingly, very few publications show the fluorescence signal of a solvent or system in this kind of 2D representation. In Figure 4.2A (left-hand side), the 2D

spectrum corresponds to the response of pure water with the first and second harmonic Rayleigh intense (red) bands with emission at the same wavelength (elastic scattering). The two other bands, less intense (orange or yellow), are attributed to the Raman inelastic scattering process.[12,13]

Higher-order scattering from the monochromators makes second-order bands, which are observed at twice the wavelength of the excitation. For an excitation wavelength of 313 nm (or 366), the water Raman band position is at 350 nm (418). They appear separated from the incident radiation by the same frequency difference, irrespective of the wavelength of the exciting light. At high energies of excitation ($\lambda < 250$ nm), we detected a strong and continuous background in emission that diminished the sensitivity of our detection in this range. By increasing NaCOSAN concentration, the scattering bands are attenuated, certainly due to NaCOSAN absorption phenomena, and other emission bands appear but are independent of the excitation wavelength.

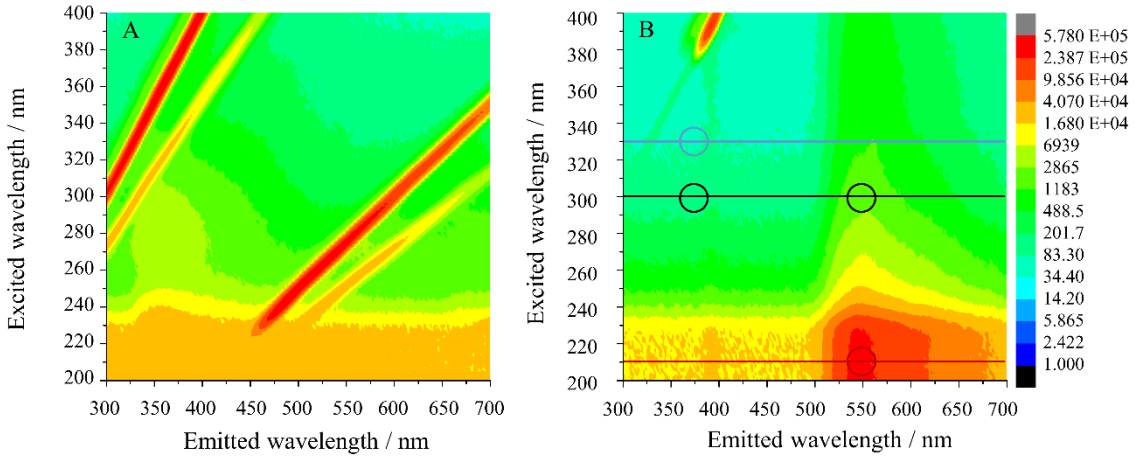

***Figure 4.2**. 2D fluorescence spectrum of (A) water and (B) of 0.017 mmol L^{-1} NaCOSAN in H_2O.*

In the next step, we exported the 1D fluorescence spectra (Figure 4.3) from the 2D plots at different excitation wavelengths: 210 nm (the red line on Figure 4.2B), 300 nm (the dark line on Figure 4.2B), and 330 nm (the blue line on Figure 4.2B).

Figure 4.3 shows the fluorescence spectra of different NaCOSAN concentrations in H_2O at 210 nm excitation wavelength. We observed two bands: a weak and sometimes broad signal at 390 nm and a strong and asymmetric band just below 550 nm, for which the intensity varies a lot. It is worth highlighting at this point that the characteristic absorption ranges of NaCOSAN are around 280 (230–350) and 450 (400–500) nm.

The fluorescence intensity of the peak at around 390 nm increases with a NaCOSAN concentration, which is followed by a decrease and a broadening at around 5-6 mmol L^{-1}. The fluorescence intensity of the peak at around 550 nm increases as well when NaCOSAN concentration increases (see Figure 4.4) and shows a sudden step increase at around 10 mmol L^{-1}. The decrease of the first peak and the strong asymmetry of the second peak in fluorescence are certainly affected by the absorption of the excited wavelength at respective lower wavelengths, as mentioned above. If we correlate this observation with the structural change from monomer/vesicles to NaCOSAN micellar type aggregation between 10 and 20 mmol L^{-1}, thus we can suggest that fluorescence spectroscopy is a very sensitive technique to follow the COSAN aggregation.

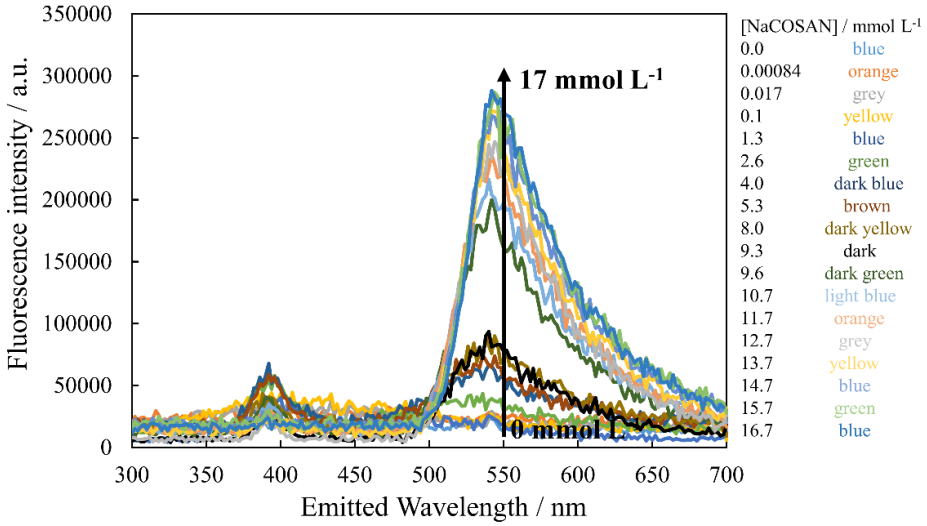

***Figure 4.3**. Fluorescence spectra of different NaCOSAN concentrations at λ^{exc}= 210 nm (red line Figure 4.3).*

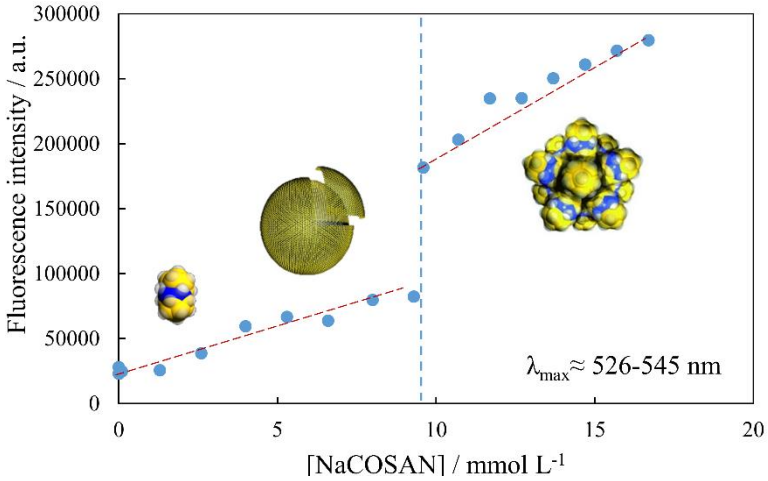

***Figure 4.4**. Fluorescence intensity at about 550 nm for λexc=210 nm (red line on Figure 4.3), as a function of NaCOSAN concentration.*

In the next step, the fluorescence intensity at about 390 and 550 nm of NaCOSAN in H_2O, but now at 300 nm excitation wavelength (the dark line on Figure 4.2 and Figure S4.5), was plotted as a function of NaCOSAN concentration.

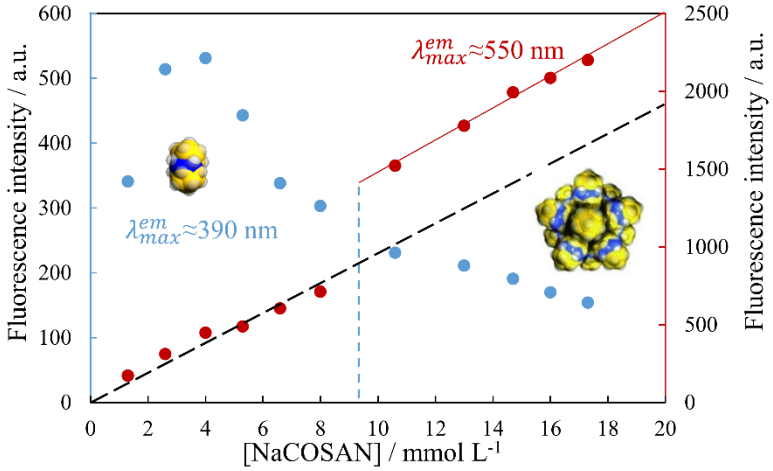

***Figure 4.5**. Fluorescence intensity at about 390 and 550 nm for λ^{exc}=300 nm (dark line on Figure 4.3), as a function of NaCOSAN concentration in H_2O.*

Similarly to the previous observation at higher energy, we observed (i) an increase and then a decrease (potential quenching effect) of the peak intensity of the first fluorescence band at about 390 nm (blue curve in Figure 4.5) and (ii) an intensity increase of the second band at about 550 nm (red curve Figure 4.5), showing a sudden step increase around 10 mmol L^{-1} NaCOSAN.

In the next step, the fluorescence intensity at an excitation wavelength of 330 nm and for the fluorescence band at λmax≈390 nm as a function of NaCOSAN concentration was recorded (Figures 4.6 and S4.6). We also observed a quenching in the fluorescence intensity. However, if we plot the fluorescence intensity as a function of the NaCOSAN concertation on log scale, we observe two transitions: a first intensity quench around 0.1 mmol L^{-1} and a second around 10 mmol L^{-1} NaCOSAN. As mentioned before, both variations seem to be correlated to supramolecular changes in the NaCOSAN self-assemblies: the first one may be related to the monomers/vesicles transition (never reported in the literature due to the lack of sensitivity of other techniques), and the second one is attributed to the vesicle/micelle transition.[11,14]

Moreover, these transitions are also reflected by two successive shifts in the fluorescent band position (see orange dots in Figure 4.6). We know that issues in fluorescence spectroscopy are often caused by the presence of impurities; therefore, great care should be taken in the interpretation of the results. However, various supramolecular transitions of nano-ions have

already been determined through scattering analysis; this is the case of with the monomer-to-micelle transition that occurs at approximately 10 mmol L^{-1}. [11]

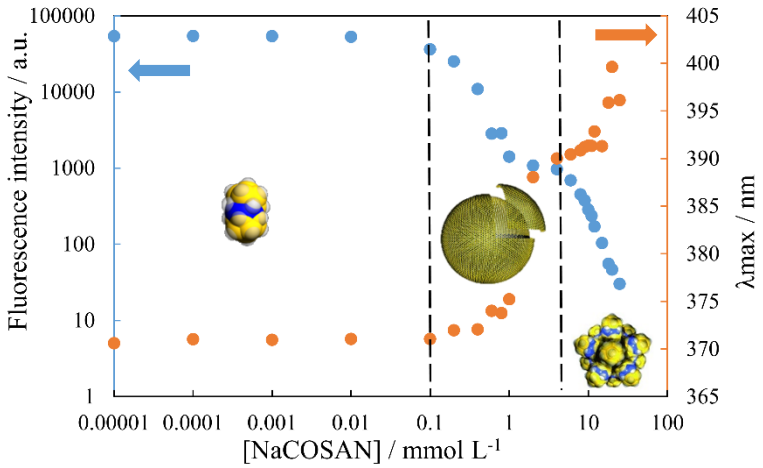

***Figure 4.6**. Fluorescence intensity and peak shift at about 390 for λexc=330 nm (blue line on Figure 4.3), as a function of NaCOSAN concentration.*

To reinforce our conclusion, we studied the fluorescence of aqueous solutions containing different reference compounds with increased concentrations: a classical salt (NaCl) and a surfactant that forms micelles above a certain concentration, such as Triton X-100. We exported the 1D fluorescence spectra (Figures S4.8 and S4.10) at different excitation wavelengths from the 2D fluorescence spectra of NaCl and Triton X 100 (Figures S4.7 and S4.9). At the excitation wavelength of 210 nm, neither NaCl nor Triton X 100 show any fluorescence peaks like in the case of NaCOSAN; only the Rayleigh and Raman elastic and inelastic scattering of water are observed and remain much more intense than the fluorescence signal. When the concentration of the Triton X 100 surfactant is increased, a broad signal is collected around the Raman band and is also present around the second harmonic signal, implying a scattering signal and not a fluorescent one (Figure S4.10). To summarize, the presence of NaCl or a classical surfactant such as Triton X 100 does not affect the fluorescence signature of the aqueous solution as observed with NaCOSAN. Therefore, the micellization of Triton X 100 does not affect the fluorescence spectra compared to NaCOSAN.

In conclusion, fluorescence analysis, particularly when utilizing a 2D intensity collection (emission versus excitation), provides complementary and new information about the supramolecular evolution of NaCOSAN in water. This result is new, as it has never been reported that COSAN fluoresces. As could be expected, the vibrational state and the emitted light from their relaxation are very sensitive to the NaCOSAN association. 2D analysis allows for the rapid selection of the most appropriate excitation energy and, in that case, a wavelength

of around 330 nm between the two absorption UV peaks. Simulation of the spectra, for example by TD-DFT or by molecular dynamics using reactive force fields, and their intensity variation should give in the future the energy levels of the local structural configuration of the COSAN in vesicles and in aggregates, information that is still in debate.[15]

IV.3 Photoluminescence of NaCOSAN in H_2O

In last sections, we integrated the light-emitted signal to obtain a static fluorescence signature of the excited solution system. To get more information from the various excited electronic states under different energies, time-resolved photoluminescence spectroscopy was carried out in order to probe the radiative decay and the lifetime of these excited states, which have a radiative decay channel. According to the nature of the excited state (singlet or triplet state), the lifetime can be extremely different, varying from ps to ms. Decay channels, from excited to ground state, can be classified as radiative and non-radiative. The emission decay is dependent on both radiative and non-radiative processes because both influence the excited state population, resulting in a strong dependence of the lifetime on the microenvironment. As a result, this analysis contains information about chemical modifications affecting emitters.[16]

In this section, we studied the time-resolved photoluminescence of NaCOSAN in H_2O at emission wavelengths in the range of 520–570 nm (the position of the second band in our precedent spectra) and at excitation pulses of 400 nm laser (the lower energy of excitation in our precedent static study). Time-resolved photoluminescence (PL) was measured on a NanoLog FL3 Horiba spectrofluorimeter, using a monochromator-based time-correlated single-photon counting (TCSPC) method and an infrared photomultiplier tube (PMT).

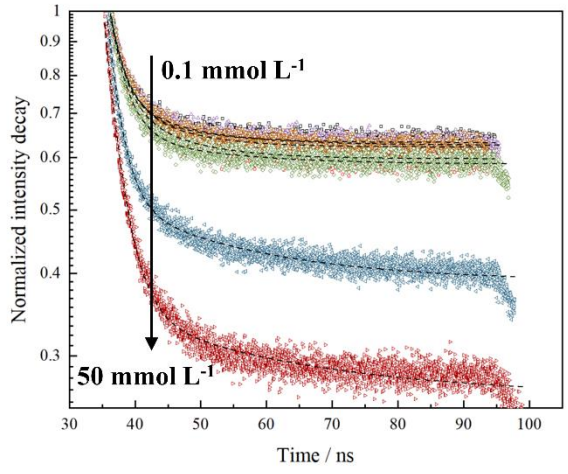

***Figure 4.7**. Normalized intensity decay at excitation wavelength 400 nm as a function of time in ns.*

This study was performed in collaboration with Pr. Leontidis and Pr. Itskos at the Experimental Condensed Matter Physics Lab (ECMPL) at the Physics Department of the University of Cyprus.[17]

Figure 4.7 depicts the normalized intensity decay of different NaCOSAN concentrations as a function of time. We observed qualitatively that the increase in NaCOSAN concentration leads to shorter lifetimes of the luminescence.

To be quantitative in the analysis, the fluorescence intensity decays of different NaCOSAN concentrations in H_2O as a function of time were fitted using a multi-exponential function (Figure S4.11). Figure 4.8 presents an example of 0.1 mmol L^{-1} NaCOSAN, which was fitted with a double exponential function. The single and triple exponential functions were also examined, but the double exponential function provided the best fit to the experimental data, as shown in Figures 4.8 and S4.11.

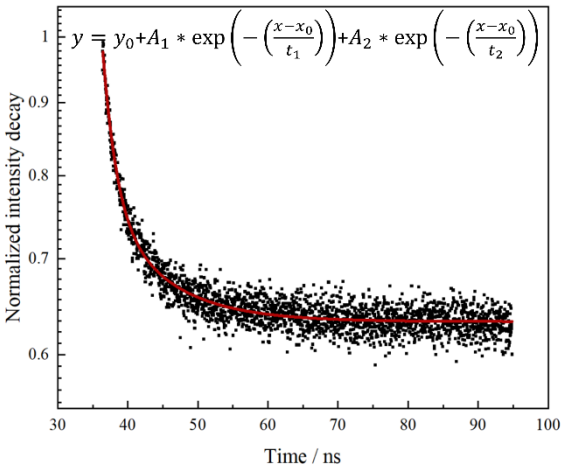

***Figure 4.8**. Normalized intensity decay of 0.1 mmol L^{-1} NaCOSAN concentration (dark circles) and fitted normalized intensity decay (red line) as a function of time in ns.*

In order to adequately characterize the fluorescence decay of NaCOSAN in H_2O, two discrete lifetimes in the range of nanoseconds (Table S4.1) are required. The lifetime of NaCOSAN and associated amplitudes are shown in Figures 4.9 and 4.10, respectively, as a function of NaCOSAN concentration. We observed that the t_1, the shortest lifetime, remains unaffected by the increase in NaCOSAN concentration, whereas the t_2, the longer one, is increasing with the increase in NaCOSAN concentration.

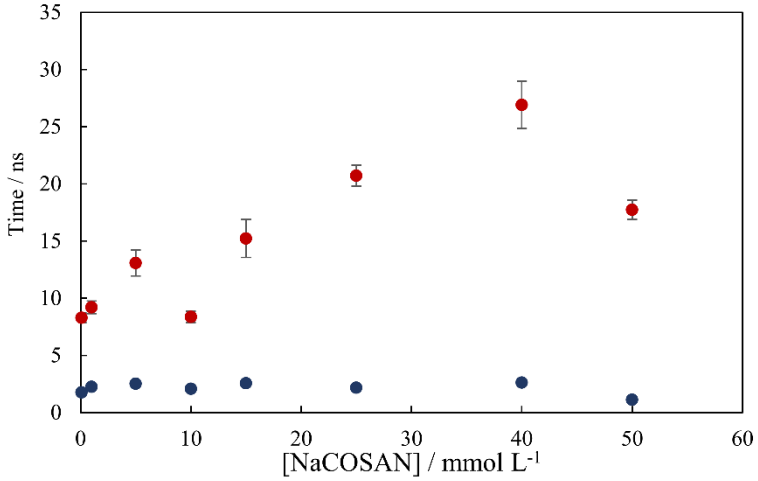

***Figure 4.9**. Two characteristic lifetimes in the nanosecond range of the fluorescent signal at 530 nm and under an excitation at 400nm, as a function of NaCOSAN concentration in H_2O (from fitting data figure 4.8 and S4.11).*

Figure 4.10 depicts the corresponding amplitude of the exponential functions as a function of NaCOSAN concentration. A_1, the amplitude of the shortest time, is increased by increasing NaCOSAN concentration, whereas A_2 remains unaffected.

When examined in detail, it seems that the A_1 amplitude variation displays a pseudo plateau at concentrations below 10 mmol L^{-1} (which is close to the aggregation concentration, CAC, of COSAN) before increasing for concentrations above 10 mmol L^{-1} in a manner that may be described as linear at the first order. This apparent break in the evolution of A_1 versus concentration is then possibly connected to the micellization of COSAN.

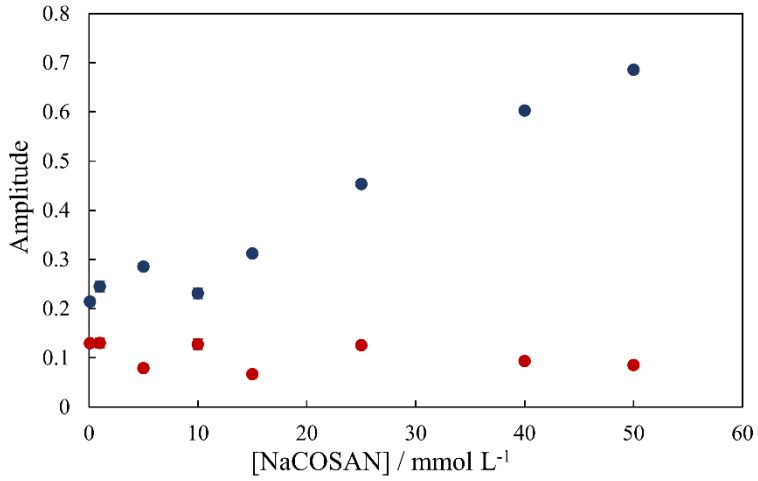

***Figure 4.10.** Amplitudes as a function of NaCOSAN concentration in H_2O, where blue circles represent the A_1 and red circles the A_2 of the double exponential function, which were used for the fitting.*

In the next step, we probed the fluorescence decay at shorter times, at the picosecond scale, using the pump-probe technique.

IV.4 Pump probe photoluminescence of NaCOSAN in H_2O

Pump-probe photoluminescence provides fundamental information about electronic energy levels and intermolecular energy transfer. The pump-and-probe (excite-and-probe) technique, an ultrashort laser pulse is split into two pulses, the pump and the probe, with a variable optical delay between them (Δt). On the investigated sample, the two incident ultrashort laser pulses are made to spatially overlap. The intense pump pulse excites the sample, altering its properties. A weaker probe pulse monitors these sample changes induced by the pump pulse. By varying the time delay (Δt) between the pump and probe pulses, the evolution of the excited state over time is investigated.[18] The fluorescence decay of NaCOSAN was collected at different concentrations at the visible wavelength (420-750 nm) and at two-excitation wavelengths (266 and 400 nm). This part of the study was performed in collaboration with Pr. Leontidis and Pr. Othonos at the Laboratory of Ultrafast Science at the Physics Department of the University of Cyprus.[19]

IV.4.1 Pump probe results of NaCOSAN in H_2O

The pump-probe data were presented in a 3D graph with in abscise, the luminescence wavelength, the ordinate for the time and the z-axis for the differential transmission. For clarity, differential transmission is defined as the change in transmission $dT = T - T_o$ induced by the pump divided by the transmission T_o of the probe in the absence of the pump, that is, $dT/T_o = (T - T_o)/T_o$. So, the signal is negative as soon as COSAN increase in concentration (Figure S4.12). Following excitation by the pump pulse carriers will move from the ground state to higher energy states as shown by the vertical arrow (Figure 4.11). These carriers will move into nearby states (lower energy) and they will occupy states that were normally unoccupied. Therefore, if we probe that state with the probe pulse it will have reduced absorption or increase in transmission (this is called state filling). A second effect is known as photo-induced absorption (or free carrier absorption) which occurs when the excited carriers will be further excited by the probe pulse into even higher energy states as shown in the diagram (Figure 4.11). This will appear as a negative signal in the transmission.

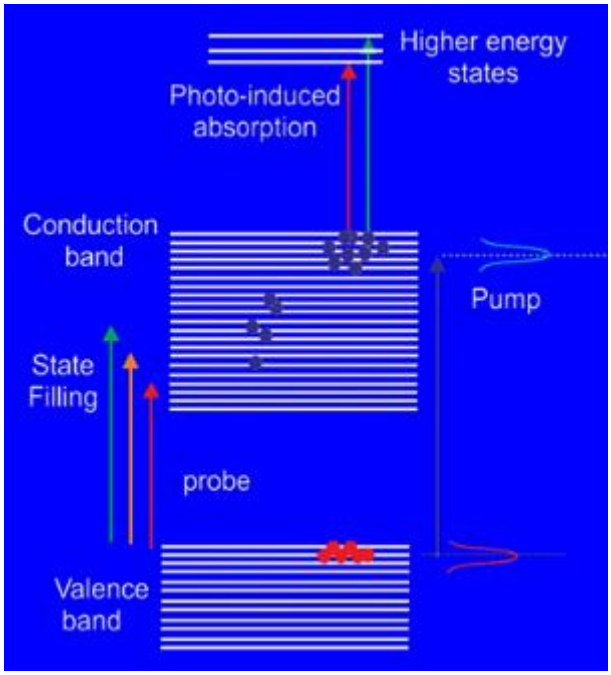

Figure 4.11. *Schematic diagram illustrating the evolution of carriers to explain space-filling effects.*

All NaCOSAN concentrations in H_2O exhibited distinct maxima (in absolute value) in differential transmission (dT/To) versus probe wavelength, as shown in Figure S4.12 A−I. The time evolution at a given probed wavelength is in the ps timescale. The exact probe wavelength at which the maxima occur (520 nm, dark arrow on Figure 4.12) in each case is presented in Figures 4.12 and S4.12. [19]

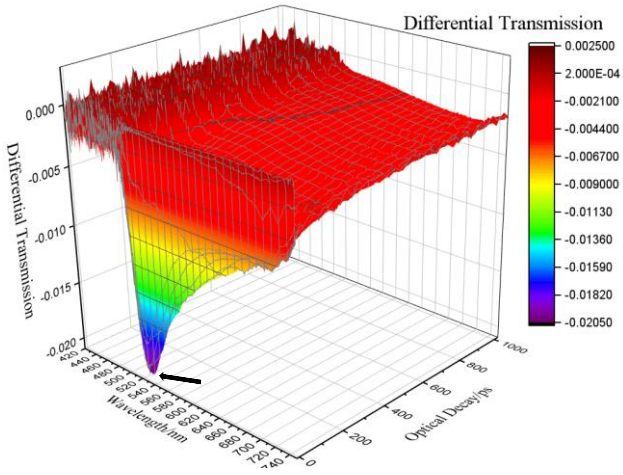

Figure 4.12. *Pump probe 3D-spectra of 0.05 mmol L^{-1} NaCOSAN in H_2O. The excitation wavelength was 400 nm.*

In Figure 4.13, the signal decay at the optimal differential transmission around 520 nm as a function of time and for various NaCOSAN concentrations is plotted in a semi-log graph. A triexponential model was found to be adequate to fit all the decays.

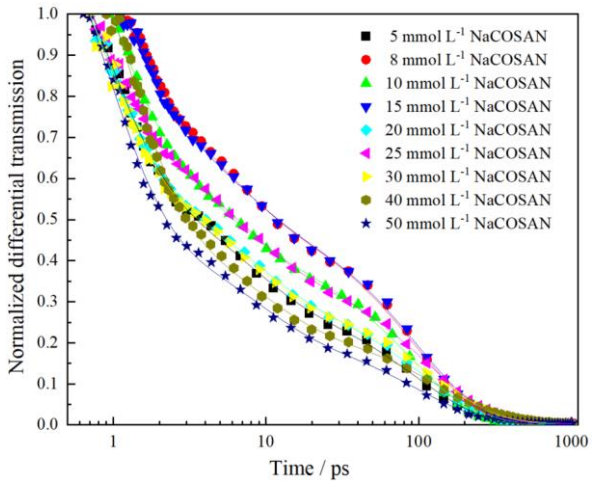

Figure 4.13. *Normalized differential transmission of different NaCOSAN concentrations at the maxima around 520 nm as a function of the time in ps derived from the pump probe spectra. The excitation wavelength was 400 nm.*

All the traces were fitted at different wavelengths around the maxima for better statistics (see Figure S4.13). The exponential amplitudes as well as the corresponding characteristic ultrafast decay times are presented in Table S4.2 and plotted for the latter in Figures 4.14 and S4.13.

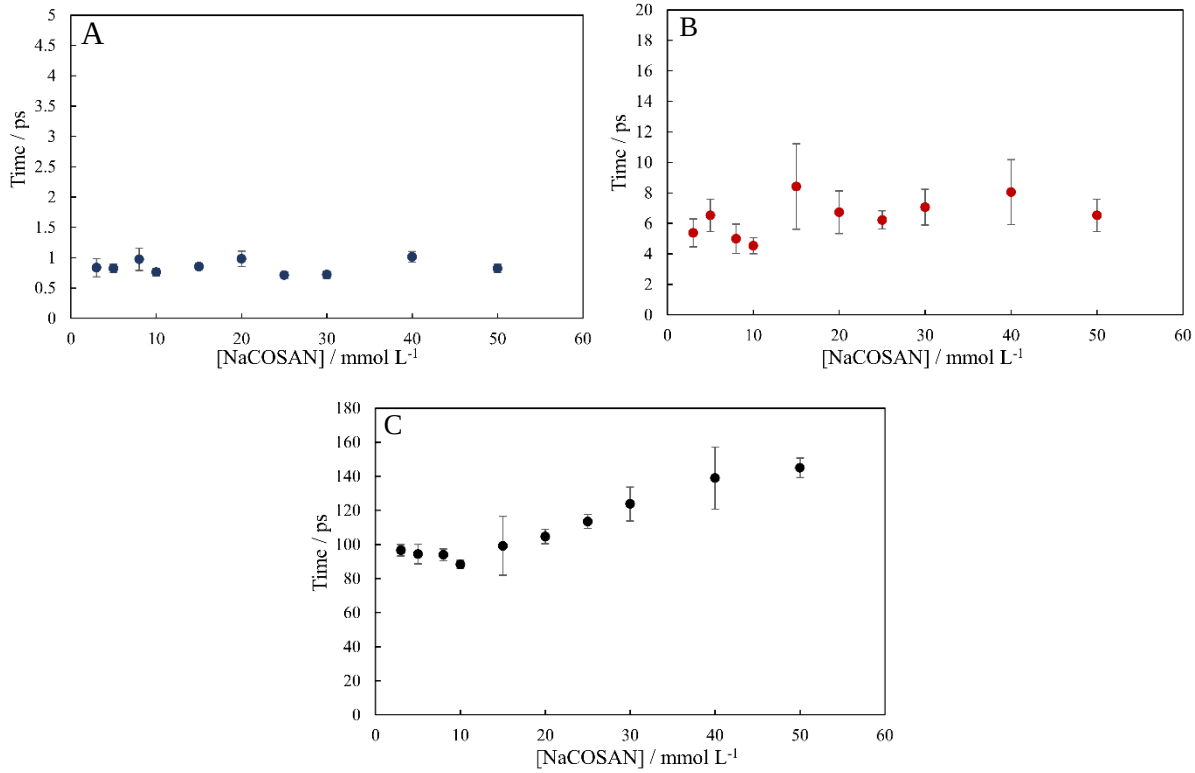

Figure 4.14. *Relaxation times (A) t_1, (B) t_2, and (C) t_3 at the maximum probe wavelength in ps as a function of NaCOSAN concentrations.*

The shortest decay time (t_1) and the intermediate one (t_2) are around 1 and 10 ns, respectively, and are independent of the nano-ion concentration. The longest relaxation time t_3 is rather constant below 10 mmol L^{-1} NaCOSAN and increases with increasing NaCOSAN

concentration. Once more, we discovered a signal that bears the hallmark of the NaCOSAN in a solution's supramolecular evolution. However, we cannot provide a more in-depth study because we are unable to yet link these defining times to any electronic states within COSAN.

In the next parts, we studied another derivative of NaCOSAN, the NaI_2COSAN in H_2O, and then modified the solvent (2-BuOH) for NaCOSAN as in chapter II in order to study the electronic energy levels and the intermolecular energies transfer in a different environment for which we have a good knowledge, the supramolecular environment.

IV.5 Photophysical study of NaI_2COSAN

IV.5.1 Steady state absorption of NaI_2COSAN

UV-visible spectra of NaI_2COSAN were recorded in H_2O by UV-Vis spectrophotometer NanoDrop (Figure 4.15). The extinction coefficient and the λmax values, (ε = 11215 L mol^{-1} cm^{-1} at λmax = 280 nm and ε = 9080.1 L mol^{-1} cm^{-1} at λmax = 330 nm). In Figure 4.16, we observed a linear increase in absorption with the increase in NaI_2COSAN concentration but no effect around CMC as for the case of NaCOSAN (Figure 4.1).

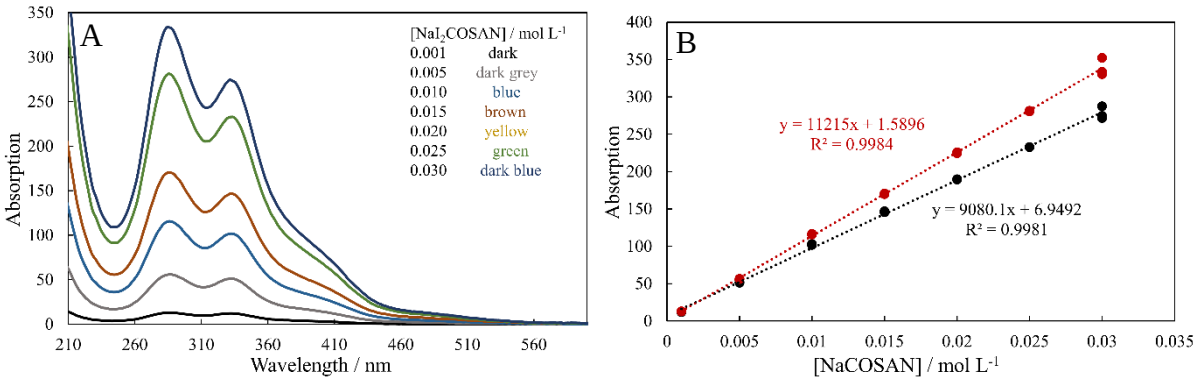

***Figure 4.15**. (A) UV-Vis spectra of different NaI_2COSAN concentrations in H_2O. (B) Calibration curve of NaCOSAN obtained by UV-VIS data of (A).*

IV.5.2 Fluorescence of NaI_2COSAN in H_2O

Figure 4.16A shows the fluorescence spectra of different NaI_2COSAN concentrations in H_2O at 210 nm excitation wavelength. The fluorescence intensity of NaI_2COSAN (Figure 4.16B) increases as the concentration of NaI_2COSAN increases. At low NaI_2COSAN concentrations, a peak centered at around 480 nm is observed. The peak shifts up to 580 nm by increasing NaI_2COSAN concentration up to 30 mmol L^{-1}.

The fluorescence of NaI_2COSAN did not show a sudden increase (or gap) in intensity like that of NaCOSAN (Figure 4.4). Additional NaI_2COSAN concentrations between 1 and 5 mmol L^{-1} are required to determine if this increase occurs or not with NaI_2COSAN. However, we can assume that the gap appears at a lower concentration than that of NaCOSAN. The fact that NaI_2COSAN is more hydrophobic than NaCOSAN indicates that it has a lower CAC. At this point, it is evident that we should record the fluorescence at excitation wavelengths of 300 and 330 nm in order to determine structural changes.

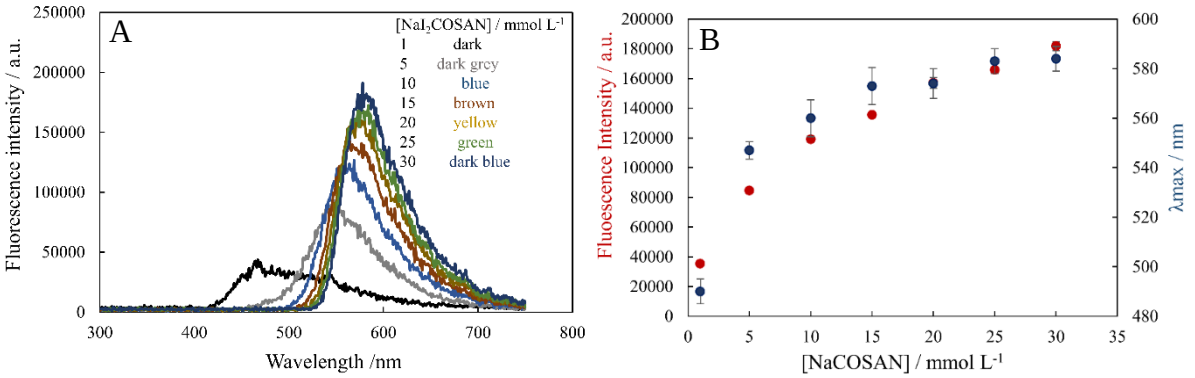

Figure 4.16. *(A) Fluorescence spectra and (B) fluorescence intensity of different NaI_2COSAN concentrations in H_2O at λ^{exc}= 210 nm.*

IV.5.3 Pump probe results of NaI_2COSAN in H_2O

Figure 4.17 depicts the normalized differential transmission decay at 5, 10, 15, and 20 mmol L^{-1} NaI_2COSAN in H_2O as a function of decay time, in the ps range. The lines correspond to the fits using a triexponential model around the maxima (Figure S4.14).

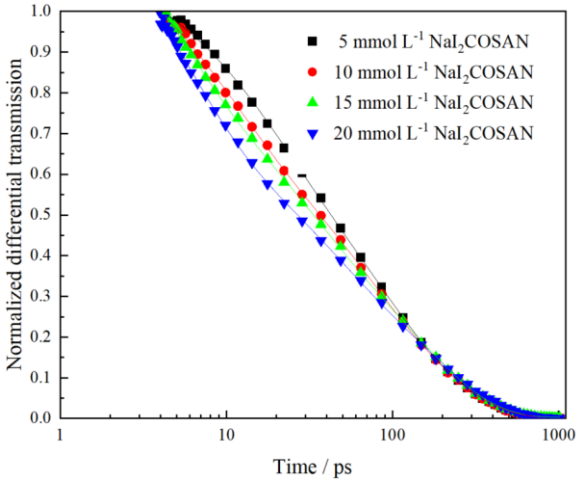

Figure 4.17*. Normalized differential transmission of different NaI_2COSAN concentrations at the maxima as a function of the time in ps derived from the pump probe spectra. The excitation wavelength was 400 nm.*

In comparison with NaCOSAN data, the characteristic decay times (t_1, t_2, and t_3) for NaI_2COSAN are shifted to a longer time scale, around 10, 100, and 200 ps, compared to 1, 7, and 150 for NaCOSAN.

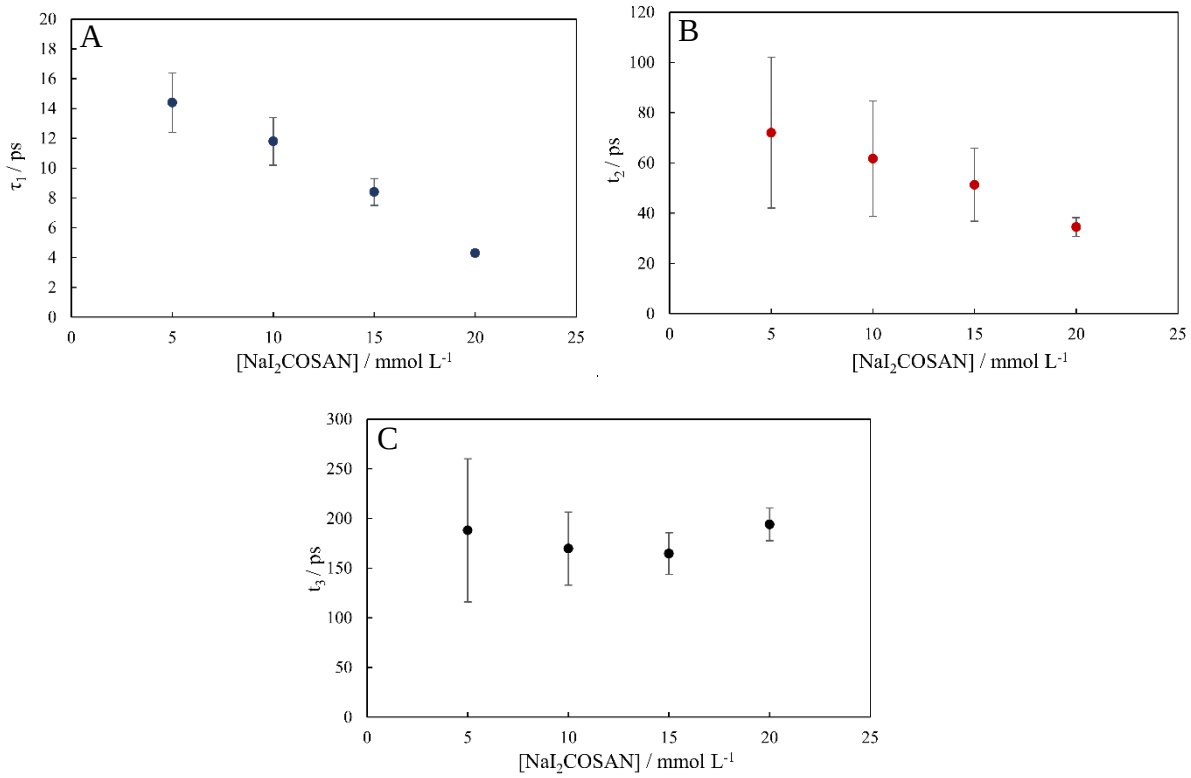

***Figure 4.18**. Relaxation times of (A) t_1, (B) t_2 and (C) t_3 as a function of NaI2COSAN concentration.*

Figure 4.18 depicts the relaxation times t_1, t_2, and t_3 as a function of NaI_2COSAN concentration. We observed that the relaxation times t_1 and t_2 strongly decrease as the NaI_2COSAN concentration increases, which is surprising as for NaCOSAN, t_1 and t_2 were rather constant (Figure 4.14). On the other hand, the relaxation time t_3 practically remains unaffected by the concentration of NaI_2COSAN. This difference in the variation in the ultrafast decay times between NaI_2COSAN and NaCOSAN has not yet been explained. Maybe the strong difference between NaCOSAN and NaI_2COSAN can be attributed to the presence of the two iodine atoms in NaI_2COSAN, which produce a steric hindrance that prevents (or slows down) the free rotation of the two semi-cages.

IV.6 Photophysical study of NaCOSAN in the presence of 2-BuOH

In Chapter II, the UV-Visible spectroscopy of NaCOSAN in 2-BuOH was studied. As mentioned in Chapter II, as the concentration of 2-BuOH increases, up to the point where it reaches the solubility limit, a bathochromic shift occurs in the UV adsorption peak of

NaCOSAN, shifting it from its λ_{max} in pure water, which is 281 nm, to 299 nm, which is similar to the λ_{max} in pure 2-BuOH. This shift in λ_{max} that was observed when the concentration of 2-butanol was increased was attributed to the exchange of the hydration shell of NaCOSAN with a solvation shell of 2- BuOH.

In the next step, we studied the steady state and time resolved fluorescence spectroscopy of NaCOSAN in water in the presence of 2-BuOH.

IV.6.1 Fluorescence of NaCOSAN in the presence of 2-BuOH

Figure 4.19 depicts the fluorescence spectra of NaCOSAN (left) and the evolution of the fluorescence intensity at 395 nm and 550 nm (right) in the presence of different 2-BuOH concentrations. We observed that the fluorescence intensity of NaCOSAN at 210 nm excitation wavelength is continuously quenched with the increase of 2-BuOH concentration until it reaches a threshold value above a ratio $S/S_0 > 1$. It is interesting to recall that the shift of the absorption band in the UV-vis experiment (see chapter II) is observed up to $S/S_0 \approx 1$, i.e., when the hydration shell of NaCOSAN was replaced by a solvation alcohol shell.

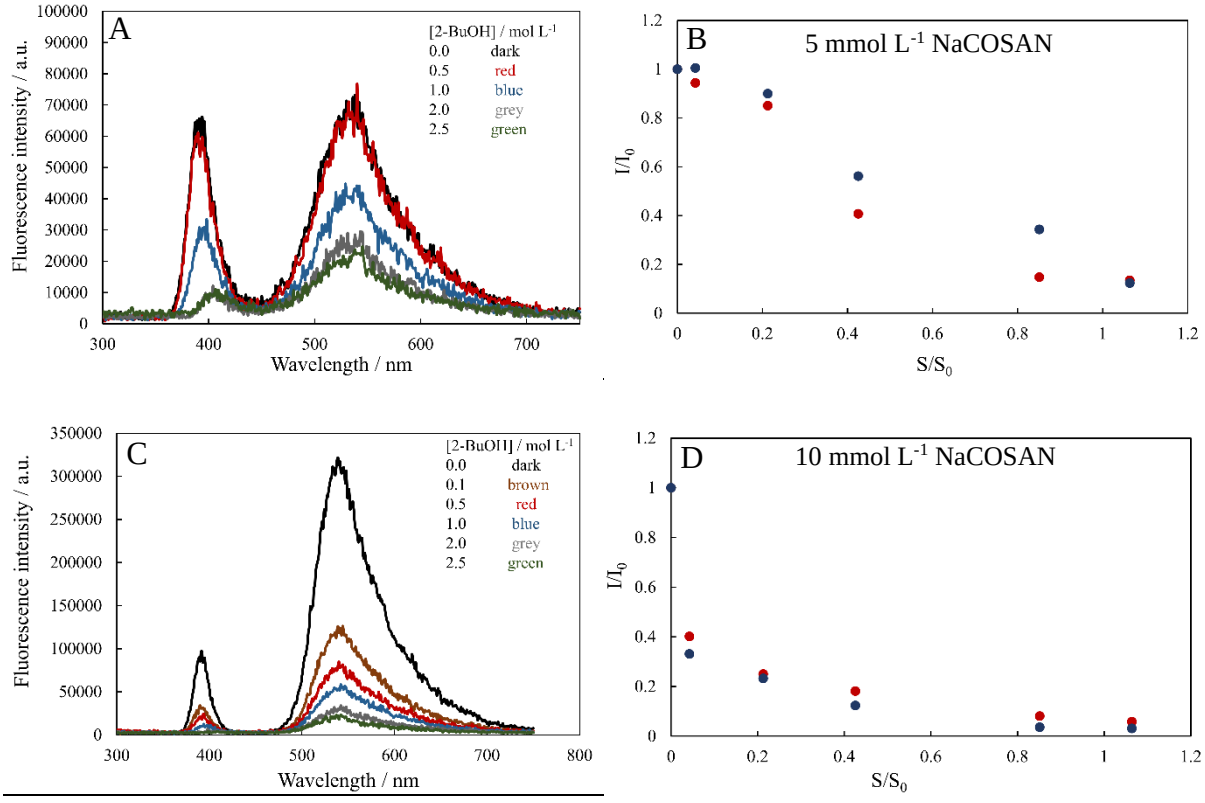

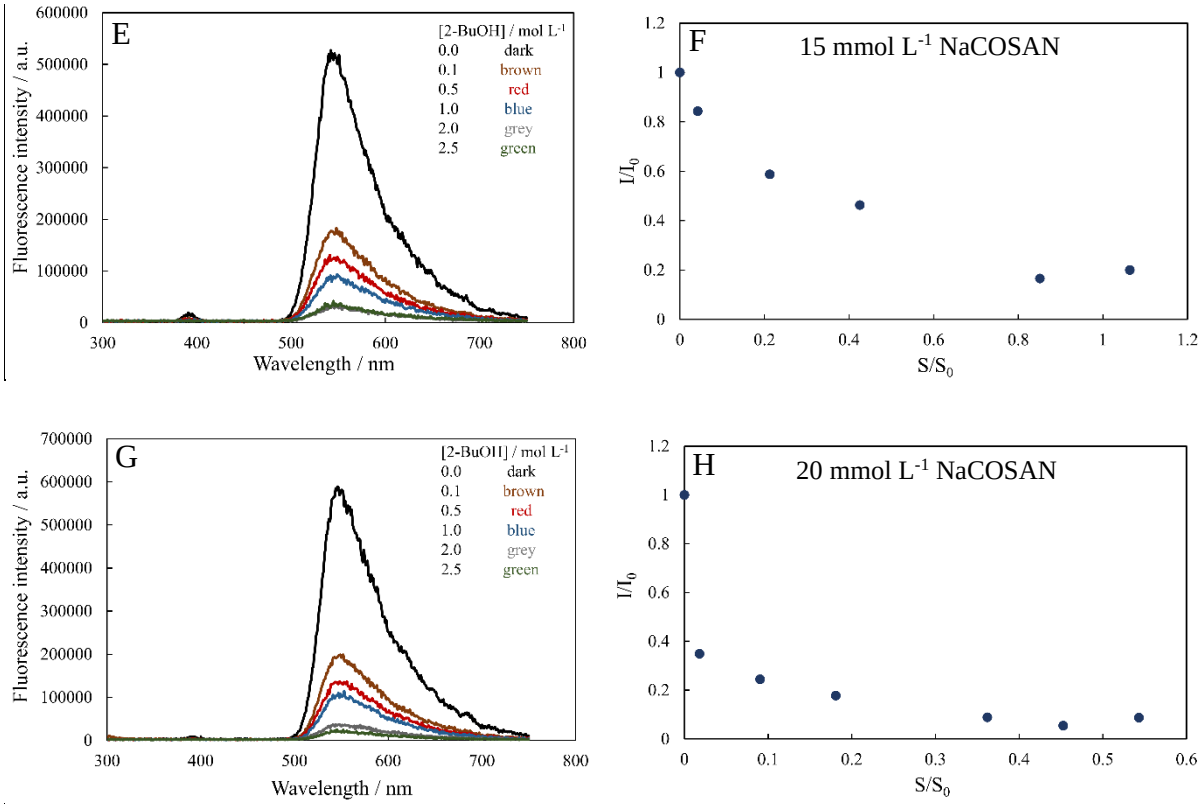

Figure 4.19. *Fluorescence spectra of (A) 5, (C) 10, (E) 15 and (G) 20 mmol L^{-1} NaCOSAN in the presence of different 2-BuOH concentrations at λ^{exc}= 210 nm. Fluorescence intensity of (B) 5, (D) 10, (F) 20 and (H) 25 mmol L^{-1} NaCOSAN in the presence of different 2-BuOH concentrations as a function of 2-BuOH concentrations. The red points correspond to the fluorescence intensity at 390 nm and the blue points at 550 nm.*

Here, we observed a quenching effect that gets stronger as the concentration of alcohol increases and as the concentration of NaCOSAN goes from below to above the CAC. Figure 4.20 depicts the fluorescence intensity at around 390 nm (left) and 550 nm (right) at different 2-BuOH concentrations as a function of NaCOSAN concentration.

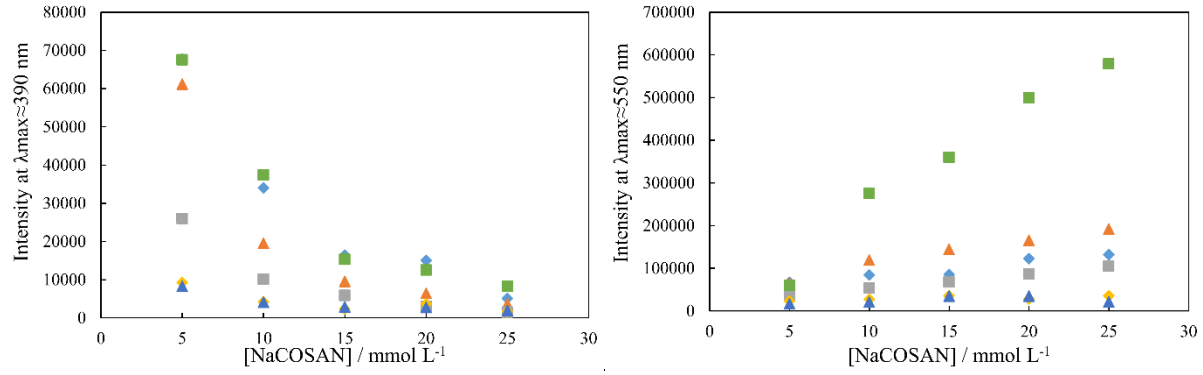

Figure 4.20. *Fluorescence intensity at around λmax≈390 nm (left) and at around λmax≈550 nm (right) of 0 (green squares, S/S_0=0), 0.1 (blue rhombus, S/S_0=0.04), 0.5 (orange triangles, S/S_0=0.2), 1 (grey squares, S/S_0=0.4), 2 (yellow rhombus, S/S_0=0.85) and 2.5 (blue triangle, S/S_0=1.1) mol L^{-1} 2-BuOH as a function of NaCOSAN concentration.*

We observed that the fluorescence intensity of NaCOSAN in the presence of 2-BuOH at around 390 nm (Figure 4.20, left) is decreased by increasing NaCOSAN concentration, as in the case

of NaCOSAN in aqueous solution, and the presence of 2-BuOH quenches this fluorescence band of NaCOSAN. We also observed that the fluorescence intensity of NaCOSAN in the presence of 2-BuOH at around 550 nm (Figure 4.20, right) is increased by increasing NaCOSAN concentration, but with an effect that is tempered in the presence of alcohol, becoming even quenched above $S/S_0 = 1$. However, the alcohol affects the luminescence as soon as it is added to the solution, so even when no hybrid nanometer-sized assemblies are observed, this is likely to be due to the change in the NaCOSAN hydration shell. A deeper analysis would require a larger NaCOSAN concentration range, starting from very low concentrations, and more data points to observe some variation in the luminescence quenching behavior.

IV.6.2 Pump probe results of NaCOSAN in the presence of 2-BuOH

All NaCOSAN concentrations in the presence of different concentrations of 2-BuOH exhibited distinct maxima in differential transmission versus probe wavelength, as shown in Figure S15.

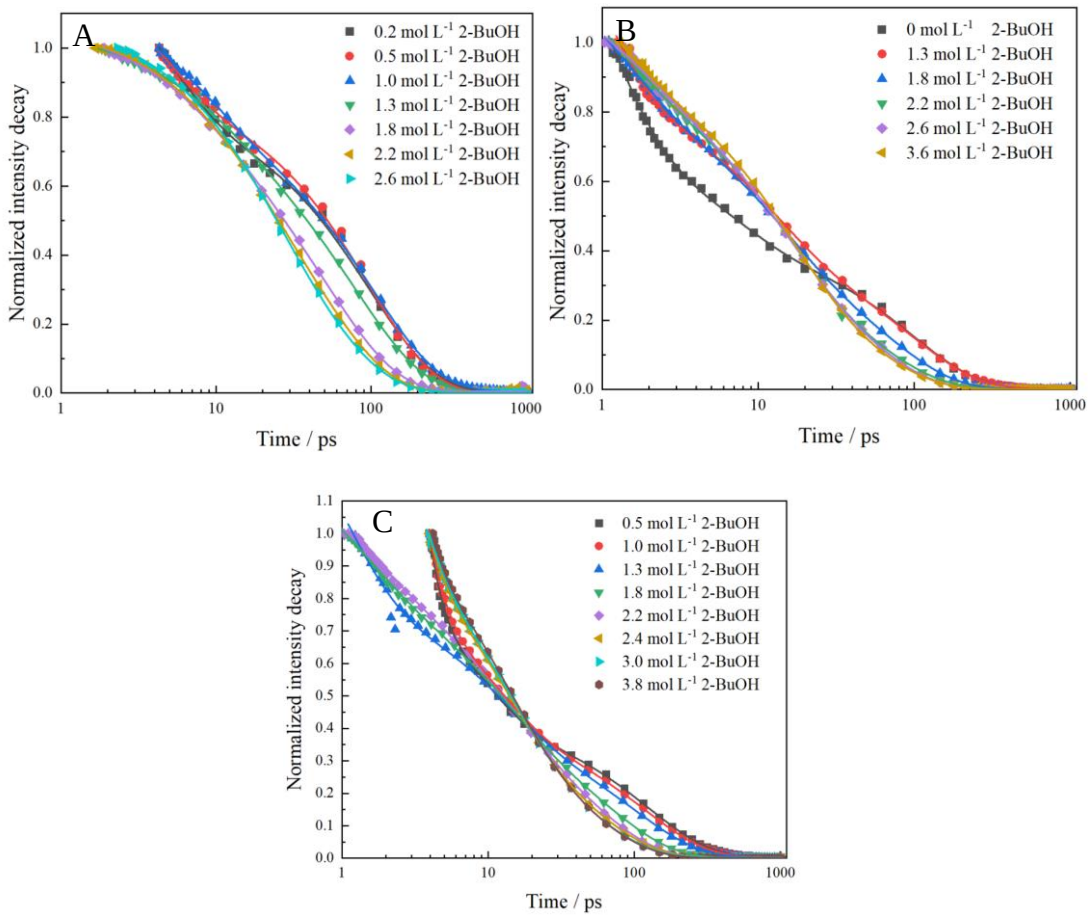

Figure 4.21. *Normalized intensity decay at maxima of (A) 5, (B) 15 and (C) 20 mmol L^{-1} NaCOSAN in the presence of different 2-BuOH concentrations as a function of time in ps.*

Figure 4.21 depicts the normalized intensity decay of 5, 15, and 20 mmol L^{-1} NaCOSAN in the presence of different 2-BuOH concentrations as a function of time in the ps range and is extracted around the maximum (≈ 500 nm) of the differential transmission. The femtosecond fluorescence decay of NaCOSAN follows an exponential function with two or three ultrafast decay times, between 0.75 and 125 ps.

Figure 4.22 depicts the relaxation times t_1, t_2 and t_3 evolution as a function of S/S_0 of 2-BuOH, and Table S4.4 presents the results of the fits.

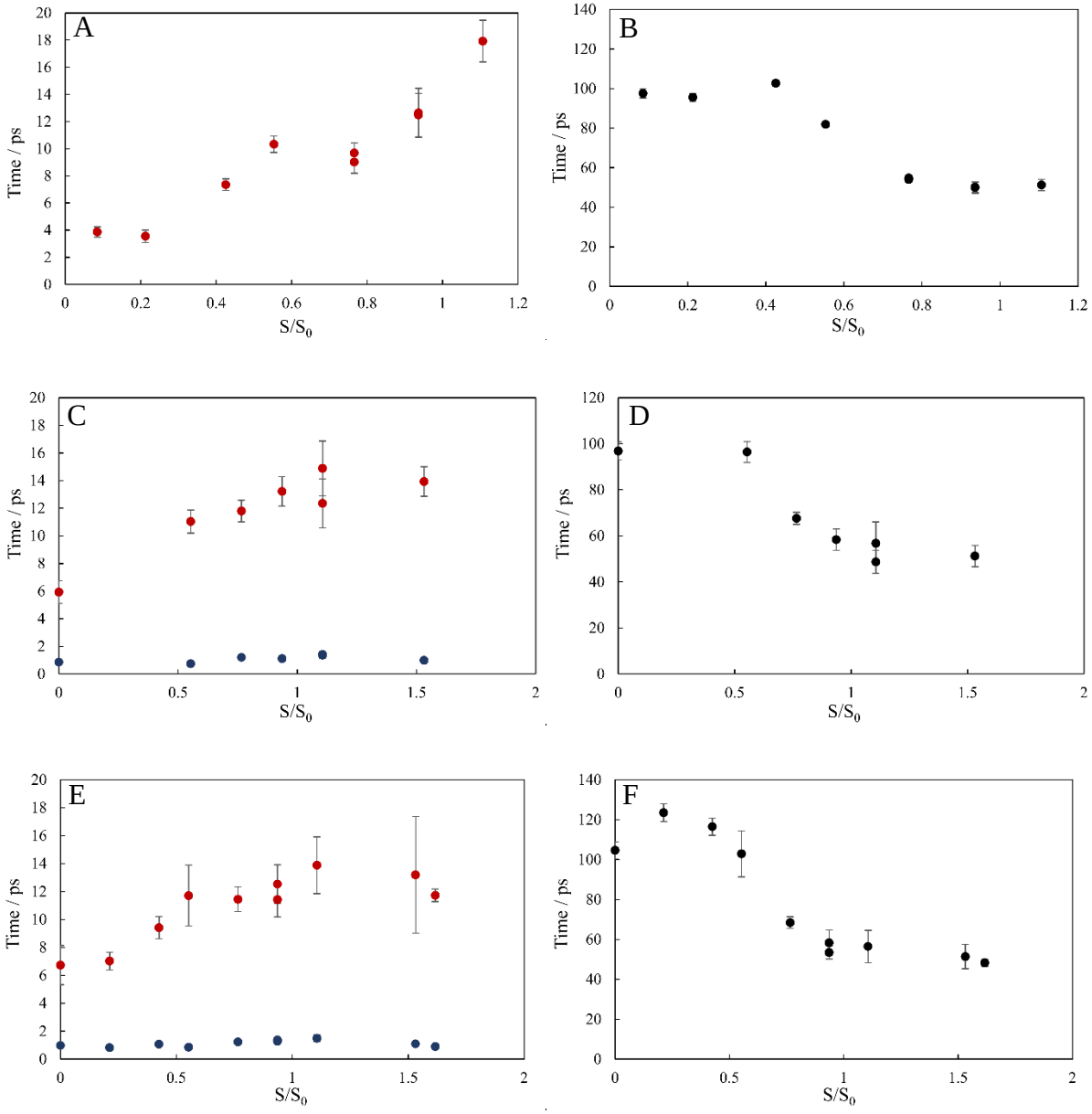

Figure 4.22. *Relaxation times of (A), (B) 5 mmol L^{-1}, (C), (D) 15 mmol L^{-1} and (E), (F) 20 mmol L^{-1} NaCOSAN as a function of S/S_0. The blue circles correspond to t_1, the red circles to t_2 and the dark circles to t_3.*

Whereas no evolution is observed for the shortest relaxation time t_1, the variations of t_2 and t_3 follow an S-shaped evolution that increase for t_2 and decrease for t_3 and again a threshold value

is achieved above $S/S_0 \approx 1$. Just the inflexion point seems to depend on the NaCOSAN concentration.

IV.7 Conclusions of Chapter IV

The photophysical properties of NaCOSAN in aqueous and partial organic environments were investigated in this chapter. The photophysical properties of NaI_2COSAN, which is a derivative of NaCOSAN with a higher electron density, were also investigated in an aqueous environment. The photophysical properties of NaCOSAN were studied using steady-state and time-resolved fluorescence spectroscopy.

Initially, we proved by excitation at different wavelengths and then comparison with no fluorophore molecule, a classical ion NaCl, and a surfactant Triton X 100 that NaCOSAN has significant fluorescence. The steady-state emission spectra of NaCOSAN show two regimes at excitation wavelengths centered at around 210 and 300 nm, depending on NaCOSAN concentration, presumably indicating the transition from the monomeric to the aggregated state of NaCOSAN. The steady-state emission spectra of NaCOSAN show three regimes at excitation wavelength 330nm depending on NaCOSAN concentration, indicating a transition from monomers to vesicles and then to aggregates of NaCOSAN.

The pump probe photoluminescence appears to have three discrete lifetimes in the ps range. Pump probe photoluminescence shows that the shortest relaxation time t_1 remains unaffected by increasing NaCOSAN concentration, whereas the relaxation time t_2 remains nearly constant until 10 mmol L^{-1} and then increases. The relaxation time t_3 is also nearly constant until 10 mmol L^{-1} NaCOSAN and increases with the increase in NaCOSAN concentration. This increase above 10 mmol L^{-1} NaCOSAN, which appears for t_2 and t_3, could also suggest the transition from the monomeric to aggregated state of NaCOSAN.

In the next step, we investigated the fluorescence of NaI_2COSAN in H_2O. We found that the fluorescence intensity of NaI_2COSAN is increasing and shifting to higher wavelengths with the increase in NaI_2COSAN concentrations. The pump probe photoluminescence of NaI_2COSAN shows three discrete lifetimes in the range of ps. In contrast to what was found for NaCOSAN, the relaxation times t_1 and t_2 of NaI_2COSAN are decreasing with the increase in NaI_2COSAN concentration, and the relaxation time t_3 remains unaffected by the increase in NaI_2COSAN concentration.

Subsequently, the photophysical properties of NaCOSAN in the presence of different 2-BuOH concentrations were studied. We found that the presence of 2-BuOH quenches the fluorescence of NaCOSAN. The concentrations of NaCOSAN below and above the CAC show two discrete

and three discrete lifetimes in the ps range, respectively. The relaxation time t_1 is practically constant with the increase in 2-BuOH concentration. On the other hand, the relaxation time t_2 remains nearly constant until $S/S_0 \approx 0.5$ and then increases. Surprisingly, the relaxation time t_3 above $S/S_0 \approx 0.5$ decreases with increasing 2-BuOH concentration, leading to a plateau around $S/S_0 \approx 1$.

In conclusion, steady-state and time-resolved fluorescence spectroscopy enables us to validate the type of preferable rotamers based on aggregation or solvation conditions. Time-resolved fluorescence studies reveals that NaCOSAN self-assembly has multiple species in excited states in the range of ps and ns.

References

[1] I. Guerrero, Z. Kelemen, C. Viñas, I. Romero, F. Teixidor, Metallacarboranes as Photoredox Catalysts in Water, Chem. - A Eur. J. 26 (2020) 5027–5036. https://doi.org/10.1002/chem.201905395.

[2] M. Tarrés, V.S. Arderiu, A. Zaulet, C. Viñas, F. Fabrizi De Biani, F. Teixidor, How to get the desired reduction voltage in a single framework! Metallacarborane as an optimal probe for sequential voltage tuning, Dalt. Trans. 44 (2015) 11690–11695. https://doi.org/10.1039/c5dt01464f.

[3] D.C. Malaspina, C. Viñas, F. Teixidor, J. Faraudo, Atomistic Simulations of COSAN: Amphiphiles without a Head-and-Tail Design Display “Head and Tail” Surfactant Behavior, Angew. Chemie - Int. Ed. 59 (2020) 3088–3092. https://doi.org/10.1002/anie.201913257.

[4] M. Bühl, D. Hnyk, J. Machácek, Computational study of structures and properties of metallaboranes: Cobalt bis(dicarbollide), Chem. - A Eur. J. 11 (2005) 4109–4120. https://doi.org/10.1002/chem.200401202.

[5] A.M.A. Abdelgawwad, J.A.M. Xavier, D. Roca-Sanjuán, C. Viñas, F. Teixidor, A. Francés-Monerris, Light-Induced On/Off Switching of the Surfactant Character of the o -Cobaltabis(dicarbollide) Anion with No Covalent Bond Alteration , Angew. Chemie. 133 (2021) 25957–25961. https://doi.org/10.1002/ange.202111493.

[6] M. Uchman, A.I. Abrikosov, M. Lepšík, M. Lund, P. Matějíček, Nonclassical Hydrophobic Effect in Micellization: Molecular Arrangement of Non-Amphiphilic Structures, Adv. Theory Simulations. 1 (2018) 1–10. https://doi.org/10.1002/adts.201700002.

[7] A. Das, S. Ghosh, Supramolecular assemblies by charge-transfer interactions between donor and acceptor chromophores, Angew. Chemie - Int. Ed. 53 (2014) 2038–2054. https://doi.org/10.1002/anie.201307756.

[8] X. Kuang, L. Meng, C.Z. Lu, Unveiling electron transfer in a supramolecular aggregate for adaptive and autonomous photochromic response, IScience. 24 (2021) 102956. https://doi.org/10.1016/j.isci.2021.102956.

[9] Ľ. Mátel, F. Macášek, P. Rajec, S. Heřmánek, J. Plešek, B-Halogen derivatives of the bis(1,2-dicarbollyl)cobalt(III) anion, Polyhedron. 1 (1982) 511–519. https://doi.org/10.1016/S0277-5387(00)81604-6.

[10] P.M. Gassin, L. Girard, G. Martin-Gassin, D. Brusselle, A. Jonchère, O. Diat, C. Viñas, F. Teixidor, P. Bauduin, Surface activity and molecular organization of metallacarboranes at the air-water interface revealed by nonlinear optics, Langmuir. 31 (2015) 2297–2303. https://doi.org/10.1021/acs.langmuir.5b00125.

[11] P. Bauduin, S. Prevost, P. Farràs, F. Teixidor, O. Diat, T. Zemb, A theta-shaped amphiphilic cobaltabisdicarbollide anion: Transition from monolayer vesicles to micelles, Angew. Chemie - Int. Ed. 50 (2011) 5298–5300. https://doi.org/10.1002/anie.201100410.

[12] J.R. Lakowicz, Principles of Fluorescence Spectroscopy, 3rd ed., Springer, New York, 2006.

[13] I.J. Bigio, J.R. Mourant, Ultraviolet and visible spectroscopies for tissue diagnostics: Fluorescence spectroscopy and elastic-scattering spectroscopy, Phys. Med. Biol. 42 (1997) 803–814. https://doi.org/10.1088/0031-9155/42/5/005.

[14] M. Uchman, V. ɯormɲovič, Z. Tošner, P. Matějíček, Classical Amphiphilic Behavior of Nonclassical Amphiphiles: A Comparison of Metallacarborane Self-Assembly with SDS Micellization, Angew. Chemie - Int. Ed. 54 (2015) 14113–14117. https://doi.org/10.1002/anie.201506545.

[15] T.P. Senftle, S. Hong, M.M. Islam, S.B. Kylasa, Y. Zheng, Y.K. Shin, C. Junkermeier, R. Engel-Herbert, M.J. Janik, H.M. Aktulga, T. Verstraelen, A. Grama, A.C.T. Van Duin, The ReaxFF reactive force-field: Development, applications and future directions, Npj Comput. Mater. 2 (2016). https://doi.org/10.1038/npjcompumats.2015.11.

[16] A. Nevin, A. Cesaratto, S. Bellei, C. D'Andrea, L. Toniolo, G. Valentini, D. Comelli, Time-resolved photoluminescence spectroscopy and imaging: New approaches to the analysis of cultural heritage and its degradation, Sensors (Switzerland). 14 (2014) 6338–6355. https://doi.org/10.3390/s140406338.

[17] D.N. Dirin, S. Dreyfuss, M.I. Bodnarchuk, G. Nedelcu, P. Papagiorgis, G. Itskos, M. V. Kovalenko, Lead halide perovskites and other metal halide complexes as inorganic capping ligands for colloidal nanocrystals, J. Am. Chem. Soc. 136 (2014) 6550–6553. https://doi.org/10.1021/ja5006288.

[18] A. Othonos, Probing ultrafast carrier and phonon dynamics in semiconductors, J. Appl. Phys. 83 (1998) 1789–1830. https://doi.org/10.1063/1.367411.

[19] M. Zervos, A. Othonos, M. Sergides, T. Pavloudis, J. Kioseoglou, Observation of the direct energy band gaps of defect-tolerant Cu3N by ultrafast pump-probe spectroscopy, J. Phys. Chem. C. 124 (2020) 3459–3469. https://doi.org/10.1021/acs.jpcc.9b10303.

Supporting information of Chapter IV

IV.2 Fluorescence of NaCOSAN in H_2O

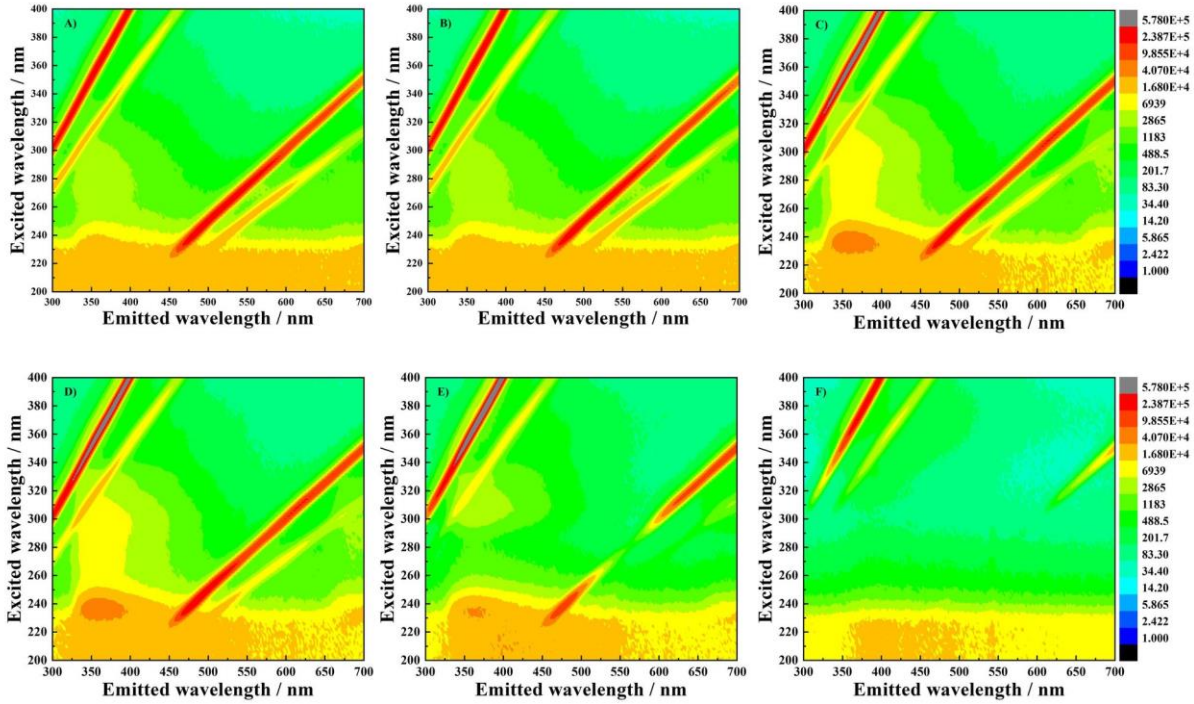

Figure S4.1. *2D fluorescence spectra of (A) H_2O, (B) 0.00084, (C) 0.002, (D) 0.017, (E) 0.1 and (F) 0.5 mmol L^{-1} NaCOSAN in H_2O.*

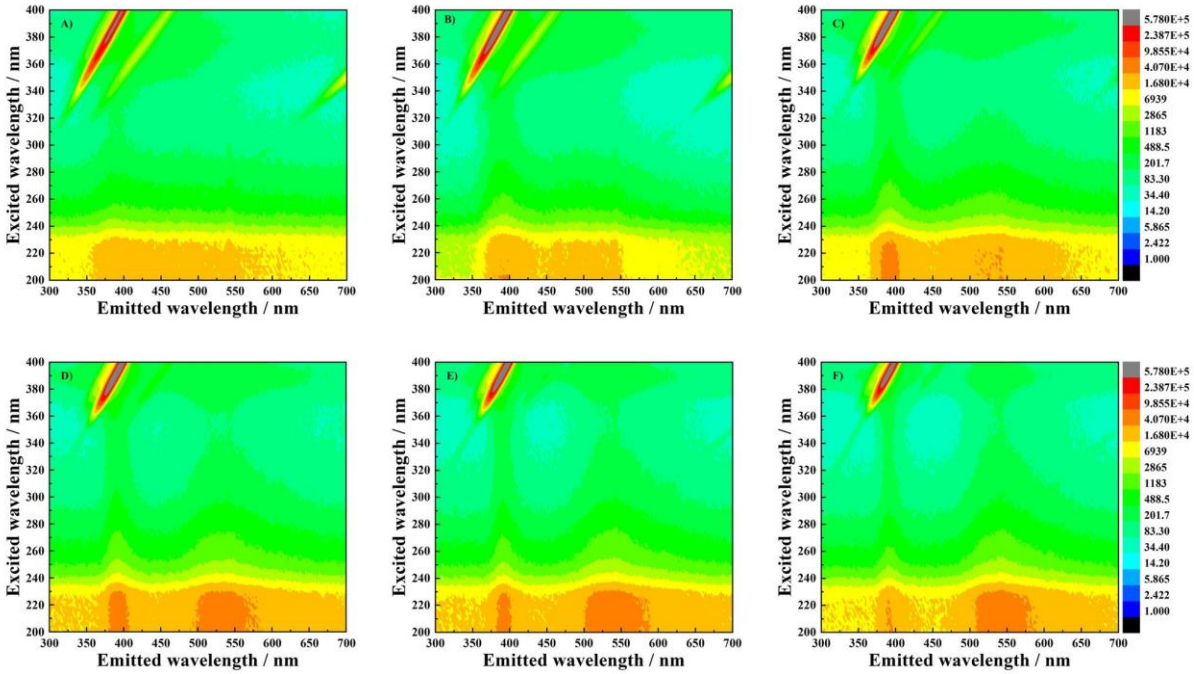

Figure S4.2. *2D fluorescence spectra of (A) 1, (B)1.3, (C) 2.6, (D) 4, (E) 5.3 and (F) 6.6 mmol L^{-1} NaCOSAN in H_2O.*

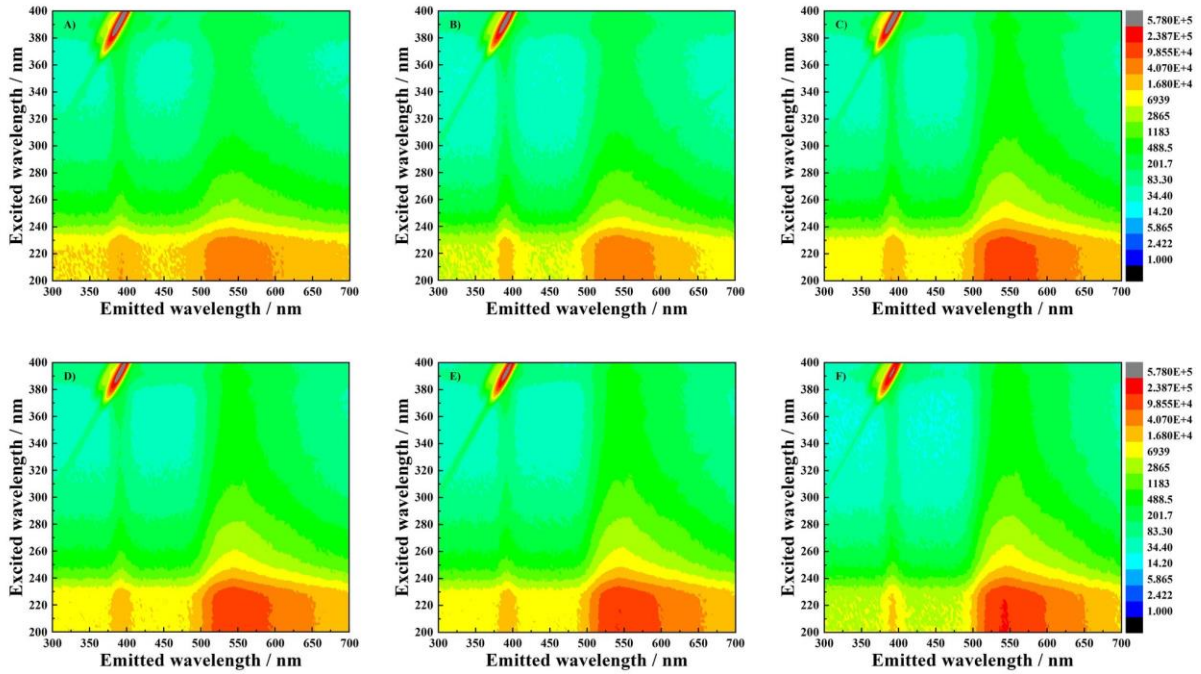

Figure S4.3. *2D fluorescence spectra of (A) 8, (B) 9.3, (C) 9.6, (D) 10.7, (E) 11.7 and (F) 12.7 mmol L^{-1} NaCOSAN in H_2O.*

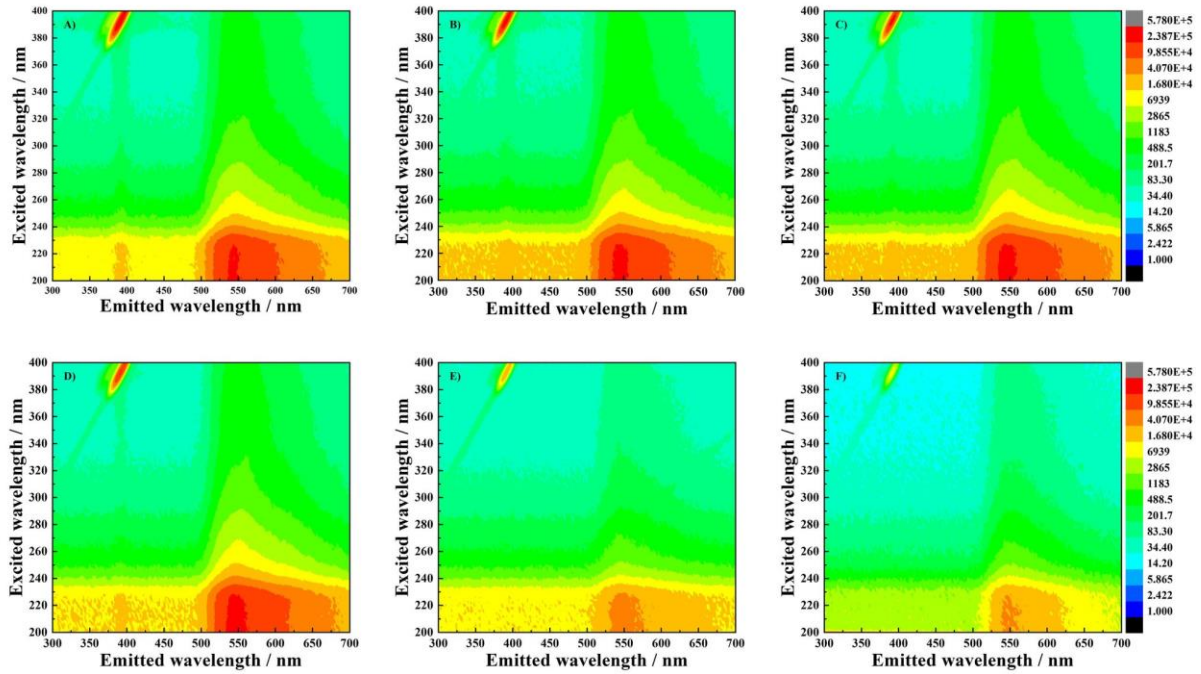

Figure S4.4. *2D fluorescence spectra of (A) 13.7, (B) 14.7, (C) 15.7, (D) 16.7, (E) 20 and (F) 25 mmol L^{-1} NaCOSAN in H_2O.*

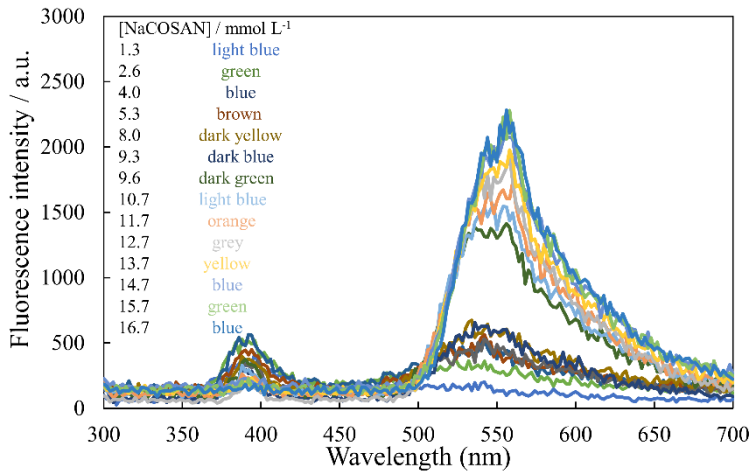

Figure S4.5. *Fluorescence spectra of different NaCOSAN concentrations at λ^{exc}= 300 nm.*

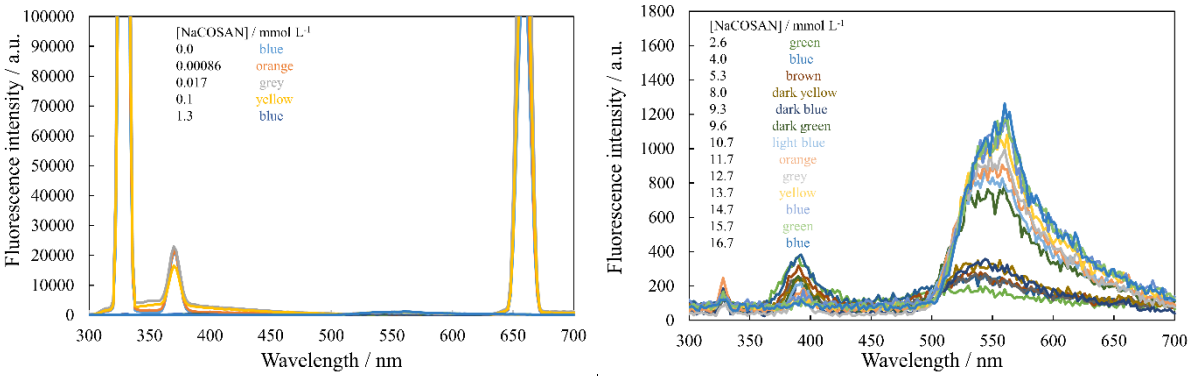

Figure S4.6*. Fluorescence spectra of different NaCOSAN concentrations at λ^{exc}= 330 nm.*

IV.2.1 Fluorescence of a classical chaotrope (NaCl) and a surfactant (Triton X 100)

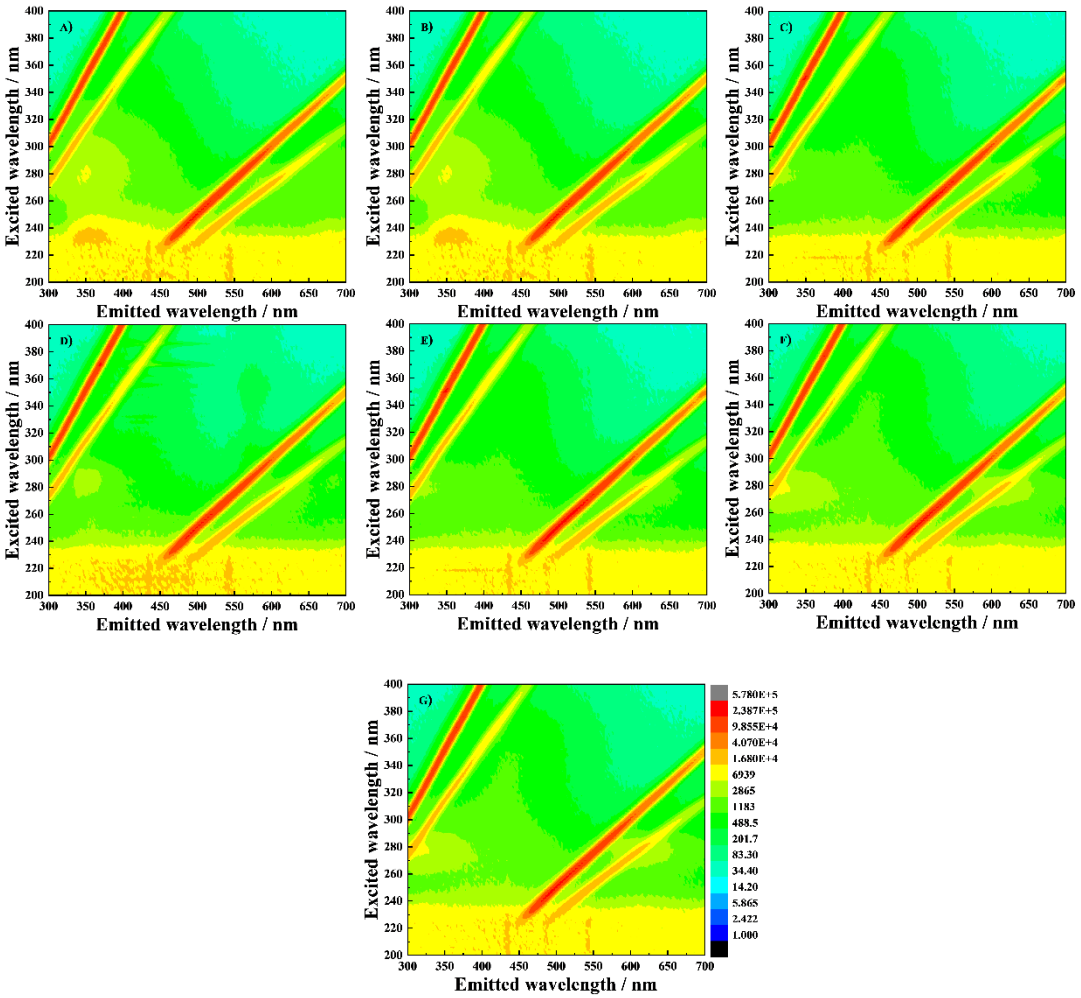

Figure S4.7. *2D fluorescence spectra of (A) 0.002, (B) 0.1, (C) 0.5, (D) 1, (E) 10, (F) 20 and (G) 30 mmol L^{-1} NaCl in H_2O.*

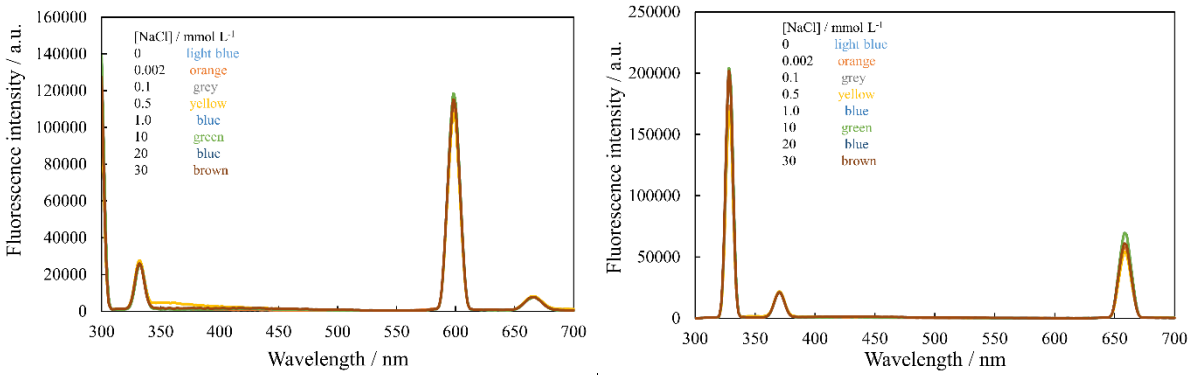

Figure S4.8*. Fluorescence spectra of different NaCl concentrations at λ^{exc}= 300 nm (left) and λ^{exc}= 330 nm (right).*

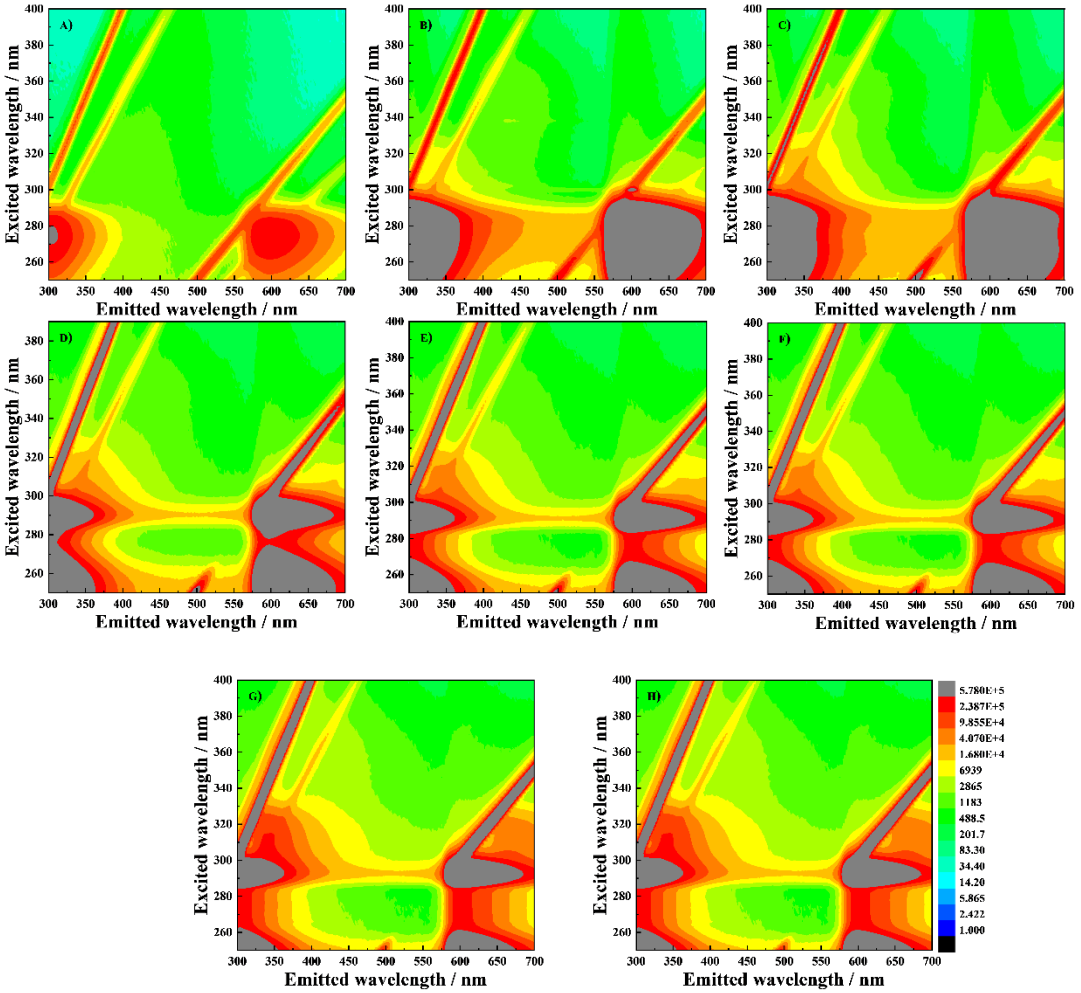

Figure S4.9. *2D fluorescence spectra of (A) 0.01, (B) 0.1, (C) 0.5, (D) 1, (E) 4, (F) 6, (G) 8 and (H) 10 mmol L^{-1} Triton X 100 in H_2O.*

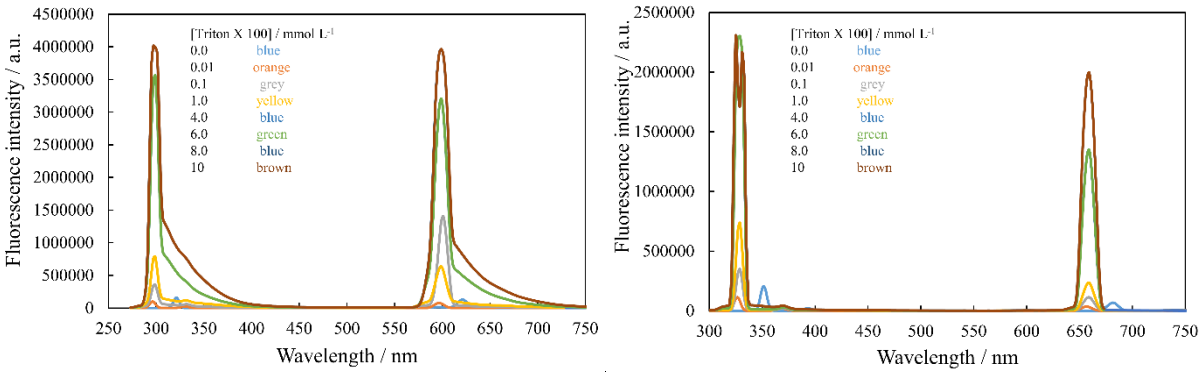

Figure S4.10*. Fluorescence spectra of different Triton X 100 concentrations at λ^{exc}= 300 nm (left) and λ^{exc}= 330 nm (right).*

IV.3 Photoluminescence of NaCOSAN in H_2O

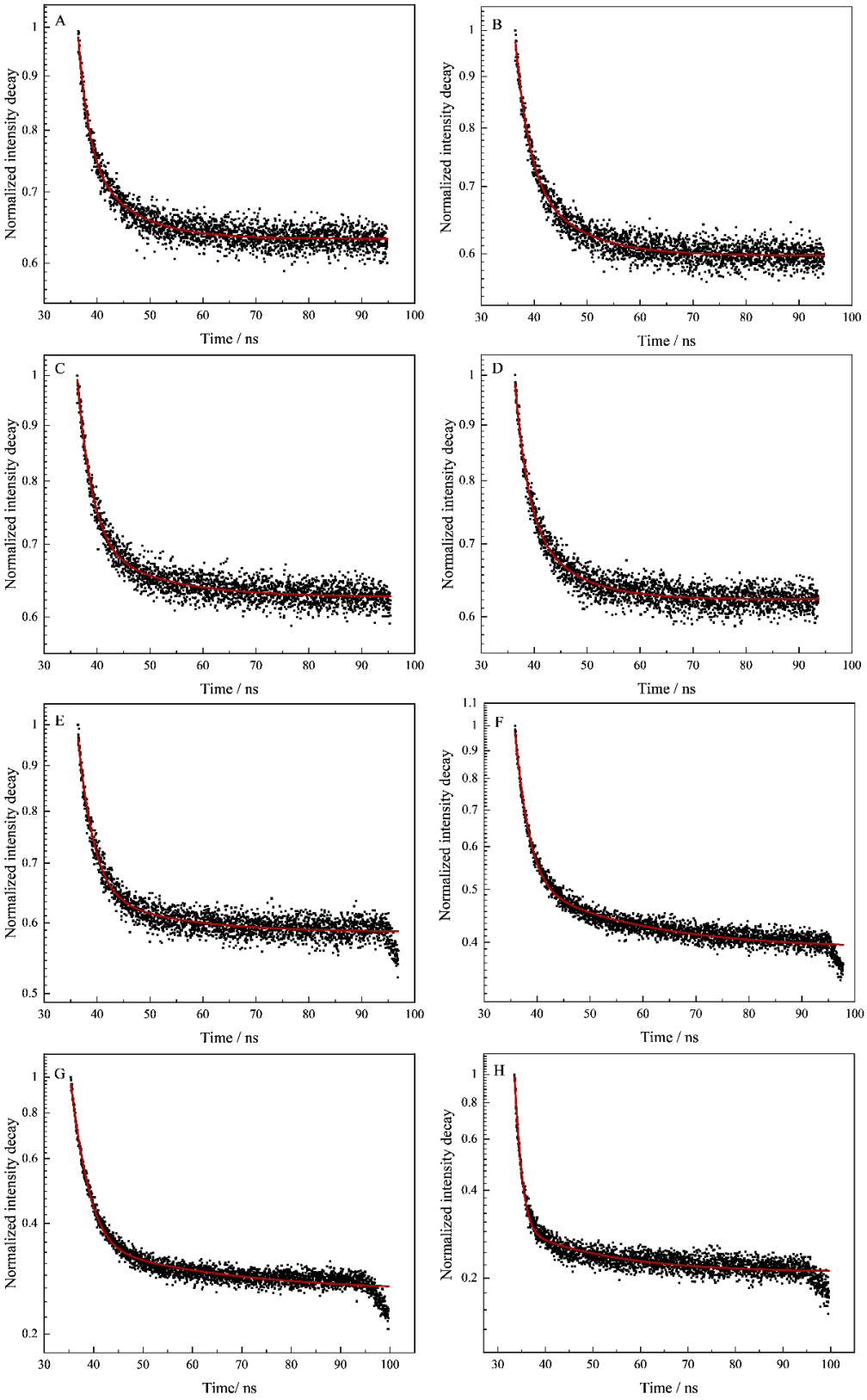

Figure S4.11. *Normalized intensity decay of (A) 0.1, (B) 1, (C) 5, (D) 10, (E) 15, (F) 25, (G) 40 and (H) 50 mmol L^{-1} NaCOSAN concentration (dark circles) and fitted normalized intensity decay (red line) as a function of time in ns.*

Table S4.1. Results of double exponential function fittings.

[NaCOSAN] mmol L^{-1}	y_0	A_1	t_1 / ns	A_2	t_2 / ns
0.1	0.63 ± 0.0005	0.21 ± 0.008	1.77 ± 0.09	0.13 ± 0.008	8.3 ± 0.42
1	0.59 ± 0.0005	0.24 ± 0.009	2.25 ± 0.11	0.13 ± 0.01	9.2 ± 0.54
5	0.62 ± 0.0008	0.28 ± 0.006	2.51 ± 0.08	0.08 ± 0.006	13.1 ± 1.1
10	0.62 ± 0.0005	0.23 ± 0.01	2.08 ± 0.11	0.12 ± 0.011	8.4 ± 0.51
15	0.58 ± 0.001	0.31 ± 0.006	2.57 ± 0.08	0.06 ± 0.006	15.2 ± 1.7
25	0.39 ± 0.001	0.45 ± 0.003	2.16 ± 0.03	0.13 ± 0.002	20.7 ± 0.9
40	0.26 ± 0.002	0.60 ± 0.003	2.62 ± 0.03	0.09 ± 0.002	26.9 ± 2.1
50	0.21 ± 0.0008	0.68 ± 0.004	1.11 ± 0.01	0.85 ± 0.0019	17.7 ± 0.85

IV.4 Pump probe photoluminescence of NaCOSAN in H_2O

IV.4.1 Pump probe results of NaCOSAN in H_2O

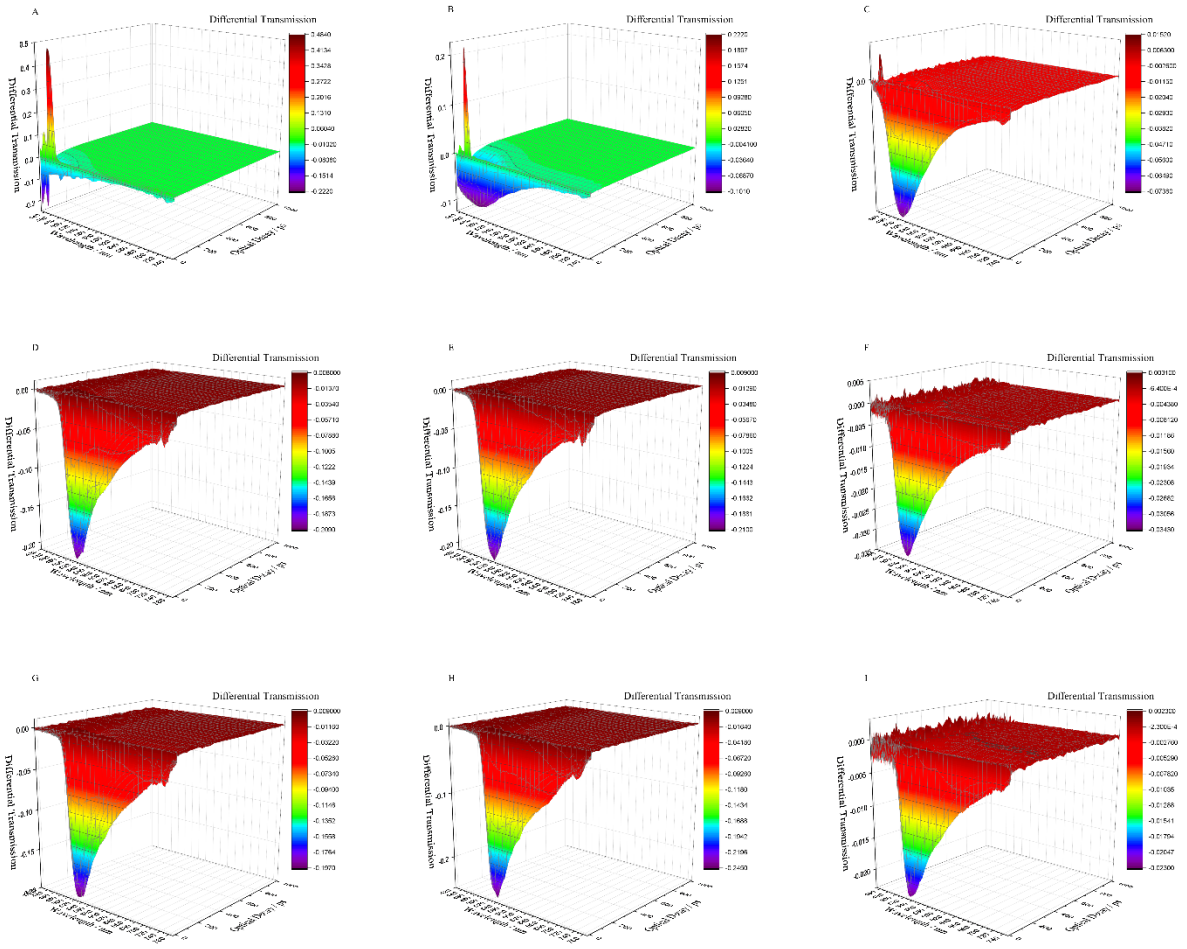

Figure S4.12. *Pump probe spectra of (A) 1, (B) 5, (C) 10, (D) 15, (E) 20, (F) 25, (G) 30, (H) 40 and (I) 50 mmol L^{-1} NaCOSAN in H_2O. The excitation wavelength was 400 nm.*

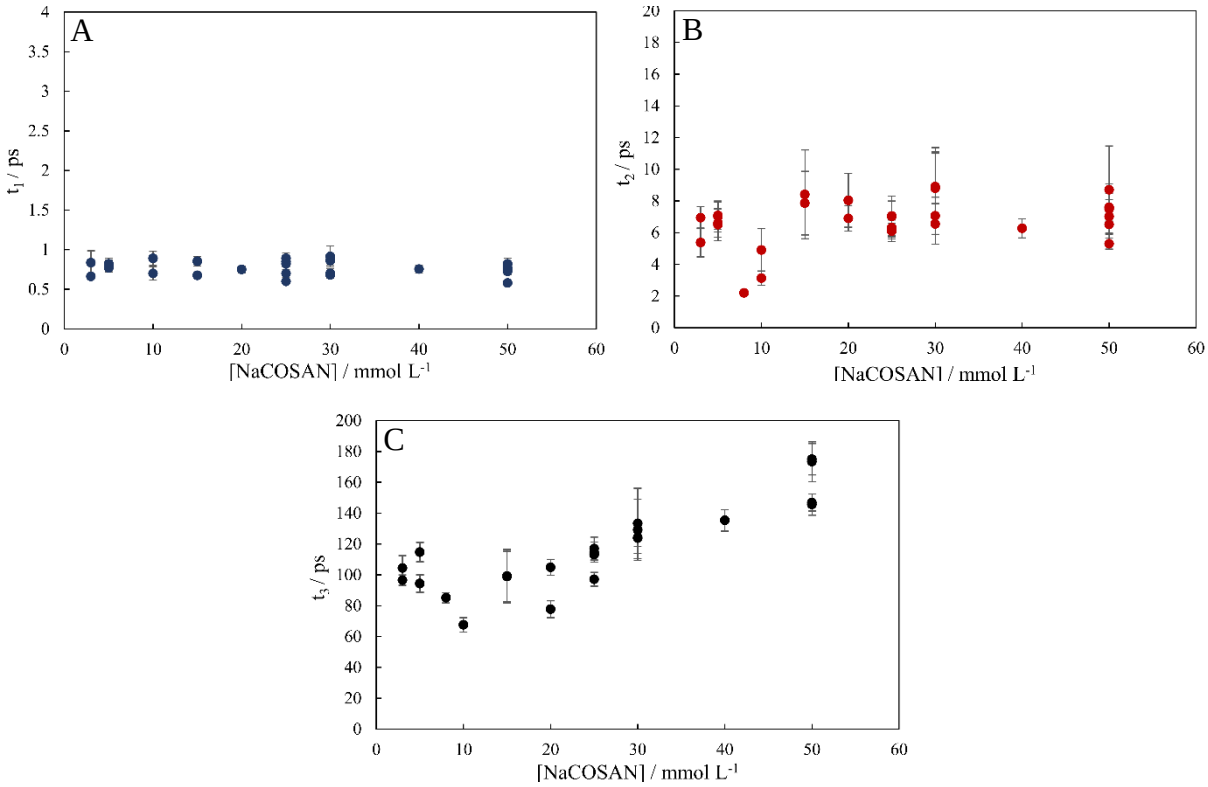

Figure S4.13. *Relaxation times (A) t_1, (B) t2, and (C) t_3 in ps at different wavelengths around the maxima are a function of NaCOSAN concentrations.*

Table S4.2. Pump probe results of NaCOSAN in H_2O

[NaCOSAN]/ mM	Wavelength/nm	τ_1/ps	Error bars	τ_2/ps	Error bars	τ_3/ps	Error bars
50	540	0.77	0.04	7.6	1.1	173.4	12.9
50	550	0.74	0.02	7.6	0.9	174.9	10.2
50	525	0.73	0.03	7.01	0.58	145.6	6.9
50	560	0.73	0.04	8.71	2.8	102.9	21.2
50	520	1.24	0.26	6.7	0.5	178.13	4.01
50	530	0.94	0.11	6.75	0.32	190.23	3.9
50	550	0.56	0.06	5.31	0.1	186.66	4.51
40	520	0.75	0.05	6.27	0.6	135.3	6.9
30	500	0.91	0.1	6.54	1.3	124.2	5.6
30	540	0.86	0.06	8.90	2.5	129.1	19.8
30	520	0.70	0.06	7.06	1.2	123.8	9.9
30	560	0.68	0.03	8.80	2.2	133.4	22.8
25	510	0.85	0.07	6.32	0.9	97.1	4.5
25	520	0.89	0.07	7.05	1.3	117.0	7.4
25	525	0.82	0.04	7.02	1	114.7	6.5
25	510	0.70	0.05	6.20	0.6	113.5	4
25	520	0.60	0.03	6.10	0.5	113.1	5
25	525	0.60	0.02	6.10	0.4	113.1	3.8
20	500	1.23	0.16	8.04	7.1	77.7	5.5
20	520	0.75	0.04	6.90	0.8	104.9	5.2
20	530	1.23	0.16	8.04	7.1	77.7	5.5
15	540	0.85	0.06	8.41	2.8	99.2	17.3
15	560	0.68	0.03	7.86	2.0	98.9	16.3
10	510	0.70	0.09	3.13	0.5	53.2	1.7
10	520	0.89	0.09	4.91	1.3	67.6	4.7
8	500	-	-	2.19	0.1	85.1	3.3
5	520	0.82	0.04	7.02	1	114.7	6.5
5	525	0.78	0.03	7.08	0.9	114.8	6.2
5	520	0.82	0.07	6.50	1	94.3	5.7
5	525	0.77	0.05	6.60	0.9	94.4	5.7
3	500	0.84	0.15	5.38	0.9	96.5	3.3

IV.5 Photophysical study of NaI_2COSAN

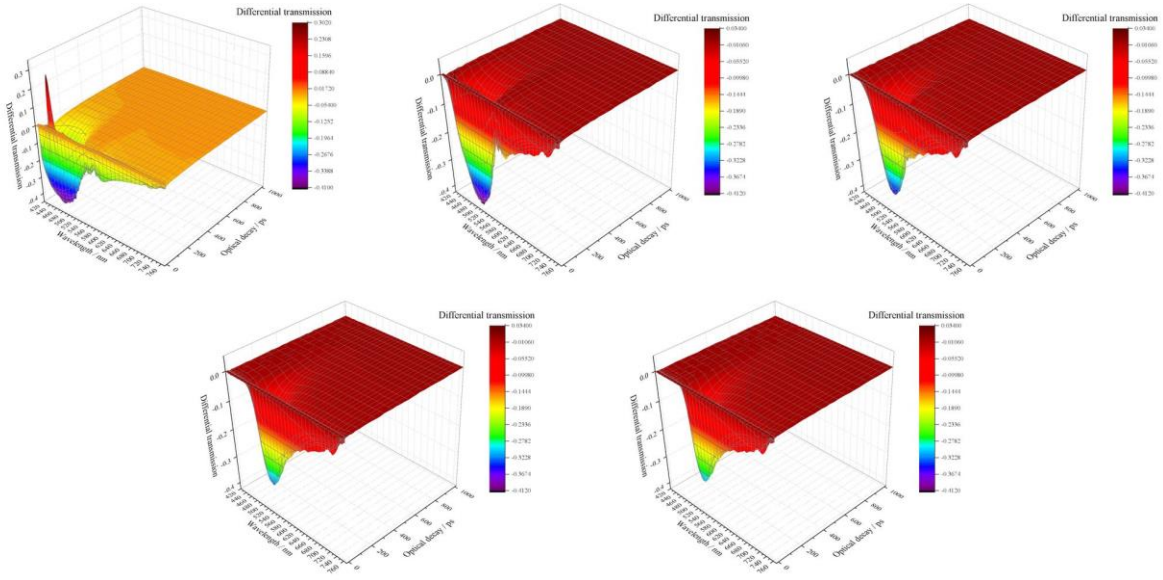

Figure S4.14. *Pump probe spectra of (A) 1, (B) 5, (C) 10, (D) 15 and (E) 20 mmol L^{-1} NaI_2COSAN in H_2O.*

Table S4.3: Pump probe results of NaI_2COSAN in H_2O.

[NaI_2COSAN] /mmol L^{-1}	**Wavelength / nm**	**t_1/ps**	**t_2/ps**	**t_3/ps**
5	500	9.9 ± 1.4	38.1 ± 2.9	164.1 ± 7.1
5	510	14.3 ± 1.9	69.8 ± 26.5	181.2 ± 49.7
10	510	11.7 ± 1.6	60.3 ±20.6	166.4 ± 27.7
10	520	8.5 ± 0.9	50.9 ± 13.8	163.8 ± 19.2
15	500	4.1 ± 0.4	24.3 ± 2.7	150.7 ± 4.5
15	520	8.4 ± 0.9	50.9 ± 13.7	163.8 ± 19.2
20	540	4.8 ± 0.3	31.4 ± 0.02	174.1 ± 7.9

IV.6 Photophysical study of NaCOSAN in the presence of 2-BuOH

IV.6.2 Pump probe results of NaCOSAN in the presence of 2-BuOH

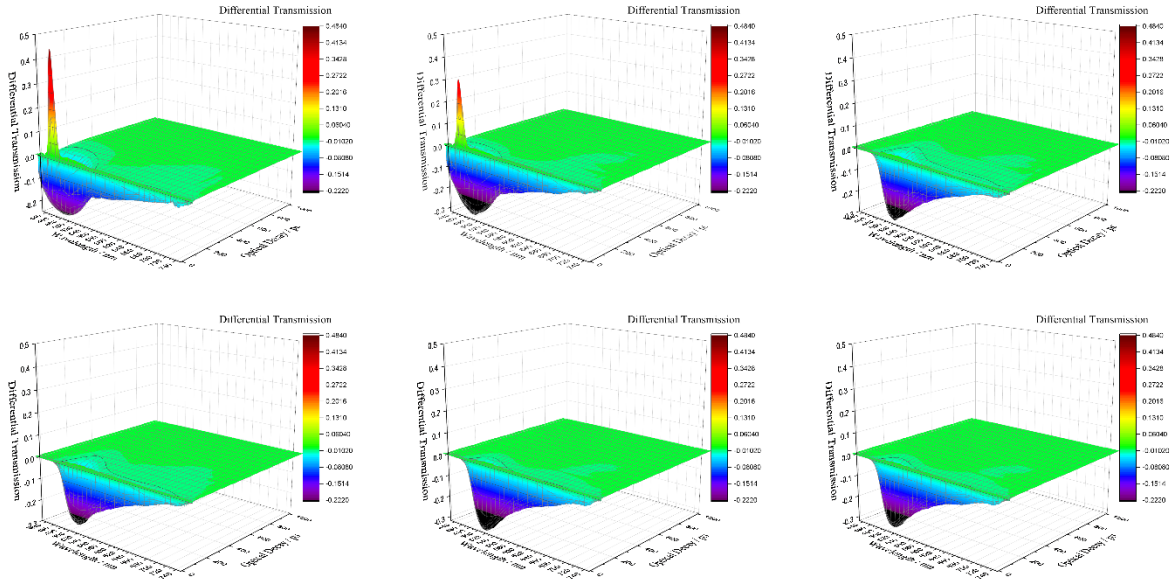

Figure S4.15. *Pump probe spectra of (A) 5, (B) 15 and (C) 20 mmol L^{-1} NaCOSAN in in the presence of different 2-BuOH concentrations.*

Table S4.4: Pump probe results of NaCOSAN in the presence of different 2-BuOH concentrations.

[NaCOSAN] mmol L^{-1}	[2-BuOH] mmol L^{-1}	Wavelength nm	t_1/ps	t_2/ps	t_3/ps
5	0.2	480		3.87 ± 0.38	97.57 ± 2.35
5	0.5	480		3.55 ± 0.45	95.54 ± 2.1
5	1.0	480		7.35 ± 0.43	102.67 ± 1.47
5	1.3	480		10.33 ± 0.59	81.88 ± 1.24
5	1.8	500	1.19 ± 0.20	9.68 ± 0.74	54.01 ± 1.58
5	1.8	480		9.02 ± 0.82	54.84 ± 1.31
5	2.2	500	1.92 ± 0.44	12.48 ± 1.59	49.96 ± 2.85
5	2.2	480		12.63 ± 1.81	50.12 ± 2.58
5	2.6	480		17.92 ± 1.54	51.27 ± 2.89
15	0	510	0.85 ± 0.07	5.92 ± 0.81	96.84 ± 3.90
15	1.3	510	0.74 ± 0.06	11.03 ± 0.84	96.37 ± 4.56
15	1.8	510	1.21 ± 0.07	11.79 ± 0.79	67.61 ± 2.61
15	2.2	510	1.11 ± 0.11	13.22 ± 1.07	58.35 ± 4.65
15	2.6	510	1.41 ± 0.21	12.35 ± 1.78	48.67 ± 4.96
15	2.6	510	1.37 ± 0.21	14.88 ± 1.98	56.72 ± 9.30
15	3.6	510	0.98 ± 0.12	13.93 ± 1.07	51.21 ± 4.61
20	0	500	0.98 ± 0.13	6.73 ± 1.40	104.67 ± 4.21
20	0.5	510	0.82 ± 0.08	7.02 ± 0.64	123.50 ± 4.44
20	1	510	1.07 ± 0.09	9.41 ± 0.79	116.47 ± 4.34
20	1.3	510	0.86 ± 0.13	11.71 ± 2.18	102.9 ± 11.56
20	1.8	510	1.23 ± 0.09	11.44 ± 0.88	68.41 ± 2.96
20	2.2	510	1.28 ± 0.09	12.53 ± 1.38	58.34 ± 6.31
20	2.2	510	1.38 ± 0.14	11.42 ± 1.24	53.42 ± 3.20
20	2.6	510	1.49 ± 0.24	13.88 ± 2.03	56.44 ± 8.08
20	3.6	510	1.10 ± 0.14	13.19 ± 4.17	51.43 ± 6.11
20	3.8	510	0.90 ± 0.05	11.73 ± 0.46	48.26 ± 1.79

General Conclusions

In this thesis, the ionic specific effect (ISE) with boron clusters such as cobalta-bis dicarbolide (Co $(C_2B_9H_{11})_2^-$, COSAN) and their monovalent derivatives, as well as the divalent dodecaborates clusters ($B_{12}X_{12}^{2-}$ with X=H, F, Cl, Br, and I), have been investigated. They are all qualified as superchaotropic nano-ions and as an extension on the Hofmeister series for anions. This extension is essentially based on the decrease in charge density, from 14 down to 2 charges per nm^3. The ion specific effect of a chaotropic agent is commonly a salting-in effect which at the first order increases the solubility of macromolecules or colloids in solution.

The first part of this work was thus focused on the capacity of COSAN and its di-iodinated derivative (I_2COSAN), the inorganic anion with the lowest charge densities, to solubilize organic compounds with different hydrophobic characters. On the one hand, starting with short-chain alcohols with the lowest hydrophobic character (partially soluble organic compounds), it has been shown that COSAN and derivatives significantly increase their solubility in water. On the other hand, the solubilization efficiency of the boron clusters is significantly decreased as the hydrophobic character (log *P* value) of the organic compound increases. However, unlike the solubilization mechanism of a surfactant, which necessitates the formation of micelles, COSAN and its derivatives are effective at increasing the solubility of short-chain alcohols from the first additions and achieving at higher concentrations the same solubility as an ionic surfactant like SDS. Our investigations at the molecular and supramolecular levels have revealed the formation of nanometric co-assemblies. The hydration shell of COSAN is exchanged for an alcohol solvation shell during the formation of these co-assemblies, explaining why the mechanism is efficient—typically one nano-ion for approximately hundreds of alcohol molecules. The solubilization mechanism based on organic-inorganic co-assemblies differs significantly from all the classical solubilization methods. The second peculiarity of these organic-inorganic co-assemblies is that they can be used to efficiently solubilize organic compounds with a much higher hydrophobic character. The solubilization ability of COSAN (and derivatives) arises from its nanometric size, rigid structure, delocalized charge (3D aromaticity), and peculiar way of interacting with other molecules that combines electrostatics, dihydrogen bond formation, and superchaotropic effects. Other boron clusters, such as the halogenated dodecaborate such as $B_{12}Cl_{12}^{2-}$, $B_{12}Br_{12}^{2-}$ and $B_{12}I_{12}^{2-}$ solubilize alcohols with a comparable solubilization mechanism to COSAN, still based on the formation of organic-inorganic co-assemblies. These water/halogenated

dodecaborate/alcohol co-assemblies increase the solubilization efficiency of hydrophobic compounds with high hydrophobic character.

The second part of this thesis was dedicated to the ion specific effect for still the boron anionic clusters but with more complex molecules, proteins, and keeping in mind the salting-in effect associated with a protein denaturation classically observed for chaotropic anions. We observed that proteins with diverse molecular and supramolecular characteristics interact strongly with the superchaotropic boron clusters at very low concentrations, around the millimolar range. Unlike what is known with chaotropic agents, it has been observed that nano-ions/proteins assemblies form at molar ratios around the unit. The size of these assemblies is well defined and depends on the molar ratio. The proteins within these assemblies are partially protecting against denaturation (the formation of nano-ions/proteins assemblies shifts the denaturation process to a higher temperature). The efficiency of interaction to induce the formation of nano-ions/proteins assemblies increases with the superchaotropicity of the nano-ion ($B_{12}H_{12}^{2-}$ < $Na_2B_{12}Cl_{12}^{2-}$ < $Na_2B_{12}I_{12}^{2-}$ < COSAN). These superchaotrope nano-ions can be considered that act as molecular glue.

These two ISE studies make it abundantly evident that superchaotropicity is defined in ways that go far beyond simply observing the salt-in effect at lower salt concentrations. As with neutral polymers or copolymers, it is possible to observe novel self-assemblies, which opens up a new area of study.

The impact of self-assembly and co-assembly with organic solutes on the photophysical characteristics of the cobalta-bis dicarbollide boron cluster was examined. It was found that cobalta-bis dicarbollide boron clusters exhibit fluorescence. In addition, the transitions from monomers to aggregates via vesicles in the self-assembly sequence of cobalta-bis dicarbollide in water were identified by a significant variation in the fluorescence signal. Pump-probe photoluminescence was also used to pinpoint the potential novel transitions that could emerge as a result of supramolecular assembly formation. When COSAN was present in concentrations that were close to those at which assembly formation occurs, the picosecond lifetime of COSAN assemblies and co-assemblies with organic solutes was impacted. This section reveals new research avenues for a comprehensive understanding of the interactions underlying the term "superchaotropicity."

In conclusion, the remarkable behavior of nano-ions is applicable to any colloidal soft matter system, such as polymers or nanoparticles. This dissertation highlights that the superchaotropic behavior of nano-ions is a versatile and novel formulation tool for soft matter materials and applications.

Perspectives

The purpose of this doctoral dissertation was to investigate the superchaotropic effect of anionic boron clusters on weakly soluble compounds and proteins in aqueous solutions, which was accomplished to a significant degree and numerous results were obtained. However, the study has left some questions unanswered or has raised new questions that could be further investigated through additional experimental and theoretical research.

In Chapter II, we investigated the ability of anionic boron clusters, specifically cobalta-bis dicarbolide (Co $(C_2B_9H_{11})_2^-$, COSAN) and its di-iodinated derivative (I_2COSAN), as well as closo-dodecaborates ($B_{12}X_{12}^{2-}$ with X=H, F, Cl, Br, and I) to solubilize organic compounds with different hydrophobic characters, such as alcohols and hydrophobic dyes. In this chapter, an extensive study into the solubilization of a wide range of organic compounds by COSAN was carried out. However, this was not the case for closo-dodecaborates, for which the range of tested organic compounds was considerably fewer. In fact, only 2-butanol was used to investigate the solubility of closo-dodecaborates. At this point, it is of major importance to investigate the solubilization efficiency of closo-dodecaborates in a broader range of organic compounds. Inorganic superchaotropic nano-ions, such as polyoxometalates, could also be interesting to investigate; they may also be efficient solubilizers. The COSAN/2-butanol/water and $B_{12}X_{12}^{2-}$/2-butanol/water co-assemblies can efficiently solubilize much more hydrophobic compounds with diverse chemical natures used as organic solvents, fragrances, pharmaceutical active ingredients, and dyes. This promising solubilization mechanism, which differs considerably from conventional solubilization methods, should be studied in a much broader range of organic compounds, as it can be applied to a variety of application domains. We can also consider these nano-ions as hydrotropes, and thus, looking for synergistic effects coupling standard hydrotropes such as ethanol and nano-ions can also be another way of investigating solubilization.

In Chapter III, we investigated the effect of interactions between different boron clusters and different proteins. The structural effects induced by their interactions were investigated at the molecular and supramolecular levels by combining spectroscopic and scattering techniques. Fluorescence was one of the spectroscopic techniques used to study the interactions between nano-ions and proteins. It was observed fluorescence quenching upon the increase of the nano-ions concentration. At this point, it may be of interest to determine whether the quenching mechanism is static or dynamic. The static quenching is caused by the ground-state complex

formation between fluorophores and quenchers, whereas the dynamic quenching is caused by collisional encounters between fluorophores and quenchers. The two mechanisms can be distinguished by their dependence on temperature and excited-state lifetime. The binding constant and the number of binding sites of the complex nano-ion/protein were calculated by the Stern-Volmer equation as described in Chapter III (Section III.2.3). In the binding process, several binding forces can be engaged, including hydrogen bonding interactions, van der Waals forces, electrostatic interactions, and hydrophobic interactions. The distinction between those forces can be made based on the signs and magnitudes of the thermodynamic parameters, such as the Gibbs free energy change (ΔG_0), enthalpy change (ΔH_0) and entropy change (ΔS_0). It seems quite interesting to identify the binding forces that take place in the interactions between nano-ions and proteins. As revealed by scattering techniques, the investigated proteins with distinct molecular and supramolecular properties interacted with the boron clusters and formed assemblies. The efficiency of the boron clusters to promote protein assembly increases with their (super)chaotropicity. Transmission electron microscopy (TEM) could provide significant details regarding the morphological characteristics of these assemblies at that point. Considering that controlled protein assemblies have applications in a variety of domains, any further research in this chapter could be beneficial.

In Chapter IV, we investigate the effect of self-assembly and co-assembly with organic solutes on the photophysical properties of the cobalta-bis dicarbollide boron clusters. At this point, it is of major importance to investigate the photophysical properties of a broader range of boron clusters. The photophysical properties have been studied extensively by fluorescence and photoluminescence techniques in steady state and time-resolved. DFT calculations and molecular dynamic simulations could be useful to validate the experimental results were obtained.

Résumé en français

Le terme "effet ionique spécifique" désigne un phénomène dans lequel des ions de même charge ont des effets très différents sur des fluides complexes en phase aqueuse. A concentration identique des sels de nature différente peuvent soit augmenter la solubilité d'un soluté ou à l'inverse provoquer sa précipitation, un phénomène indépendant des effets électrostatiques. Il y a environ 150 ans, Franz Hofmeister, professeur tchèque en pharmacologie, a été l'un des premiers scientifiques à étudier ces effets sur des systèmes biologiques et a donc classé les ions en fonction de l'intensité des effets.[1] Avant les travaux d'Hofmeister, Poiseuille, un physicien français, avait observé que l'ajout de sels à l'eau affectait sa viscosité.[2] Une découverte qui avait déjà posé les bases des recherches qui allaient suivre sur l'effet ionique spécifique.

Les ions de la série élaborée par F. Hofmeister sont classés de kosmotropes à chaotropes, en fonction de leur capacité à interagir avec les molécules d'eau et à affecter le réseau d'hydrogène dans les solutions aqueuses. Les ions kosmotropes diminuent la solubilité des macromolécules et des colloïdes hydrophiles en réorganisant les molécules d'eau autour d'eux (ordre, kosmos), créant ainsi un environnement défavorable à la dispersion des macromolécules et des colloïdes en solution. Les ions kosmotropes diminuent l'activité de l'eau et induisent un effet appelé « salting-out » qui réduit le domaine de stabilité des colloïdes dispersés, la solubilité des composés organiques, etc. En revanche, les ions chaotropes augmentent la solubilité des macromolécules et des colloïdes en perturbant l'organisation des molécules d'eau autour d'eux (désordre, chaos), créant ainsi un environnement plus favorable à la dispersion des macromolécules et des colloïdes dans la solution. En conséquence, les ions kosmotropes provoquent un effet de « salting-in ». En d'autres termes, les chaotropes sont des ions faiblement hydratés capables d'augmenter la solubilité des macromolécules et des colloïdes dans les solutions aqueuses. En revanche, les kosmotropes sont des ions fortement hydratés qui diminuent la solubilité des macromolécules et des colloïdes hydrophiles.[3]

Récemment, les effets ioniques spécifiques avec des anions de taille nanométrique ont été étudiés. Ces ions de taille nanométrique ont été inclus dans la série d'Hofmeister dans une extension de cette série au-delà des anions chaotropes et ont été qualifiés d'anions « superchaotropes ».[4,5] Il a en effet été constaté en autres au travers d'expérience de mesures de point de trouble sur des assemblages de tensioactifs non ioniques que l'effet de salting-in des ions de taille nanométrique (ou nano-ions) est beaucoup plus fort que celui des ions

chaotropiques classiques.[6] Plus précisément, il a été démontré que certains anions de type polyoxométalates ou clusters de bore ont la capacité à faible concentration (de l'ordre du millimolaire) s'adsorbent sur des surfaces hydrophiles formées à partir d'auto-assemblages de tensioactifs à base de sucre [4,7] ou polyéthoxylés [4,8] ou encore peuvent interagir avec les cavités hydrophobes formées par des macrocycles tels que les cyclodextrines.[9,10]

Dans le cadre de cette thèse, notre étude s'est concentrée sur les effets ioniques spécifiques de clusters de bore anioniques, en particulier le cobalta-bis dicarbolide (Co $(C_2B_9H_{11})_2^-$, COSAN) et ses dérivés, mais aussi les clusters de type dodécaborates halogénés ($B_{12}X_{12}^{2-}$ avec X=H, F, Cl, Br, et I). Les clusters de bore sont intéressants pour de nombreuses applications en raison de leurs propriétés chimiques et physiques uniques, une grande stabilité chimique et thermique et une structure électronique accordable.[11–16]

L'anion bis-dicarbollide de cobalt ou COSAN (Co = cobalt ; SAN = sandwich) est un anion inorganique de taille nanométrique de forme ellipsoïdale. Il se compose d'un cation métallique central, généralement Co^{3+}, pris en sandwich entre deux semi-cages dicarbollides volumineuses et hautement hydrophobes $(C_2B_9H_{11})_2^-$, chacune d'entre elles portant deux charges négatives. La charge résultante est donc une fois négative.[17]

Dans le chapitre I, l'état actuel des connaissances sur les effets ioniques spécifiques et les nano-ions est passé en revue. Parmi toutes les caractéristiques classiques des agents de surface, la capacité à solubiliser les composés hydrophobes n'a jamais été évaluée pour les nano-ions inorganiques. Dans le chapitre II, nous avons étudié la capacité du COSAN (et de son dérivé di-iodé, I_2COSAN) à solubiliser des composés organiques présentant différents caractères hydrophobes, tels que des alcools et des colorants hydrophobes. Des diagrammes de phase eau/COSAN/systèmes ternaires d'alcool ont été établis pour évaluer l'extension des domaines monophasiques et ainsi l'efficacité de solubilisation du COSAN. Les comparaisons dans cette mesure de l'efficacité ont été faites avec un agent tensioactif anionique très classique tel que le SDS mais aussi avec des cyclodextrines. Afin de déchiffrer le mécanisme qui permet de gagner un facteur d'environ deux sur la solubilisation du 2-butanol par le COSAN, différentes techniques de diffusion et spectrales ont été combinées pour obtenir des informations aux échelles moléculaires et supramoléculaires. Des mesures UV-vis ont été effectuées pour sonder l'évolution de la sphère de solvatation du COSAN, c'est-à-dire son environnement moléculaire local, dans l'eau et en augmentant la concentration d'alcool. Des expériences de diffusion des rayons X et des neutrons aux petits angles (SAXS et SANS) ont été également réalisées pour

caractériser les assemblages hybrides COSAN/2-butanol que nous avons pu mettre en évidence. En utilisant la même stratégie expérimentale, nous avons étudié l'efficacité de la solubilisation des assemblages COSAN/2-butanol afin de permettre dans un second temps la solubilisation de composés plus hydrophobes que le 2-butanol et de diverses natures chimiques. En outre, nous avons poussé la comparaison entre l'effet du COSAN et des closo-dodécaborates sur la solubilité des composés hydrophobes et de vérifier une classification d'efficacité qui suit celle de la série superchaotrope liée à la densité de charge des nano-ions.

Dans le chapitre III, nous avons étudié les effets ioniques spécifiques des nano-ions sur des protéines, des molécules bien plus complexes. Les protéines présentent une grande diversité en termes d'environnement physico-chimique local, de charge électrique et de polarité. Par conséquent, l'étude des nano-ions avec les protéines permet d'étudier un large éventail de forces intermoléculaires, des interactions hydrophobes aux interactions électrostatiques en passant par les liaisons hydrogène et les interactions stériques. Dans ce chapitre, nous avons étudié ces effets ioniques pour trois protéines différentes et différents nano-ions borés. Afin de déchiffrer les effets clés des interactions nano-ions avec les protéines aux niveaux moléculaires et supramoléculaires différentes techniques ont été combinées. Des mesures de spectroscopie UV-visible et de dichroïsme circulaire ont été effectuées pour obtenir des informations sur l'environnement local des nano-ions et sur les effets induits sur la structure secondaire des protéines. Des techniques de diffusion, telles que la diffusion de lumière dynamique (DLS), de diffusion de rayons X et de neutrons aux petits angles (acronymes anglais SAXS et SANS respectivement) ont également été utilisées et les données analysées pour obtenir des informations sur les assemblages de protéines qui ont été observé. Les trois protéines sélectionnées ont été la myoglobine, l'anhydrase carbonique et l'inhibiteur de la trypsine - qui présentent des caractéristiques chimiques et structurelles très différentes. Afin de mettre en évidence la spécificité des nano-ions par rapport à ceux des anions classiques chaotropes ou de tensioactifs anioniques, des comparaisons sur les effets mesurés ont été développé afin de démontrer l'importance de la caractéristique superchaotrope de ces espèces ioniques nanométrique, de faible densité de charge.

Dans une dernière partie, la réponse photo-physique du COSAN et de ses dérivés dans des solutions aqueuses a été étudié alors que cette propriété n'avait jamais été explorée. Nous avons examiné l'influence des auto-assemblages de NaCOSAN sur ses propriétés photophysiques dans des solutions aqueuses et organiques, telles qu'elles ont été observées et étudiées au chapitre II, en utilisant la spectroscopie de fluorescence statique et résolue dans le temps. Il a

été constaté que les changements significatifs dans les signaux de fluorescence sont fortement corrélés avec les transitions dans la séquence d'auto-assemblage du cobalta-bis dicarbollide dans l'eau, du monomère à la vésicule puis à la micelle. Les travaux de cette thèse ont aussi mis en évidence une augmentation du temps caractéristique d'une transition électronique de l'ordre de la picoseconde, une augmentation aussi très dépendante de l'état d'agrégation du COSAN en solution aqueuse. Cette dernière partie de ce travail de thèse nous a permis de démontrer l'importance de ces techniques de fluorescence et de photoluminescence qui pourront à terme permettre d'approfondir nos connaissances des propriétés d'assemblage moléculaire des nano-ions en phase aqueuse et organique et des forces intermoléculaires associées.

La section suivante décrit les conclusions tirées des trois chapitres.

Comme décrit ci-dessus, la première partie de ce travail s'est concentrée sur la capacité de COSAN et de son dérivé di-iodé (I_2COSAN) à solubiliser des composés organiques présentant différents caractères hydrophobes. D'une part, en commençant par les alcools à chaîne courte ayant le caractère hydrophobe le plus faible (composés organiques partiellement solubles), il a été démontré que COSAN et ses dérivés augmentent de manière significative leur solubilité dans l'eau. D'autre part, l'efficacité de la solubilisation des clusters de bore diminue de manière significative lorsque le caractère hydrophobe (valeur log*P*) du composé organique augmente. Cependant, contrairement au mécanisme de solubilisation d'un tensioactif, qui nécessite la formation de micelles, COSAN et ses dérivés sont efficaces pour augmenter la solubilité des alcools à chaîne courte dès les premières additions et atteindre, à des concentrations plus élevées, la même solubilité qu'un tensioactif ionique comme le SDS. Nos recherches aux niveaux moléculaire et supramoléculaire ont révélé la formation de co-assemblages nanométriques. La coquille d'hydratation de COSAN est échangée contre une coquille de solvatation d'alcool pendant la formation de ces co-assemblages, ce qui explique l'efficacité du mécanisme - typiquement un nano-ion pour environ des centaines de molécules d'alcool. Le mécanisme de solubilisation basé sur les co-assemblages organiques-inorganiques diffère considérablement de toutes les méthodes de solubilisation classiques. La deuxième particularité de ces co-assemblages organiques-inorganiques est qu'ils peuvent être utilisés pour solubiliser efficacement des composés organiques ayant un caractère hydrophobe beaucoup plus élevé. La capacité de solubilisation de COSAN (et de ses dérivés) est due à sa taille nanométrique, à sa structure rigide, à sa charge délocalisée (aromaticité 3D) et à sa façon particulière d'interagir avec d'autres molécules, qui combine l'électrostatique, la formation de

liaisons dihydrogènes et les effets superchaotropes. D'autres clusters de bore, comme le dodécaborate halogéné tel que $B_{12}Cl_{12}^{2-}$, $B_{12}Br_{12}^{2-}$ et $B_{12}I_{12}^{2-}$, solubilisent les alcools avec un mécanisme de solubilisation comparable à COSAN, toujours basé sur la formation de co-assemblages organiques-inorganiques. Ces co-assemblages eau/dodécaborate halogéné/alcool augmentent l'efficacité de la solubilisation des composés hydrophobes à fort caractère hydrophobe.

La deuxième partie de cette thèse, comme mentionné ci-dessus, est consacrée à l'effet spécifique des ions pour les clusters anioniques de bore mais avec des molécules plus complexes, les protéines, et en gardant à l'esprit l'effet de salting-in associé à une dénaturation des protéines classiquement observée pour les anions chaotropiques. Nous avons observé que des protéines présentant diverses caractéristiques moléculaires et supramoléculaires interagissent fortement avec les amas de bore superchaotropes à des concentrations très faibles, de l'ordre du millimolaire. Contrairement à ce qui est connu avec les agents chaotropes, il a été observé que des assemblages nano-ions/protéines se forment à des rapports molaires de l'ordre de l'unité. La taille de ces assemblages est bien définie et dépend du rapport molaire. Les protéines au sein de ces assemblages protègent partiellement contre la dénaturation (la formation d'assemblages nano-ions/protéines déplace le processus de dénaturation à une température plus élevée). L'efficacité de l'interaction pour induire la formation d'assemblages nano-ions/protéines augmente avec la superchaotropicité du nano-ion ($B_{12}H_{12}^{2-} < B_{12}Cl_{12}^{2-} < B_{12}I_{12}^{2-} <$ COSAN). Ces nano-ions superchaotropes peuvent être considérés comme des colles moléculaires.

Ces deux études ISE montrent clairement que la superchaotropicité est définie d'une manière qui va bien au-delà de la simple observation de l'effet de salinité à des concentrations de sel plus faibles. Comme pour les polymères ou copolymères neutres, il est possible d'observer de nouveaux auto-assemblages, ce qui ouvre un nouveau domaine d'étude.

L'impact de l'auto-assemblage et du co-assemblage avec des solutés organiques sur les caractéristiques photophysiques de l'amas de bore cobalta-bis dicarbollide a été examiné. Il a été constaté que les amas de bore cobalta-bis dicarbollide présentent une fluorescence. En outre, les transitions des monomères aux agrégats en passant par les vésicules dans la séquence d'auto-assemblage du cobalta-bis dicarbollide dans l'eau ont été identifiées par une variation significative du signal de fluorescence. La photoluminescence de type pumpe-probe a également été utilisée pour identifier les nouvelles transitions potentielles qui pourraient

résulter de la formation d'assemblages supramoléculaires. Lorsque COSAN était présent à des concentrations proches de celles auxquelles la formation des assemblages a lieu, la durée de vie en picosecondes des assemblages de COSAN et des co-assemblages avec des solutés organiques a été affectée. Cette section révèle de nouvelles pistes de recherche pour une compréhension complète des interactions sous-jacentes au terme "superchaotropicité".

En conclusion, le comportement remarquable des nano-ions est applicable à tous systèmes de fluides complexes. Cette thèse souligne que le comportement superchaotropique des nano-ions peut être utilisé comme un outil de formulation polyvalent et nouveau pour élaborer de nouveaux solvants, des matériaux et être exploités dans de nombreuses applications au sein de la matière molle.

References

[1] W. Kunz, J. Henle, B.W. Ninham, “Zur Lehre von der Wirkung der Salze” (about the science of the effect of salts): Franz Hofmeister’s historical papers, Curr. Opin. Colloid Interface Sci. 9 (2004) 19–37. https://doi.org/10.1016/j.cocis.2004.05.005.

[2] J.L. Poiseuille, Sur le mouvement des liquides de nature très différente dans les tubes de très petits diamètres, Ann Chim Phys. 21 (1847) 76–110.

[3] Y. Marcus, Effect of ions on the structure of water, Pure Appl. Chem. 82 (2010) 1889–1899. https://doi.org/10.1351/PAC-CON-09-07-02.

[4] B. Naskar, O. Diat, V. Nardello-Rataj, P. Bauduin, Nanometer-Size Polyoxometalate Anions Adsorb Strongly on Neutral Soft Surfaces, J. Phys. Chem. C. 119 (2015) 20985–20992. https://doi.org/10.1021/acs.jpcc.5b06273.

[5] K.I. Assaf, M.S. Ural, F. Pan, T. Georgiev, S. Simova, K. Rissanen, D. Gabel, W.M. Nau, Water structure recovery in chaotropic anion recognition: High-affinity binding of dodecaborate clusters to γ-cyclodextrin, Angew. Chemie - Int. Ed. 54 (2015) 6852–6856. https://doi.org/10.1002/anie.201412485.

[6] K.I. Assaf, W.M. Nau, The Chaotropic Effect as an Assembly Motif in Chemistry, Angew. Chemie - Int. Ed. 57 (2018) 13968–13981. https://doi.org/10.1002/anie.201804597.

[7] T. Merhi, A. Jonchère, L. Girard, O. Diat, M. Nuez, C. Viñas, P. Bauduin, Highlights on the Binding of Cobalta-Bis- (Dicarbollide) with Glucose Units Accepted Article Accepted Article, Chem. - A Eur. J. 26 (2020) 13935–13947. https://doi.org/10.1002/chem.202002123.

[8] M. Hohenschutz, I. Grillo, O. Diat, P. Bauduin, How Nano-Ions Act Like Ionic Surfactants, Angew. Chemie Int. Ed. 59 (2020) 8084–8088. https://doi.org/10.1002/anie.201916193.

[9] K.I. Assaf, B. Begaj, A. Frank, M. Nilam, A.S. Mougharbel, U. Kortz, J. Nekvinda, B. Grüner, D. Gabel, W.M. Nau, High-Affinity Binding of Metallacarborane Cobalt Bis(dicarbollide) Anions to Cyclodextrins and Application to Membrane Translocation, J. Org. Chem. 84 (2019) 11790–11798. https://doi.org/10.1021/acs.joc.9b01688.

[10] J. Warneke, C. Jenne, J. Bernarding, V.A. Azov, M. Plaumann, Evidence for an intrinsic binding force between dodecaborate dianions and receptors with hydrophobic binding pockets, Chem. Commun. 52 (2016) 6300–6303. https://doi.org/10.1039/c6cc01233g.

[11] J. Cebula, K. Fink, J. Boratyński, T.M. Goszczyński, Supramolecular chemistry of anionic boron clusters and its applications in biology, Coord. Chem. Rev. 477 (2023). https://doi.org/10.1016/j.ccr.2022.214940.

[12] J.C. Axtell, L.M.A. Saleh, E.A. Qian, A.I. Wixtrom, A.M. Spokoyny, Synthesis and Applications of Perfunctionalized Boron Clusters, Inorg. Chem. 57 (2018) 2333–2350. https://doi.org/10.1021/acs.inorgchem.7b02912.

[13] A.B. Buades, Z. Kelemen, V.S. Arderiu, A. Zaulet, C. Viñas, F. Teixidor, A fast and simple B-C bond formation in metallacarboranes avoiding halometallacarboranes and transition metal catalysts, Dalt. Trans. 49 (2020) 3525–3531. https://doi.org/10.1039/c9dt04695j.

[14] S. Mukherjee, P. Thilagar, Boron clusters in luminescent materials, Chem. Commun. 52 (2016) 1070–1093. https://doi.org/10.1039/c5cc08213g.

[15] B.P. Dash, R. Satapathy, J.A. Maguire, N.S. Hosmane, Polyhedral boron clusters in materials science, New J. Chem. 35 (2011) 1955–1972. https://doi.org/10.1039/c1nj20228f.

[16] A. Barba-Bon, G. Salluce, I. Lostalé-Seijo, K.I. Assaf, A. Hennig, J. Montenegro, W.M. Nau, Boron clusters as broadband membrane carriers, Nat. |. 603 (2022) 637. https://doi.org/10.1038/s41586-022-04413-w.

[17] P. Bauduin, S. Prevost, P. Farràs, F. Teixidor, O. Diat, T. Zemb, A theta-shaped amphiphilic cobaltabisdicarbollide anion: Transition from monolayer vesicles to micelles, Angew. Chemie - Int. Ed. 50 (2011) 5298–5300. https://doi.org/10.1002/anie.201100410.